

OBSERVATION OF DEFECTS IN DEVICE SILICON

Thesis submitted for the Degree of  
Doctor of Philosophy of the  
University of London

by

Raymond Ogden  
Imperial College of Science and Technology.

The Allen Clark Research Centre  
The Plessey Company Limited  
Caswell, Towcester, Northants

January 1977

To my Grandparents

Reuben and Ella.

ABSTRACT

The results are presented of two studies of materials problems encountered in an industrial laboratory concerned with silicon device manufacture. Both deal with the observation of structural defects such as dislocations and stacking faults in silicon. In each case the defects encountered were process-induced and the results are relevant to programmes which aim to control process parameters to minimise yield hazards.

The first study (Part I) used mainly transmission electron microscopy (TEM) techniques to assess the influence of trace amounts of gaseous contaminants on the structural perfection of Si epitaxial layers grown by the pyrolysis of silane under ultra high vacuum conditions. In particular, ethylene was found to have a marked effect causing the formation of stacking fault structures in  $\{111\}$  layers. Two types of faults were produced, depending upon the growth temperature: at low temperatures ribbon faults formed by Shockley partial dislocation loops were found, but at higher temperatures these gave way to configurations such as stacking fault tetrahedra. It is proposed that the fault structures are nucleated by carbon contamination during epitaxial growth and the difference in structure with temperature is interpreted by changes in the way carbon is incorporated in the layer. The presence of Shockley loops suggests a simple mechanism for the formation of stacking fault tetrahedra by the intersection of three loops on adjacent inclined  $\{111\}$  planes.  $\{110\}$  and  $\{100\}$  layers grown under similar conditions to  $\{111\}$  layers did not form ribbon stacking faults and examination of layer surfaces using the replica technique is useful in explaining such differences in defect structure.

The second study (Part II) used several assessment techniques to characterise defects in a simple silicon device and to investigate their effect on the electrical properties of the device. X-ray topography was used to map the dislocation arrays on two processed slices of photo-transistors. Comparison with the yield maps of the slices showed strong correlations between dense dislocation areas and failed devices. The correlations, however, were far from 1 to 1 and other microscopy techniques, in particular Scanning Electron Microscopy (SEM) were used to examine selected devices in more detail. The specimen current mode of SEM was found useful in locating defects which were electrically active. Spots of contrast found in devices using this mode were shown to be due to dislocations threading the collector:base junction. No

evidence was established for the direct influence of dislocations on premature breakdown of the devices but TEM studies of dislocation structures in these slices gave some insight into possible breakdown mechanisms.

A serious yield hazard was shown by SEM to be oxide bars lying across the emitter region. A mechanism for their formation, based on photo-engraving mask scratches, is given and their effect on p n junctions in the device is explained.

FOREWORD

The work reported here was carried out in the Allen Clark Research Centre of The Plessey Company Limited and in the Department of Metallurgy at Imperial College. It concerns problems of practical importance to Si device manufacturers. A characteristic of industrial research is that it must deal with a variety of inter-related and changing problems. The two studies presented here involve quite different technologies but are unified in several ways. The basic aim is the same: to improve the quality of Si devices. This is done by understanding how defects are introduced by processing steps involved in device production, leading to control of these defects by choice of processing conditions.

In Part I defects are characterised in epitaxial layers grown under closely specified conditions. This section is mainly concerned with mechanisms for the formation of the defects. It treats a rather narrow subject in some depth and the results will be of more interest to a materials scientist than to a production engineer.

Part II is much wider in scope and consequently its conclusions are more tentative than the first investigation. The apparently simple result of correlation between device yield and dislocation density was not fully explained, neither was slice to slice variation of device characteristics. Utilisation of several microscopy techniques and electrical measurements produced many interesting results but also raised further problems which could not be sufficiently examined within the terms of available time and cost.

Current studies are mentioned in the Conclusions to demonstrate how techniques learned from the present studies are being applied to newer problems.

ACKNOWLEDGEMENTS

This Thesis incorporated work carried out under a C.V.D. Contract and is published by permission of the Ministry of Defence (Procurement Executive) and the Directors of The Plessey Company Limited. The author wishes to thank the many colleagues at the Allen Clark Research Centre for their contribution to this work. In particular I would mention Mr. G.V.Smith, my industrial supervisor and Dr. R.W.Bicknell to whom I am greatly indebted for their patience and tuition over the years I have spent in the Structure Laboratory. The dependence of this work on the experimental skills of Mr. R.R.Bradley is acknowledged in the text and I record my appreciation of the many stimulating discussions with him and with Drs. B.E.Watts and B.Lewis.

I acknowledge the practical help and many discussions held with the staff of the Development Area and Pilot Plant at Caswell in connection with Part II of the thesis. Thanks are due to Mr. G.Chilton for suggesting the problem and for supplying the material and electrical measurement facilities. I also thank Mr. R. Tomalin and Mrs. P.Hales for the preparation of specimens for the SEM investigation, and Mr. C. Hill for help with the calculations in Appendix C. I am grateful to Mr. W.E.Wilkinson for the photographic reproductions, to Mrs. A.Mansfield for careful <sup>typing</sup> preparation of the manuscript and to members of the Report Section for the art work on several of the line drawings.

It is a pleasure to thank Dr. D.B.Holt, my supervisor at Imperial College for the enthusiasm and encouragement he has always shown me and for the painstaking proof reading and criticism of the text. I must also thank Mr. J.B.Steyn for his assistance with the operation of the SEM at Imperial College. I am also grateful for helpful discussions held at various times with Dr. W.J.Tunstall at Oxford University, Drs. A.Howie and L.M.Brown at the Cavendish Laboratory and Dr.M.H.Loretto at Birmingham University.

TABLE OF CONTENTS

TITLE PAGE	.i.
DEDICATION	.ii.
ABSTRACT	.iii. - iv.
FOREWORD	.v.
ACKNOWLEDGEMENTS	.vi.
TABLE OF CONTENTS	.1.
LIST OF TABLES	.3.
LIST OF FIGURES	.3.
TITLE PAGE (PART I)	.5.
<u>CHAPTER 1.</u> INTRODUCTION	.6.
1.1. Silicon epitaxy, general	.6.
1.2. Growth Studies in epitaxial Si.	.8.
1.3. Stacking faults in epitaxial Silicon	.15.
<u>CHAPTER 2.</u> EXPERIMENTAL	.27.
2.1. Preparation of epitaxial layers	.27.
2.1.1. Growth System	.27.
2.1.2. Substrate preparation	.27.
2.1.3. Growth schedule	.27.
2.2. Examination techniques	.29.
2.3. Specimen preparation	.32.
<u>CHAPTER 3.</u> Results: Ethylene contamination studies, $\{111\}$ layers.	.35.
3.1. Control runs, no deliberate contamination	.35.
3.2. Low temperature growth (830-860°C)	.41.
3.2.1. Annealing experiments	.46.
3.2.2. Termination of ethylene during growth	.50.
3.2.3. Heavy ethylene contamination	.53.
3.3. Moderate and high temperature growth (860-1200°C)	.53.
3.4. Silicon carbide	.60.
<u>CHAPTER 4.</u> Results: Ethylene contamination studies, $\{110\}$ & $\{100\}$ layers.	.66.
4.1. $\{110\}$ layers	.66.
4.2. $\{100\}$ layers	.70.
<u>CHAPTER 5.</u> Results: Contamination studies with other gases	.77.
5.1. Methane	.77.
5.2. Oxygen	.80.
5.3. Water Vapour	.80.
<u>CHAPTER 6.</u> Discussion	.84.
6.1. Tetrahedron-type stacking fault structures	.84.
6.2. Nucleation of ribbon stacking faults	.86.
6.3. Propagation of ribbon faults	.91.
6.4. Model for nucleation of stacking fault tetrahedra	.94.
6.5. The effect of layer orientation: ethylene contamination	.97.
6.6. The effect of other contaminant gases	.99.

	<u>.2.</u>
6.6.1. Methane	.99.
6.6.2. Oxygen and Water Vapour	.99.
<u>CHAPTER 7.</u> Summary and Conclusions	.101.
TITLE PAGE - PART II	.103.
<u>CHAPTER 8.</u> Introduction	.104.
8.1. Effect of imperfections in electrical properties	.107.
8.1.1. Dislocations	.107.
8.1.2. Current leakage and precipitates	.107.
8.2. Outline of present investigation	.108.
<u>CHAPTER 9.</u> Experimental	.109
9.1. Operation of phototransistor	.109
9.2. Fabrication of phototransistors	.111.
9.3. Examination technique	.111.
9.3.1. Electrical	.111.
9.3.2. X-ray topography (XRT)	.115.
9.3.3. Optical microscopy	.123.
9.3.4. Scanning electron microscopy (SEM)	.123.
9.3.5. Transmission electron microscopy (TEM)	.124.
9.4. Examination procedure	.126.
<u>CHAPTER 10.</u> Results	.127.
10.1. Electrical failure correlation with slip	.127.
10.2. SEM observations	.135.
10.2.1. Photoengraving faults	.135.
10.2.2. Dislocation imaging using the BEVE mode	.137.
10.2.3. Metallisation pits	.145.
10.3. TEM observations	.145.
10.3.1. Pitting	.145.
10.3.2. Dislocations	.145.
10.3.3. Oxidation-induced stacking faults	.152.
10.3.4. Emitter-edge dislocations	.152.
10.4. Miscellaneous results	.156.
10.4.1. Bevel and Stain	.156.
10.4.2. Sheet resistance results	.156.
10.4.3. Photocurrent measurements	.158.
10.4.4. Cause of slip in device slices	.160.
<u>CHAPTER 11.</u> Discussion	.164.
11.1. First observation of individual dislocations by	.164.
11.2. Electrical behaviour of dislocations <sup>BEVE</sup> contrast.	.165.
11.3. Photoengraving faults	.167.
11.4. Photocurrents and defects	.170.
11.5. Summary	.170.
<u>CHAPTER 12.</u> Conclusions	.172.
<u>APPENDICES:</u>	
A. Diffraction contrast analysis in TEM	.174.
A1. Stacking fault ribbons	.174.
A2. Inclined dislocations	.187.
A3. Stacking fault pyramids in $\{100\}$ epitaxial Si.	.188.

B. Elastic energy calculations .197.

    B1. The shear modulus at the growth temperature .197.

    B2. The elastic energy of a carbon atom in a Si crystal .197.

    B3. The binding energy of a carbon atom to an edge Shockley dislocation. .198.

    B4. The self energy of an edge Shockley dislocation .199.

    B5. Summary .200.

C. The Depletion Width of Z45 Base:collector junction .202.

    C1. Estimation of boron diffusion profile .202.

    C2. Calculation of depletion width W .204.

    C3. Diffusion length calculations .210.

REFERENCES

.211.

LIST OF PUBLICATIONS

.212.

LIST OF TABLES

Table 1.1 Si Epitaxial Growth Studies

    1.2 Stacking Fault Studies in Epitaxial Si

        2.1 Examination Techniques

        3.1 Ethylene contamination {111} Epitaxial Si layers

        3.2 Summary of TEM results on ethylene-contaminated {111} layers

        3.3 Identification of SiC layer

        4.1 Ethylene contamination {110} layers

        4.2 Ethylene contamination {100} layers

        5.1. Methane experiments

        5.2 Oxygen experiments

        5.3 Water Vapour experiments

        5.4 Si ring patterns from Fig.5.2c(d)

    8.1. Crystal imperfections in Semiconductor Si.

    9.1 Process Schedule for phototransistor slices

    10.1 Dow Corning slice

    10.2 Texas Instruments' slice

    10.3 D.C. Slice (data from Table 10.1)

    10.4 T.I. Slice (data from Table 10.2)

    10.5 Zero values of  $g \cdot b$  for  $\frac{1}{2} \langle 110 \rangle$  type dislocations for reflections used in Fig. 10.16.

    10.6 Sheet resistance of double-diffused slice regions

    10.7 (a) Photocurrent measurements on Dow Corning devices

        (b) Photocurrent measurements on Texas Inst. devices

    A1.  $g \cdot b$  values of possible partials bounding stacking faults on (111) planes.

    A2.  $g \cdot b$  values of perfect dislocations for [110] zone reflections, Fig.A2.

    A3.  $g \cdot b$  values of possible low energy stair-rod dislocations

    C1. Estimated carrier concentrations versus depth for boron diffusion.

LIST OF FIGURES

Fig. 1.1. The Diamond-Cubic structure showing Tetrahedral Bonding of atoms.

    1.2. The Diamond Lattice with [111] vertical viewed near the [110] axis

    1.3. Stacking Faults in the Diamond Lattice of Intrinsic and Extrinsic Type.

    1.4. Booker & Stickler's(1962) Model of Stacking Fault Nucleation

    1.5. Jaccodine (1963) & Booker & Stickler (1963) Models of Stacking Fault Tetrahedra Nucleation on {111} substrate.

    2.1. UHV System for Epitaxial Growth of Silicon from silane.

    2.2. Micrographs of epitaxial Si layer showing defective growth

    2.3 Diagram of jet-etching apparatus

    3.1. Examples of viewing techniques used in study, as applied to control layers (no deliberate contamination)

    3.2. Stacking fault Structures in control layer RB19

    3.3. Saucer-like depressions in control layer RB26

    3.4. Ribbon stacking faults in low temperature, high ethylene layer RB1

- Fig. 3.5. Burgers vector analysis of extended dislocation (R) in low temperature, ethylene contamination layer RB37
- 3.6. Surface study of low temperature, heavy ethylene layer RB14
- 3.7. Defect & surface structures at medium & low ethylene levels.
- 3.8. Anneal at 1055°C,  $2 \times 10^{-5}$  torr, of layer RB14 containing ribbon faults showing SiC contamination film.
- 3.9. Anneal at 1200°C in UHV epitaxy system immediately after growth of layer.
- 3.10. Ethylene termination during epitaxial growth RB35B
- 3.11. Surface studies & microstructure of very heavy ethylene contamination layer RB35A
- 3.12. Moderate temperature growth (940°C) 50ppm ethylene present, RB63A
- 3.13. Growth at 1065°C showing stacking fault tetrahedra and line faults, RB38B
- 3.14. Nucleation of stacking fault tetrahedra during epitaxial growth, RB63B
- 3.15. Growth at 1075°C showing few stacking faults & pin sites.
- 3.16. Extracted material in Pt/C replicas of ethylene contaminated layer.
- 3.17. SiC filaments in epitaxial Si.
- 3.18. Layer RB14 showing speckled background in  $s > 0$  condition
- 3.19. Anomalous pitting in low temp. growth runs
- 4.1. Stacking fault configuration in  $\{110\}$  layers (RB25)
- 4.2. Complex stacking fault structure in (110) layer, (RB25)
- 4.3. Surface pitting in RB25
- 4.4. Structure of  $\{110\}$  layer growth with 100ppm ethylene, RB27B
- 4.5. Resolution of stacking fault structure of  $\{110\}$  layer, RB27.
- 4.6. Inclined dislocations in  $\{100\}$  epitaxial Si, cont. layer RB5.
- 4.7. Growth centres in  $\{100\}$  epi-layers, various viewing techniques
- 4.8. Growth centres in RB13
- 4.9. Pt/C replicas of 'spangles' in RB44A
- 5.1. Stacking faults & microtwinning in RB56B
- 5.2. Polycrystalline Si in RB48B grown with water vapour contm.
- 5.3. Stacking faults & precipitation in RB47B grown with water vapour contamination
- 6.1.  $\langle T10 \rangle$  carbon filament on surface step
- 6.2. Bond configurations of edge Shockley dislocations bounding intrinsic and extrinsic stacking faults
- 6.3. Configuration of  $60^\circ$  dislocation lying in  $[1\bar{1}0]$  orientation in (111) substrate plane, having Burgess vectors of  $\frac{1}{2} [011]$  inclined to substrate plane.
- 6.4. Diagram representing growth step retardation by carbon impurity atoms & their subsequent incorporation in epitaxial layer.
- 6.5. (a) Analysis of ribbon intersection shown in Fig. 3.12.  
(b) Formation of intrinsic stacking fault tetrahedra from three Shockley loops.
- 6.6. Intersection of extrinsic stacking fault loops at acute angle.
- 9.1. Z45 Phototransistor
- 9.2. Curve traces showing various breakdown characteristics of Z45 devices
- 9.3. Breakdown voltages  $BV_{CEO}$  Results on portion of Dow Corning Z45 slice
- 9.4. The Lang X-ray topography camera
- 9.5. Transmission XRT micrographs of Dow Corning half-slice
- 9.6. Demonstration of Automatic Bragg Angle Control on T.I half-slice.
- 9.7. Optical Micrograph of "scratch" on probe tested Dow Corning Z45 slice.
- 9.8. Circuit diagram showing a.c. coupling of phototransistor to specimen current amplifier.

- Fig. 10.1 (a) D.C. slice yield map  
(b) D.C. slice XRT montage
- 10.2 (a) T.I. slice yield map  
(b) T.I. slice XRT montage
- 10.3 Surface XRT micrographs of D.C. half-slice
- 10.4 SEM Micrographs of scratch features on D.C. slice
- 10.5 First observation of SEM contrast at dislocations in phototransistor.
- 10.6 Comparison of XRT & BEVE mode SEM in heavily slipped device
- 10.7 D.C. device C8R26 ( $BV_{CEO}=94V$ ) crossed by narrow slip band
- 10.8 Effect of increased reverse bias on collector:base junction of device shown in Fig.10.7.
- 10.9 Comparison of XRT & optical microscopy on device shown in Figs10.7 and 10.7 after prolonged examination by SEM.
- 10.10 Y modulation line scan traces of a row of 3 dislocations
- 10.11 Comparison of d.c. and a.c. coupling to SCA of device containing dislocations
- 10.12 SEM micrographs of metallisation pits in Al-coated regions of device slice
- 10.13 Pits on Scribe Channel of D.C. slice
- 10.14 Pitting in end strip of T.I slice
- 10.15 Helical dislocation band in double-diffused end strip region of T.I. slice
- 10.16 Analysis of a dislocation band in T.I. end strip
- 10.17 Dislocation band in base area of T.I. device
- 10.18 Dislocations in scribe channels
- 10.21 Montage of dislocations in emitter region of T.I. device
- 10.22 Sections of double-diffused regions obtained by the bevel and staining technique
- 10.23 XRT micrographs of D.C. slices
- 10.24 Typical observed temperature cycle of Si slice on RF heated susceptor during gas polishing
- 10.25 Dislocation generation during successive heat treatments
- 11.1 Formation of oxide bar photoengraving faults in base window
- 11.2 Effect of oxide bars on diffusion fronts
- A1.  $[111]$  stereogram of cubic crystal, showing great circle of  $(1\bar{1}1)$  and  $(110)$  planes
- A2. Analysis using reflections in  $[110]$  zone
- A3. Analysis using reflections in or near  $[111]$  zone
- A4. Outer fringe contrast of intrinsic and extrinsic stacking faults using 2 beam,  $s = 0$  diffraction conditions
- A5. Representation of Shockley partial dislocations analysis in Appendix A1.
- A6. The Thompson tetrahedron showed opened out, apex A originally pointing into plane of paper
- A7. Finish/start, Right hand (FS/RH) (perfect crystal) convention for Burgers vector circuit to define the Burgers vector of a dislocation
- A8. Inclined dislocations in RB14
- A9. Analysis of stacking fault pyramid in  $\{100\}$  epitaxial Si
- A10. Analysis of stair-rod dislocations in stacking fault pyramid, all micrographs bright field,  $s > 0$  condition
- A11. Diagram showing stacking fault pyramid orientation and Burgers vectors.
- A12. Intrinsic Shockley loops which could form on served stair-rods
- A13. Series showing pyramid ' dislocation half-loop in  $\{100\}$  epi-layer.
- B1. Elastic energy variation of carbon atom and edge Shockley partial dislocation close to Si surface
- C1. Calculated boron profile for diffused base of Z45 base.
- C2. Carrier concentrations close to collector/base junction.

PART I

TRANSMISSION ELECTRON MICROSCOPY OBSERVATIONS ON EPITAXIAL SILICON

## CHAPTER 1. INTRODUCTION

In the technology of silicon device manufacture, the deposition of high quality Si epitaxial layers is vitally important. The term "epitaxial" means that there is a definite relationship between the orientation of the grown layer and the substrate. In the silicon on silicon system these orientations are identical, e.g.  $\{111\}$  layer //  $\{111\}$  substrate and  $\langle\bar{1}10\rangle$  layer //  $\langle\bar{1}10\rangle$  substrate. The low temperature ( $<1000^\circ\text{C}$ ) growth of epitaxial Si using the decomposition of silane ( $\text{SiH}_4$ ) is highly relevant to present-day needs of the industry (Bloem 1973). The involvement in research in this field since the early 1960's at the Allen Clark Research Centre at Caswell has added substantially to the understanding of processes occurring in Si epitaxy.

The work presented here is a study, chiefly by Transmission Electron Microscopy (TEM), of the structure of epitaxial layers grown from silane which was deliberately contaminated with trace amounts of gases. In particular, ethylene was found to induce various stacking fault structures and preliminary results of this aspect of the work was presented by Ogden, Bradley and Watts in 1971. An analysis of stacking fault loops occurring in  $\{111\}$  layers was reported the following year (Ogden 1972) and more recently a model was proposed for the nucleation and growth of these features (Ogden, Bradley and Watts 1974). The work was supported by C.V.D. contract and under the direction of Dr.B.E.Watts. All epitaxial layers were prepared by Mr.R.R.Bradley using the UHV system and growth techniques which he developed at Caswell and it was his expertise in this field that has made this study successful. It will be shown in Section 1.2 that the achievement of good quality Si epitaxial layers grown at low temperatures has been hard won and is not widely reported. The effect of traces of contaminant gases could only have been established with carefully controlled experiments.

### 1.1. Silicon epitaxy, general

The impetus to exploit Si epitaxy came in the early 1960's with the introduction of planar technology in the fabrication of Si transistors and integrated circuits. Chemical Vapour Deposition (CVD) techniques for the growth of high purity polycrystalline Si were developed in the preceding decade and were modified to allow the deposition of single crystal silicon layers epitaxially on Si substrates (Glang & Wajda 1962). By 1961, epitaxial growth from the gases  $\text{SiCl}_4$  and  $\text{SiHCl}_3$  was well established commercially. Basically the gas, diluted with  $\text{H}_2$ , is passed over the Si substrate which sits on the R-F heated graphite

susceptor. The required dopant is introduced as a gaseous compound into the gas stream and substrate temperatures are typically 1100 - 1200°C. The use of silane at low partial pressures to lower the temperature at which epitaxial growth could be achieved was reported two years later by Joyce & Bradley (1963). The advantage of low temperature growth is the limitation of out-diffusion from the substrate (auto doping), allowing the formation of extremely abrupt p-n junctions. Many device applications depend on highly controlled dopant profiles, e.g. high frequency transistors. Evaporation techniques have been used to grow epitaxial films down to 400°C (Widmer 1964) but as yet do not rival CVD techniques because of the difficulty in controlling dopant additions (Watts 1973).

The most commonly observed crystallographic defects in Si epitaxial layers are stacking faults and it was soon demonstrated that these could be initiated by contaminants or damage on the substrate. Many studies of stacking fault structures in epitaxial Si have been made and models of nucleation proposed. These are discussed in Section 1.3. By 1966 the state of the art enabled epitaxial layers to be produced routinely with low defect densities ( $< 10^2 \text{ cm}^{-2}$ ) at high growth temperatures ( $> 1100^\circ\text{C}$ ). The achievement of low defect densities became progressively more difficult as the growth temperature was lowered. By using ultra-high vacuum (UHV) techniques and careful substrate preparation, Joyce et al (1969a,b) grew essentially defect-free epitaxial layers from silane at temperatures as low as 800°C. The growth system used in the present work was developed from the system described by Joyce, Neave & Watts (1969b).

Today the emphasis in Si epitaxy is on the process control of parameters affecting device performance, notably layer thickness and resistivity, using semi-empirical means. For the former, this means control of growth rate and since the deposition systems are rarely in thermodynamical equilibrium, the rate is strongly influenced by the geometry of the particular system used, i.e. it is dependent on the gas flow conditions. Fortunately the thickness can be monitored in-situ using infra-red spectrometry and controlled to within a few percent. No similar technique has been found for resistivity control, however, and point to point variations of 15% are normal. With the trend to microwave-frequency ( $> 10^{10} \text{ Hz.}$ ) transistors employing active areas a few microns square with  $< 1 \mu\text{m}$  thick epitaxial layers, the need to overcome this problem is urgent (Bloem 1973). The present work is not particularly relevant to this need but hopefully it may contribute to the understanding of the formation of defect structures which are still a recurring problem in epitaxial silicon (e.g. Baker & Ogden 1975).

## 1.2. Growth Studies in epitaxial silicon

The mechanisms of crystal growth from the vapour phase by adsorption and surface diffusion have been studied intensively for many years. In a key paper, Burton, Cabrera and Frank (1951), developed a theory whereby growth proceeds by the nucleation of monolayers, i.e. two-dimensional (2D) steps containing kinks in equilibrium with a supersaturated vapour. The theory predicts that for the case of low-index planes at low supersaturation levels, steps created by the emergence of dislocations at the surface are necessary for growth to proceed. It has since become apparent experimentally that this is not always the case and Lewis (1974), for example, has developed a model which can be used to compare growth rates with and without dislocations under different supersaturation conditions.

Initial growth experiments on epitaxial Si using both CVD and evaporation methods invariably showed growth centres which were three-dimensional (3D) and usually faceted and contamination of the substrate was blamed. Frank (1958) and Cabrera & Vermilyea (1958) discuss how impurity atoms may be less readily adsorbed into the growing layer than majority atoms and cause slowing down of step motion. This allows repeated fresh step nucleation on top of uncompleted steps leading to step bunching, i.e. 3D growth occurs. Impurity atoms concentrate ahead of the step pile-up but eventually 'step-hopping' occurs and the impurity atoms are buried beneath the surface.

Details of the experimental techniques employed and of the progress achieved in particular growth studies are now reviewed and the results have been summarised in Table 1.1.

In an early paper by Charig et al (1962), the surfaces of thin Si layers were examined by platinum/carbon replicas in the transmission electron microscope. 3D growth centres invariably formed and it was believed that residual contamination, possibly oxygen, on the substrate was responsible. The paper emphasised that surface studies were as useful as thin foil TEM observations of stacking fault configurations in understanding their nucleation mechanisms. Examination techniques were assembled which were adopted in the present work, i.e. interference contrast optical microscopy, etching, glancing angle electron diffraction (G.A.E.D) (otherwise known as reflection high energy electron diffraction, R.H.E.E.D), Pt/C replica and thin foil transmission

TABLE 1.1. Si EPITAXIAL GROWTH STUDIES

Reference	System	Substrate plane	Growth temp. °C	Observation techniques	Results
Charig et al (1962)	SiHCl <sub>3</sub> + H <sub>2</sub> Resistance-heated substrate, quartz reactor	110	1250	Pt/C replica, GAED, TEM etching, interference contrast (i.c.) microscopy	3D growth centres, probably due to contamination, possibly oxygen
Joyce & Bradley (1963)	Si H <sub>4</sub> + H <sub>2</sub> quartz reactor	110	920-1260	i.c., Pt/C GAED	epitaxial growth achieved down to 920°C
Unvala & Booker (1964)	Evap. electron beam heated source 10 <sup>-5</sup> -10 <sup>-6</sup> torr.	111	1080-1220	etching, C replica, GAED	high deposition rates gave no 3D growth centres or stacking faults, but layers strained & eventually polycrystalline. Amorphous contamination suspected as cause of 3D nucleation. High sf densities in growth centres on thermal etch pitted substrate. Low rates gave 3D centres but after coalescence, growth 2D.
Booker & Unvala (1965)	substrate thermally cleaned 1200°C 15 min.	111	1200	TEM	
Booker, Joyce & Bradley (1964)	Si H <sub>4</sub> at 0.3 - 1.3 torr in vacuum system	110	1180-1240	i.c., GAED, TEM	sf density progressively fell as deposition rate increased but overall crystalline perfection poorer.
Joyce & Bradley (1966)	Molecular beam Si H <sub>4</sub> ~ 10 <sup>16</sup> Mols.cm <sup>-2</sup> sec. <sup>-1</sup> . UHV 10 <sup>-9</sup> torr.	111 110	845	i.c., GAED, Pt/C	UHV system described in detail.
Booker & Joyce (1966)	"	111	845	Ditto + TEM	Under "clean" conditions, growth centres defect-free and no misfit defects on coalescence. Carbon contam. gave SiC after 1200°C anneal. Subsequent growth gave inverted centres & multiple twinning.
Joyce, Bradley & Booker (1967)	Chem. pol. or HCl gas pol. substrate	111	800-940	"	induction period noted during which SiO <sub>2</sub> removal from substrate as SiO by Si influx before growth can commence.

Abbink, Broudy & McCarthy (1968)	UHV evap. $\sim 10^{-9}$ torr.	111	800	special Pt/C replica	Resolved monolayer steps on coalesced film, i.e. 2D growth. Initial growth nuclei always 3D, indicating contam. Role of contam., step motion, discussed
Joyce et al (1969a)	improved version of J&B(1966). H Br gas pol, HF, ethanol quench for substrate	100	790-1050	as earlier work + SEM	1250°C 'thermal - clean' prior to growth gave 2D nucleation, No SiC detected. Pump oil vaps. gave 3D growth
Joyce, Neave & Watts (1969b)	"	111	850	as earlier work	ethylene contam. gave 3D centres, carbon Auger signal. Both absent after pregrowth anneal at 1200°C of substrate.
Charig & Skinner (1969)	UHV, LEED system	111	850	LEED, Auger spectro-copy GAED	C, O detected on substrate prior to thermal clean. Criterion of Si (111) -7 pattern as characterising "clean" surface shown as inadequate, since C <sub>2</sub> H <sub>4</sub> gave C on surface without pattern change. SiC detected after heavy C <sub>2</sub> H <sub>4</sub> exposure & heated 900-1100°C
Brown & Watts (1970)	UHV + ethylene at 10 <sup>-6</sup> torr	100 111 110 311	800-1250	TEM, GAED, extraction replica	SiC found 800-1150°C, usually epitaxial, little polycrystalline deposn., as discrete particles, also SiC detected on substrate 830-1050°C in absence of C <sub>2</sub> H <sub>4</sub>
Cullis & Booker (1971)	UHV electron beam sublimation. Substrate 1250°C T/C	111	800-1000	TEM, i.c.	growth on non-T/C substrates gave 3D centres and roughness. 1250°C T/C gave 2D evaporation steps, then deposn. gave 2D growth + SiC pinning centres.
Henderson & Helm (1972)	ion pumped UHV in-situ argon sputter, SiH <sub>4</sub>	111	823-923	in-situ GAED, Auger & mass spectrom. i.c. Pt/C rep.	Avoids T/C by Ar. Sputt. + 400 - 600°C anneal. SiH <sub>4</sub> decompn. energy & surface diffusion energy $\sim 1$ eV. 'Clean' surface characterised by limit of Auger spectrom. ( $\sim 10^{13}$ cm <sup>-2</sup> ) gave defect-free growth down to $\sim 820$ °C.

electron microscopy (TEM). Joyce & Bradley (1963) were able to grow Si epitaxial layers at temperatures down to  $920^{\circ}\text{C}$  by using silane at  $< 2$  torr pressure which suppressed homogeneous gas phase reactions. The growth rate was typically  $1 \mu\text{m}/\text{min}$ , being determined by chemisorption or by reaction and desorption processes at lower temperatures. Higher deposition rates gave better surfaces and lower stacking fault densities possibly because contaminants were swamped by majority atoms. Unvala & Booker (1964) demonstrated a similar effect in evaporated Si layers. Contamination with oxygen greatly increased the number of stacking faults whilst coal gas induced the multiple-twinned structures known as tripyramids, probably due to the formation of SiC crystallites on the substrate (Miller et al 1963). In their subsequent paper, Booker & Unvala (1965) showed, using TEM, that a predeposition thermal clean at  $1200^{\circ}\text{C}$  produced pitting, probably due to oxidation and that epitaxial growth at  $1200^{\circ}\text{C}$  gave growth centres in pitted areas which were heavily faulted. There was evidence of a build-up of amorphous contamination to form a continuous film between the growth islands. It was suggested that contamination piled up ahead of the growth centres and slowed down the lateral spread. Eventually Si growth forced past these barriers, leaving the buried debris behind. At a later stage of growth when the substrate was entirely covered, the surface was very smooth, i.e. 2D growth occurred. Alternatively 2D growth could be established very quickly using deposition rates  $> 1 \mu\text{m}/\text{min}$  although the quality of the epitaxial layers, as judged by the diffuse Kikuchi band pattern in G.A.E.D, deteriorated. At rates  $> 3 \mu\text{m}/\text{min}$ . layers were always polycrystalline. A possible explanation was that  $\text{SiO}_2$  contamination was converted to SiO by the high influx of Si atoms. The SiO then evaporated leaving a "clean" surface for 2D growth. In a parallel experiment, Booker, Joyce & Bradley (1964) used silane to deposit layers at growth rates up to  $17 \mu\text{m}/\text{min}$ . and found that although stacking fault densities fell with increasing growth rate, the overall crystalline perfection as indicated by diffuse transmission electron diffraction Kikuchi patterns became poorer.

In the series of papers discussed below, the team at Caswell developed a technique to study the initial growth of Si from silane. Their molecular beam apparatus was described by Joyce & Bradley (1966). A well characterised stream of silane molecules ( $\sim 10^{16} \text{cm}^{-2} \text{sec}^{-1}$ ) was directed onto a Si substrate

held typically at 850°C in a UHV system. The purpose was to study nucleation mechanisms and kinetics of CVD of Si. This would be done more readily than in a conventional system where gas diffusion is often the rate controlling step, i.e. where the system geometry is critical, and where the time taken to reach steady state conditions is often greater than nucleation times. A shutter enabled growth to be controlled and typical growth rates of 0.01  $\mu\text{m}/\text{min}$ . were achieved. The gases in the system were monitored by a mass spectrometer. Substrates were chemically polished and annealed at  $\sim 900^\circ\text{C}$  in the UHV system by direct resistance heating prior to growth. Growth centres on  $\{111\}$  substrates were shaped as truncated tetrahedra with facets of probable  $\{113\}$  orientation and were entirely defect-free (Booker & Joyce 1966). Where growth centres had merged, no defects had formed as a result of mismatch. The use of UHV conditions enabled the effect of hydrocarbon vapours deliberately introduced from the pumping system to be studied. On subsequent annealing at high temperatures,  $\beta$ -SiC was detected on the substrate. Initial growth gave inverted and multiple-twinned growth centres. Joyce, Bradley & Booker (1967) noted an induction period due to the removal of oxide before any growth commences. They confirmed that the oxide reacts with the influx of Si atoms to form SiO which then evaporated and subsequent growth was defect-free. Further improvements to the UHV system enabled substrates to be annealed at high temperatures without SiC being detected and it was found that subsequent growth occurred without the formation of 3D growth centres (Joyce et al 1969a). The addition of trace amounts of carbon-containing gases into the system caused the reappearance of 3D centres even though no change in the "clean" Si (111) - 7 low energy electron diffraction (LEED) pattern could be detected. In a later paper Joyce, Neave & Watts (1969b) firmly established the effect of carbon contamination. Exposure of  $\{111\}$  substrates to trace amounts of ethylene at room temperature and at 500°C led to the formation of 3D nuclei, but recycling to 1230°C prior to growth again gave 2D growth. In parallel experiments using LEED and Auger spectroscopy, Charig & Skinner (1969) detected carbon and oxygen on pre-annealed substrates even when the system was not deliberately contaminated with ethylene. Other gaseous contaminants, CO, CO<sub>2</sub> & O<sub>2</sub> in concentrations comparable with ethylene, did not disturb the 2D growth. Unlike ethylene, CO & CO<sub>2</sub> did not produce a detectable carbon Auger signal. Although O<sub>2</sub> caused a deterioration of the LEED indicating absorption, the pattern

recovered at growth temperature consistent with its rapid removal. A carbon Auger signal was not detected on substrates after heating above  $1200^{\circ}\text{C}$  and Charig & Skinner discussed the possibilities of SiC crystallite formation on the substrate or of diffusion of carbon into the bulk of the Si. Brown & Watts (1970) subsequently showed, using GAED and extraction replicas, that although  $\beta$ -SiC formed epitaxially on substrates exposed to ethylene at temperatures from about  $800$  to  $1100^{\circ}\text{C}$ , it was absent on substrates held at  $1200^{\circ}\text{C}$ . The latter was possibly due to thermal etching or to a reduced "sticking" probability of ethylene at this temperature. SiC was also detected on substrates heated under UHV conditions even when ethylene was not present. Two possible sources of this contamination were substrate preparation reagents and pump oil vapours.

Similar results to those of Joyce, Neave and Watts on evaporated  $\{111\}$  Si films, had been reported earlier by Abbink, Broudy & McCarthy (1968). By refining the Pt/C replica technique they were able to resolve monolayer steps on  $1000\text{\AA}$  thick layers evaporated under UHV conditions. Pinning sites were observed where Si growth had been suppressed and their cause was believed to be  $\beta$  SiC crystallites detected on substrates which were annealed at  $900^{\circ}\text{C}$  prior to growth. On layers only  $100\text{\AA}$  thick, rough areas and very large 3D nuclei  $\sim 1\ \mu\text{m}$  across were observed and ascribed to contamination. The authors argued that the observed 2D growth on thicker layers was only possible under very clean conditions, i.e. when contamination had been buried under the layer. The molecular beam work described above was called into question and it is now clear that since these studies were made at the pre-coalescent stage, contamination of the substrate by carbon led to 3D nucleation. In fact, Abbink's result had been foreshadowed by Booker & Unvala's TEM study discussed above. Abbink et al discussed in general the role of impurities in step behaviour but also pointed out that the regular array of steps observed could be explained without the presence of impurities using the theory of Schwoebel & Shipsey (1966). Thus adsorbed atoms could have lower capture probability when approaching the step from the top rather than the bottom. Applied to the  $\{111\}$  surface of silicon, this could lead to the observed propagation in  $\langle \bar{1}\bar{1}2 \rangle$  directions of steps lying in the  $\langle \bar{1}10 \rangle$  directions normal to the direction of step motion when the difference in bonding of adatoms to  $\langle \bar{1}\bar{1}2 \rangle$  versus  $\langle 11\bar{2} \rangle$  steps was considered. Cullis & Booker (1971) observed very similar results using thickness fringe contrast in TEM on layers deposited by sublimation on substrates

directly heated to the growth temperature. However, when substrates were preheated to 1250°C, 2D growth was found with occasional pinning centres, i.e. regions of suppressed Si growth often several thousand Angstroms deep. These were believed to be due to particles of SiC which were identified using transmission electron energy loss analysis (Ditchfield & Cullis 1970). The SiC particles sit on the growing layer surfaces and locally slow down Si epitaxial growth probably as discussed above. Very few crystal defects were observed. The preheated substrates themselves showed a terraced structure where evaporation of surface atoms had occurred and the process was regarded as the reverse of the deposition case.

Henderson & Helm (1972) avoided the 'thermal cleaning' stage by in-situ argon ion sputtering followed by a low temperature anneal to recrystallise the amorphous top layer created by the ion bombardment. In the absence of any contamination observable by in-situ Auger and mass spectrometry, i.e.  $< 10^{12} - 10^{13}$  atoms  $\text{cm}^{-2}$ , defect-free layers were grown from silane down to about 820°C. There was evidence of Ni segregation to the surface on annealing at 900°C. This was associated with pit formation although stacking faults did not nucleate at these sites during subsequent epitaxial growth. A study of reaction kinetics showed that the decomposition of silane was a first order reaction as opposed to second order as found by Joyce, Bradley & Booker (1967) although the activation energy of decomposition ( $\sim 1\text{eV}$ ) was similar. It was proposed that the growth rate was controlled by the chemical reaction of the adsorbed molecules. Application of Burton, Cabrera & Frank's theory gave the activation energy of surface diffusion as  $\sim 1\text{eV}$ , which was significantly lower than the value of  $\sim 2\text{eV}$  obtained by Joyce, Bradley & Booker, but the latter was calculated from data on 3D nuclei on contaminated substrates where step inhibition occurs.

#### SUMMARY

Under "clean" conditions ( $< 10^{12}$  contaminant atoms/ $\text{cm}^2$ ). epitaxial growth of Si occurs by monolayer step propagation for both CVD and evaporation methods. Specific contaminants, carbon and oxygen, affect growth. Oxygen can be generally removed before growth commences but can cause pitting. Carbon is invariably present on substrates even under UHV conditions and leads to the formation of 3D growth centres. It can be removed by ion-etching but

high temperature annealing leads to the formation of  $\beta$ -SiC crystallites which locally suppress growth.

1.3. Stacking Faults in Epitaxial Si

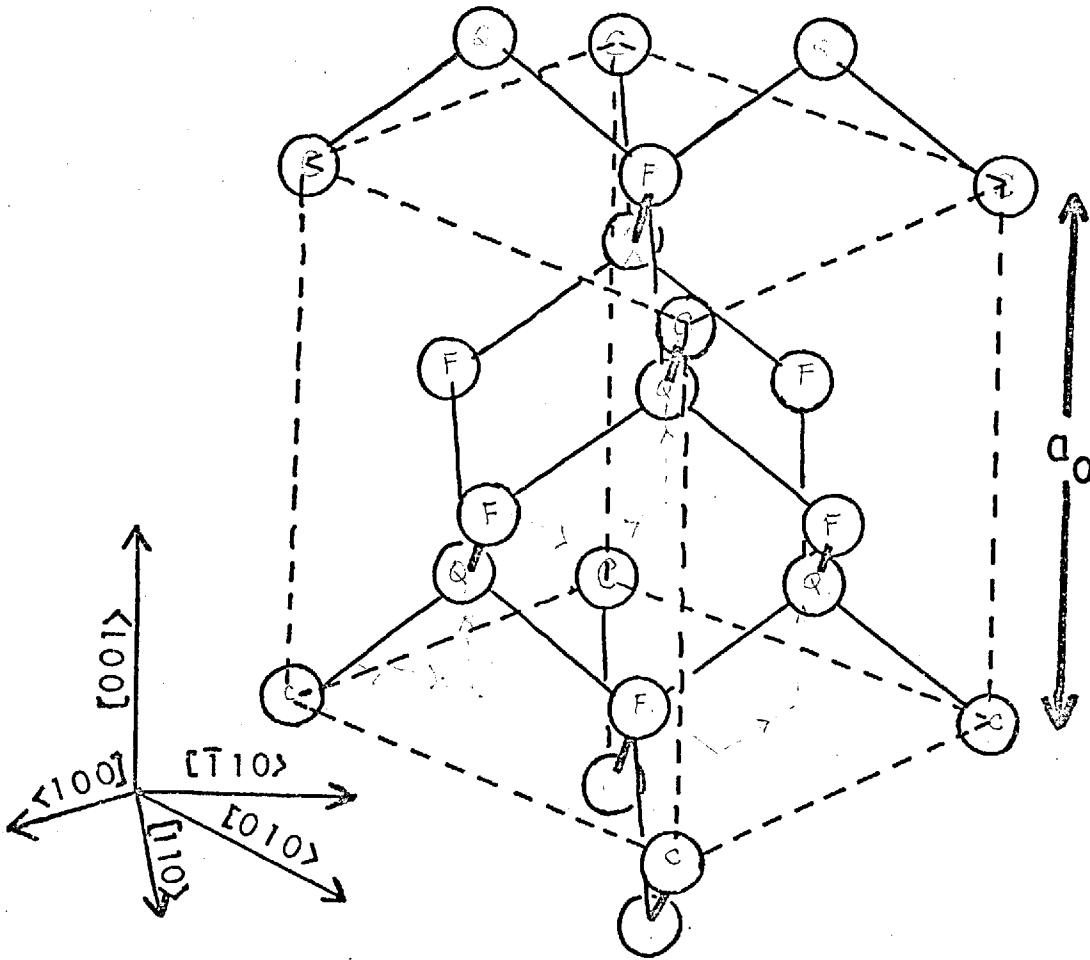
Silicon has the diamond-cubic structure, consisting of two interpenetrating f.c.c. lattices, one of which is displaced by  $(\frac{1}{4}, \frac{1}{4}, \frac{1}{4})$  with respect to the other. Each atom has 4 covalent bonds which are tetrahedrally arranged in  $\langle 111 \rangle$  orientations, Fig.1.1. The layer structure consists of double  $\{111\}$  planes in the sequence A<sub>a</sub> B<sub>b</sub> C<sub>c</sub> A<sub>a</sub> B<sub>b</sub> - - - as shown in Fig.1.2, where atoms in 'a' positions lie directly above atoms in 'A' positions etc. Stacking faults require the insertion or removal of pairs of layers of the same index, A<sub>a</sub> etc. which involves no change in nearest neighbour bonding and so the stacking fault energy (SFE) is relatively low ( $\sim 50$  ergs cm<sup>-2</sup>; Ray & Cockayne 1971). Intrinsic and extrinsic stacking faults are shown in Fig.1.3 which is a  $\{\bar{1}10\}$  projection so that the "short" bonds in fact represent two superimposed bonds which lie out of the plane of the paper. The stacking sequence for an intrinsic fault is A<sub>a</sub> B<sub>b</sub> C<sub>c</sub> | B<sub>b</sub> C<sub>c</sub> - - - whilst an extrinsic fault is A<sub>a</sub> B<sub>b</sub> C<sub>c</sub> | B<sub>b</sub> | A<sub>a</sub> B<sub>b</sub> - - -. Both can be represented by a displacement  $R = \pm \frac{1}{3} \langle 111 \rangle$  normal to the plane of the fault or by a shear of  $R = \pm \frac{1}{6} \langle 11\bar{2} \rangle$  in the fault plane. The sign of the displacement defines its intrinsic or extrinsic nature. The stacking fault introduces a phase change between transmitted and diffracted beams in TEM giving rise to fringes in the image which run parallel to the line of intersection of the fault and the surface of the foil. Many examples are shown in Chapter 3.

If a stacking fault terminates inside a crystal, it must be bounded by a partial dislocation. In the diamond-cubic structure there are several possible kinds of partials:

- a) Frank with Burgers vector  $\underline{b} = \pm \frac{1}{3} \langle 111 \rangle$
- b) Shockley " "  $= \pm \frac{1}{6} \langle 112 \rangle$
- c) Stair-rod " "  $= \frac{1}{6} \langle 110 \rangle, \frac{1}{3} \langle 110 \rangle, \frac{1}{3} \langle 100 \rangle$  etc.

Stair-rod dislocations are formed by the intersection of stacking faults on differently inclined  $\{111\}$  planes and their Burgers vectors are the vector sums of those component partial dislocations before intersection. For example, a Shockley partial on the  $(111)$  plane with  $\underline{b} = \frac{1}{6} [\bar{1}\bar{1}2]$  collides with another Shockley on the  $(\bar{1}\bar{1}1)$  plane with  $\underline{b} = \frac{1}{6} [2\bar{1}\bar{1}]$  to form a stair-rod dislocation lying in the common  $[\bar{1}01]$  direction with  $\underline{b} = \frac{1}{6} [\bar{1}01]$ . Hornstra (1958) proposed configurations of bonds to represent dislocations in the diamond-cubic structure where dislocation cores contain

THE DIAMOND-CUBIC STRUCTURE SHOWING TETRAHEDRAL BONDING OF ATOMS.



THE DIAMOND LATTICE WITH  $[111]$  VERTICAL VIEWED NEAR THE  $[1\bar{1}0]$  AXIS

(after Hornstra 1958)

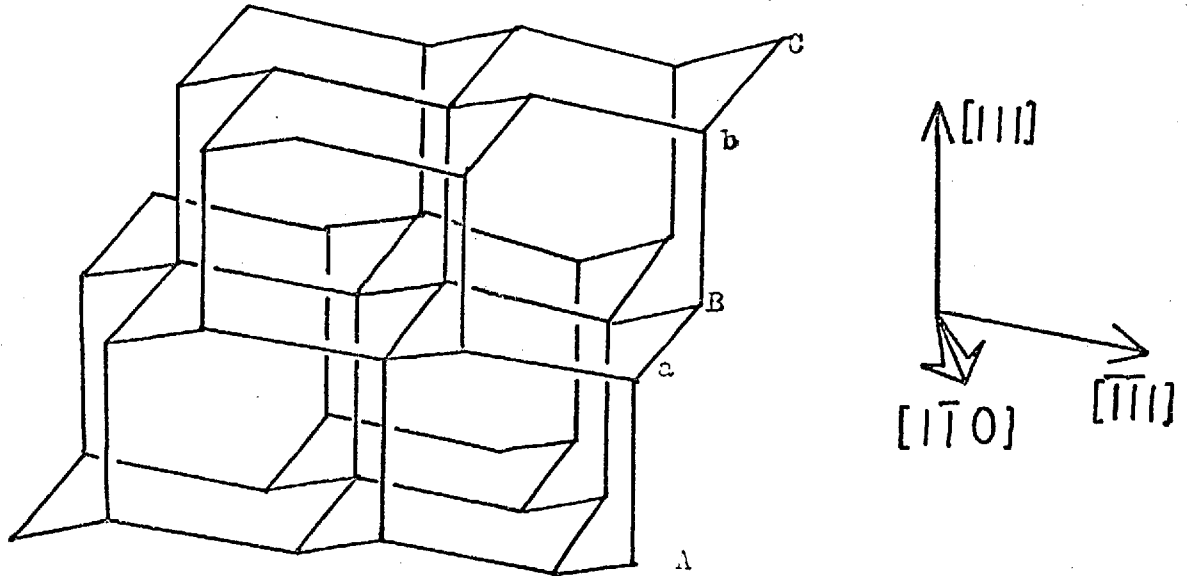
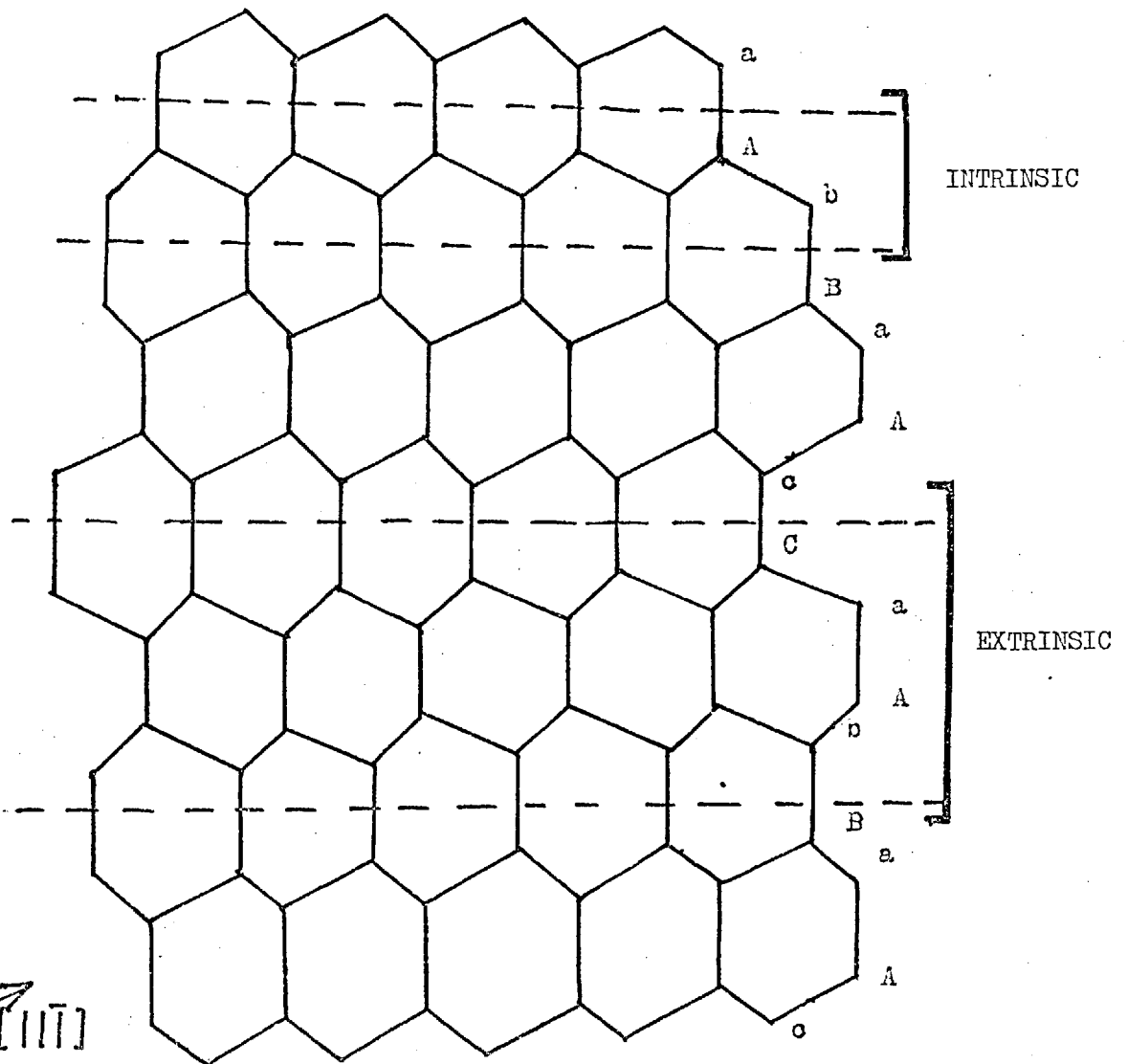


FIG. 1.3

STACKING FAULTS IN THE DIAMOND LATTICE OF INTRINSIC AND EXTRINSIC TYPE;  
THE BROKEN LINES DEMOTE TWIN PLANES, PROJECTED ON  $(1\bar{1}0)$  PLANES.

(after Hornstra 1958)



broken or distorted bonds and are very localised. Detailed consideration of these configurations is given in Chapter 6.

We shall now attempt to survey the study of stacking faults in epitaxial Si in a similar way to that of growth studies in the previous section. Table 1.2. summarises the work which will be reviewed.

In the early 1960's there was initially some confusion as to the identity of defects found in epitaxial Si layers. This was because workers had to rely mainly on etching and optical microscopy since specimen thinning techniques (e.g. Booker & Stickler 1962a) for TEM were still being developed. Light (1962), working mainly on germanium, noted "open triangle" etch figures in  $\{111\}$  layers and assessed causes as impurities or damage at the substrate/layer interface. Although Light did not correctly identify the figures, a TEM micrograph was shown of a defect in epitaxial Ge which appears to be a stacking fault tetrahedra. It is interesting to note in view of the present study, that at the same time Haase (1962) showed TEM micrographs of stacking fault ribbons and dislocations in evaporated  $\{111\}$  Ge layers, whilst in  $\{100\}$  layers dislocations only were observed.

Using their jet-etching technique for TEM specimen preparation, Booker & Stickler (1962b) were able to establish that the etch figures in  $\{111\}$  layers were due to various configurations of stacking faults. In addition to tetrahedra, prisms and zig-zags, single stacking fault structures and fault annihilations were observed and explained in terms of geometry of stacking faults lying on  $\{111\}$  planes which mutually intersect along  $\langle 110 \rangle$  directions. Measurements showed that the faults were nucleated on or close to the substrate/layer interface and from the separation of parallel stacking faults it was found that the initial size of the nuclei could be as small as a few hundred Angstroms across. Two-dimensional growth was assumed with  $\langle \bar{2}11 \rangle$  fast growing directions. A theory of stacking fault formation was proposed based on incorrect positioning of a two-dimensional nucleus on the substrate, i.e. a stacking fault is formed which creates mismatch boundaries when the nucleus impinges on correctly stacked nuclei as shown in Fig.1.4. As the layer grows the boundaries extend as stacking faults on inclined  $\{111\}$  planes. Stacking faults cannot terminate within the layer unless annihilated by collision with another stacking fault of the appropriate sign and so propagate with the layer. Nucleation within the layer was envisaged by an impurity atom from the system being incorrectly positioned on the layer surface during epitaxial growth.

TABLE 1.2. STACKING FAULT STUDIES IN EPITAXIAL Si

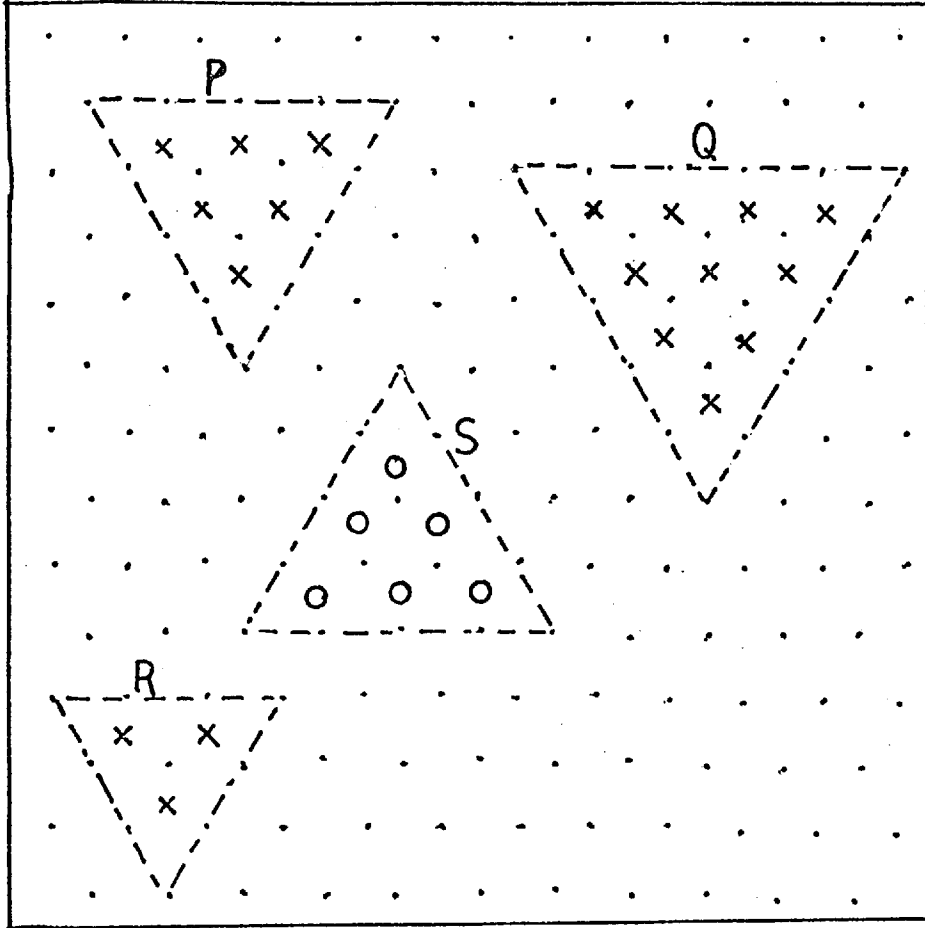
Reference	System	Substrate plane	Growth Temp. °C	Observation techniques	Results
Light (1962)	Prob. CVD no details	111	-	etching, opt. micros.	"open triangle" etch figs. originating from substrate/layer interface, caused by contamination or damage.
Haase (1962)	evap. Ge	111 100	700	TEM	ribbon stacking faults (sf) & dislocations in {111} layers, dislocations, only in {100}.
Booker & Stickler (1962b)	SiCl <sub>4</sub> + H <sub>2</sub>	111	1200	etching TEM	etch figs. established as sfs on {111} planes. Geometry of various structures. Theory of nucleation based on initial mistake positioning at interface. Gaseous impurity may nucleate sf away from interface.
Finch et al (1963)	"	100 110 111	1180-1210	Opt. micros. TEM	ribbon sf, thought to be Shockleys, no analysis, Sf fringe contrast considered. Scribe damage & oxide gave sfs. Mechanical displacement theory of sf nucleation
Chu & Gavalier (1963)	CVD unspecified chloride	211 100 111 110	no details	Dash, Sailors, CP4 etches	layers 100-150 μm thick. Differences in etch rate at some bounding partials. Unspecified local stresses causes sfs in addition to contamination, damage.
Miller et al (1963)	H <sub>2</sub> or HCl at 1250°C, SiCl <sub>4</sub>	111	1250	etching, GAED extraction replica	needles α - SiC oriented along <110>. Tripyramids & microtwins in epitaxial layers
Schwuttke & Sils (1963)	SiCl <sub>4</sub> + H <sub>2</sub>	111	1265	X-ray topography (XRT)	Compared etch figs. with contrast using various reflections in XRT. Ascribed single line contrast to Shockley ribbons + stair-rods in substrate plane - incorrect
Jaccodine (1963)	Model	111	-	-	Model for sf tetrahedra nucleation. Vacancy cluster collapses to disc on {111}, grows to Frank loop. Frank decomposes to 3 stair-rods and 3 Shockleys on inclined {111}. Shockleys react on adjacent planes to form 3 more stair-rods. Once formed, tet. propagates with layer
Booker & Stickler (1963)	Model	111	-	TEM	Above model modified since observed tet. intrinsic ∴ original Frank loop extrinsic to preserve low energy stair-rod. Vacancy collapse would give intrinsic Frank

Mendelson (1964)	$\text{SiCl}_4 + \text{H}_2$	Various	1250	etching	Various causes of s f formation, confirming earlier work. Substrate dislocations propagate but don't nucleate sfs. Growth on mechanical pol. {111} substrates gave v. high sf densities. Jaccodine's model criticised - not enough vacancies available
Booker (1964)	evap.	111	1200	TEM	amorphous contamination associated with sf nucleation. Small patches or dislocation loops at apex of tetrahedra.
Booker & Unvala (1965)					
Booker (1965)	-	111	-	TEM	analysis of multiple twinning leading to tripyramids, suggested nucleated by SiC on substrate
Booker & Joyce (1966)	$\text{SiH}_4$ mol. beam	111	845	i.c., GAED Pt/C, TEM	
Mendelson (1965, 1967a), 1968, 1970)	$\text{SiCl}_4 + \text{H}_2$ models	111	1100- 1350	etching	sf model of shear across A/a type plane giving highly distorted, high-energy fault - unlikely to occur. Various sf displacements considered - not observed in TEM
Thomas & Francombe (1967, 1971)	UHV sublimation	111	400- 800	LEED, TEM	1967 note, sf nucleated by Si (111) - 5 domains. 1971 paper showed LEED patterns contam. sensitive, sf nucleated by impurities on substrate.
Dyer (1969, 1971)	Model $\text{SiHCl}_3$	211 110	-	optical microsc.	Ball model of twin formation due to single or small groups of impurity atoms deposited on key sites, specifically oxygen or carbon.

FIG. 1.4

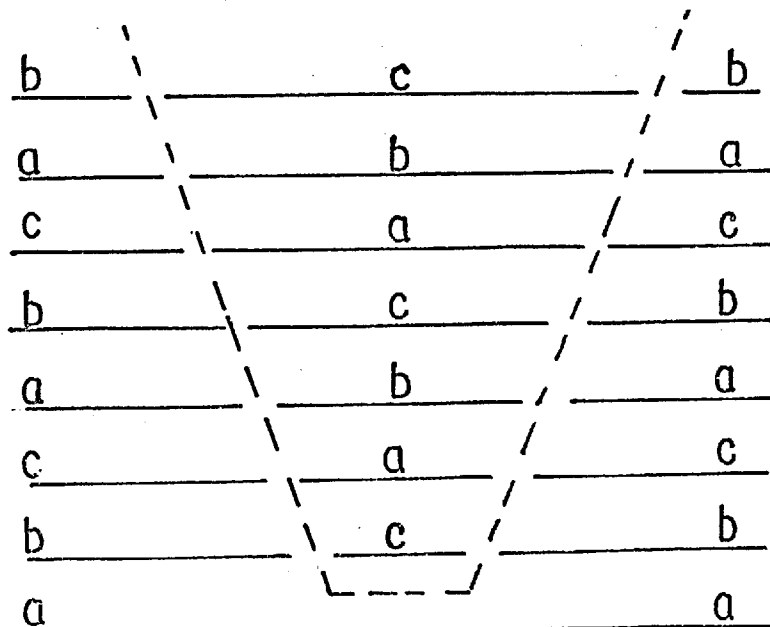
BOOKER & STICKLER (1962) MODEL OF STACKING FAULT NUCLEATION.

a) Initial stages of epitaxial growth nuclei, P, Q & R with correct positioning, but S incorrectly positioned.



- substrate type a position
- × epitaxial layer type b position
- epitaxial layer type c position

b) Sectional view through S after deposition of several atomic layers.



Dotted lines represent projection of stacking faults lying on inclined  $\{111\}$  planes.

Finch & co-workers (1963) extended TEM observations to  $\{110\}$  and  $\{100\}$  layers and again found stacking fault structures consistent with nucleation at the interface and propagation on inclined  $\{111\}$  planes. These authors considered the fringe contrast in detail and attempted a Burgers vector determination of the bounding partials but diffraction contrast analysis of partial dislocations was not worked out fully until the work of Silcock & Tunstall (1964). Stacking fault ribbons were found, usually overlapped by longer stair-rod bounded stacking faults, and inferred to be bounded by Shockley partials. Mechanical damage and contamination, in particular oxide contamination, on the substrate were demonstrated to be causes of stacking fault nucleation, whereas 'grown-in' dislocations in the substrate did not act as nucleation sites and did not form extended dislocations, i.e. did not split into two partial dislocations separated by a stacking fault ribbon. A mechanism based on a hole in a monolayer of oxide or on an oxide patch was proposed to show how either intrinsic or extrinsic stacking faults could be generated by shear depending on the position of the nuclei. It is now clear from the growth studies outlined in the previous section that a monolayer of oxide is unlikely to remain on the surface during epitaxial growth, but this "mechanical displacement" mechanism is a useful concept and is developed in Chapter 6.

Chu & Gavalier (1963) studied thick vapour grown layers using various etchants and optical microscopy. They reported differences in etch rate at some bounding dislocations which they suggested to be Shockley partials. Earlier work using more direct techniques, i.e. TEM and X-ray topography (XRT), had to be invoked to support their study and we consider that discussion of Burgers vectors based on etching behaviour is largely speculative. It was believed that local stresses created stacking faults during growth but how such stress could arise was not discussed.

Miller, Watelski & Moore (1963) extracted needles of  $\alpha$ -SiC lying along  $\langle 110 \rangle$  steps on  $\{111\}$  substrates which had been annealed in  $H_2$  at  $1250^\circ C$ . When these substrates were deposited on, tripyramids and microtwins were found and it was argued that twinning occurred when the SiC was overgrown with Si. Schwuttke & Sils (1963) compared etching results with XRT using the Lang transmission technique on thick  $\{111\}$  Si layers. They suggested that single stacking faults were bounded by Shockley dislocations but to explain the observed contrast in the topographs these faults must be associated with the stacking faults in the  $\{111\}$  substrate plane,

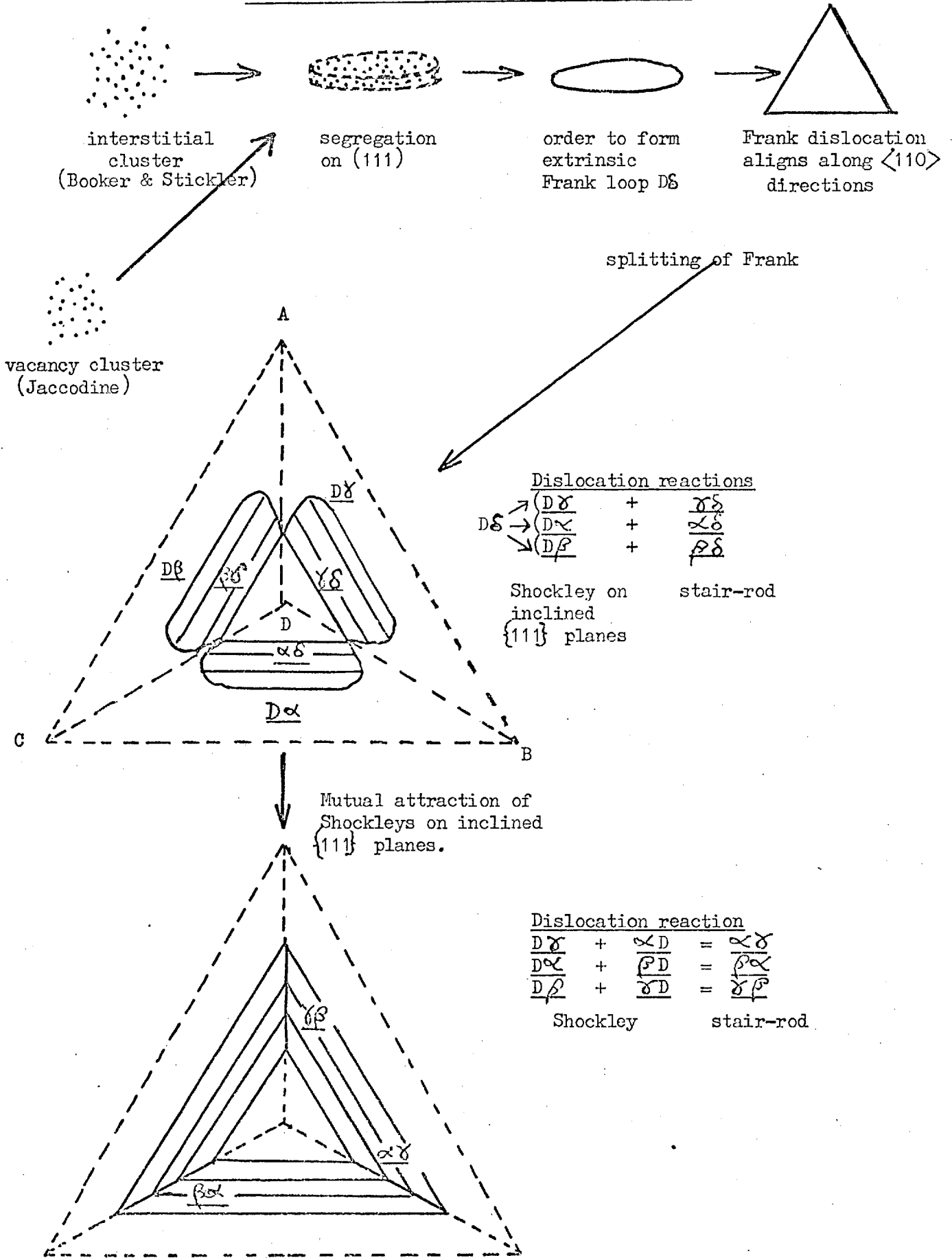
forming stair-rods parallel to  $\langle \bar{1}10 \rangle$  orientations in this plane. As pointed out above in the case of Finch et al, the interpretation of contrast at partials was not fully developed at this time, but reanalysis of Schwuttke & Sils' results shows that the observed contrast can be explained by the presence of stair-rod dislocations bounding the "single" faults of the same type which occur in tetrahedra and other closed configurations, e.g.  $\frac{1}{6} \langle 110 \rangle$ . In addition the poor resolution of XRT compared with TEM made interpretation doubtful. It is interesting to note that Meieran & Blech (1967) were able to analyse very large stacking fault networks grown in Si web dendrite and found both intrinsic and extrinsic faults bounded by Shockley partial dislocations using XRT methods.

Jaccodine (1963) proposed a new model for the nucleation of stacking fault tetrahedra in  $\{111\}$  epitaxial Si. He noted the similarity between stacking faults in f.c.c. and diamond-cubic structures and adapted a mechanism used by Silcox & Hirsch (1959) to account for the formation of stacking fault tetrahedra in quenched and aged gold foils. Applied to Si epitaxy, the mechanism starts with the collapse of a vacancy cluster to form a circular disc on the  $\{111\}$  substrate plane. This grows into a triangle bounded by a Frank partial loop with sides along  $\langle \bar{1}10 \rangle$  directions. Because of the relatively high energy of the dislocation, reactions follow which lower the dislocation energy. The sequence is illustrated in Fig.1.5 with the appropriate reactions written using the Thompson notation (see Appendix A). The final products are 6 stair-rod dislocations with Burgers vectors  $\frac{1}{6} \langle 110 \rangle$  and the stacking faults on the inclined  $\{111\}$  planes continue to propagate as the layer grows. Shortly afterwards Booker & Stickler (1963) noted from fringe contrast observations in TEM that the three inclined stacking faults in each tetrahedron occurring in  $\{111\}$  layers were all intrinsic. This meant that to ensure low energy stair-rod products in the reactions shown in Fig.1.5, the original Frank loop on the substrate plane had to be extrinsic and so could not have formed by the collapse of a vacancy cluster as suggested by Jaccodine.

Mendelson (1964) also criticised Jaccodine's model from considerations of the elastic energies of the reactant and product dislocations and concluded that the proposed mechanism was unlikely to occur because of insufficient vacancy concentrations during epitaxial growth. He also showed that

JACCODINE (1963) & BOOKER & STICKLER (1963) - MODELS OF STACKING FAULTS

TETRAHEDRA NUCLEATION ON {111} SUBSTRATE



NOTES: 1. Direction of growth into paper.  
 2. See Appendix A for rules of partial dislocation reactions.

dislocations in the substrate propagated with the layer, but did not nucleate stacking faults as noted earlier by Finch et al (1963). Interrupted runs however, when the substrate was allowed to cool between growth periods, led to fresh stacking fault nucleation. A density of stacking faults  $> 10^3 \text{ cm}^{-2}$  was noted in layers grown on mechanically polished substrates orientated close to  $\langle 111 \rangle$  although this density fell off quickly at orientations  $> 5^\circ$  away from  $\langle 111 \rangle$ . Chemically polished substrates gave very low stacking fault densities and it was proposed that the risk of stacking fault nucleation depended on exposing  $\{111\}$  areas on the substrate which were large enough to permit stable incorrectly deposited nuclei. Mendelson also observed, using etching techniques, that stacking faults could be 'annealed out' by prolonged heating at  $1250^\circ\text{C}$  in  $\text{H}_2$  (but not in Argon) and it was postulated that hydrogen reduces the nucleating particle, possibly oxide, at the substrate/layer interface and the stair-rods 'unzip' into Shockley partials which glide to the surface and annihilate the stacking faults.

Booker & Unvala (1965) showed that stacking fault nucleation in evaporated Si layers was associated with amorphous debris on the substrate. Close examination by TEM of thin layers by Booker (1964) showed that stacking faults mostly started from small patches or dislocation loops at the substrate/layer interface but analysis of the features was not carried out, presumably since they were so small. The multiple-twinning occurring in tripyramid defects in  $\{111\}$  Si layers was analysed by Booker (1965) and a similar TEM investigation of twinned nuclei in initial growth of CVD layers (Booker & Joyce 1966) strongly suggested that these nuclei developed into tripyramids. It was believed that particles of SiC on the substrate caused twinning when overgrown by Si although no direct evidence was presented.

In a series of papers, Mendelson (1965, 1967a) & b), 1968 & 1970) developed a 'twinned deposit' mechanism of stacking fault nucleation based on etching results and using ball and wire models. In addition, the view of Hornstra (1958) of stacking faults consisting of two twin planes, Mendelson considers that stacking can also be created by shear between A ; a type planes. This would produce highly distorted bonds in the stacking fault plane where the co-ordination number would exceed four, leading to a faster etch rate than the twinned variety. In the later papers various displacements such as  $\frac{1}{2} \langle 001 \rangle$  and  $\frac{1}{4} \langle 111 \rangle$  are considered but no confirmation of these structures by fringe contrast experiments in TEM appears to have been made. In view of the moderately low SFE of Si, Mendelson's models seem unlikely to be correct.

Thomas & Francombe (1967) proposed a model of stacking fault nucleation based on the results of LEED and TEM studies of sublimed Si layers grown under UHV conditions. Above 600°C defect-free layers were observed corresponding to the 'clean' Si (111) - 7 surface structure but as the growth temperature was lowered an increasing proportion of the Si (111) - 5 structure occurred, together with an increase in stacking fault density. It was suggested that the Si (111) - 5 domains nucleated stacking faults, as an alternative process to contamination and damage effects. In view of subsequent work, reviewed in Section 1.2, it is now known that LEED patterns are influenced by surface contamination. In a later paper Thomas & Francombe (1971) show evidence that micro-precipitates on the substrate nucleate stacking faults and that these precipitates also modify the LEED patterns.

Dyer (1969) proposed that single impurity atoms in key sites could produce twinning, using a ball model approach. Specifically oxygen atoms on {211} facets could cause next and subsequent rows of Si to be deposited in twin positions. The effect could be enhanced by the co-operative effect of more impurity atoms on the second row. However, experimental evidence was not very strong since very high levels of oxygen (600 ppm) were needed to produce 11 twins cm<sup>-2</sup>. In a later paper Dyer (1971) suggested that short chains of carbon atoms, due to methane contamination, create a similar effect.

#### SUMMARY

1. CAUSES OF STACKING FAULT FORMATION: SiC, SiO<sub>2</sub>, various impurities, mechanical damage, interrupted growth.
2. THEORIES OF STACKING FAULT NUCLEATION:  
Booker & Stickler (1962/3), mis-positioned nuclei; decomposition of extrinsic Frank loop.  
Finch et al (1963) "mechanical displacement" due to oxide contamination.  
Mendelson (1965 etc.), twinned deposit model.  
Thomas & Francombe (1967), Si (111) - 5 domain model.

## CHAPTER 2. EXPERIMENTAL

### 2.1. Preparation of epitaxial layers

#### 2.1.1. Growth system

Fig.2.1 shows the layout of the growth system. Two stainless steel chambers, each a 4-way flanged crosspiece made from 2" diam. tubing, were separated by large, all metal throttle valve and evacuated by a 4" oil diffusion pump. The chamber above the pumps was fitted with an ionisation gauge and an AEI MS10 mass spectrometer which was used for residual gas analysis and to monitor the composition of gases introduced into the system. The second chamber was fitted with a viewport, specimen flange and a gas inlet which contained a leak valve and a Pirani gauge to monitor the chamber pressure. The gas lines were pumpable back to the cylinders to minimise contamination and the silane line contained a molecular sieve absorbent to remove water vapour. The system was assembled with bolted flanges and sealed with gold wire compression seals. A run was commenced by pumping overnight with the system baking at 250°C to achieve base pressures of  $5 \times 10^{-10}$  torr or better.

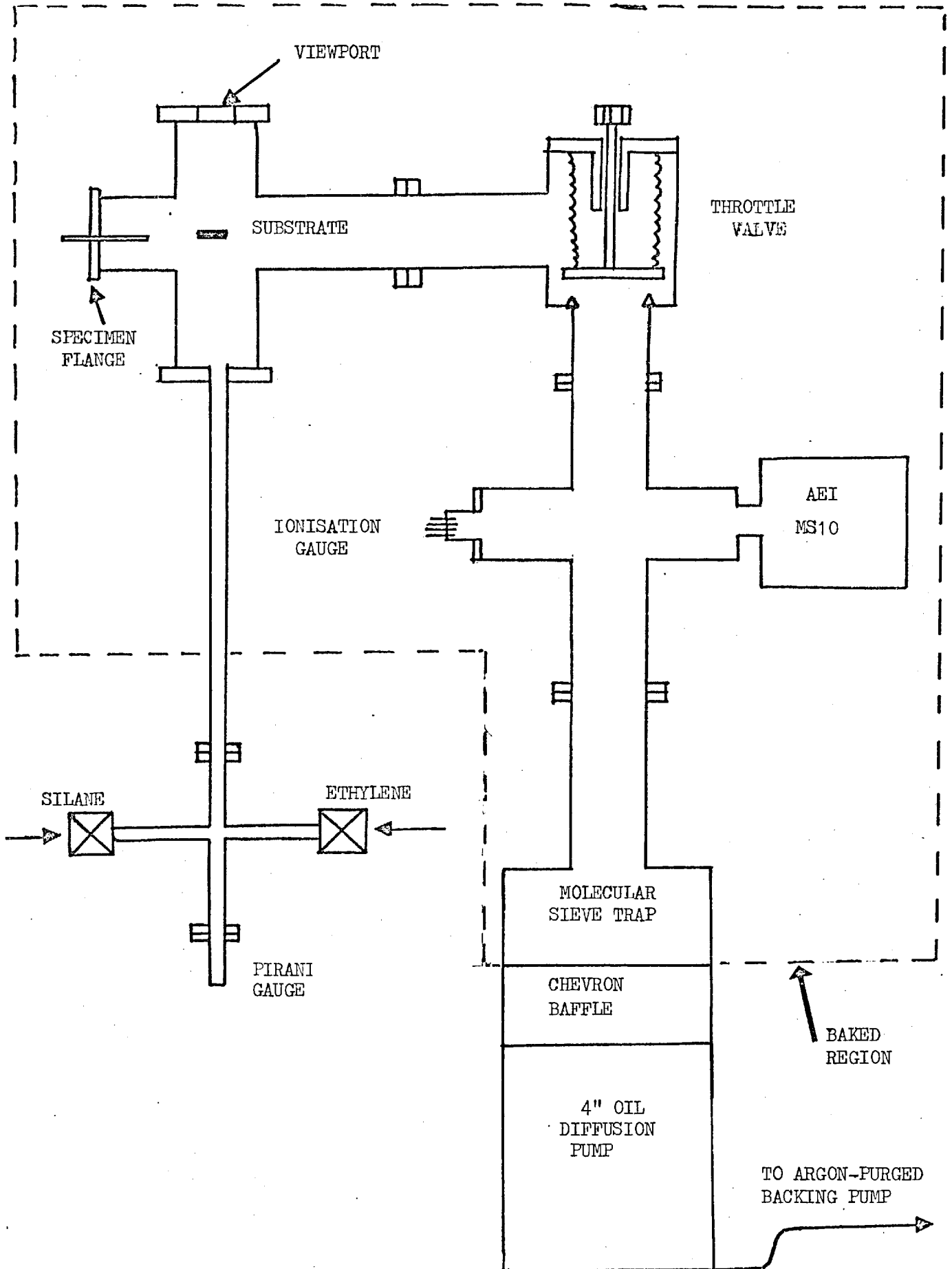
#### 2.1.2. Substrate preparation

Bars were cut from 50  $\Omega$  cm. p-type Si to dimensions of approximately 60 x 7 x 1 mm. so that the largest faces were  $\sim 2^\circ$  from the selected orientations, i.e.  $\langle 111 \rangle$ ,  $\langle 110 \rangle$  or  $\langle 100 \rangle$ . One of the largest faces was then lapped, mechanically polished and finally gas polished in HCl at 1250°C. The bar was then mounted in the growth chamber with polished face towards the viewport in tantalum clips attached to high current feed-throughs to allow a low tension heating current to pass through the substrate bar. The temperature of the substrate was monitored through the viewport using a calibrated continuous radiation pyrometer corrected for emissivity (Allen 1957). Water cooling of the walls of the deposition chamber was used to reduce outgassing due to radiation heating. In later runs the system was modified to incorporate two substrates which were independently heated.

#### 2.1.3. Growth schedule

After bake-out with the throttle valve fully open, the substrate was heated to 1200°C for 2 min. which caused the pressure to rise to excess of  $10^{-8}$  torr due to outgassing of H<sub>2</sub>, CO & CO<sub>2</sub>. When the vacuum had recovered to  $\sim 10^{-9}$  torr, the required contaminant gas (research grade) was admitted to a predetermined pressure as indicated by the calibrated ionisation gauge.

UHV SYSTEM FOR EPITAXIAL GROWTH OF SILICON FROM SILANE.



The gases chosen in this study: hydrocarbons, oxygen and water vapour can be present in a conventional flow system. Water vapour was obtained by fracturing a sealed ampule of high purity water in a special chamber attached by a gas line to the growth chamber. Silane (semiconductor grade) was then introduced into the growth chamber to give the desired silane:contaminant ratio. After stabilisation, the specimen temperature was quickly raised to  $1200^{\circ}\text{C}$  and the magnetically operated throttle valve closed to raise the growth chamber pressure to the growth pressure, typically 0.3 torr. The substrate temperature was then lowered to the growth temperature. This procedure was adopted when using ethylene contamination to minimise the formation of SiC on the substrate prior to growth. Throughout the run, the throttle valve was adjusted so that the maximum pressure in the mass spectrometer chamber did not exceed  $3 \times 10^{-4}$  torr. This way the spectrometer was always operative and excessive oil backstreaming into the growth chamber was avoided. Si growth rates of typically  $0.5 \mu\text{m}/\text{min}$ . were achieved and layers 4-6  $\mu\text{m}$  thick were deposited. The run was terminated by switching off the substrate heating current, closing the gas inlet and opening the throttle valve.

## 2.2. Examination Techniques

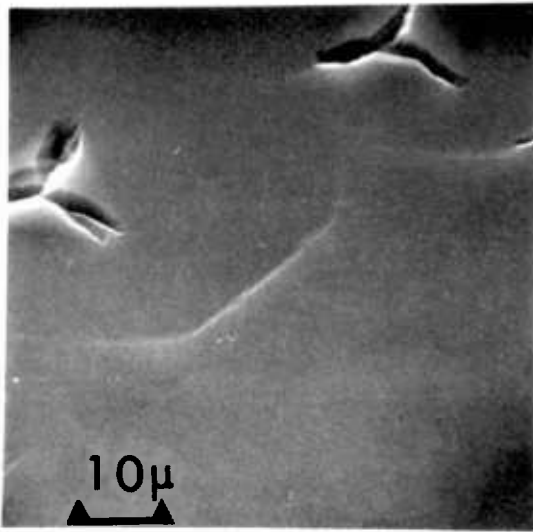
Preliminary optical assessment using a) interference contrast on the layer surface structure and b) etching to reveal bulk defects in the layers, was made by R.R. Bradley before GAED, Pt/C replica and TEM examination were carried out. Table 2.1 gives details of these techniques. Scanning electron microscopy (SEM) was not adopted as a means of studying surface structure since interference contrast optical examination provided better contrast. Fig.2.2 compares SEM and interference contrast microscopy on the same specimen which was found to have a high density of saucer-like depressions on the surface. The overall rippled texture of the surface and the saucers are only revealed at shallow beam angles to the surface in SEM, Fig. 2.2(b), but are clearly seen in the interference contrast micrographs, Fig. 2.2(c). The layer had been grown under UHV conditions in an earlier experiment.

The principal techniques used in this study were the high resolution replica and thin foil work performed on the Siemen's Elmiskop I electron microscope since it was quickly established that the defect structure and surface topography were closely related.

TABLE 2.1. EXAMINATION TECHNIQUES

Technique	Apparatus	Specimen preparation	Advantages
Optical Interference contrast	Nomarski i.c. stage on Reichart microscope	-	Very sensitive to surface topography; detects steps tens of Angstroms high, including stacking fault traces.
Optical Sirtl etching	Reichart microscope	Cr <sub>2</sub> O <sub>3</sub> / HF etch	Reveals dislocations, stacking faults. Good for assessment of overall layer quality, especially defect densities <math>10^4 \text{ cm}^{-2}</math>.
Glancing angle electron diffraction (GAED)	Metropolitan-Vickers electron diffraction camera . 60-100kV beam	-	Quick assessment of layer quality, second phase presence on surface. Very shallow penetration of flat surfaces.
Pt/C replica	Edwards coating unit, simultaneous evaporatn of Pt/C at $\sim 10^\circ$ to substrate surface. Examine in TEM	Remove replica film in 1:18 HF : HNO <sub>3</sub> etch	Much higher resolution than i.c. microscopy and SEM on Si surfaces. Examination of contrast and shadow dirn. gives surface relief <math>20\text{\AA}</math> steps. Extraction of identifiable crystalline second phase possible.
Transmission electron microscopy TEM	Siemens Elmiskop I electron microscope 100kV beam. High tilt Ward goniometer cartridge	Lapping, ultrasonic drilling, jet etching.	Principal tool for analysis of dislocations and stacking faults. High resolution, $10\text{\AA}$ routinely achieved. Defect densities in range $10^4 - 10^{12} \text{ cm}^{-2}$ examined.

Micrographs of epitaxial Si layer showing defective growth



a) SEM, secondary electron emission mode, beam normal to surface

b) SEM, beam  $75^{\circ}$  to surface normal

(SEM micrographs by courtesy of N.S.Griffin)

c) Interference contrast optical micrograph.



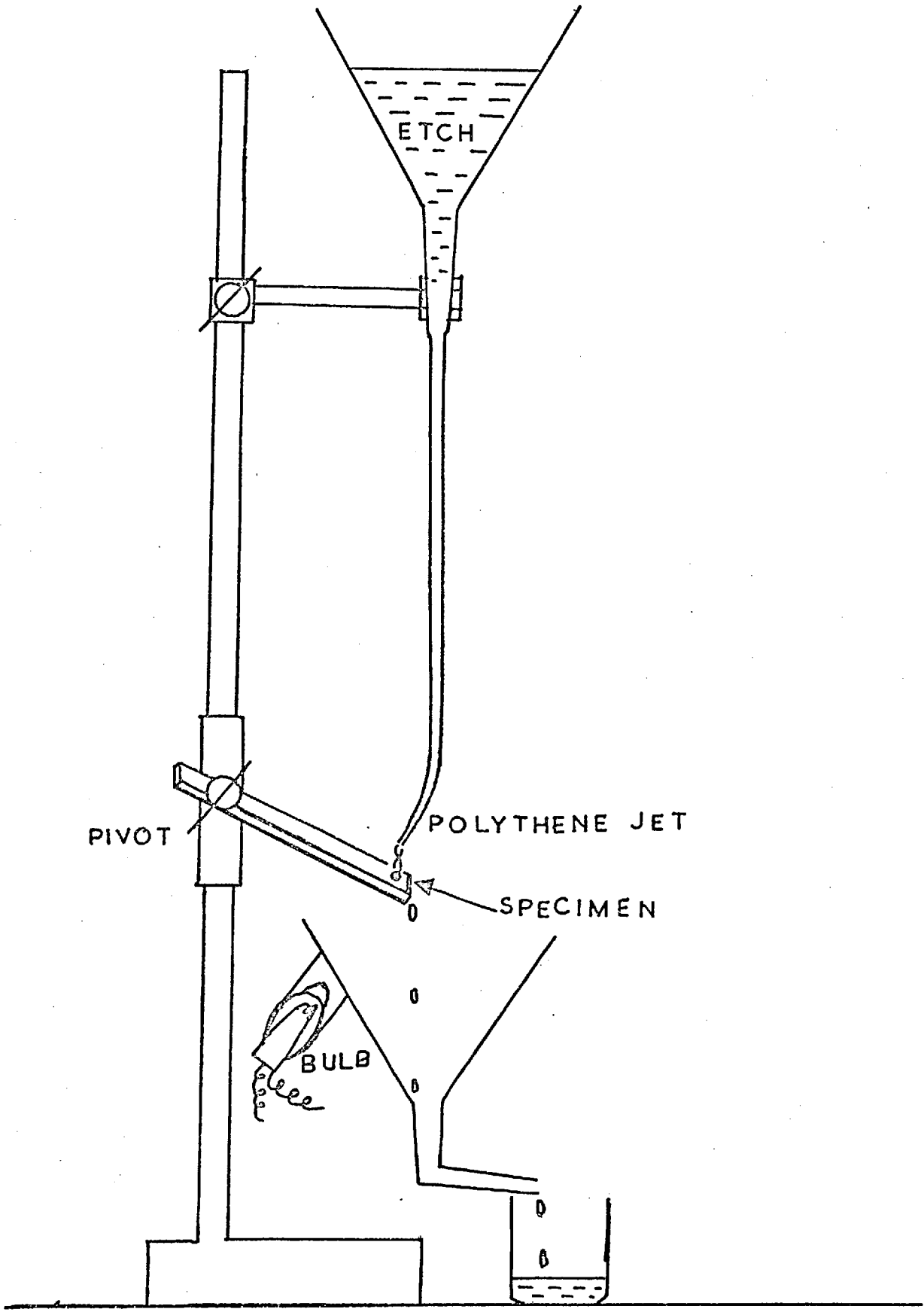
### 2.3. Specimen preparation

After removal from the growth system, the layer surface was examined all over by i.c. microscopy. The centre portion  $\sim 3$  cm long was cut from the bar and the end portions, which were known to be contaminated by the Ta supporting tapes, were discarded. A 1 cm. portion was cut from the remaining bar for Sirtl etching, and after examination by GAED a further 5 mm. portion was taken for Pt/C replication. Shadowing at a low angle ( $\sim 10^\circ$ ) to the surface was used throughout to enhance the often very smooth surface topography (Bradley 1959, 1960).

Thin foils for direct TEM examination were prepared as follows. The remaining portion of the bar, measuring approximately 7 x 15 mm. was waxed face down onto the centre of a glass microscope slide using black Apiezon Wax. The back of the bar was then lapped down by hand using 220 grit SiC in a water slurry on a plate glass surface until the substrate was  $\sim 300 \mu\text{m}$  thick. Specimen blanks were then ultrasonically cut using a 2.2 mm. internal diameter steel tube using SiC grit in water as a cutting medium. The specimen discs were removed by warming the glass slide on a hot plate, picking up the discs in tweezers and dropping them into warm trichloroethylene to wash. Using this method up to 10 discs could be prepared from each growth run.

Specimen discs were then thinned using a jet etching technique developed at Caswell by R.W. Bicknell (1973). Discs were mounted face down in a soft grease on a strip of polythene held in a swivel-mounted clamp, Fig.2.3. The jet was drawn from polythene tubing down to about 0.5 mm. diameter so as to produce a turbulent jet of etchant and the other end of the tube was welded into a polypropylene funnel as reservoir for the etch. The specimen was illuminated from below by a 2V lens fronted torch bulb set in a polythene tube welded to a second funnel which collected the used etch. A mixture of hydrofluoric and nitric acids was used to thin the specimens and the relative strengths were varied depending on the orientation of the specimen. It was found that 4 : 1  $\text{HNO}_3$  : HF was satisfactory for  $\langle 111 \rangle$  and  $\langle 110 \rangle$  orientations, but that a 2 : 1 etch was best for  $\langle 100 \rangle$  layers since a weaker HF mixture caused preferential etching. The jet produced a dished surface and when the central area was thinner than about  $5 \mu\text{m}$ ., the light from the bulb was visible through the specimen, the colour changing rapidly from deep red to straw.

FIG. 2.3  
DIAGRAM OF JET-ETCHING APPARATUS



On perforation the jet was quickly swung away from the specimen which was simultaneously flooded with water from a wash bottle. The time taken to etch the specimen was generally less than 3 min. The specimen was removed by soaking in warm trichloroethylene, washed in clean solvent, and was ready for insertion in the electron microscope. Ideally a small circular hole was produced in the specimen, surrounded by an annulus of silicon with taper angle  $< 1^\circ$  so that large areas were thin enough for TEM, i.e.  $\leq 1 \mu\text{m}$ . thick.

For thin foil work, it is necessary to accurately control the tilt of the specimen in the electron microscope and in the present work, initially a Valdré tilt cartridge was used with maximum movement of about  $\pm 10^\circ$ . Later this was replaced by a Ward goniometer cartridge which achieved tilts of  $\pm 25^\circ$ . This proved much more satisfactory and the series of diffraction contrast analyses shown in Appendix A were obtained using this device. Since one area must be viewed for prolonged periods during this operation, it was useful to employ an anti-contamination collar which surrounded, but which was thermally isolated from, the specimen. The collar was cooled to liquid nitrogen temperatures and trapped contamination, resulting from the degradation of pump vapours by the electron beam, which would otherwise build up on the specimen and lead eventually to unacceptable deterioration of image quality. The chief drawback to TEM is the very small volume sampled ( $\sim 10^{-6} \text{cm}^3$  max.) because of the low penetration of the electron beam ( $\sim 1 \mu\text{m}$  of Si for good quality imaging) and limited stage movement ( $< \pm 0.5 \text{mm}$ ). This means that defects with densities  $< 10^4 \text{cm}^{-2}$  are quite difficult to locate.

### CHAPTER 3. RESULTS: ETHYLENE CONTAMINATION STUDIES $\{111\}$ LAYERS

The most important aspects of this study arose from the effect of ethylene contamination on  $\{111\}$  epitaxial Si layers and the results of these experiments will be presented in this chapter. Results on ethylene-contaminated  $\{110\}$  and  $\{100\}$  layers will be reported in Chapter 4, followed by the results of experiments with other gaseous contaminants (Chapter 5). Table 3.1 gives details of all the growth runs made on  $\{111\}$  orientation substrates in the ethylene series. The results have been sorted into ascending growth temperatures. The gaps in numbering are due to the intervention of different experiments which are reported in later chapters or which were not part of the present study. Table 3.2 summarises the TEM and replica results with regard to growth temperature and contamination ranges. The main results in this chapter are substantially as published by Ogden, Bradley & Watts (1974) but the work is now reported in more detail.

#### 3.1. Control runs, no deliberate contamination

In general, these runs produced layers which were largely free of defects and which had very smooth surfaces. Fig.3.1 shows typical micrographs obtained from the various techniques used in the study and a corresponding GAED pattern. Stacking fault densities as revealed by Sirtl etching varied across the specimen and were never completely eliminated. Fig.3.1(b) shows a variety of etch figures of uniform size, indicating a common origin at the substrate : layer interface. Fig.3.1(a) shows that the surface is much smoother than that shown in Fig.2.2.(c), with only one shallow saucer appearing. The saucers were sometimes associated with the occurrence of stacking faults and Drum & Clark (1968) have shown how very large ledges can develop at such defects on layers oriented close to the  $\langle 111 \rangle$  direction. A definite cause of stacking fault formation was contamination from the Ta clips which held the substrate bars and for this reason observations were made away from the end portions of the bars. TEM confirmed the etching results in that the stacking fault structures in the control runs were often complex, Fig.3.2., in addition to the more common tetrahedra. Even in control runs, saucers were sometimes produced in quantity, Fig.3.3., although usually not as marked as the surfaces shown in Fig.2.2.

TABLE 3.1. ETHYLENE CONTAMINATION {111} EPITAXIAL Si LAYERS

Run No. RB	TOC Obs.	TOC* corrected	p.p.m. ethylene	Optical	Exam	Transmission Electron Microscop		pin site density cm <sup>-2</sup>	
				Sirtl etch pit counts (cm <sup>-2</sup> )	Interference contrast	Stacking fault (sf) structure	density (cm <sup>-2</sup> )		Surface structure Replica
61	800	835	0	10 <sup>7</sup>	rippled	Ribbon (R)	-	Faceted	-
23	810	845	0	< 7x10 <sup>5</sup>	rippled + fine texture.	None observd.	-	Very smooth	-
34A	"	"	0	3.4x10 <sup>4</sup>	s.f + saucers	Tetrahedra (T) etc.	-	" "	-
34B	"	"	7.5	2.1x10 <sup>5</sup>	strongly rippled	R	-	Terraced, pinning sites	7.5x10 <sup>6</sup>
35A	"	"	670	-	V.fine texture	Heavily twinned	6x10 <sup>10</sup>	Heavily pitted, SiC extracted	1.8x10 <sup>9</sup>
29	820	855	0	2.5x10 <sup>4</sup>	smooth	T	-	-	-
15	"	"	10	10 <sup>7</sup>	fine texture	R & T	-	Weakly developed facets	-
36A	"	"	31	~ 10 <sup>8</sup>	V.fine texture	R	3x10 <sup>8</sup>	Faceted	-
36B	"	"	31	Too high to count	rippled	R	2x10 <sup>8</sup>	Very smooth	-
62	"	"	50	"	rippled & granular	R	5x10 <sup>8</sup>	Pitted	2.5x10 <sup>7</sup>
14	"	"	92	"	fine texture	R	9x10 <sup>8</sup>	Strongly faceted	-
37	"	"	100	2.2x10 <sup>7</sup>	faint ripples	R	3x10 <sup>8</sup>	Faceted	-
22	825	860	4.4	9x10 <sup>6</sup>	rippled & granular	R & T	-	Terraced	5x10 <sup>6</sup>
28	"	"	20	7.3x10 <sup>6</sup>	faint ripples	R	-	-	-
35B	"	"	50	3.1x10 <sup>7</sup>	strongly rippled	R & T	-	Very smooth	-
12	830	865	36	2x10 <sup>6</sup>	strongly rippled	R	4x10 <sup>8</sup>	Weak facets	-
27A	"	"	100	too high to count	granular	R & T	9x10 <sup>7</sup>	Strongly pitted	9x10 <sup>8</sup>
26	835	870	0	3x10 <sup>4</sup>	saucers	none obs.	-	Saucers	-

39A	865	905	100	too high to count	V.faint ripples.	R & T	$3 \times 10^8$	Terraced	$2 \times 10^8$
40A	"	"	100	"	ripled	R & T	$1.6 \times 10^8$	-	-
63B	80	940	50	$2.1 \times 10^7$	f.ripples	R & T	-	Terraced	$7 \times 10^7$
18	900	945	4.4	$3 \times 10^3$	v.smooth	T	-	Very smooth	-
42A	"	"	100	too high to count	granular	T	$3 \times 10^7$	Terraced	$1.7 \times 10^7$
38A	910	955	100	too high to count	granular	T	$5 \times 10^8$	Pits in groups	$1.9 \times 10^4$
10	980	1035	0	$4.5 \times 10^3$	saucers	T	-	-	-
40B	"	"	100	too high to count	granular	T	$2 \times 10^8$	-	-
65A	1000	1055	0	-	-	none observed	-	Very smooth	-
20	"	"	4.4	$1 \times 10^4$	smooth	" "	-	" "	-
65B	"	"	50	-	-	T	$6 \times 10^6$	Terraced	$2 \times 10^7$
42B	"	"	100	$1.4 \times 10^5$	v.smooth	none observed	-	Terraced some areas smooth	$6.5 \times 10^6$
64B	1005	1060	50	too high to count	granular	T	$1.2 \times 10^7$	Terraced	$8 \times 10^6$
63A	1010	1065	50	"	strongly rippled	T	-	Terraced	$2 \times 10$
61A	"	"	0	"	granular	T	$1.8 \times 10^7$	"	$1.2 \times 10^7$
61B	0	1070	100	"	textured	T	$10^8$	"	$2 \times 10^7$
61B	1020	1075	100	$2 \times 10^4$	ft.ripples	T	$6 \times 10^5$	"	$1.5 \times 10^6$
43B	1050	1110	100	$10^4$	a few rippls.	none observed	-	Very smooth	-
24	1100	1165	4.4	none	$6 \times 10^4$ large saucers	" "	-	"	-
4 A	1140	1210	100	none	a few rippls.	" "	-	"	-

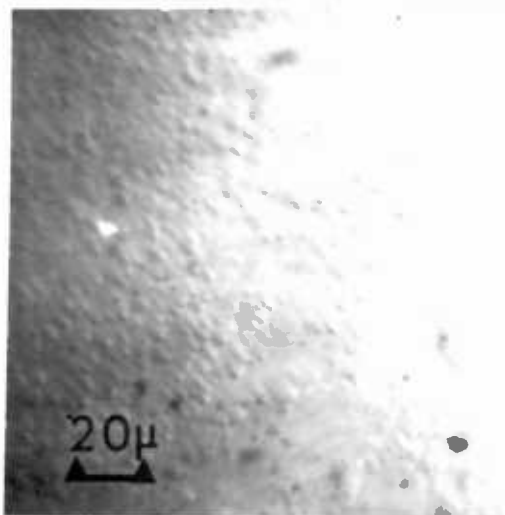
\* Allen (1957)

TABLE 3.2

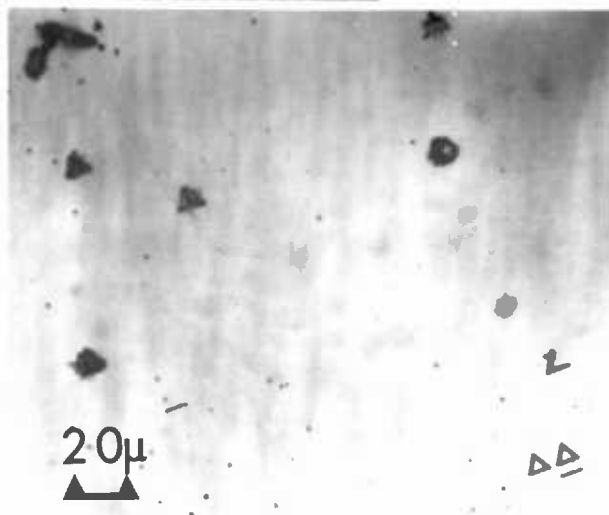
SUMMARY OF TEM RESULTS ON ETHYLENE-CONTAMINATED {111} LAYERS

Growth Temp. °C	Ethylene conc. p.p.m.	Defect Structure	Surface Structure
830-1200	0	Mainly featureless	V. smooth, some saucers
830-860	4-10	Ribbon (R) & Tetrahedra (T)-type stacking faults	Terraced, pinning sites
830-860	20-100	R	Faceted
860-940	50-100	R & T	Terraced, pinning sites
940-1160	4	T (low density)	V. smooth
940-1070	50-100	T, SiC	Terraced, pinning sites
1100-1200	100	Featureless	V. smooth

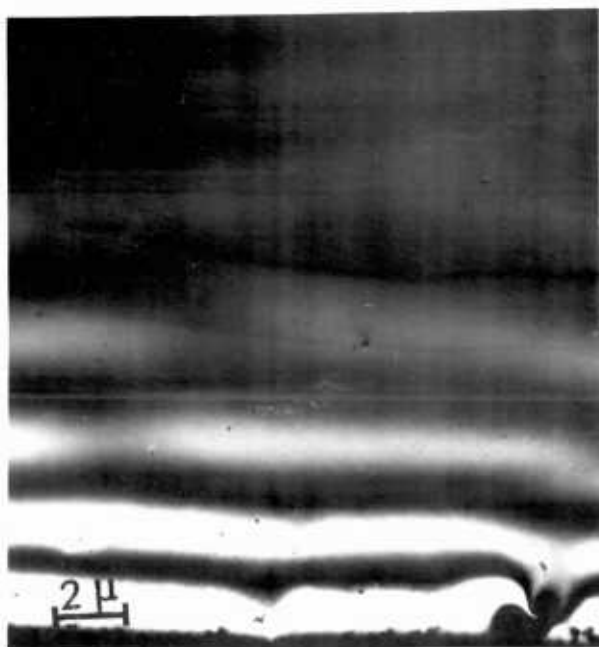
Examples of viewing techniques used in study, as applied to control layers (no deliberate contamination)



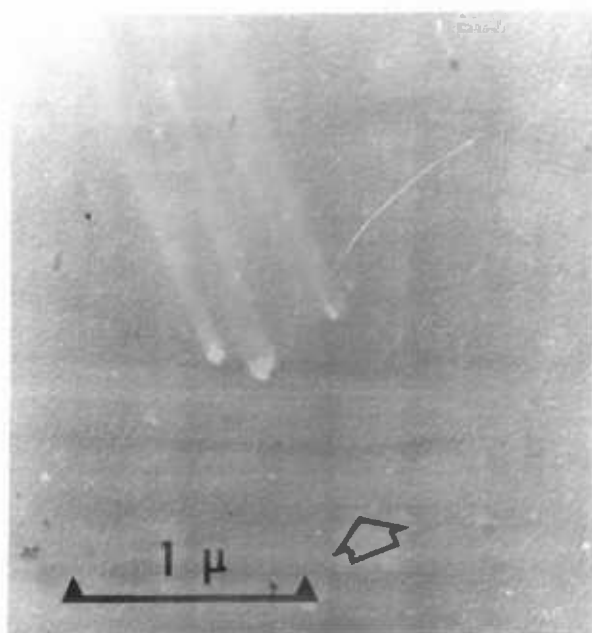
a) RB34A. Interference contrast optical micrograph



b) RB65A. Sirtl etch optical micrograph

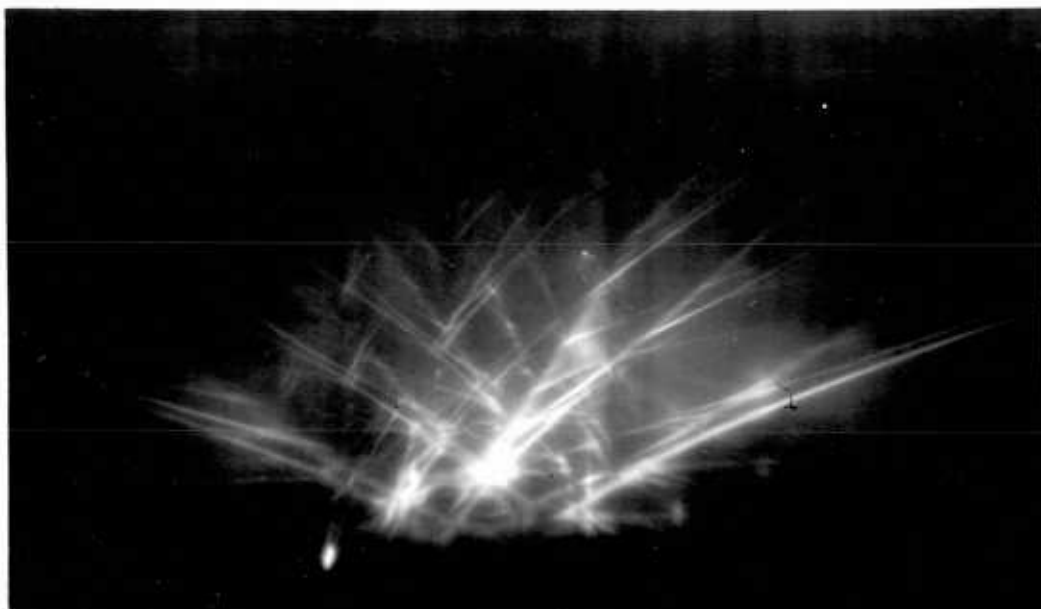


c) RB29. 2 beam dark field TEM

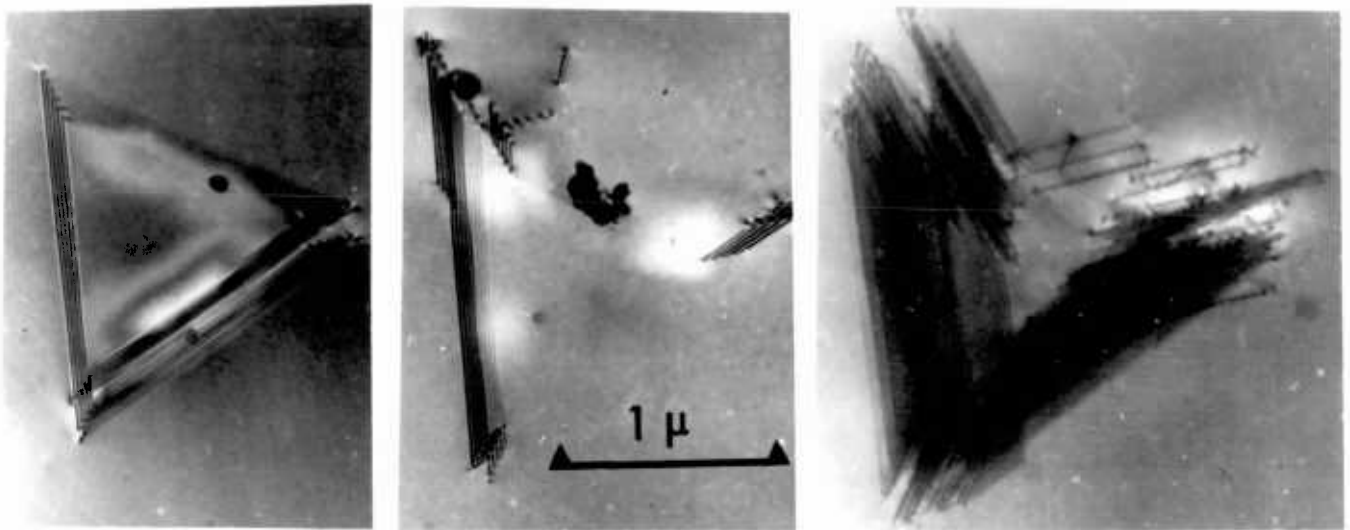


d) RB23. Pt/C replica electron micrograph shadow direction arrowed

e) RB26, GAED  
<110> projection



Stacking fault structures in control layer RB26



a)

b)

c)

Bright Field 220 reflections

FIG. 3.3

Saucer-like depressions in control layer RB26



a) Pt/C replica, TEM.



b) Interference contrast optical micrograph.

### 3.2. Low temperature growth (830-860°)

Ethylene contamination induced stacking fault structures which in the main took the form of ribbons lying on the inclined  $\{111\}$  planes. The ribbons were often overlapping and had irregular edges. A series of TEM micrographs, Fig.3.4., shows increasing foil thickness from a region near the edge of the hole to a region greater than 1  $\mu\text{m}$  thick. The micrographs were taken in the 2-beam  $s = 0$  condition using a  $\{220\}$  type reflection. The foil thickness for any area can be calculated by multiplying the number of stacking fault fringes of the larger faults which intersect each surface of the foil by  $\sim 750\text{\AA}$  which is the extinction distance for the reflection used. This layer, RB14 was grown at 855°C with a high ethylene concentration (92 ppm) and Fig.3.4 shows that the average stacking fault density is  $\approx 10^9 \text{cm}^{-2}$ . The ribbon faults are between 0.1 and 0.4  $\mu\text{m}$  wide and are usually truncated by both specimen surfaces and hence are of indeterminate length.

Many attempts were made to characterise the stacking faults by diffraction contrast analysis (DCA) before success was achieved in the two series (taken from this layer) shown in Appendix A1. The earliest attempts failed mainly due to lack of experience of this type of analysis but gradually the exacting conditions used to obtain each micrograph and the relevant reflections to utilise were realised, together with the steps necessary to quickly establish the habit plane of the selected stacking fault ribbons and to index the diffraction vectors ( $g$ ). Examination of the fringe contrast in Fig.3.4 shows that the bright outer fringe usually lies on the leading side of the fault with respect to  $g$ . Applying the rule of Gevers, Art & Amelinckx (1963), this means that the majority of stacking faults are extrinsic in nature. DCA showed (Appendix A1) that most of these were bounded by Shockley partial dislocation loops having Burgers vectors of the form  $\frac{1}{6} \langle 112 \rangle$  lying in the  $\{11\bar{1}\}$  habit plane of the faults. The Burgers vectors are perpendicular to the intersection of the  $\{111\}$  specimen surface and the  $\{11\bar{1}\}$  plane. In the notation of the Thompson tetrahedron (Fig.A6) loops on inclined planes b), c) and d) have Burgers vectors  $A\beta$ ,  $A\chi$  and  $A\delta$  respectively, where a) is the plane of the epitaxial layer, i.e.  $A\alpha$  is the  $\langle 111 \rangle$  growth direction. Occasionally examples were found of extended dislocations, i.e. ribbon faults bounded by pairs of partial dislocations having Burgers vectors such as  $A\beta$  and  $\beta C$ . The stacking fault marked R at the bottom of Fig.3.5(a) lying on  $(11\bar{1})$  is intrinsic and is bounded by Shockley partials with Burgers vectors of  $\frac{1}{6} [\bar{1}21]$  and  $\frac{1}{6} [112]$  on the L.H. and R.H. sides respectively. This is confirmed by observing contrast at the partials in the series shown in Fig.3.5 with reference to Table A.1.

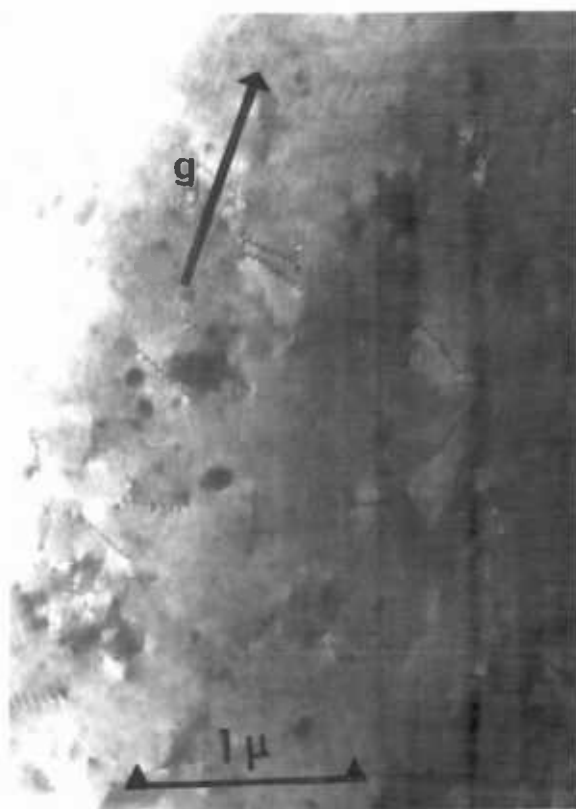
Ribbon stacking faults in low temperature, high ethylene layer RB14.



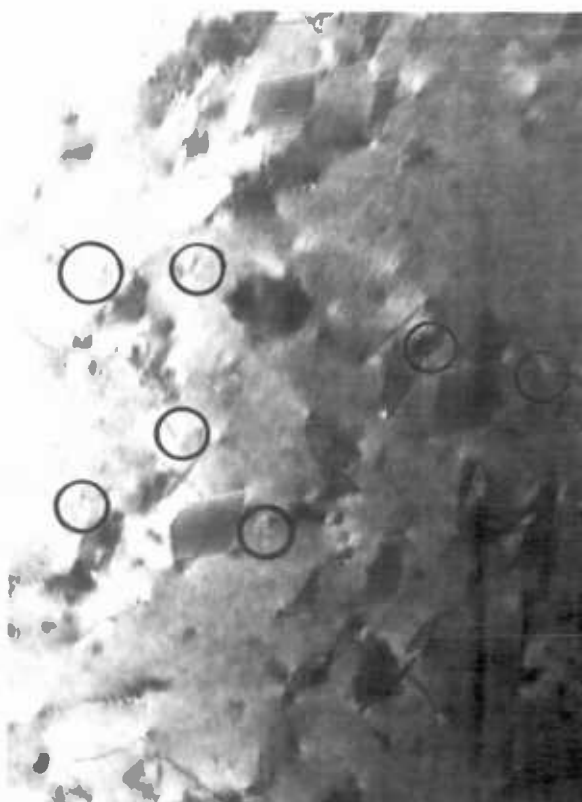
a) foil 750 - 3000Å thick



b) foil 3000 - 5250Å thick

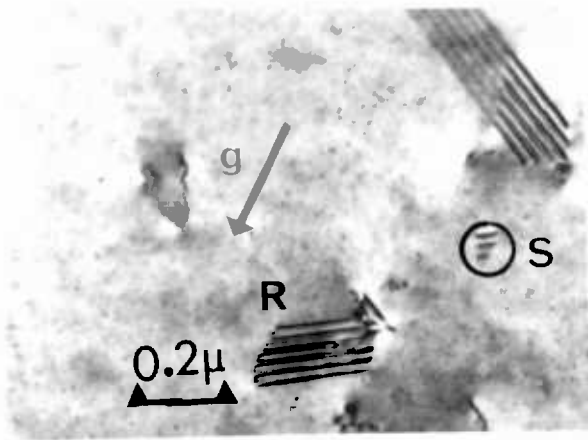


c) foil 5250 - 7500Å thick

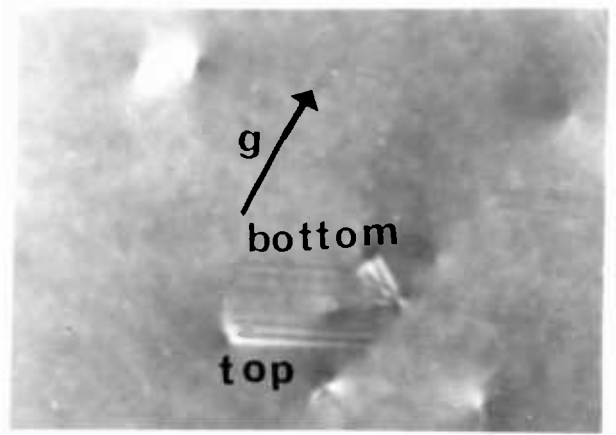


d) foil average thickness 1 μm

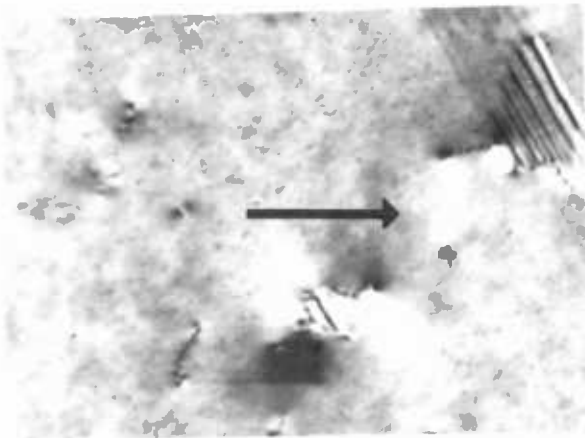
TEM micrographs taken using Dark field {220} reflection,  $s=0$



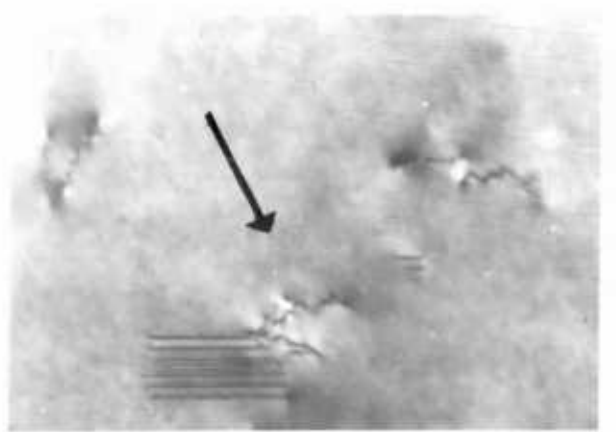
a) BF ( $\bar{2}02$ )



b) ( $20\bar{2}$ ) DF  $s < 0$



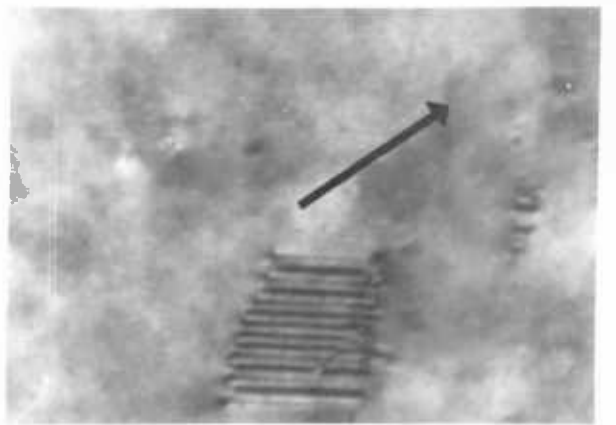
c) ( $2\bar{2}0$ )



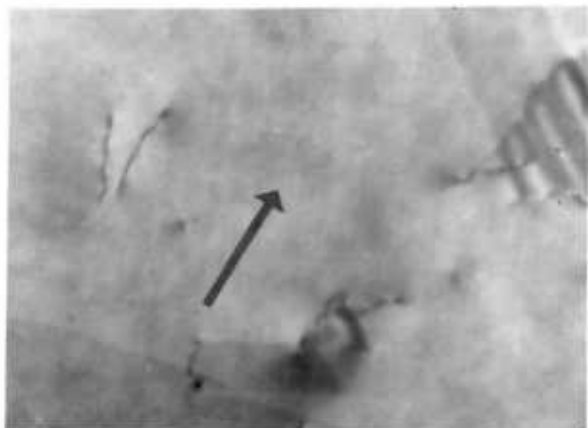
d) ( $0\bar{2}2$ )



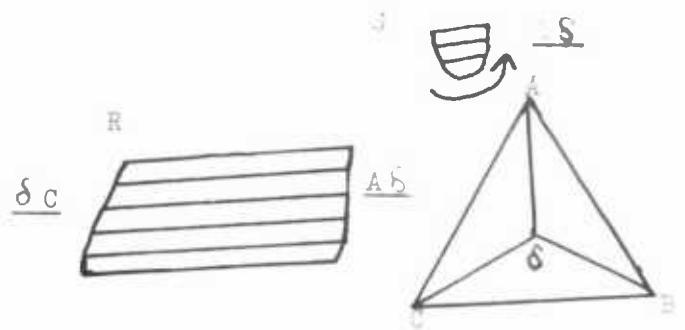
e) ( $1\bar{1}1$ )



f) ( $1\bar{1}\bar{1}$ )



g) ( $1\bar{1}\bar{3}$ )



n) Burgers vectors of partial dislocations bounding stacking faults marked R & S in Fig.3.5(a)

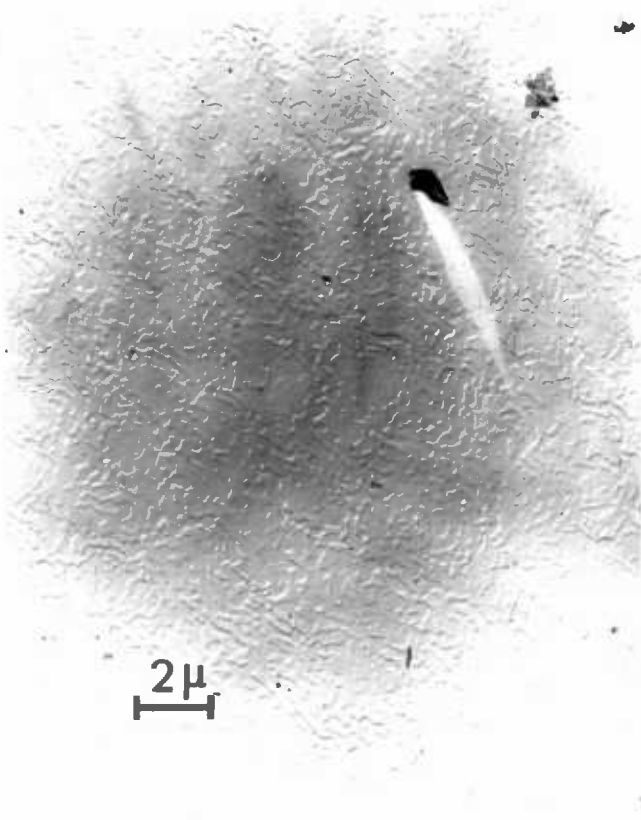
Thus the partials are visible for  $g \cdot b$  values of  $\pm 1$  &  $\pm \frac{2}{3}$  and invisible for 0 and  $\pm \frac{1}{3}$ . The simultaneous presence of fringe contrast in some of the micrographs makes observation of dislocation contrast difficult. In the Thompson notation, the extended dislocation can be written as  $\underline{A}\underline{S} + \underline{S}\underline{C}$ , Fig.3.5h, and is the dissociation product of a perfect dislocation on the  $(11\bar{1})$  glide plane with Burgers vector  $\underline{AC}$  i.e.  $\frac{1}{2} [011]$ , Appendix A2 shows that the inclined dislocations observed in these layers have Burgers vectors of this type. Also of interest in Fig.3.5a) is the small stacking fault loop, shown ringed, which also lies on  $(11\bar{1})$  and which has a Burgers vector  $= \frac{1}{6} [112]$  i.e.  $\underline{AS}$  and so is typical of the majority of ribbon faults. Notice that this defect almost vanishes in Fig.3.5(b) and so lies beneath the top of the foil with respect to the electron beam, which is also the top of epitaxial layer. Close examination of the thicker regions of Fig.3.4 reveals many such small stacking faults which are only a few fringes thick i.e. which do not extend to both foil surfaces. It was shown by similar dark field observations that some of these faults were also buried below the top of the epitaxial layer.

Fig. 3.5 also shows an example of overlapped stacking faults which show faint fringe contrast along the portion which is overlapped. Humble (1968) has shown that the contrast observed with overlapped faults can be simulated using a computer line printer when values of fault inclination, separation and diffraction conditions are inserted into the programme using Head's method (1967). Such overlapping was regarded as an unnecessary complication in the present work since many examples of isolated stacking faults were available for analysis. Also observed in Figs.3.4 and 3.5 are many undissociated dislocations. Analysis shows (Appendix A2) that these have inclined  $\frac{1}{2} \langle 110 \rangle$  Burgers vectors and have large screw components.

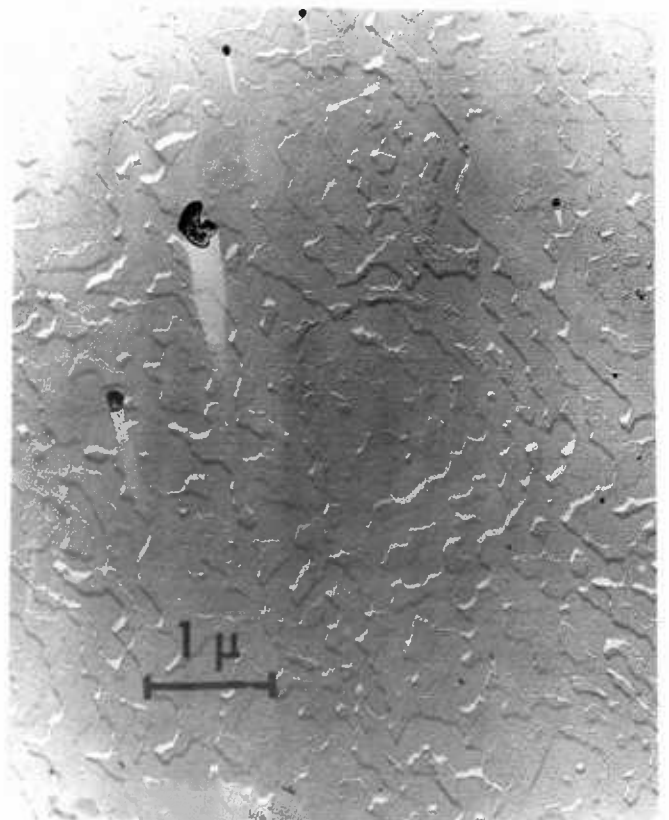
Electron micrographs of a Pt/C replica of the surface of layer RB14 are shown in Fig.3.6(a) (b). The shadowing direction is clearly seen from the shadows cast by the artefacts on the surface. The surface is faceted with steps up to about  $200\text{\AA}$  high. These steps can also be observed by direct TEM in Fig.3.4(a) in regions of the extinction bands. Straight portions of the facets tend to lie along  $\langle \bar{1}10 \rangle$  directions, i.e. parallel to the stacking fault fringes. Optical examination using interference contrast, Fig.3.6(c) showed a finely textured granular structure. Clearly, optical observations are of little use at such high defect densities.

FIG. 3.6

Surface study of low temperature, heavy ethylene layer RB14

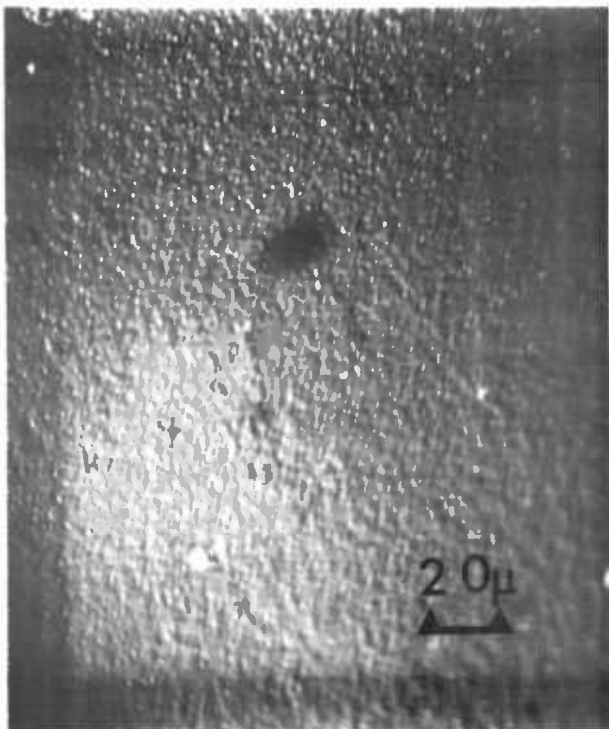


a) Pt/C Replica

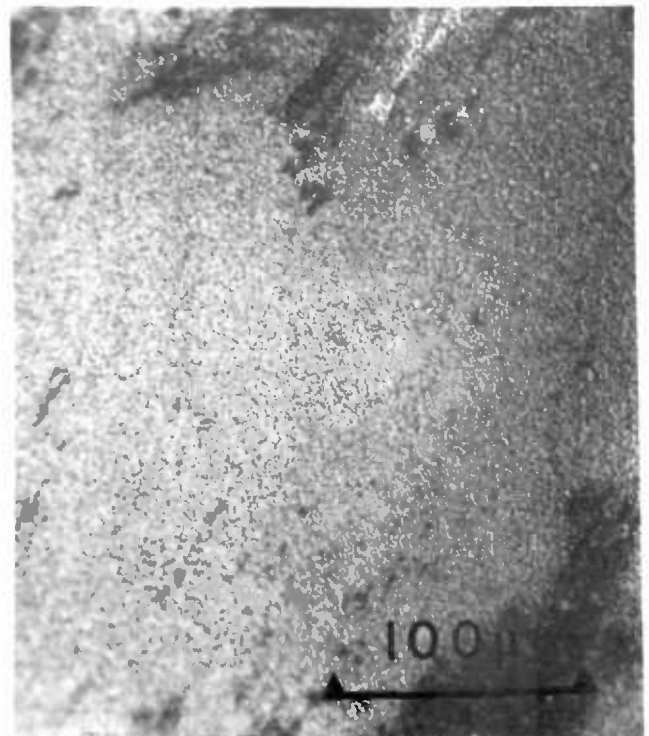


b) Pt/C Replica

TEM



c) Interference contrast



d) Sirtl etched

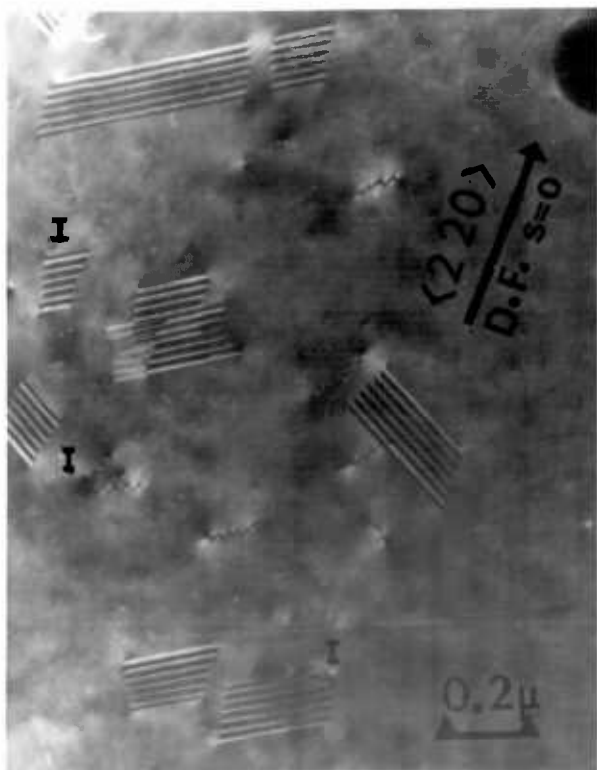
OPTICAL MICROSCOPY

As the level of ethylene contamination was reduced, the stacking fault densities dropped and the ribbon faults tended to be wider. Figs. 3.7a) and b) show the structure of layers from runs RB12 and RB34B which had 36 and 7.5 p.p.m. ethylene contamination respectively. Most of the faults are seen to be extrinsic from the outer fringe contrast although the faults labelled I are clearly intrinsic. Figs. 3.7c) and d) show that the surfaces of the layers are much less faceted than at higher ethylene levels (c f Fig.3.6a) b)). Fig. 3.7d) is more typical of higher growth temperatures (section 3.3). A most interesting stacking fault structure is shown in Fig. 3.7e). This was taken from a layer, RB22, which was grown with only 4 p.p.m ethylene contamination. The micrograph contains a long extrinsic ribbon fault marked E, but also shows two intrinsic stacking faults which have intersected to form a stair-rod dislocation. Consideration of the dislocation reactions involved in this situation led to a new model of stacking fault tetrahedron formation which is given in Chapter 6.4.

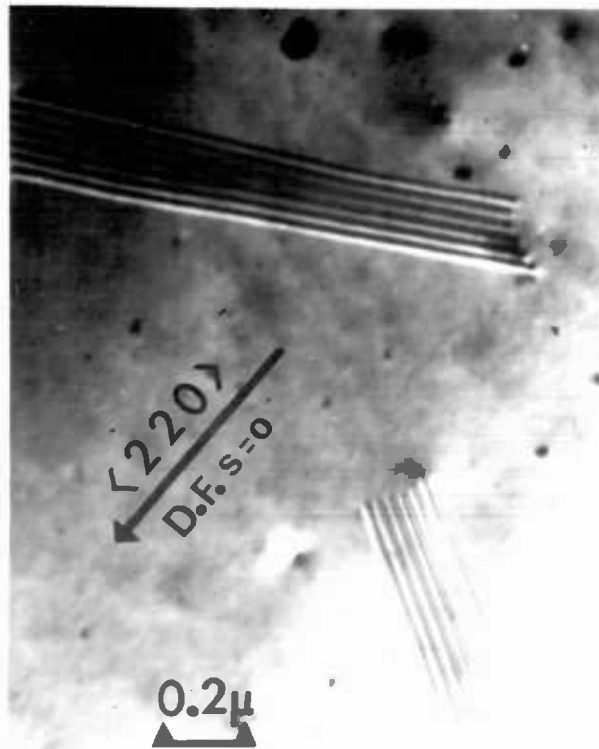
### 3.2.1. Annealing experiments

A few experiments were made to determine the effect of annealing on ribbon stacking fault structures. TEM specimen blanks were heated on a Si substrate bar at temperatures up to 1200°C for 30 min. in either H<sub>2</sub>, N<sub>2</sub> or in vacuum at  $2 \times 10^{-5}$  torr and then jet thinned and examined. No changes in size or character of the faults were detected after annealing in vacuum or in either gas although a thick polystalline layer of  $\beta$ -SiC formed on the surface of the vacuum annealed specimen, Fig.3.8(a), due to contamination from the vacuum system. The ribbon faults can be faintly seen beneath the SiC film. The surface of the layer was also extremely pitted in places, Fig. 3.8(b). Fig. 3.8(c) is a transmission electron diffraction (TED) pattern of the  $\beta$  SiC layer and in addition shows the  $\langle 111 \rangle$  Si spot pattern due to the underlying Si layer which was used as an internal standard of known lattice spacing to calculate the camera constant of the electron microscope,  $K$ . We recall that for TED,  $Dd = K$  where  $D$  is the ring diameter of a given Bragg reflection corresponding to lattice planes of spacing  $d$ . Table 3.3. compares the measured values of the lattice spacing,  $d$ , obtained from the ring pattern, with established diffraction data on  $\beta$ -SiC.

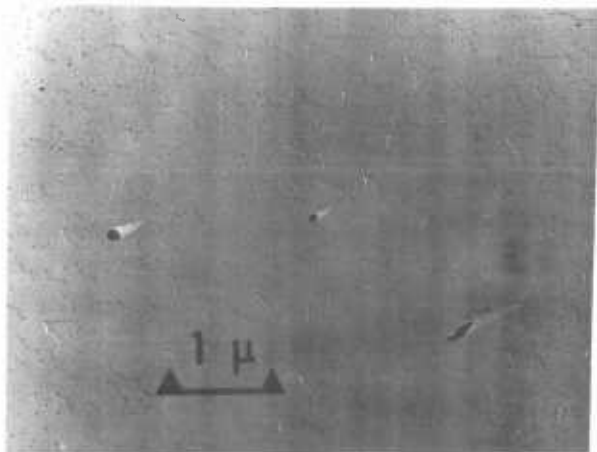
Defect and surface structures at medium and low ethylene levels



a) RB12, 36 ppm ethylene



b) RB34B, 7 ppm ethylene



c) Pt/C replica of RB12



d) Pt/C replica of RB34B

e) RB22, 4 ppm ethylene Dark field,  
s = 0 g =  $\langle 220 \rangle$

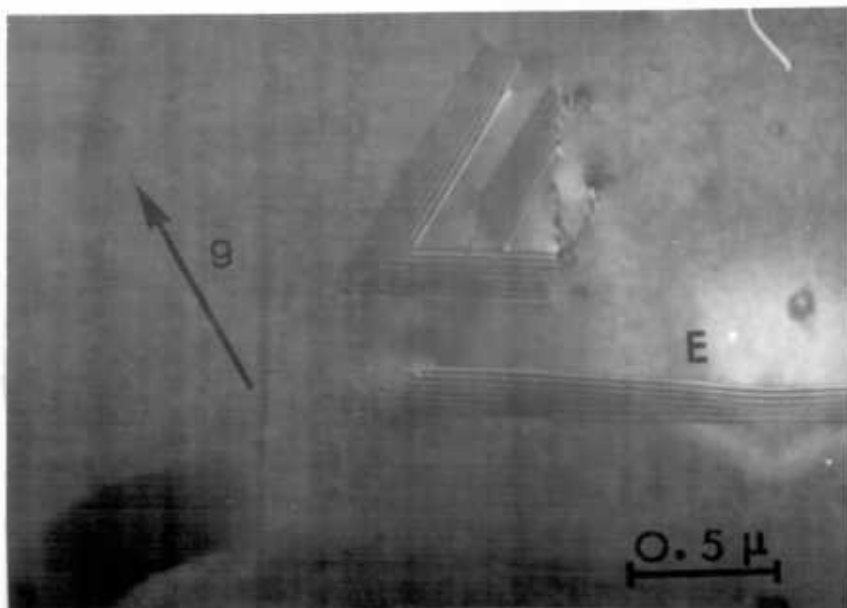
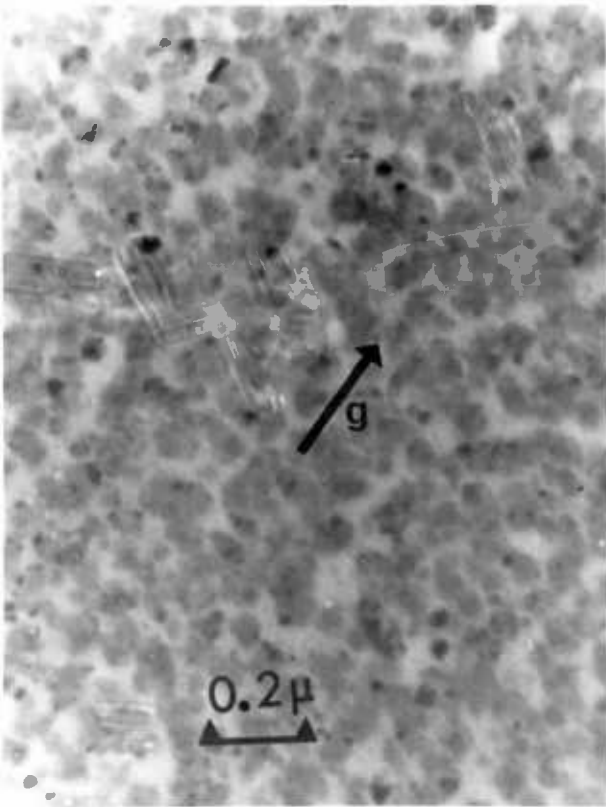
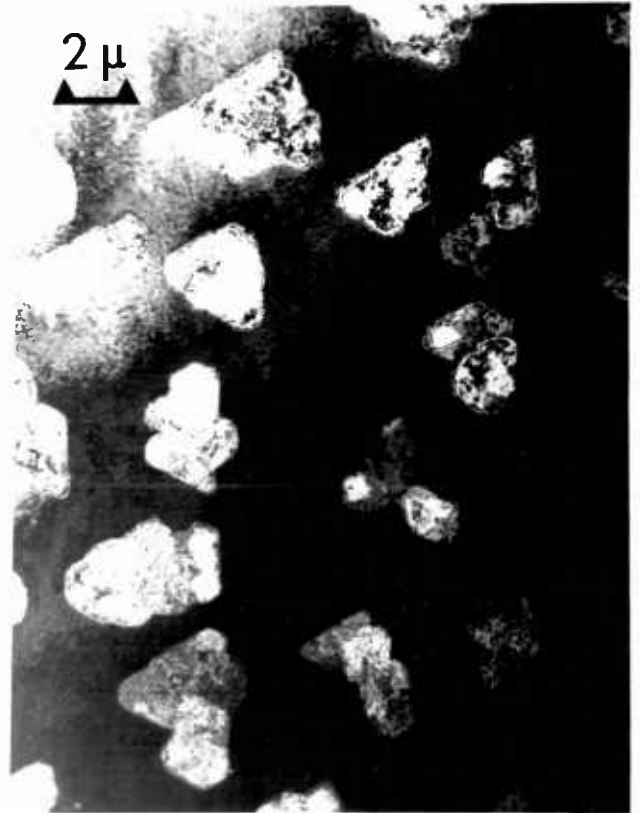


FIG. 3.8

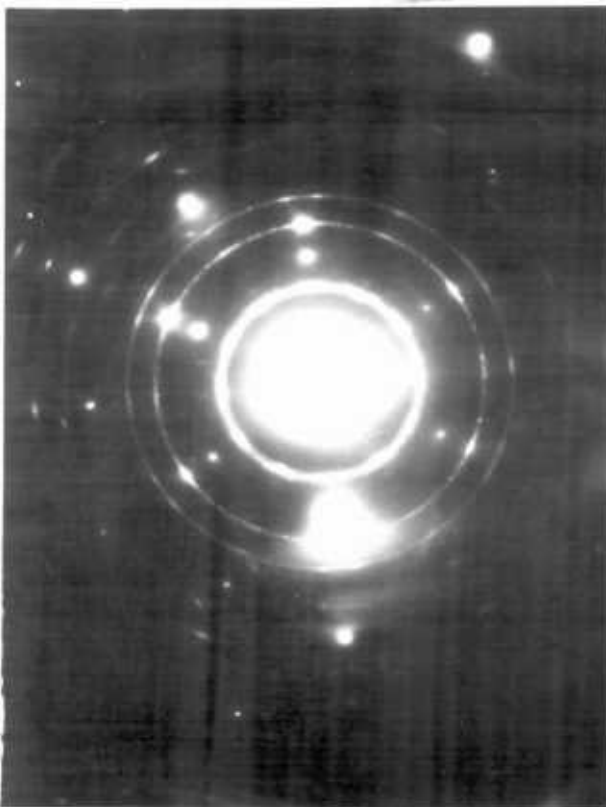
Anneal at  $1055^{\circ}\text{C}$ ,  $2 \times 10^{-5}$  torr, of layer RB14 containing ribbon faults showing SiC contamination film



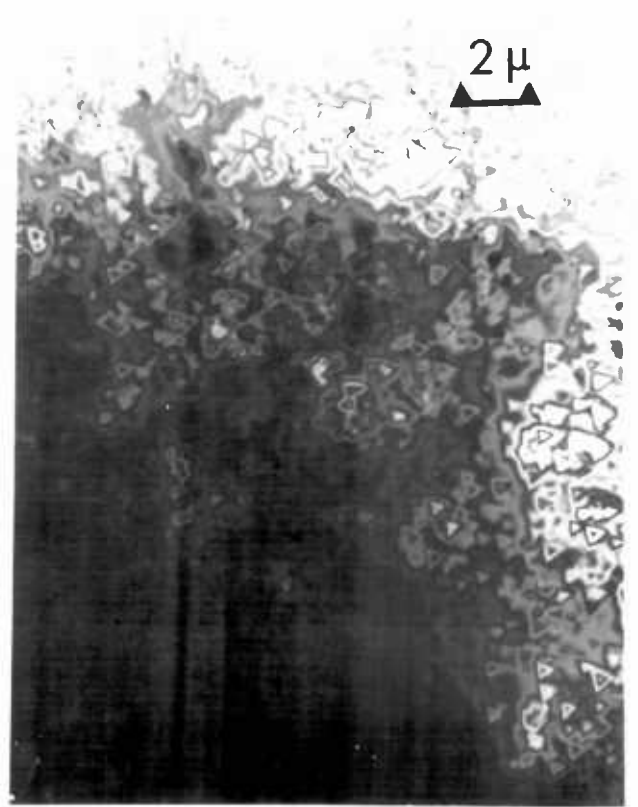
a) High magnification TEM, showing faults.



b) Low magnification showing pits



c) Diffraction pattern of area b)



d) 5 sec. etch in 1:3 HF :  $\text{HNO}_3$

TABLE 3.3. IDENTIFICATION OF THE  $\beta$  - SiC layer

D cm meas.	d Å meas.	Intensity estim.	d Å $\beta$ - SiC ASTM index	Miller indices h k l	Intensity I/I <sub>0</sub>
1.57	2.67	Sp	(2.66)	111 twin spot	-
1.66	2.51	VS	2.50	111	1
1.93	2.17	VW	2.17	200	.12
2.18	1.92	Sp	(1.92)	220 Si	-
2.70	1.55	S	1.54	220	.80
3.18	1.32	S	1.31	311	.60
3.32	1.26	VW	1.25	222	.04
3.80	1.10	Sp	(1.09)	422 Si	-
4.18	1.00	M	.997	331	.14
4.73	.886	MW	.888	422	.16
5.03	.833	W	.836	333	.12
5.74	.731	MW	.726	600	.02

NOTES:

1. abbreviations used in estimated intensity column Sp = spot diffraction (rather than ring), VS = very strong, S = strong, MW = medium weak etc.
2. Intensity I/I<sub>0</sub> is relative intensity with respect to strongest line, i.e. (111) as measured from X-ray powder diffraction pattern.

Agreement between the two sets of 'd' spacing is good and intensities of the rings agree well indicating that there is no preferred orientation of the  $\beta$  - SiC film. The extra spots inside the (111) SiC ring are attributed to twinning and double diffraction effects as demonstrated by Pashley & Stowell (1963) on evaporated Au films. Thus the ratio of d twin/d(111) = 1.06 in each case.

The SiC was removed by immersing the specimen for 5 sec. in 1 : 3 HF : HNO<sub>3</sub> and quenching in water. The surface was finely pitted, Fig.3.8(d), but examination at higher magnification revealed a similar stacking fault structure to that shown in Fig.3.4. Since SiC is resistant to this etch, its removal must have been effected by sacrificing the top of the Si epitaxial layer hence leading to the observed pitting.

On two occasions (RB28 and RB36B), layers were annealed in situ at 1135 and 1200°C for 20 and 30 mins. respectively directly after growth under UHV conditions. The structure as revealed by TEM showed the expected ribbon faults but in addition had a grainy appearance, Figs. 3.9(a) b), which was more marked in the  $s \neq 0$  condition, Fig. 3.9(c). On the basis of results in sections 3.2.3, 3.3. and 3.4, it is likely that precipitation of SiC has occurred during sublimation of the top of the epitaxial layer during the anneal. The stacking fault structure of the control layer RB36A which was not annealed, was similar to Fig. 3.9(b) but showed less granularity, Fig. 3.9(d). Further evidence that sublimation has taken place is that the surface of the annealed layer, Fig. 3.9(e), is much smoother than the faceted surface of the control layer, Fig. 3.9(f).

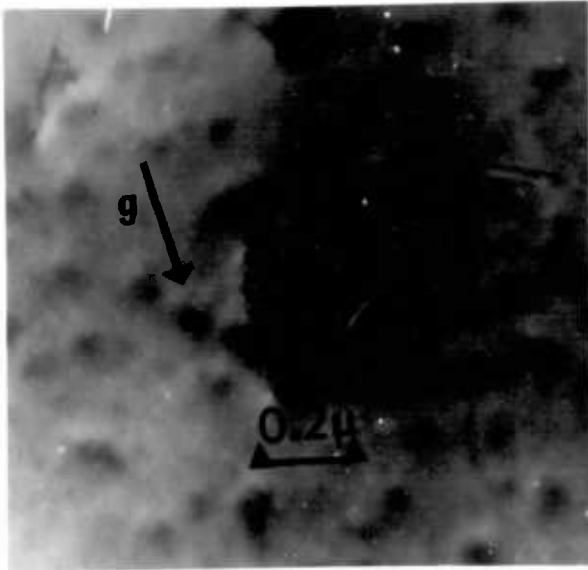
### 3.2.2. Termination of ethylene during growth

In one experiment (RB35B) growth was commenced with 50 ppm ethylene in the silane with the substrate at 860°C. The ethylene was turned off after the growth of about 2  $\mu\text{m}$  of silicon and growth continued for a further 2  $\mu\text{m}$ . The outer micron of the layer, as revealed by TEM, contained stacking fault structures which were mainly tetrahedra etc., Fig. 3.10(a), which by measurement were found to have nucleated during the period immediately after the ethylene flow was cut off. (By geometry, it can be easily shown that length of the side of the tetrahedron is equal to  $\sqrt{3/2}$  of the depth of the apex of the tetrahedron below the layer surface). Fig. 3.10(b) was taken with the specimen tilted to near a  $\langle 110 \rangle$  pole using a  $\{1\bar{1}1\}$  reflection and shows small scale surface pitting due to jet etching. Although most stacking faults terminate in  $\langle 110 \rangle$  stair-rod directions, one marked A does not, and is probably Shockley-bounded. Stacking faults lying in  $(1\bar{1}1)$  planes are normal to  $\underline{g}$  and hence are invisible because they are edge-on in this condition, but faults lying on  $(\bar{1}11)$  are not quite vertical and project as a thick line and generally intersect at their top end with  $(11\bar{1})$  stacking faults. These latter faults have a wider projection than near the  $[111]$  zone since the  $(11\bar{1})$  plane is now tilted to an angle of only  $\sim 35^\circ$  to the beam normal, compared to  $\sim 70^\circ$  in the  $[111]$  zone. Stacking fault geometries in layers grown on  $\{110\}$  substrates will be shown in Chapter 4.1.

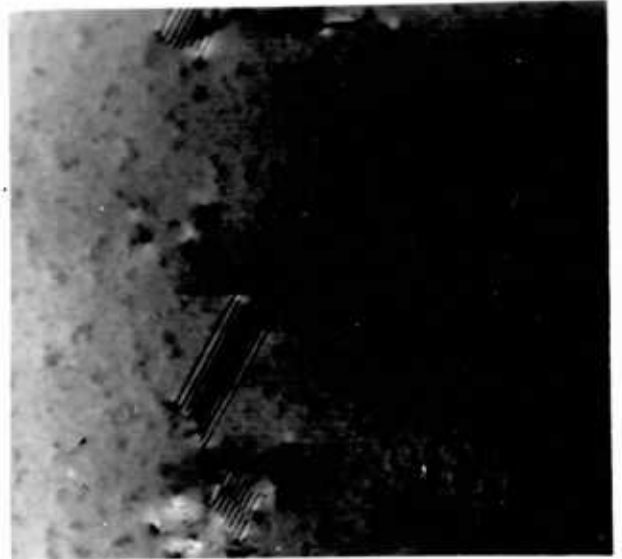
Removing the top 2  $\mu\text{m}$  of the layer by etching in 1 : 9 HF : HNO<sub>3</sub> revealed ribbon stacking faults, Fig. 3.10(c). These faults must have terminated

FIG. 3.9

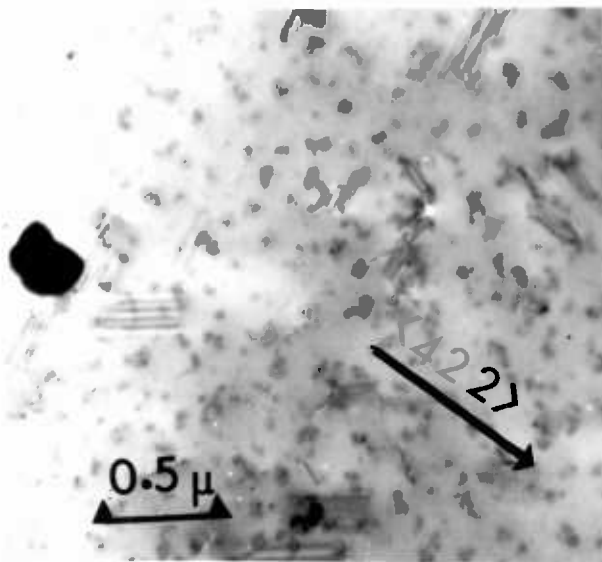
Anneal at  $\sim 1200^{\circ}\text{C}$  in UHV epitaxy system immediately after growth of layer.



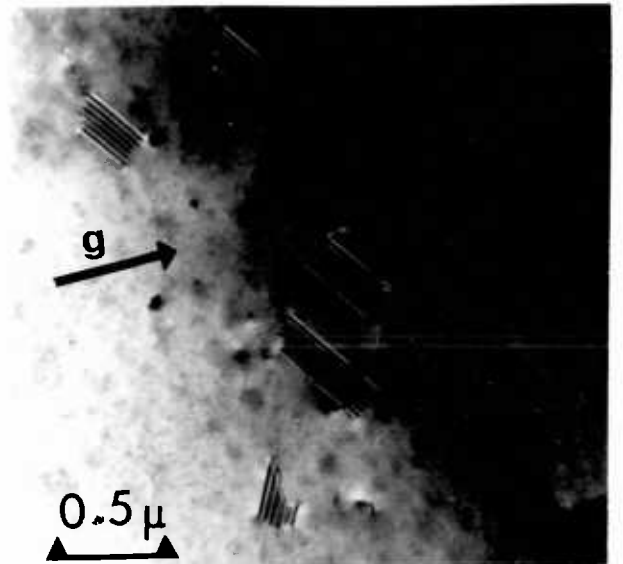
a) RB28, 20 ppm ethylene



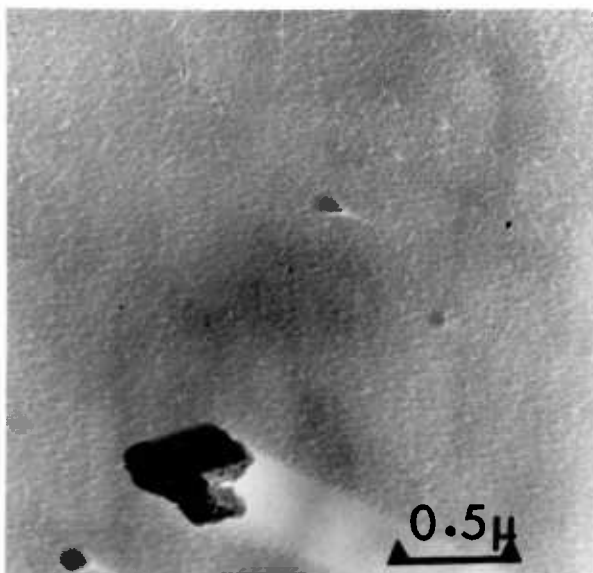
b) RB36B, 31 ppm ethylene



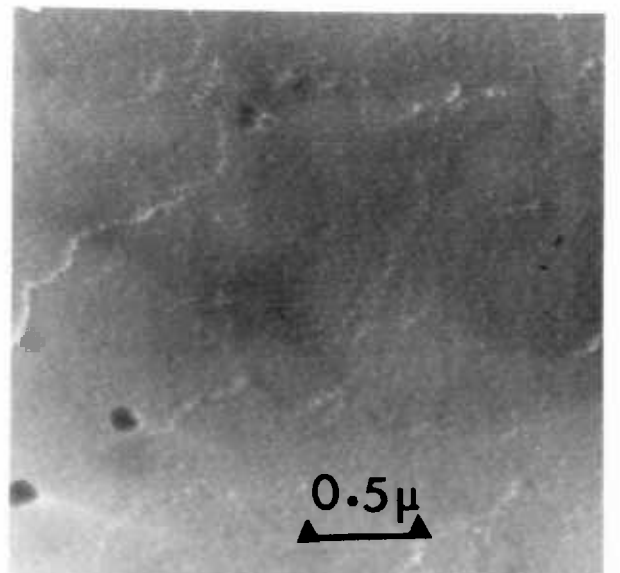
c) RB36B, 2 beam, s-ve



d) RB36A control layer, unannealed. 50 ppm ethylene

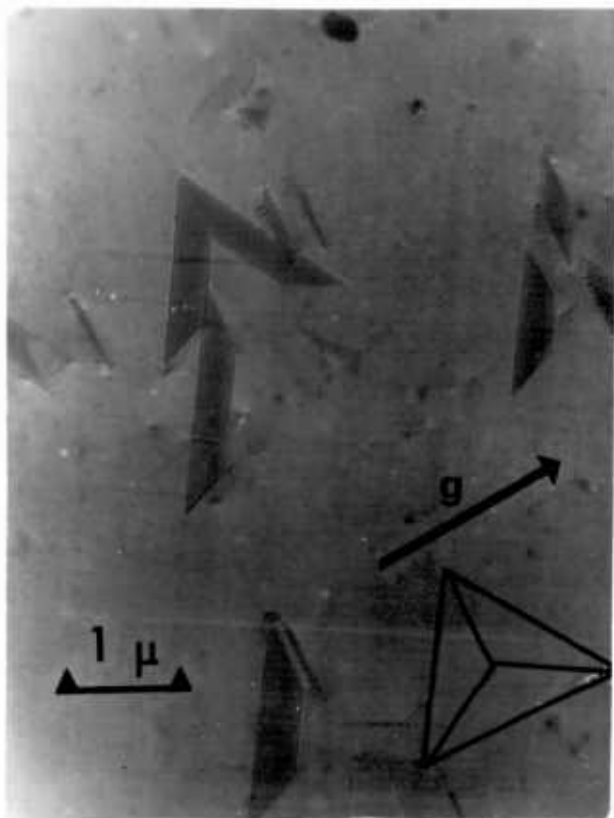


e) Pt/C replica, RB36B

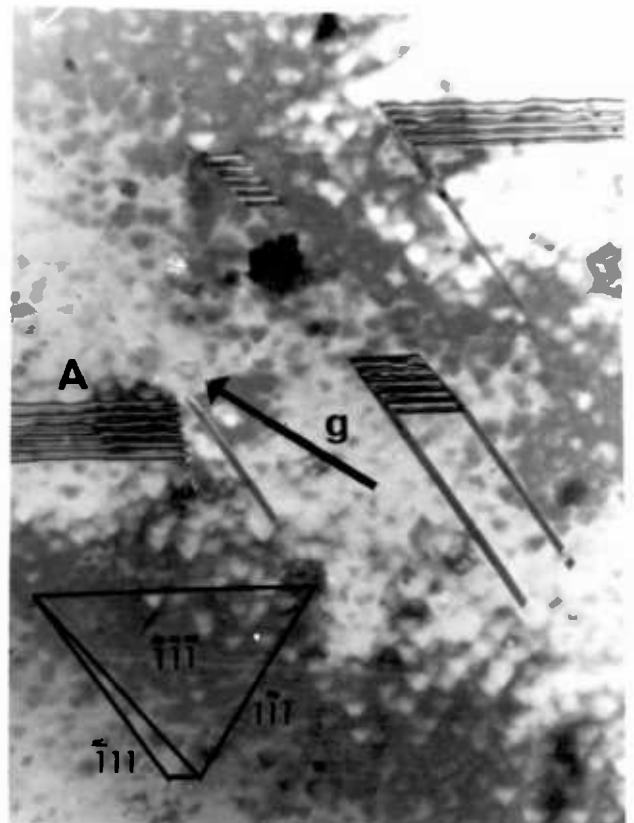


f) Pt/C replica, RB36A.

Ethylene termination during epitaxial growth RB35B



a)  $\{220\}$  refln.  $[111]$  pole.  
Outline Thompson tetrahedron shown in exact  $[111]$  orientn.



b)  $\{\bar{1}\bar{1}\bar{1}\}$  refln.  $[110]$  pole.  
Outline Thompson tetrahedra shown a few degrees off exact  $[110]$  orientation, as in micrograph.



c) same layer with 2 μm etched away.



d) as c) showing examples of intersecting faults.

within the layer as epitaxial growth continued without the presence of ethylene since such faults were seldom observed in the top of the layer. The ribbon faults were bounded with Shockley partials having similar Burgers vectors to those analysed in Appendix A1 since the partials were invisible in all three  $\{220\}$  reflections in the  $[111]$  zone. Some examples of intersecting faults were also seen, Fig.3.10(d).

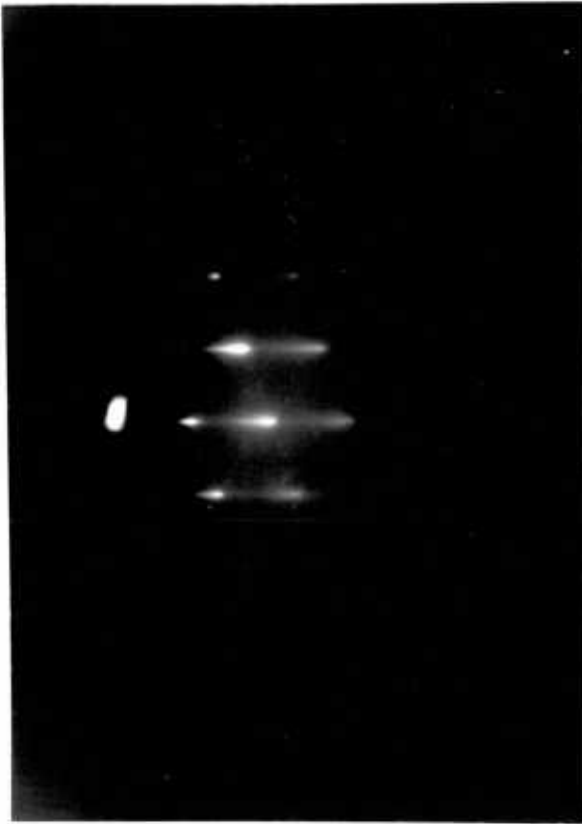
### 3.2.3. Heavy ethylene contamination

In one experiment (RB35A), a change in growth procedure inadvertently led to a very high ethylene contamination level (670 ppm). Glancing angle electron diffraction (GAED) gave a streaked spot pattern with no Kikuchi bands, Fig.3.11(a), indicating a rough surface which was confirmed by the Pt/C replica, Figs. 3.11 b) c). The structure of the layer was extremely faulted and deformed, Fig. 3.11(d). The transmission electron diffraction pattern obtained by tilting about the  $[1\bar{1}0]$  axis to the  $[332]$  pole gave no Kikuchi bands but extra spots indicating twinning and also rings due to polycrystalline  $\beta$ -SiC were found, Fig.3.11(e). Fig.3.11(f) is a diagram of the diffraction pattern giving the indexing of the spots. The twin spots lie in the projected directions of the  $\langle 111 \rangle$  axes and lie at a distance  $\frac{1}{3} \langle 111 \rangle$  from the matrix spots. The twin spots appear because of buckling since the  $[1\bar{1}1]$  and  $[\bar{1}11]$  axes lie only a few degrees from the sphere of reflection. Dark field observations on one of the twin spots showed a high density ( $\sim 10^{10} \text{cm}^{-2}$ ) of microtwin lamellae, Fig.3.11(g)

### 3.3. Moderate and high temperature growth (860-1200°C)

As the growth temperature increased, the number of ribbon stacking faults decreased. Above 860°C stacking fault tetrahedra were observed in greater numbers. Fig. 3.12(a) shows a tetrahedron and ribbon fault in a layer (RB63A) grown at 940°C. Closer examination of the defects shows that the tetrahedron has only 4 fringes compared with 8 fringes in the ribbon fault and so has nucleated in the top 0.3  $\mu\text{m}$  of the layer. Fig. 3.12(b) shows that the ribbon fault has collided with another stacking fault but unlike the case of the intersecting stacking faults in Fig.3.7(e), the stair-rod does not extend to the top of the epitaxial layer. A micrograph taken using the remaining  $\{220\}$  type reflection in the  $[111]$  zone is shown in Fig.3.12(c). The LH partial dislocation of the ribbon fault seen in this latter micrograph is visible here and also in Fig.3.12(a), although the RH partial is invisible in all three

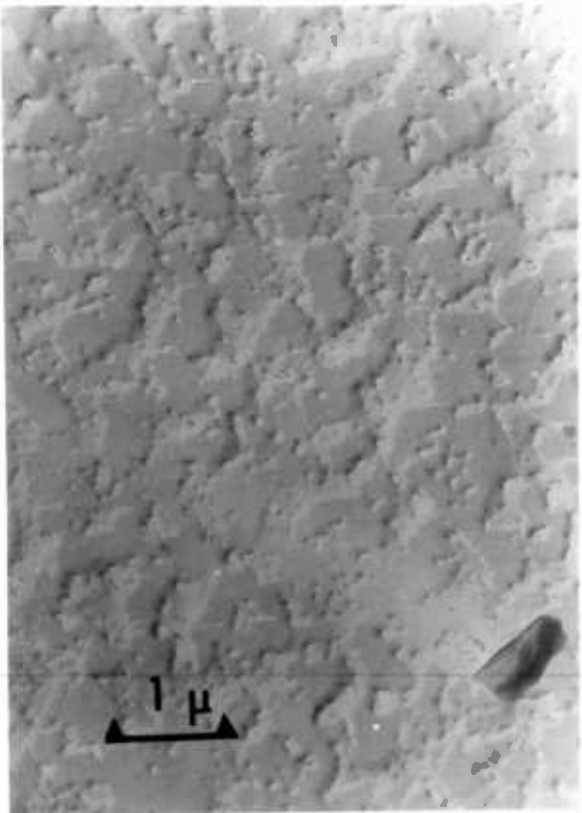
Surface studies & microstructure of very heavy ethylene contamination layer RB35A



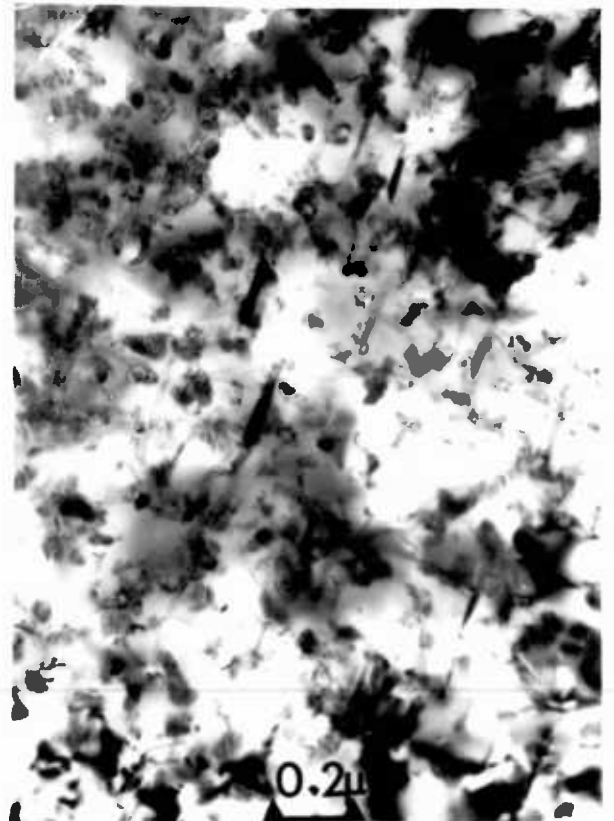
a) GAED, showing streaked spots



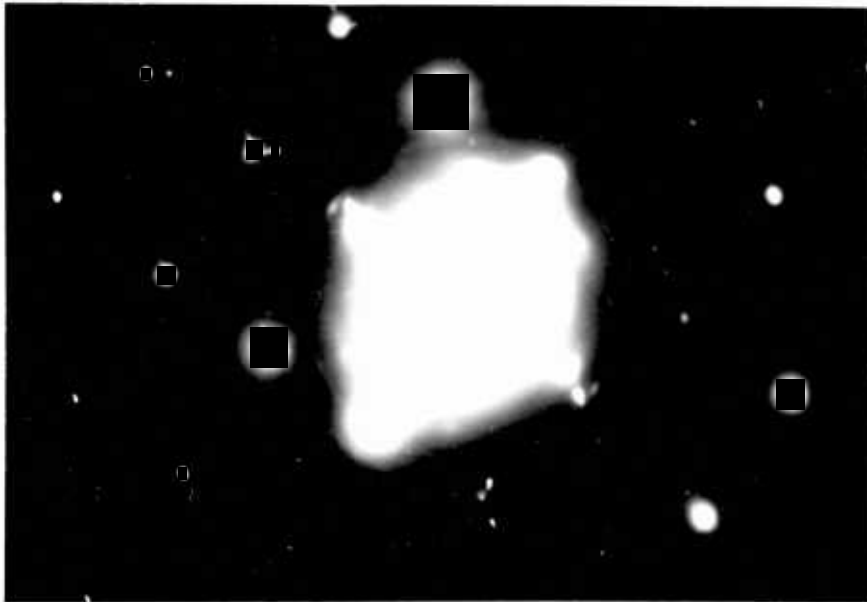
b) Pt/C replica



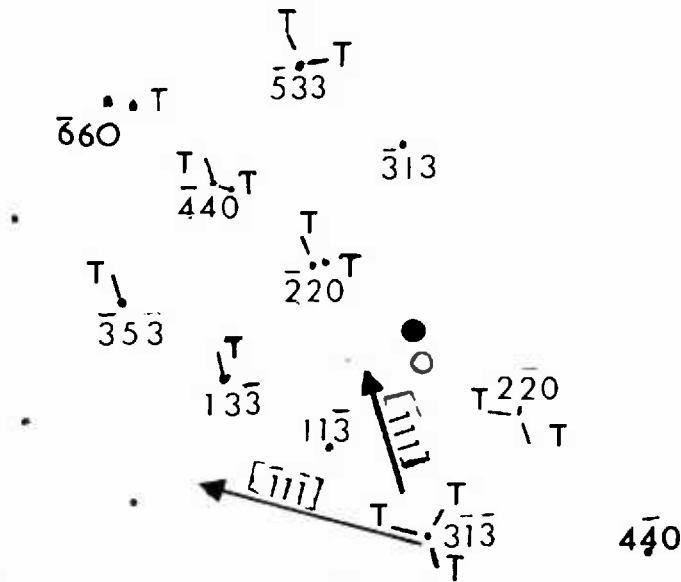
c) Pt/C replica



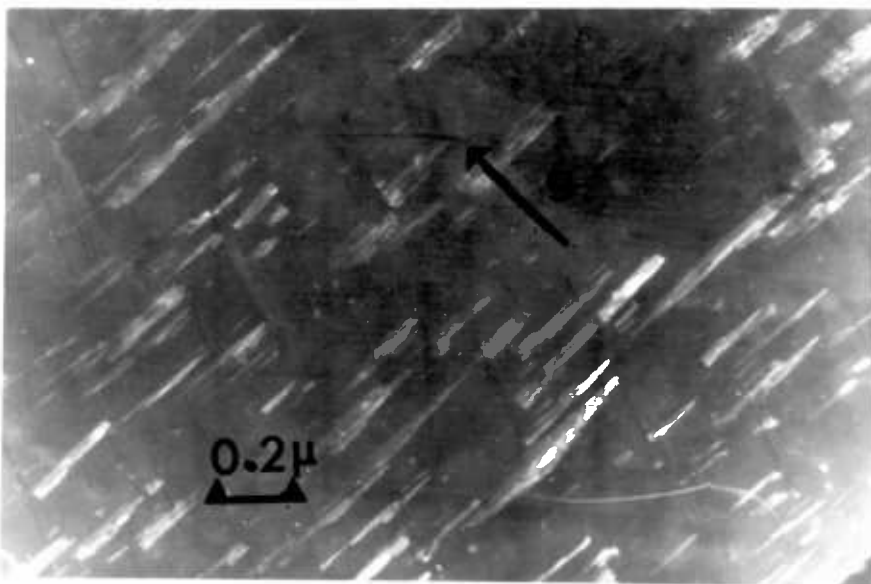
d) TEM, showing heavily faulted & precipitated structure.



e) TED showing Si twin spots and  $\beta$ -SiC rings



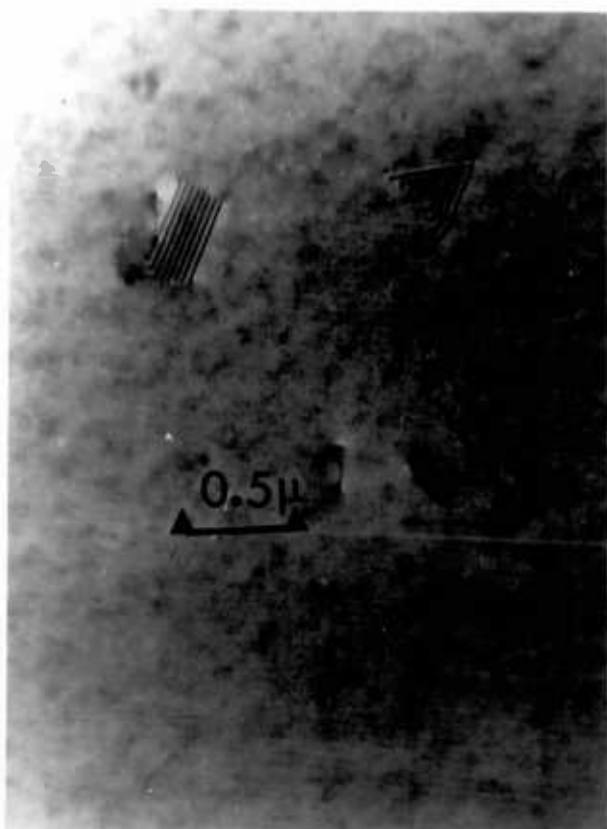
f) Indexing of pattern e). Twin spots marked T



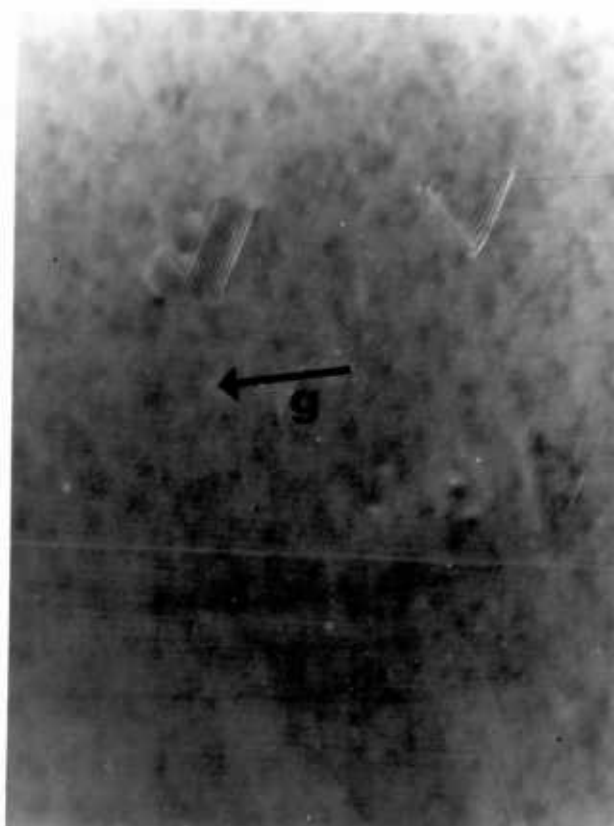
g) Dark field micrograph using twin spot near  $(\bar{2}20)$

FIG. 3.12

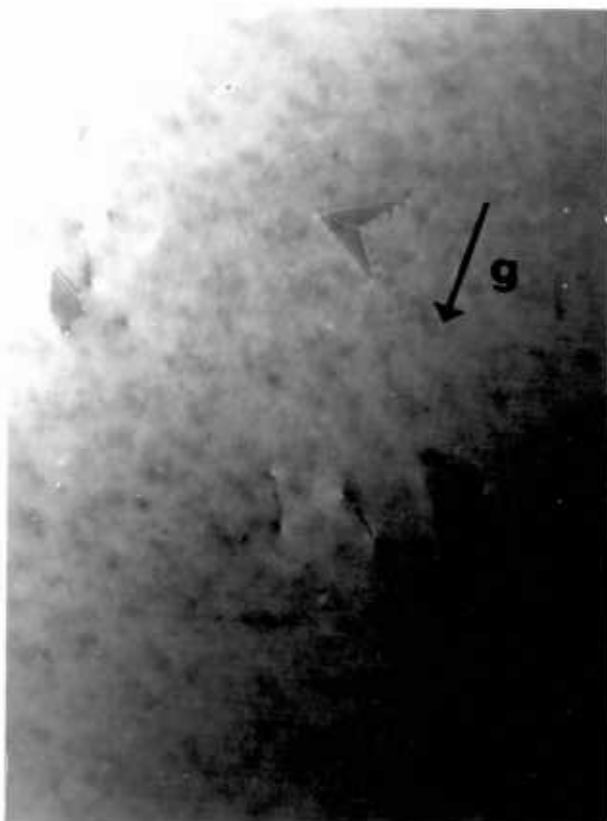
Moderate temperature growth (940°C) 50 ppm ethylene present, RB63A



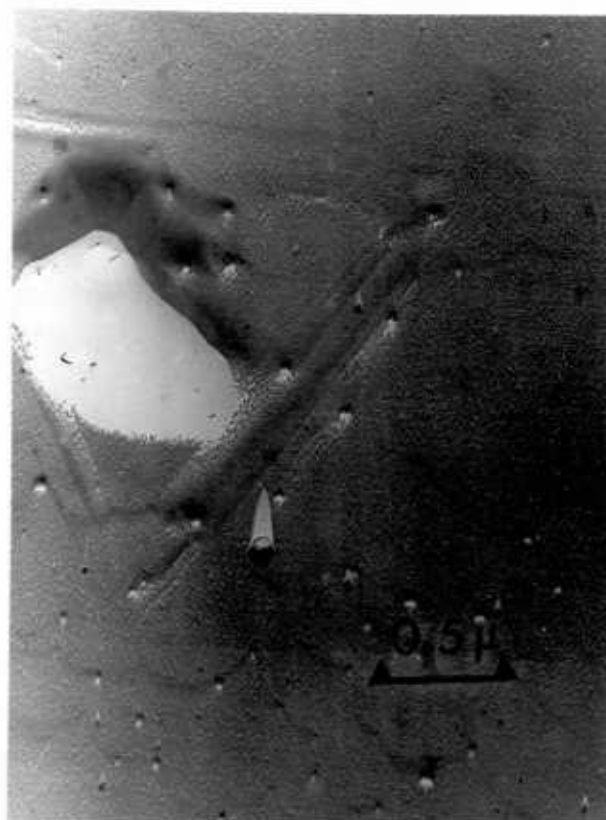
a) TEM showing tetrahedron nucleated within foil thickness



b) as a) but different diffraction vector



c) as a) but different diffraction vector



d) Pt/C replica of layer showing gross defect, possibly tripyramid.

micrographs, cf Fig. 3.5. Thus this ribbon fault is an extended dislocation. A diagram of this stacking fault structure is shown in section 6.4 (Fig. 6.5(a)) and is used in the model of tetrahedron nucleation developed there.

The surface of this layer was weakly faceted and pitted with very small cavities, Fig.3.12(d). In addition a defect containing a large depression which has been replicated in this micrograph appears to be a badly faulted tetrahedron or tripyramid similar to the etch figures shown in Fig.3.1(b)

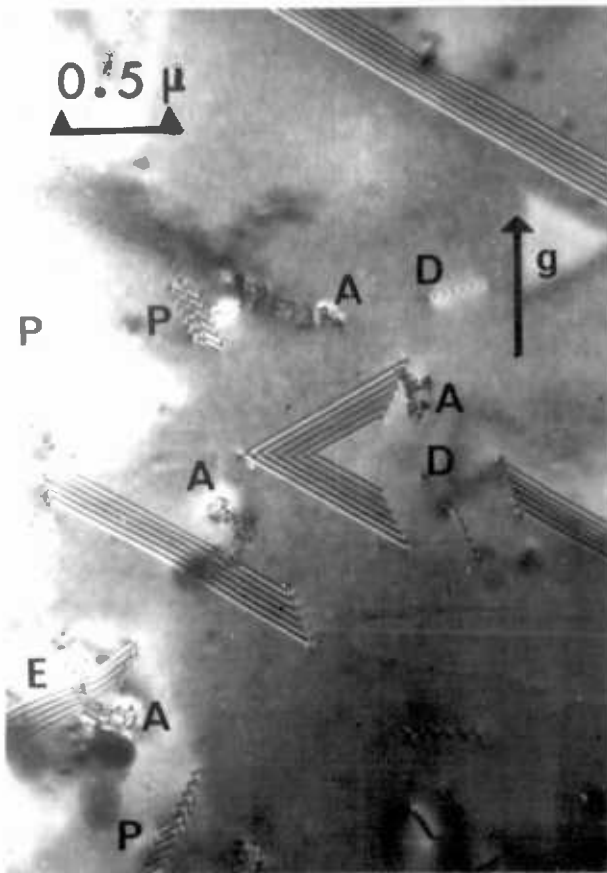
Above about  $940^{\circ}\text{C}$ , stacking fault structures were invariably in the form of tetrahedra and related closed configurations of the type observed by others (section 1.3). These structures almost always terminate in  $\langle 110 \rangle$  stair-rod dislocations, Fig.3.13(a). This is a micrograph of a layer (RB38B) grown at  $1065^{\circ}\text{C}$  with 100 ppm ethylene. Stacking fault densities as high as  $10^8 \text{cm}^{-2}$  were observed at this level of contamination and optical examination gave structures very similar to Figs.3.6c) & d). Using the contrast rule, most of the stacking faults in Fig.3.13 are seen to be intrinsic with the exception of the fault marked E. Fig.3.13(b) is a bright field micrograph taken with a different  $g$  vector to the above D.F. micrograph and comparing the set shows that the truncated tetrahedron lying at the centre of the Figures is intrinsic. Also observed are prismatic sets of stacking faults marked P consisting of two pairs of parallel faults lying on differently inclined  $\{111\}$  planes which intersect to form closed figures which are of constant cross-section throughout the layer. There are also many linear features which mainly lie in inclined  $\langle 110 \rangle$  directions, although other linear features marked D do not lie in these directions and must be perfect dislocations. No attempt was made to analyse these defects which would require weak beam techniques to resolve them adequately.

The surface of RB38B contains numerous pits, Fig.3.13(c). Closer examination, Fig. 3.13(d) shows that the surface is also terraced with long steps which bunch up around the pits. This surface structure is very similar to that found previously by Abbink et al (1968) and by Cullis & Booker (1971) on evaporated  $\{111\}$  layers, as discussed in section 1.2.

Figures 3.14a), b), show further examples of stacking fault

FIG. 3.13

Growth at 1065°C showing stacking fault tetrahedra & line faults, RB.34E



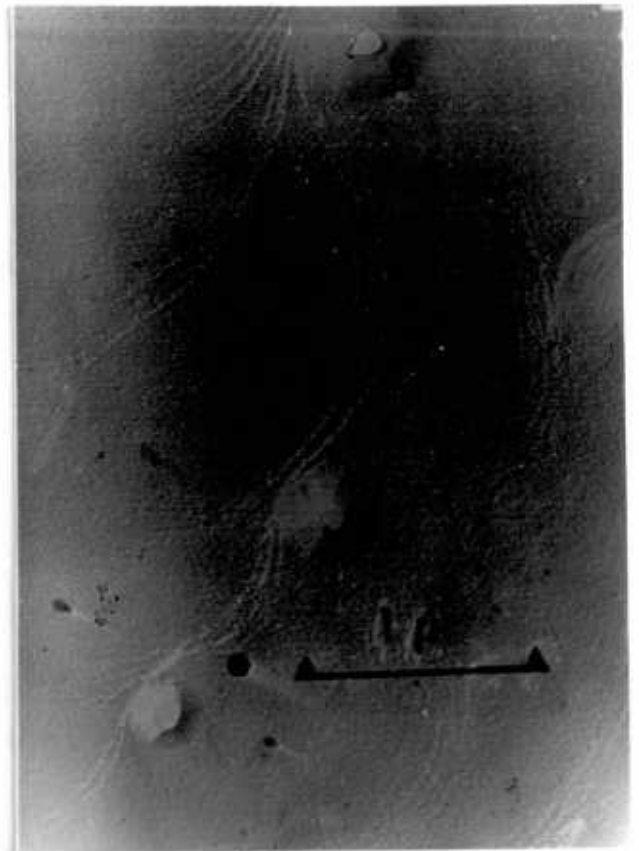
a) Dark field  $\bar{2}20$  reflection



b) area as a), bright field  $\bar{2}02$  reflection

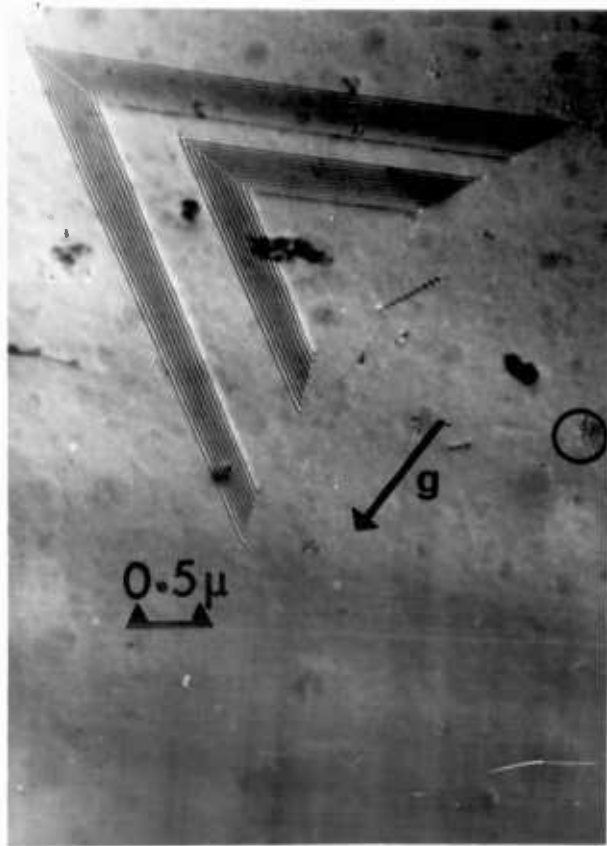


c) Pt/C replica showing pinning sites  $\sim 10^7 \text{cm}^{-2}$

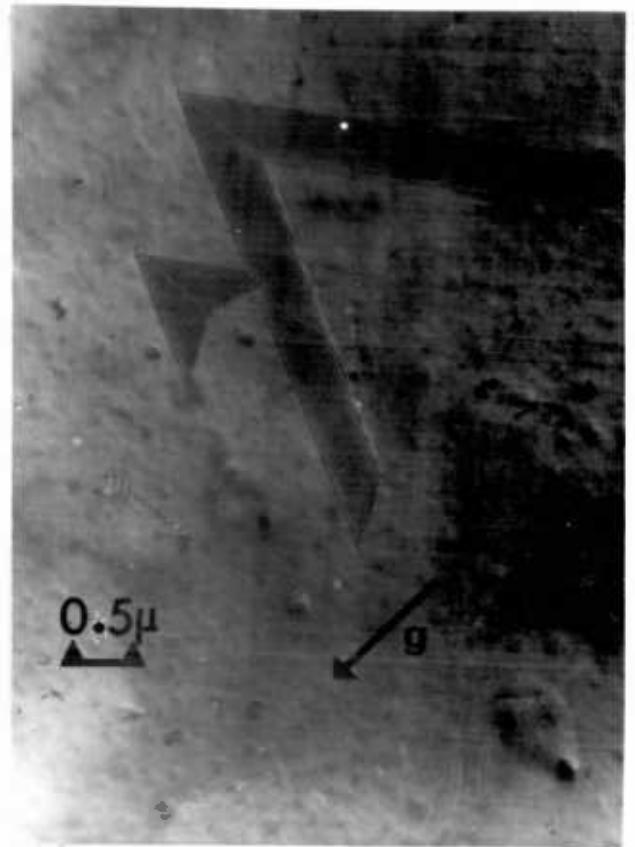


d) Pt/C replica. Fine detail of pits.

Nucleation of stacking fault tetrahedra during epitaxial growth, RB63B



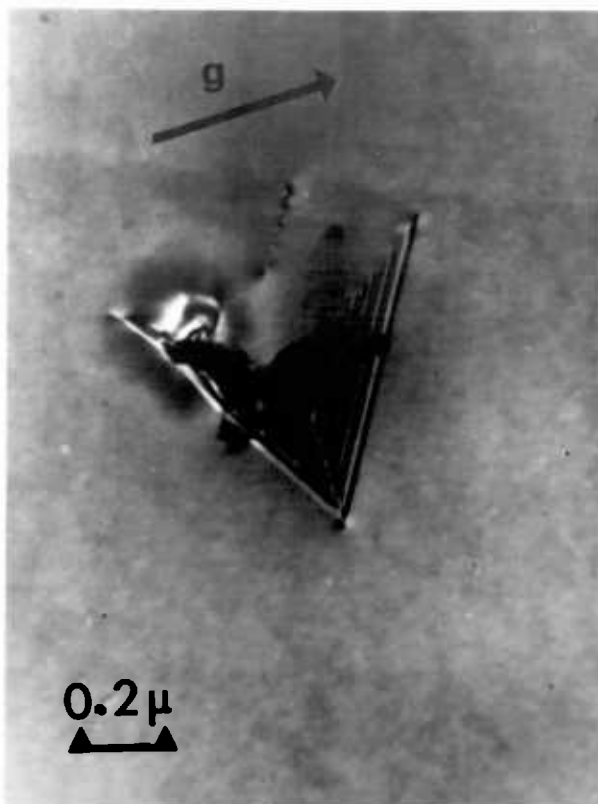
a) Large tetrahedron nucleated in layer  $\sim 1 \mu\text{m}$  below smaller one.



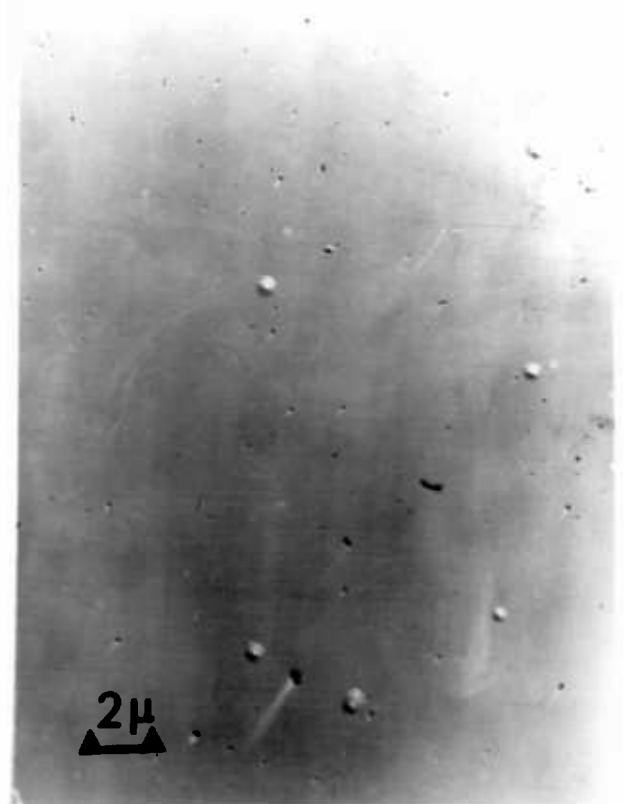
b) small tetrahedron nucleated  $\sim 0.8 \mu\text{m}$  below top of layer

FIG. 3.15

Growth at  $1075^\circ\text{C}$  showing few stacking faults and pin sites, RB39B



a) Stacking fault tetrahedron associated with inclusion



b) Pt/C replica showing pit density  $\sim 10^6 \text{cm}^{-2}$ .

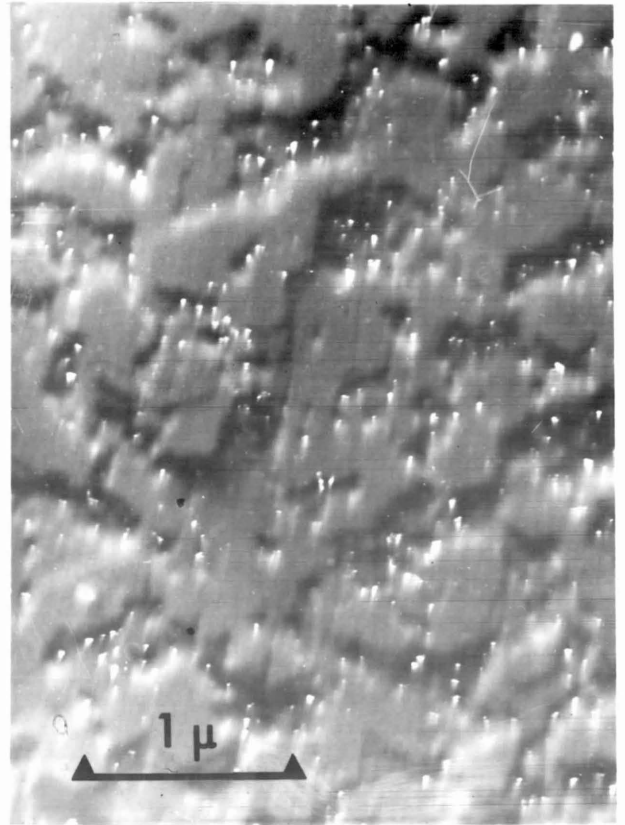
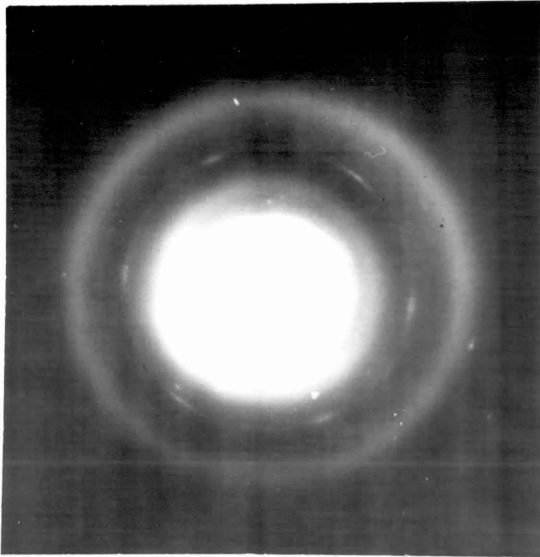
tetrahedra taken from layer RB63B. The faults have clearly formed at different times during epitaxial growth. Measurement shows that the large tetrahedron in Fig.3.14(a) nucleated from a point about  $3\ \mu\text{m}$  from the top of the epitaxial layer, i.e. at about twice the depth at which its companion was formed. Also of interest in this micrograph is the presence of a very small stacking fault structure, shown ringed, which has been nucleated within  $0.2\ \mu\text{m}$  of the top of the layer and appears to be associated with an inclusion. There is evidence, discussed in section 3.4, that this may be a crystallite of SiC. Fig.3.15(a) shows the typical defect structure of a layer (RB39B) grown under very similar conditions to RB38B. It contains far fewer defects and the surface, Fig.3.15(b), is much freer of pits as compared with Figs.3.13(c) and d).

Layers grown at the highest temperatures used in this study ( $> 1160^\circ\text{C}$ ) had no stacking faults and the surfaces were extremely smooth. The effect of both deliberate and uncontrolled contamination on defect formation has been overcome by high growth temperatures.

#### 3.4. Silicon carbide

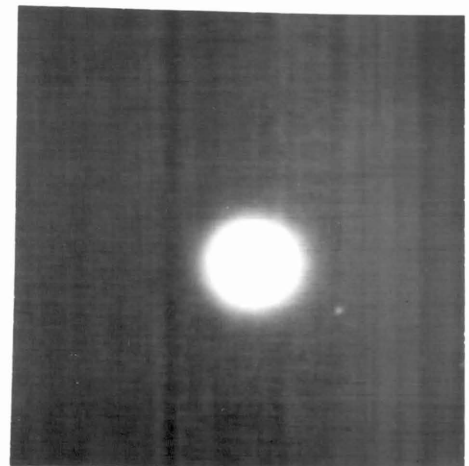
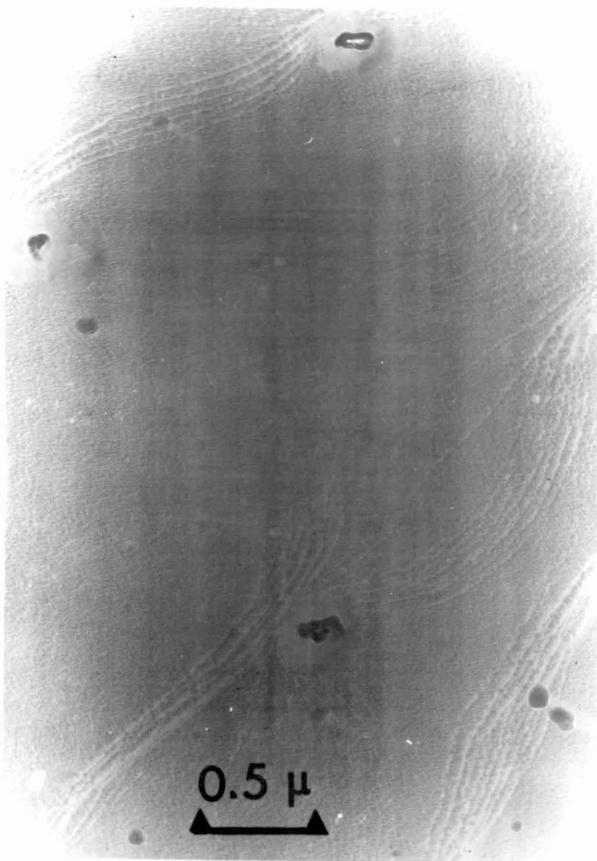
We have noted in section 1.2 that small particles of  $\beta$ -SiC were formed epitaxially on Si substrates exposed to ethylene at temperatures between 700 and  $1100^\circ\text{C}$ . Pt/C replicas were re-examined to see if SiC particles had been extracted. The replica of layer RB35A, which has already been shown to contain  $\beta$ -SiC (section 3.2.3.), was examined in the transmission electron diffraction mode. A  $\langle 111 \rangle$  spot pattern of  $\beta$ -SiC was found, Fig. 3.16(a), and dark field micrographs taken using a  $\{220\}$  spot shows grains of SiC up to  $200\text{\AA}$  across, Fig.3.16(b). On more typical layers grown at ethylene levels  $\leq 100$  ppm, although some diffraction spots were observed from some crystalline material extracted from pits in layers grown at moderate temperatures, Fig.3.16(c) (d), there was insufficient data and too great an uncertainty in the camera constant to positively identify  $\beta$ -SiC. This phase was not detected by GAED on any layer examined, even RB35A (Fig.3.11(a)). It was noticed, however, that specimens prepared for TEM from layers grown above  $940^\circ\text{C}$  were often contaminated with tangled filaments of material lying on the foil surfaces, Fig. 3.17(a).

Extracted material in Pt/C replicas of ethylene-contaminated layers



a) Diffraction pattern of SiC extracted from heavy ethylene contamination layer, RB35A

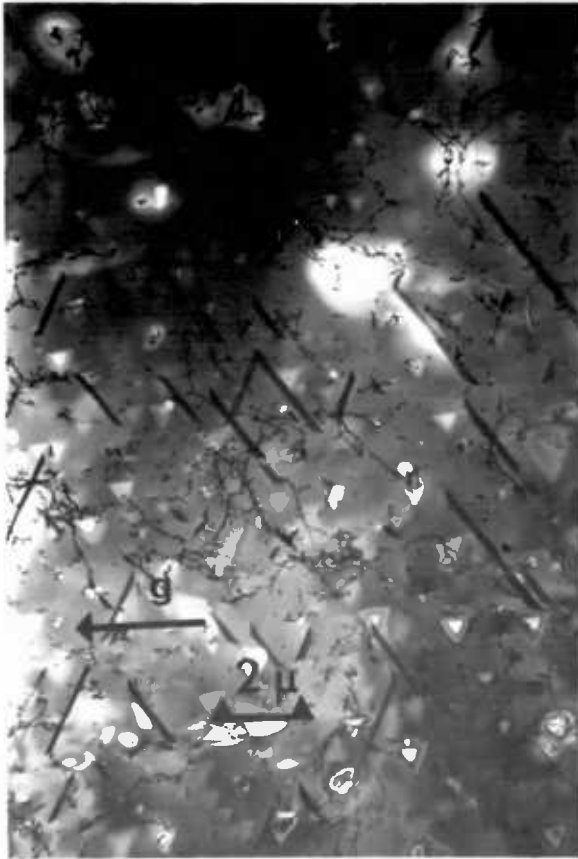
b) Dark field TEM micrograph of Pt/C replica of RB35A using {220} SiC spot.



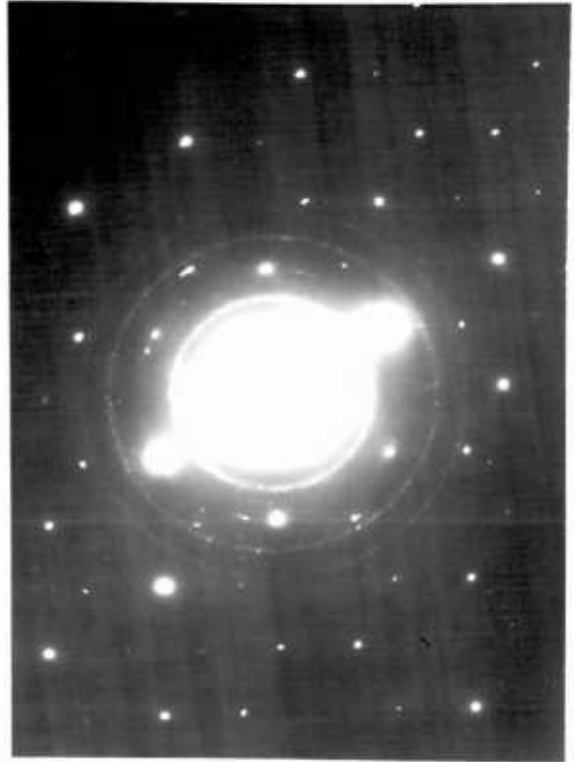
c) Pt/C replica of pin site structure showing extracted particle in pit, RB42 A

d) Diffraction pattern of extraction in pit

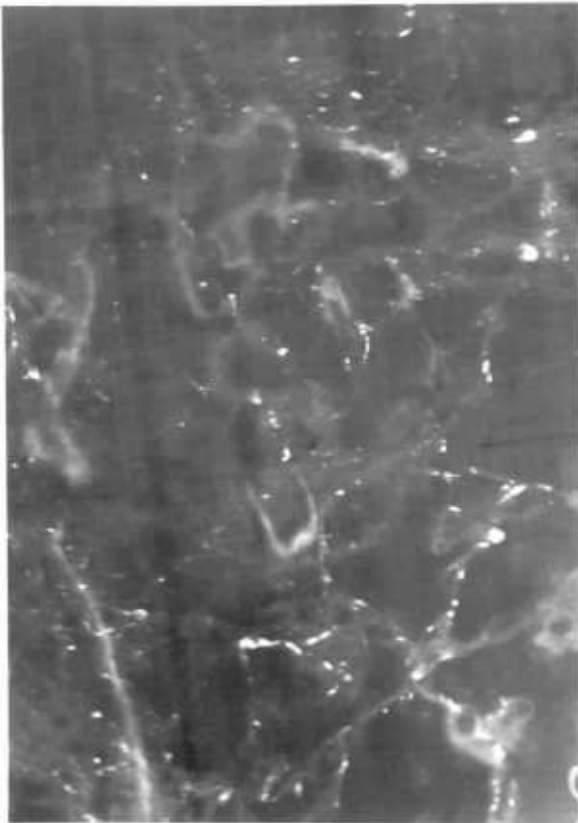
SiC filaments in epitaxial Si.



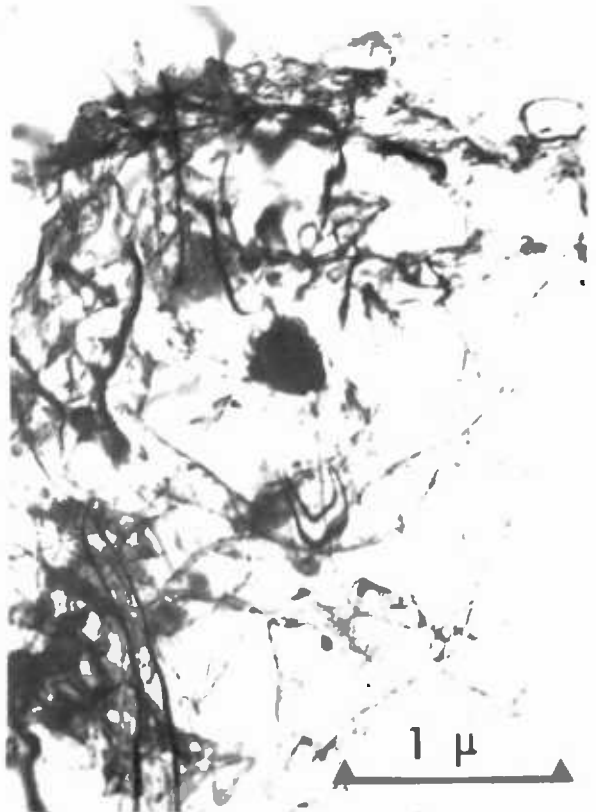
a) General view of SiC debris & stacking fault configuration RB42A



b) Diffraction pattern of  $\beta$  SiC from layer RB64B



c) Dark field TEM using  $\{111\}$  SiC ring.



d) Bright field view of c) layer RB64B

Selected area electron diffraction (SAED) on thin areas of silicon gave a spotty ring pattern of  $\beta$ -SiC, Fig.3.17(b). Dark field observations using a portion of the (111) ring showed crystallites of  $\beta$ -SiC up to  $200\text{\AA}$  across, Fig.3.17(c). The corresponding bright field view of the debris is shown in Fig.3.17(d). The underlying Si foil is very thin in this area, most of the contrast coming from bend contours. In thick areas of foil the SiC diffraction pattern was masked by the Si Kikuchi pattern but Fig.3.13(a) shows particles marked A embedded in the layer which are thought to be SiC crystallites and Fig.3.15(a) contains a filament embedded close to the stacking fault tetrahedron which could be SiC. The SiC filaments must have formed on the growing layer surface and were then incorporated into the layer during subsequent epitaxial growth. It has been noted in Chapter 1.2 that SiC particles lie in depressions, the inability to detect them by GAED is not surprising and also their extraction by low angle shadowing Pt/C replicas would be difficult. In addition to the particle extracted as in Fig.3.16(c), pinning centres often contained a small hole (e.g. B in Fig.3.13(d)) consistent with the presence of an angular particle embedded at the bottom of the site. It is evident that since  $\beta$ -SiC particles are resistant to HF : HNO<sub>3</sub>, on jet etching some remain behind on the foil as debris. Layers grown at high temperatures produced no pinning centres, or other evidence of SiC formation and no stacking faults. The layer grown at low temperatures with very high ethylene levels (RB35A) showed direct evidence of SiC formation from diffraction data as shown in section 3.2.3. and in this section but observations on runs grown at lower levels of ethylene at low temperatures did not confirm the presence of SiC. However, the micrograph showing pinning centres in layer RB34B, Fig.3.7(d) suggests the formation of SiC crystallites.

Re-examination of RB14, grown at low temperatures and with high ethylene level, in the  $s > 0$  condition shows a finely speckled structure which may be extremely fine precipitate particles  $\sim 20\text{\AA}$  across, Fig.3.18. However, no second phase was detected by SAED at the edge of the foil and Fig.3.4(a) shows black and white spots in the edge region consistent with fine holes in the foil, rather than precipitation.

Layer RB14 showing speckled background in  $s > 0$  condition

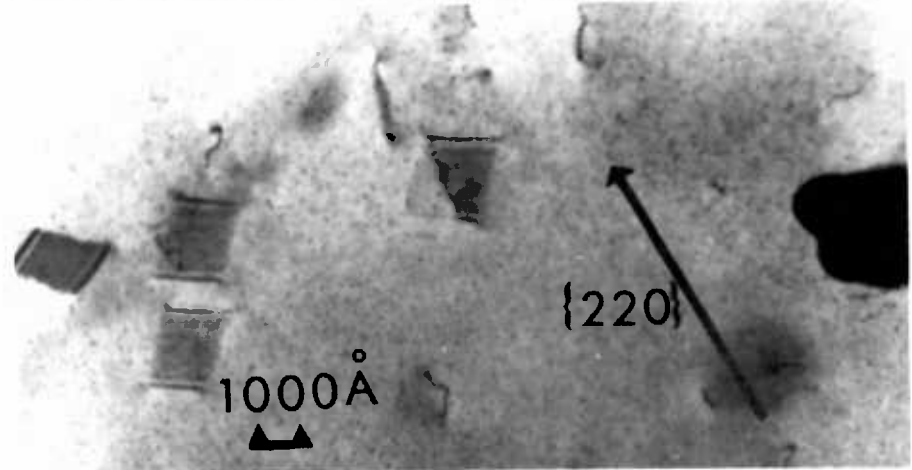
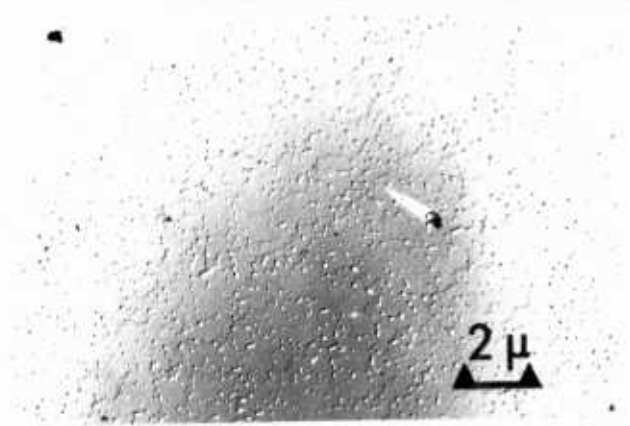
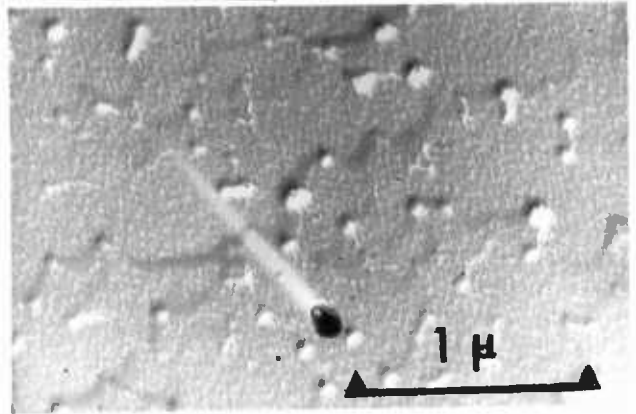


FIG.3.19

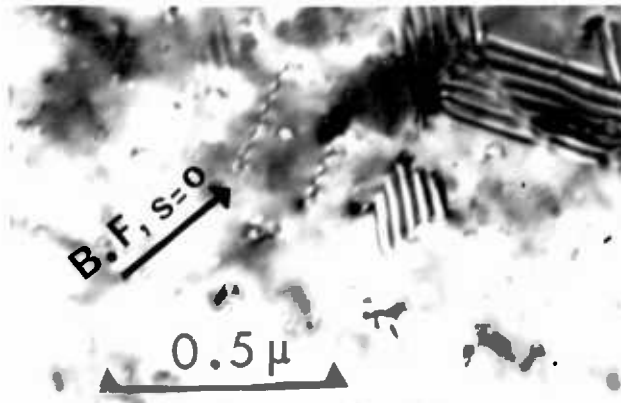
Anomalous pitting in low temperature growth runs



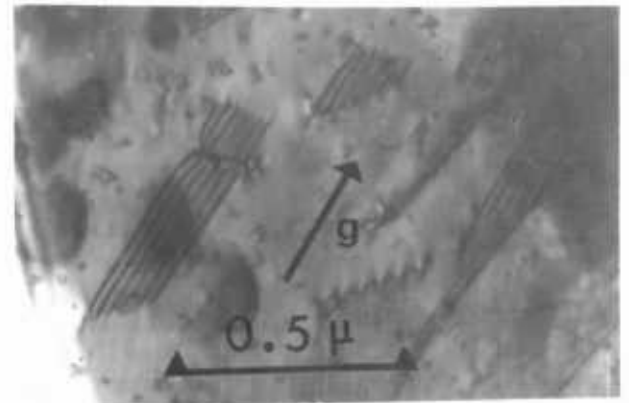
a) Pt/C replica, layer RB27A



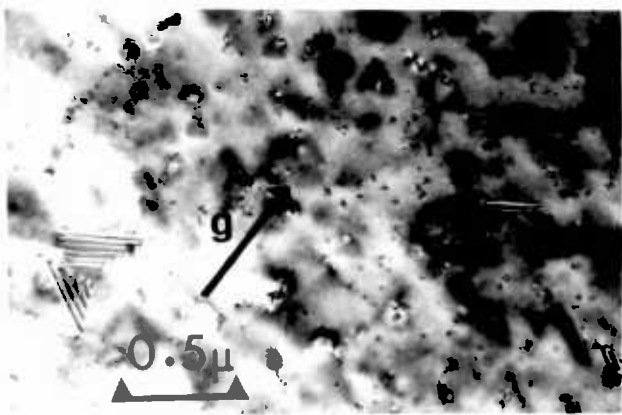
b) as a), higher magnification



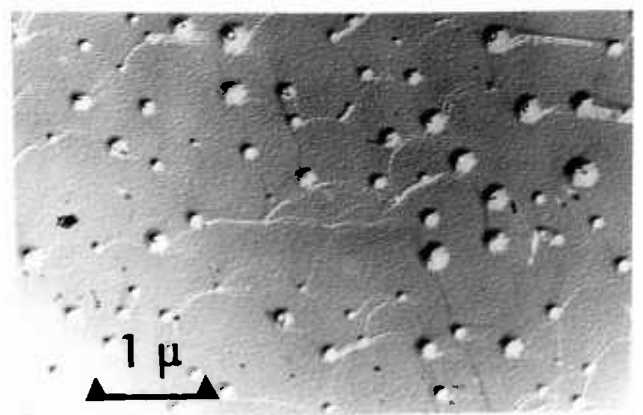
c) TEM of layer RB27A  
 $\{220\}$  refln,  $s=0$



d) as c) but  $\{111\}$  refln,  $s > 0$



e) TEM of layer RB39A showing inclusions.



f) Pt/C replica of e)

Layer RB27A is interesting because, although it was grown under conditions which produced ribbon stacking faults, the surface was highly pitted, Fig. 3.19(a) and also faceted, as is revealed at higher magnifications, Fig. 3.19(b). The defect structure showed ribbon faults with distorted fringes due to this uneven surface, with much overlapping, Fig. 3.19(c). The granular background suggests strain contrast due to the incorporation of inclusions in the layer, again more clearly seen in the  $s > 0$  condition, Fig. 3.19(d). This problem was also encountered in later runs (RB39A and 40A), grown at  $965^{\circ}\text{C}$ , where stacking fault structures were largely the tetrahedron type but the granularity and surface pitting were very similar to Fig. 3.19, as shown in Figs. 3.19(e), (f). It seems likely that high densities of SiC crystallites have formed in all three layers although the reason for this is not known. The companion run to RB27A was a layer grown on a  $\{110\}$  substrate (see Chapter 4.1), and showed tangled filaments very similar to those in Fig. 3.17(a): strong evidence for SiC formation.

CHAPTER 4. RESULTS: ETHYLENE CONTAMINATION STUDIES  $\{110\}$  and  $\{100\}$  LAYERS4.1.  $\{110\}$  Layers

Two runs only were made using  $\{110\}$  substrates and details are given in Table 4.1.

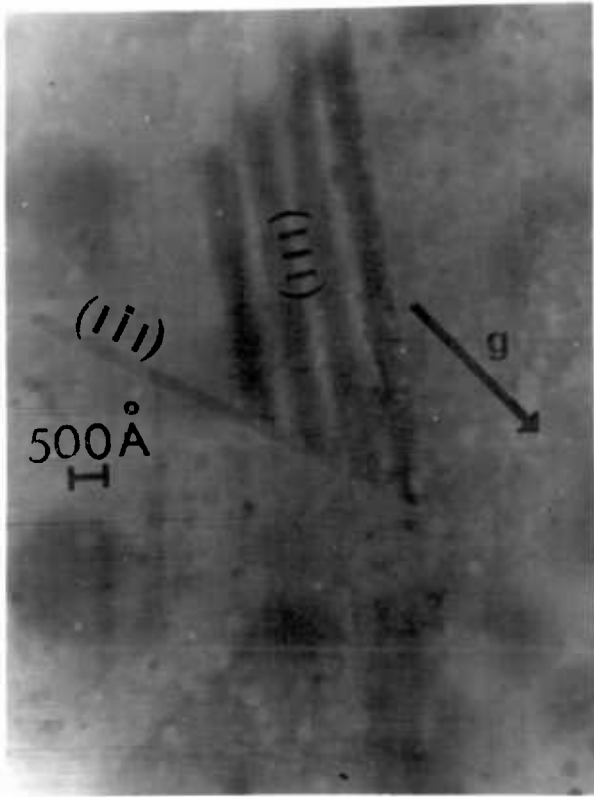
TABLE 4.1. ETHYLENE CONTAMINATION  $\{110\}$  LAYERS

RB RUN	T°C obs.	T°C corr.	ppm C <sub>2</sub> H <sub>4</sub>	Optical exam		Stacking fault		Surface structure	Pit density cm <sup>-2</sup>
				sirtl etch pit/cm <sup>2</sup>	i.c.	structure	Density/cm <sup>2</sup>		
25	810	845	16	too high to count	granular	T & R	-	Oblong pits	2x10 <sup>7</sup>
27B	830	865	100	"	V.fine grained	T and prismatic	3x10 <sup>9</sup>	Pitted and growth centres	3x10 <sup>8</sup>

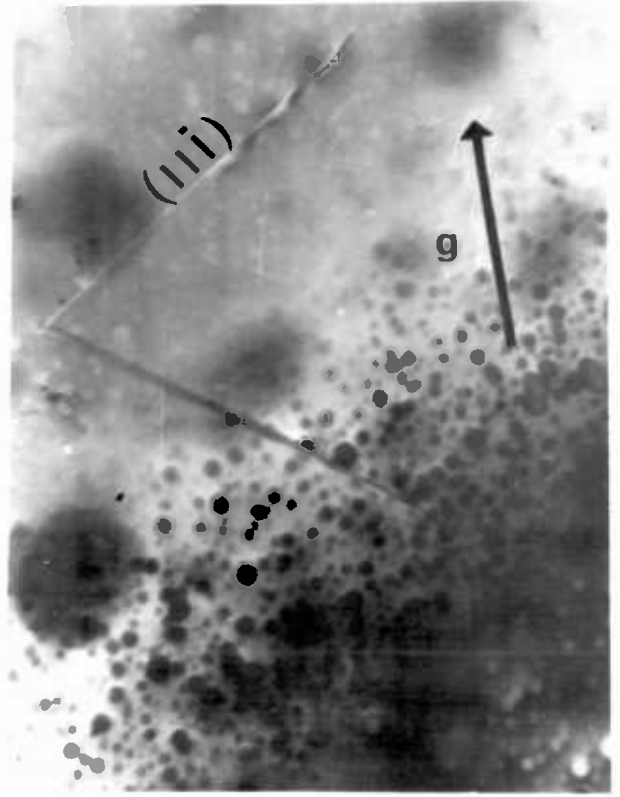
Stacking fault tetrahedra were occasionally observed in the lower contamination specimen, truncated by the foil surfaces, Figs. 4.1(a), b). Fig. 4.1(c) is a set of diagrams to show the geometry of the structure. The fault fringes on the shallowly inclined (111) plane are visible in Fig. 4.1(a) but are not seen in Fig. 4.1(b) due to the choice of diffraction vector, but stacking fault fringes on the vertical  $\{1\bar{1}1\}$  and  $\{\bar{1}11\}$  planes are visible due to tilting a few degrees off exact [110] orientation. A double stacking fault figure is shown in Fig. 4.2(a) and a more complex structure is seen in Fig. 4.2(b). Interaction of stacking faults is seen to occur in some regions to form stair-rods, whereas other faults seem to be ribbons and terminate in irregular edges. The dark field micrograph Fig. 4.2(c) shows that the top and bottom sets of faults lie on oppositely inclined  $\{111\}$  planes and have probably originated from a point below the large patch of contamination. The contrast at the ends of the ribbon faults using various reflections in the [110] zone could not be explained by the presence of a simple Frank or Shockley partial dislocation. Close examination shows that the boundaries could contain portions of stair-rod dislocations due to intersection with stacking faults on vertically inclined  $\{111\}$  planes.

The surface of RB25 was pitted with square or oblong pits, Figs. 4.3a), b), but was otherwise very smooth. The surface of RB37B, like its companion described in Chapter 3.4, was heavily pitted, but in addition contained large growth centres up to 1  $\mu$ m across, Figs. 4.4a), b). The growth centres are

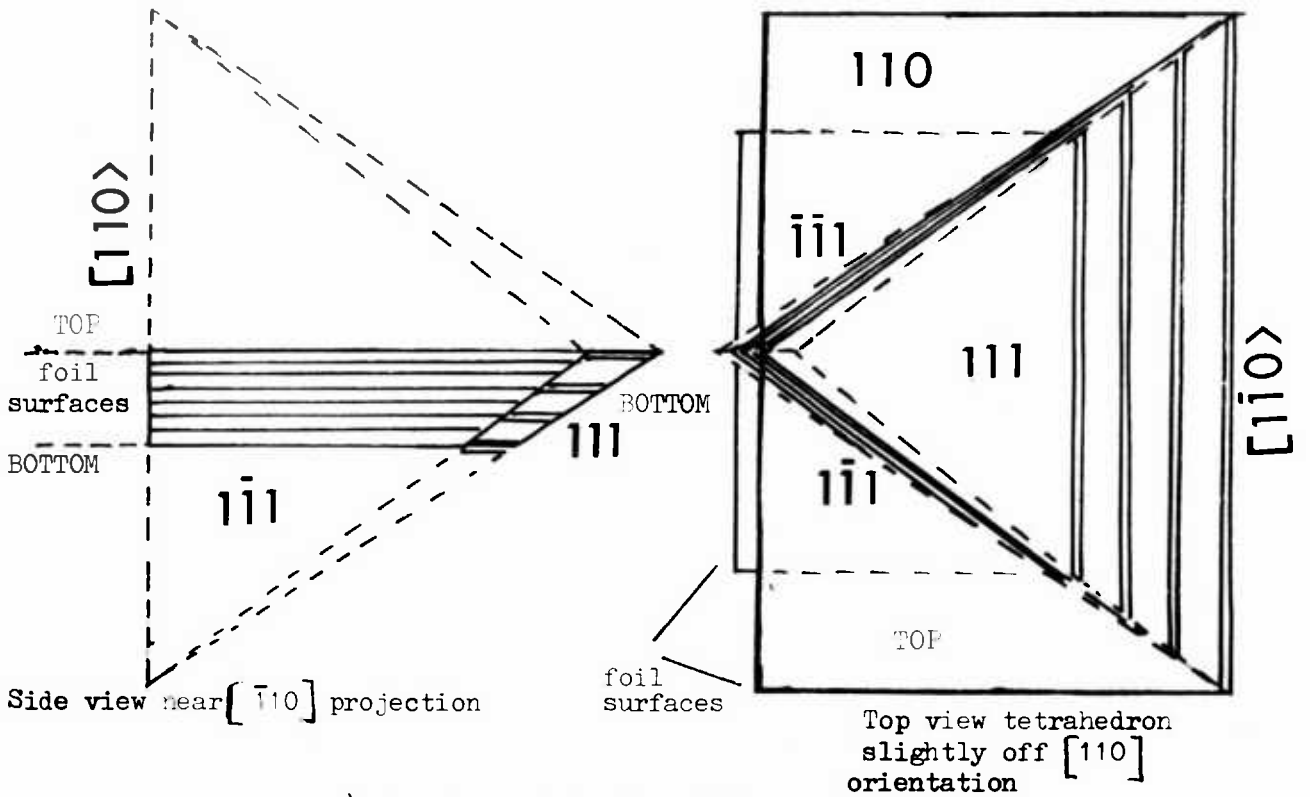
STACKING FAULT CONFIGURATION IN 110 LAYER (RBC5)



a)  $\bar{1}11$  reflection



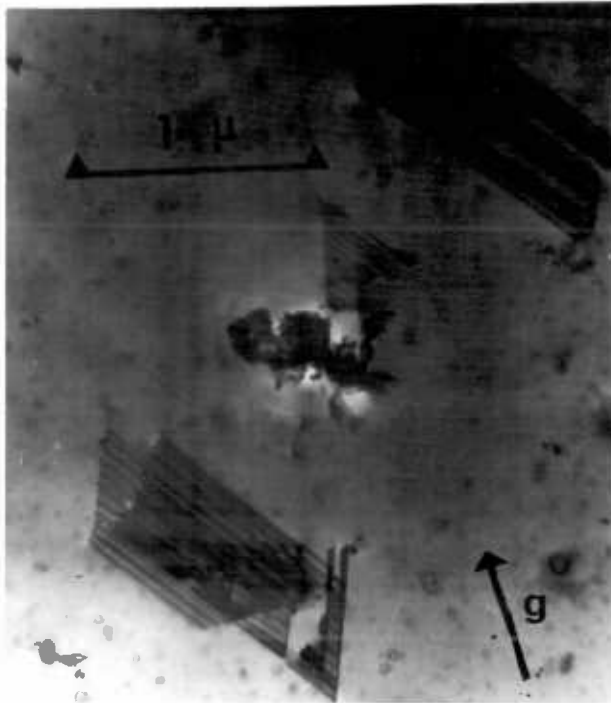
b)  $2\bar{2}0$  reflection



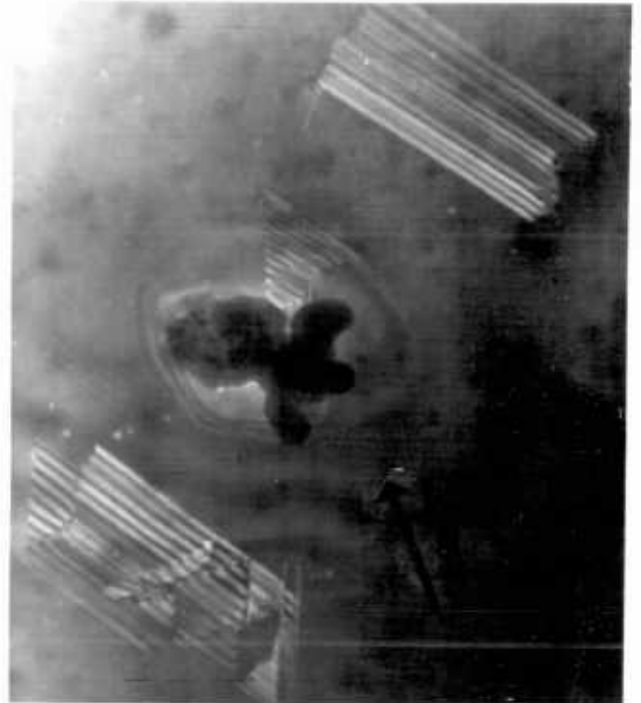
c) Geometry of stacking faults.

Complex stacking fault structures in (110) layer, RB25

a) High magnification TEM micrograph of small tetrahedra  $\{111\}$  refln.



b) Multiple stacking fault structure centred on pit,  $\{111\}$  refln.



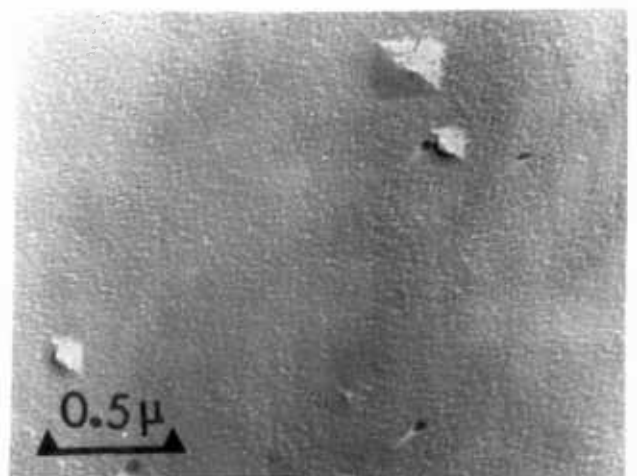
c) area as b), dark field  $\{111\}$  refln.  $s > o$

FIG.4.3

Surface pitting in RB25

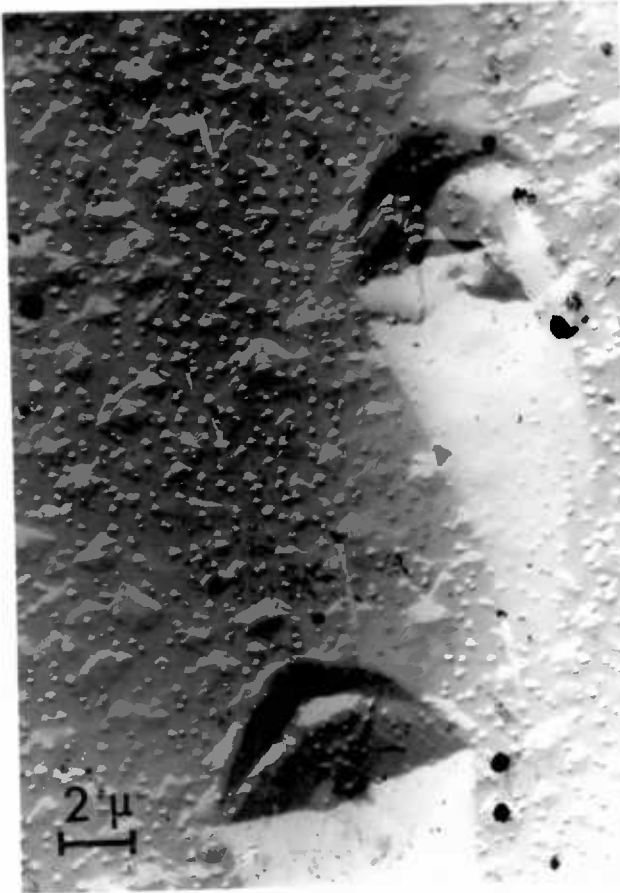


a) Pt/C replica showing  $2 \times 10^7$  pits  $\text{cm}^{-2}$

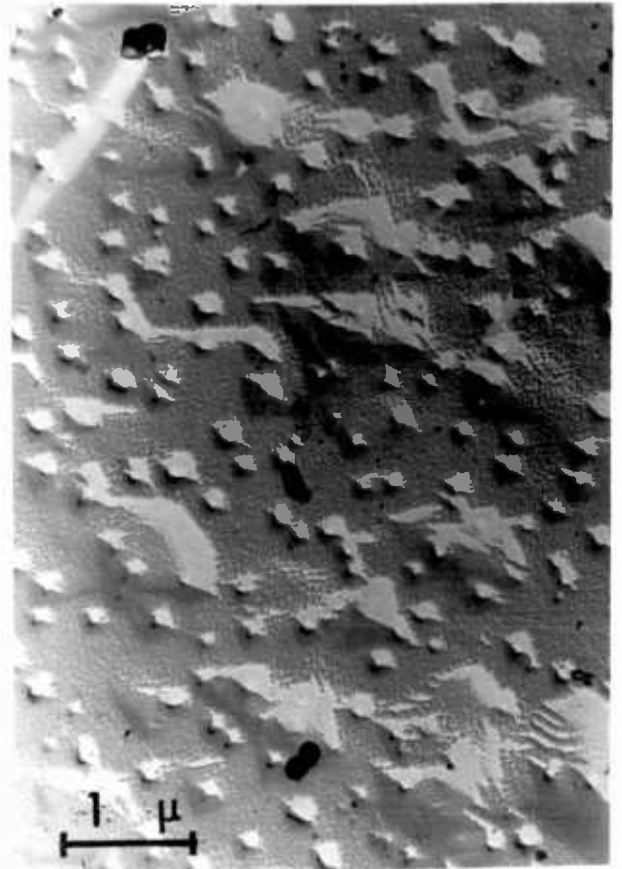


b) as a) higher magnification

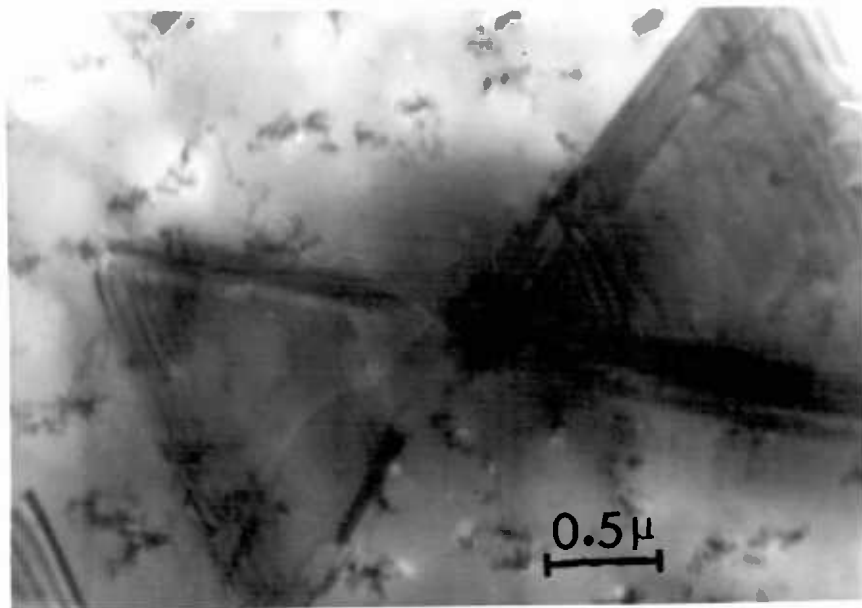
Structure of {110} layer grown with 100 ppm ethylene, RP27B



a) Pt/C replica showing pit density of  $\sim 4 \times 10^8 \text{ cm}^{-2}$  & large growth centres



b) as a) higher magnification



c) TEM showing complex faulted structure.

faceted and could be the result of complex faulting as shown in Fig.4.2(b). TEM examination of the layer revealed a similar defect, Fig.4.4(c). However, the main defects in this layer are difficult to observe in the  $[110]$  zone. Fig.4.5(a) used the  $(1\bar{1}\bar{1})$  reflection with the beam a few degrees from the  $[110]$  pole. Short lines are observed a few hundred angstroms long lying at right angles to  $g$ . Tilting about  $g$  away from the  $[110]$  pole shows that the same area, Fig.4.5(b) contains numerous stacking faults lying on  $(1\bar{1}\bar{1})$  planes and in addition many straight dislocations lying in  $[110]$  directions perpendicular to the layer surface. We can now see that the short lines in Fig.4.5(a) are the projection of stacking faults lying on  $(\bar{1}\bar{1}\bar{1})$  planes. Using the  $\bar{2}20$  reflection near the  $[111]$  zone, Fig.4.5(c) shows stacking faults lying on both  $(\bar{1}\bar{1}\bar{1})$  and  $(1\bar{1}\bar{1})$  planes which terminate in the  $[110]$  direction normal to the layer. A detailed analysis of the defects was not attempted but they are similar to the clusters of dislocations and prismatic faults found at moderate growth temperatures in  $\{111\}$  layers, e.g. Fig.3.13(a). Figure 4.5(c) also shows clearly tangled filaments very similar to those occurring at moderate growth temperatures in ethylene-contaminated  $\{111\}$  layers, e.g. Fig.3.17(a), and it is supposed that these filaments are composed of SiC particles.

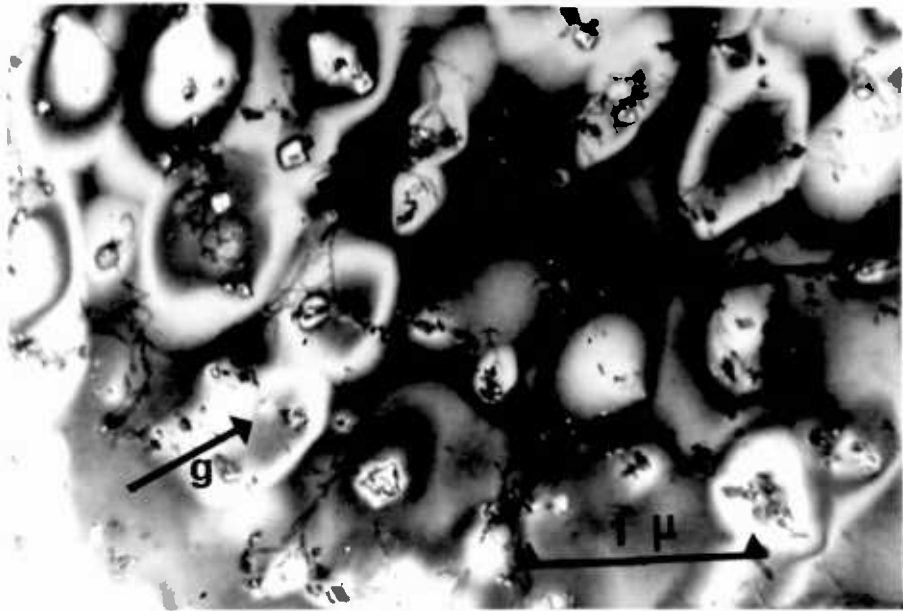
#### 4.2. $\{100\}$ layers

Table 4.2. gives details of runs using  $\{100\}$  substrates. It is seen that these were mainly carried out in the temperature range which produced ribbon stacking faults in  $\{111\}$  layers.

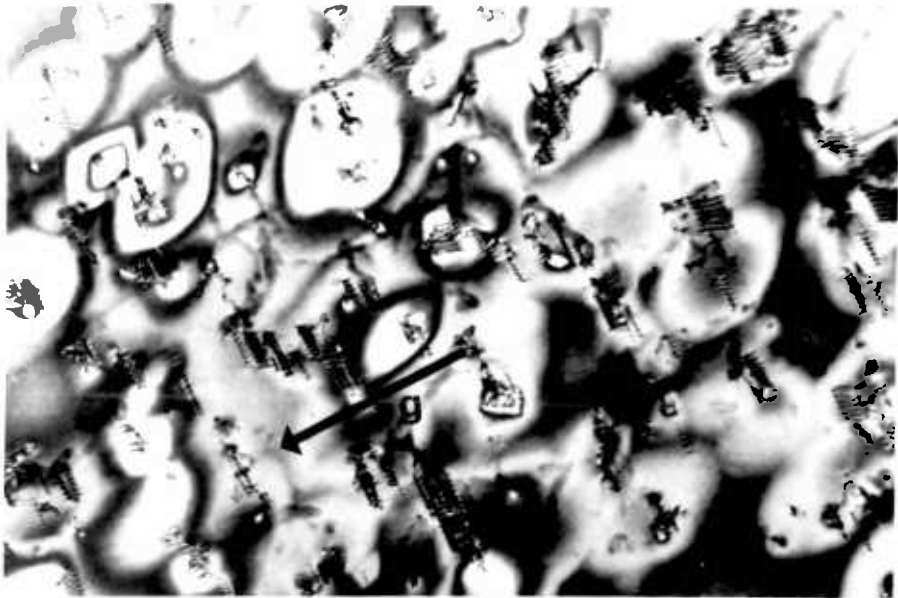
TABLE 4.2. ETHYLENE CONTAMINATION,  $\{100\}$  LAYERS

Run No. R.B.	T°C obs	T°C corr.	ppm ethyln.	Optical examn.		TEM	
				sirtl count	pit interface contrast	layer structure	surface structure
5	800	835	0	No pits	rippled + $9 \times 10^4$ growth centres	inclined dislocns V few sf obs.	-
11	815	850	24	"	$5 \times 10^3$ growth centres. V smooth	Growth centres	Growth centres
13	820	855	89	"	strongly srippled	" " containing steeply inclined dislocns. at centre	Large growth centre
44A	850	890	97	$10^5$ pits (not sf)	V.smooth, & few growth centres	No defects obs.	'spangle' growth centres
44B	1140	1210	97	$9 \times 10^5$ pits (not sf)	"	"	V.smooth, a few growth centres.

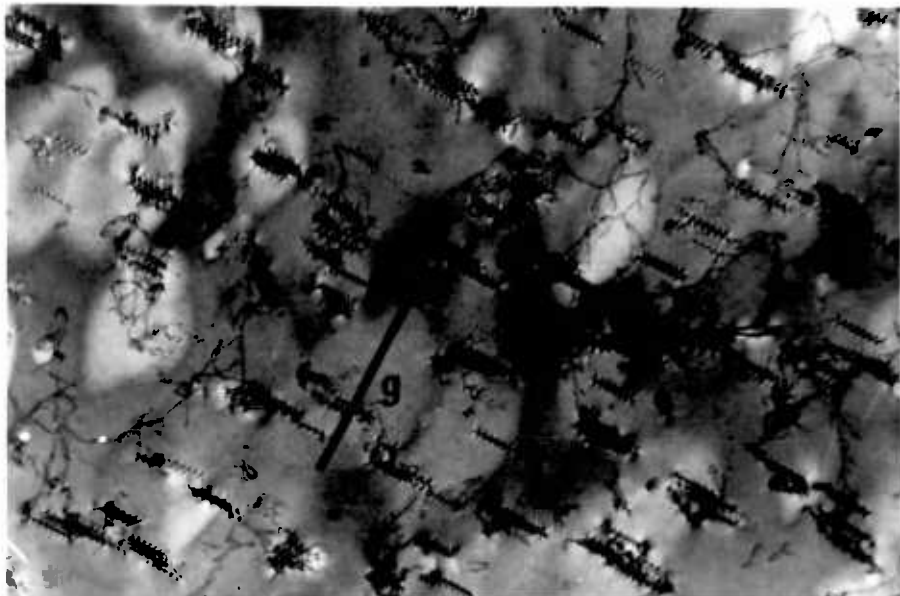
Resolution of stacking fault structure of  $\{110\}$  layer RB 7



a)  $\{111\}$  refln. near  $[110]$  zone



b) area as a),  $\{111\}$  refln. near  $[112]$  zone



c) area as a)  $\{220\}$  refln. near  $[111]$  zone

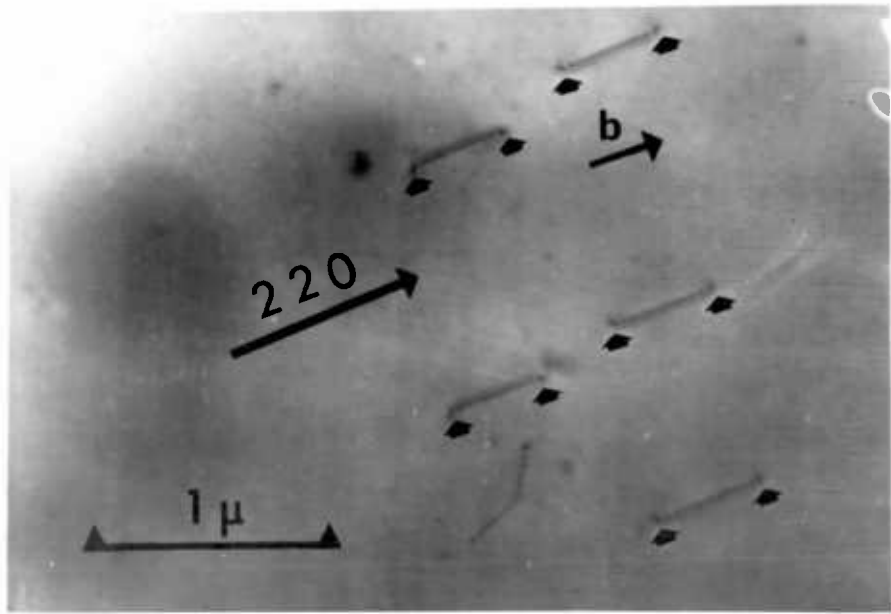
Unlike runs on  $\{111\}$  and  $\{110\}$  substrates, very few stacking faults were observed. Only one stacking fault was found in TEM and that was in a control layer with no deliberate contamination. There was also a group of inclined dislocations in this layer, Fig.4.6(a) some of which vanished or showed residual contrast when the  $\{220\}$  type diffraction vector was perpendicular to their projection in the (001) layer plane, Fig.4.6(b). These dislocations must have  $\frac{1}{2} [\bar{1}10]$  Burgers vectors parallel to this projection in the surface of the layer. The remaining dislocations which do not disappear are inclined in different directions and must have Burgers vectors inclined to the surface.

The feature common to all the  $\{100\}$  layers were growth centres which were easily seen optically using interference contrast, in Pt/C replica, and in TEM., Figs. 4.7a) b) c) respectively. The largest of these growth centres was about 40  $\mu\text{m}$  across; Fig.4.8(a) shows a portion of this centre. TEM on this layer (RB13) revealed a growth centre which contained steeply inclined dislocations at the centre, Fig.4.8b) c). The height of the centres can be calculated from the thickness fringe displacement. In Fig.4.7(c), the centre lies on a taper section of Si and it is seen that the highest portion is  $\sim 4-5$  fringes above the immediately surrounding material, corresponding to a height of  $\sim 0.3 \mu\text{m}$ . The micrograph does not show dislocations in the growth centre but contrast is poor owing to the increased thickness of silicon.

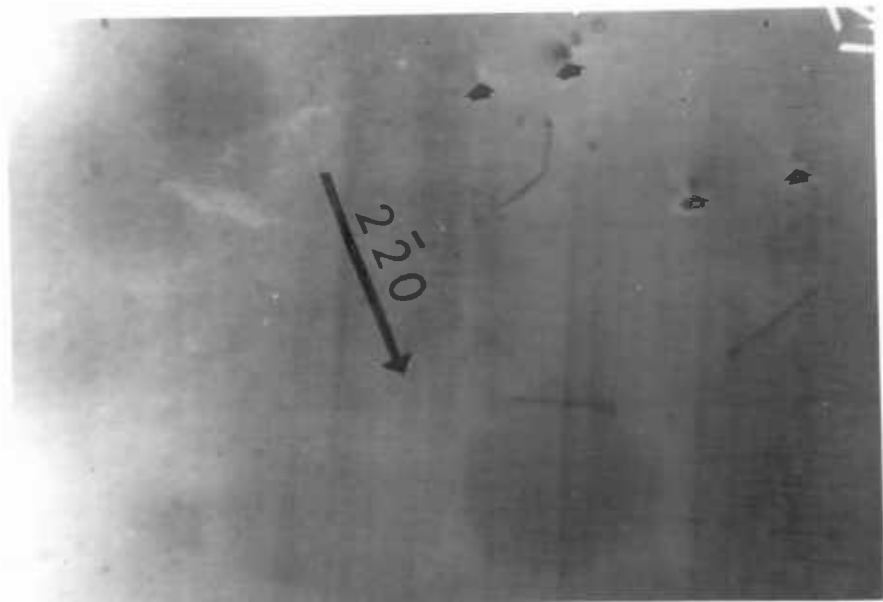
In general the surfaces were extremely smooth, but growth centres were observed even at the highest growth temperature. Fig.4.9(a) b) & c) show variants on growth centres which in run RB44A have the appearance of "spangles", i.e. square walls with a rough circular dimple at the centre. Small pits are also visible around the edge of the dimple. Unfortunately none of the features were found in the TEM specimens examined, not surprisingly since their density was so low.

FIG. 4.

Inclined Dislocations in  $\{100\}$  epitaxial Si, control layer RFS

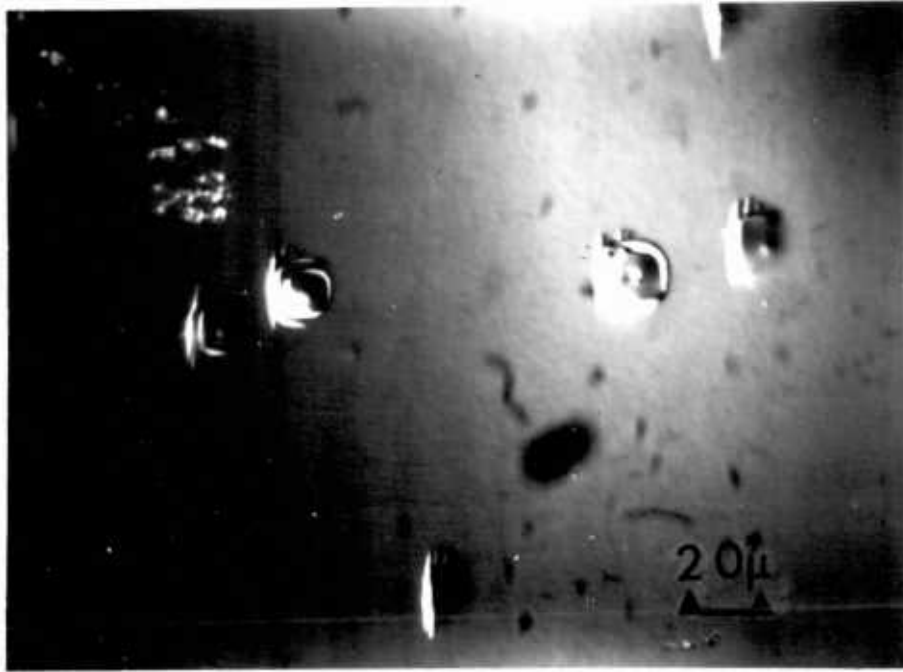


a)  $54^\circ$  dislocations marked with arrows lie on  $\{111\}$  planes in  $\langle 112 \rangle$  orientation and have  $\frac{1}{2} \langle 110 \rangle$  Burgers vectors in epi-layer plane in direction indicated.



b) as area a) residual contrast at dislocations arrowed.

Growth centres in {100} epi-layer, various viewing techniques



a) Optical microscopy, interference contrast.

RB 11

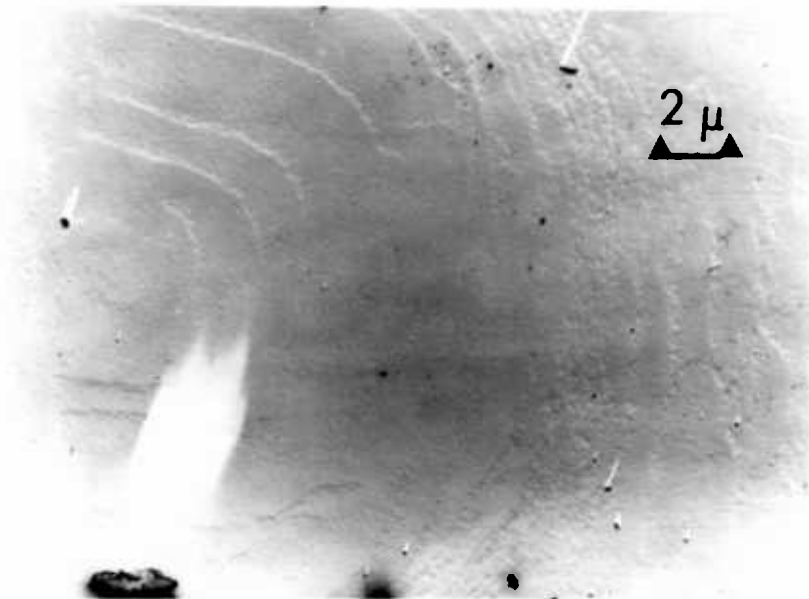


b) Pt/C replica

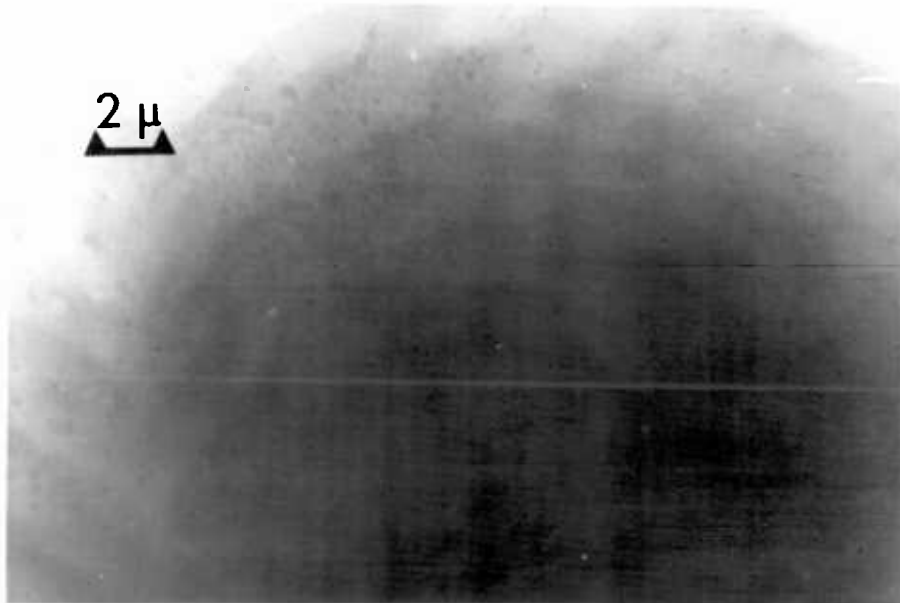


c) TEM. 2 beam, s=0 condition

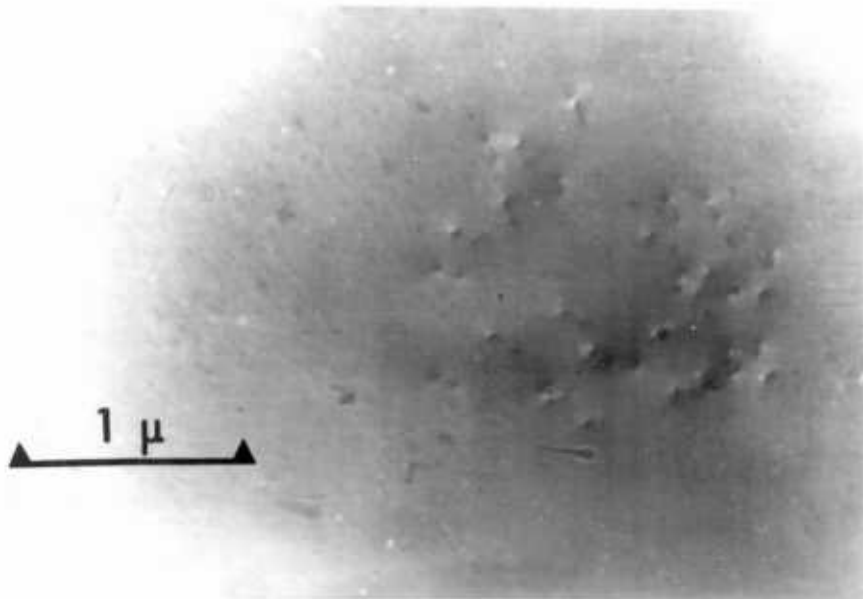
Growth centres in RP13



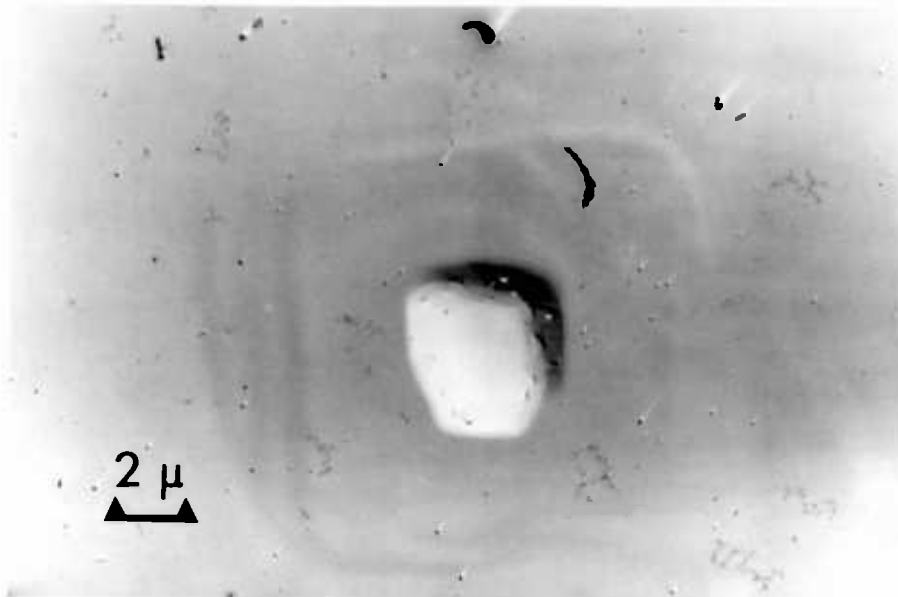
a) Pt/C replica



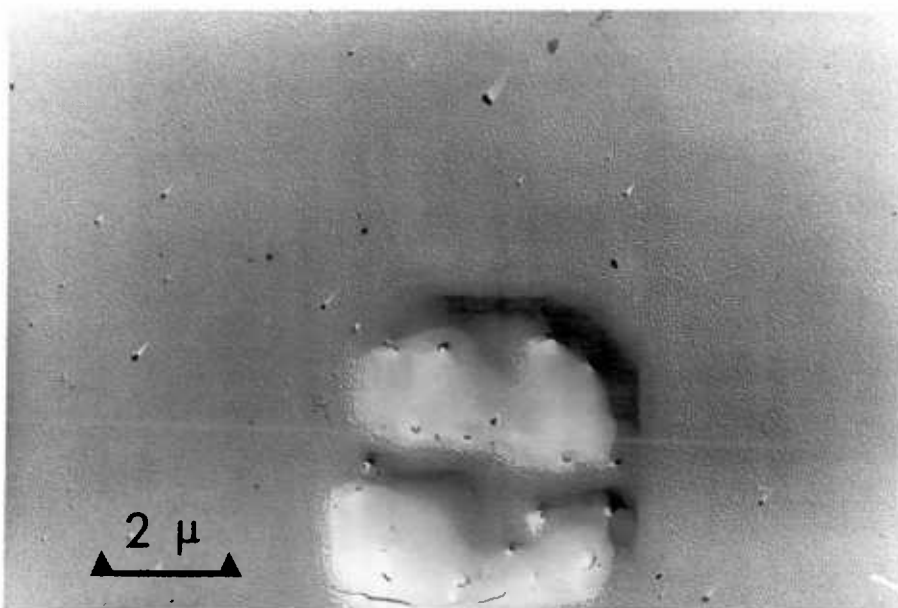
b) TEM



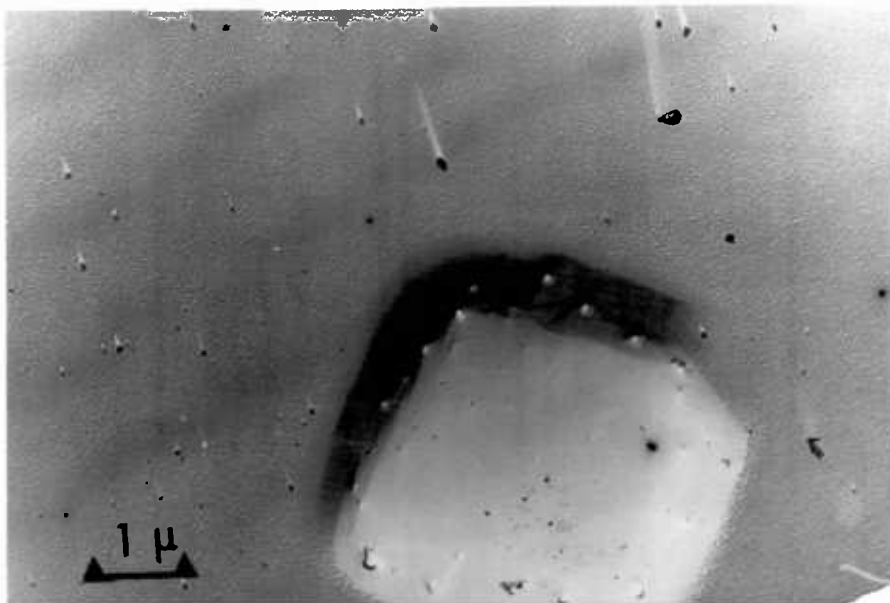
c) TEM enlargement of centre defect region

Pt/C replicas of 'spangles' in RB44A

a) shows dimple in centre of spangle



b) another spangle showing pits at edge of dimple and in-filled region bisecting dimple.



c) different specimen grid to a) and b) accounts for change in orientation of 'spangle'

## CHAPTER 5. RESULTS: CONTAMINATION STUDIES WITH OTHER GASES

## 5.1. Methane

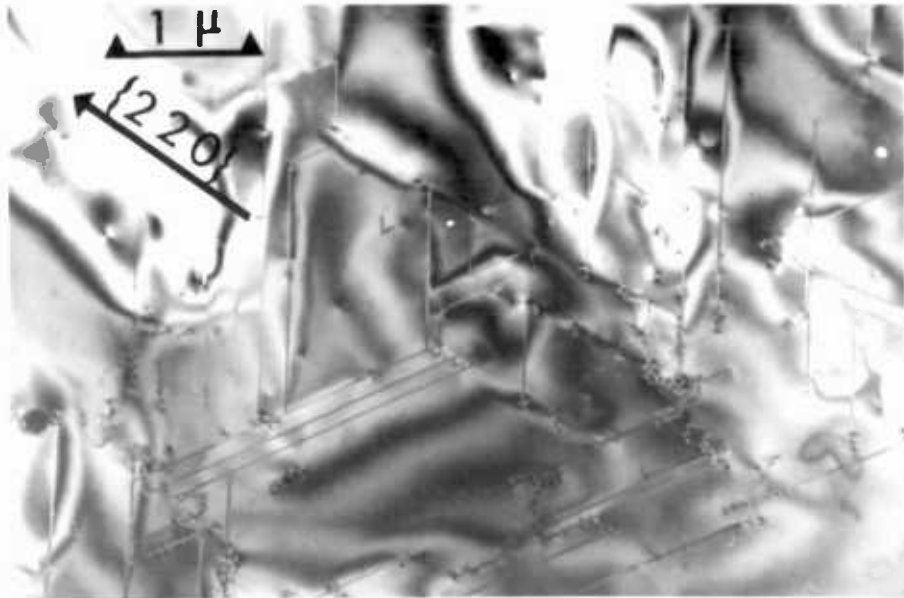
Several runs using {111} substrates with methane as contaminant were made at levels up to 10% of the gas in the silane stream. Table 5.1. gives details of the experiments.

TABLE 5.1. METHANE EXPERIMENTS

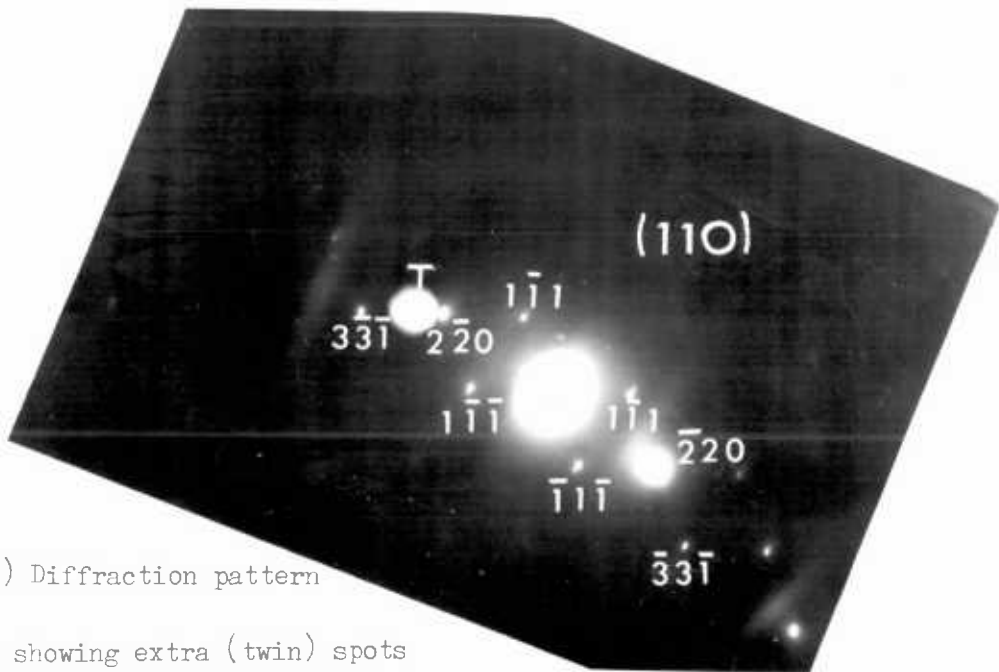
Run No RB	T <sup>0</sup> C obs.	T <sup>0</sup> C corr.	ppm CH <sub>4</sub>	Optical		TEM	
				Sirtl pit count cm <sup>2</sup>	interference contrast	defect structure	surface
54B	810	845	10 <sup>3</sup>	1.2x10 <sup>5</sup>	V.smooth	s.f tetrahedra T	V. smooth
54A	820	855	10 <sup>2</sup>	4x10 <sup>4</sup>	-	line s.f(L)	" "
59B	820	855	10 <sup>5</sup>	3x10 <sup>4</sup>	a few saucers	no defects obs.	Some small growth centres
59A	825	860	0	5x10 <sup>3</sup>	" "	" "	V. smooth
56A	825	860	10 <sup>4</sup>	8.6x10 <sup>4</sup>	V.smooth	~10 <sup>6</sup> T + Lcm <sup>-2</sup>	straight ledges
56B	880	920	10 <sup>4</sup>	too high to count	faceted	3.8x10 <sup>8</sup> T + twins	faceted
55A	925	970	10 <sup>3</sup>	2.6x10 <sup>4</sup>	saucers	T+L	V.smooth
57A	980	1035	10 <sup>3</sup>	1.4x10 <sup>4</sup>	-	no defects obs.	"
55B	1040	1100	10 <sup>3</sup>	2.2x10 <sup>4</sup>	V.smooth	" "	"
58A	1080	1145	10 <sup>3</sup>	7.8x10 <sup>4</sup>	saucers	T intersect.	"
57B	1105	1170	10 <sup>3</sup>	3x10 <sup>5</sup>	V.smooth	no defects obs.	"
58B	1130	1200	10 <sup>5</sup>	2.7x10 <sup>5</sup>	saucers	L	"

No structural effects could be attributed to the presence of methane. The badly faulted structure found in layer RB56B, Fig.5.1(a), was believed to be due to a mishap when the substrate bar went cold whilst the temperature was adjusted during growth. Tilting to near a  $\langle 110 \rangle$  pole revealed streaked twin spots in diffraction, Fig.5.1(b) and dark field on a twin spot (ringed in the diffraction pattern) showed microtwins in the layer, Fig.5.1(c). Closer examination in bright field showed an overlapped, faulted structure, Fig.5.1(d). Some stacking faults, arrowed, have irregular ends, i.e. cannot be bounded by stair-rod dislocations. Although detailed analysis was not performed, since most of these ribbon faults show no contrast at the partials, it is likely that the faults are bounded by Shockley partial loops of the type analysed in Appendix A1. The surface of this layer was strongly faceted as shown in Figs.5.1(e) and (f). Small sweeping growth steps joining the facets are clearly seen in the latter figure.

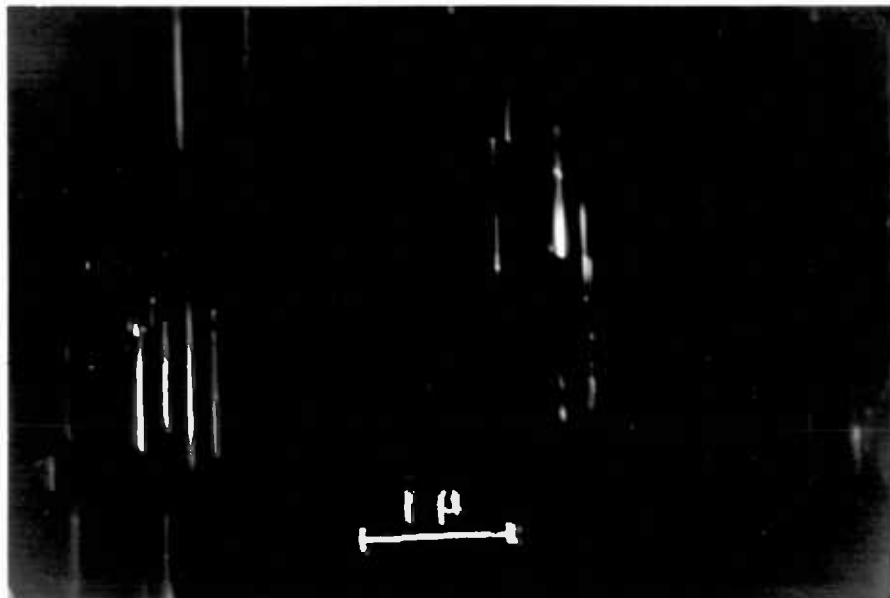
Stacking Faults & micro-twinning in BSEDB



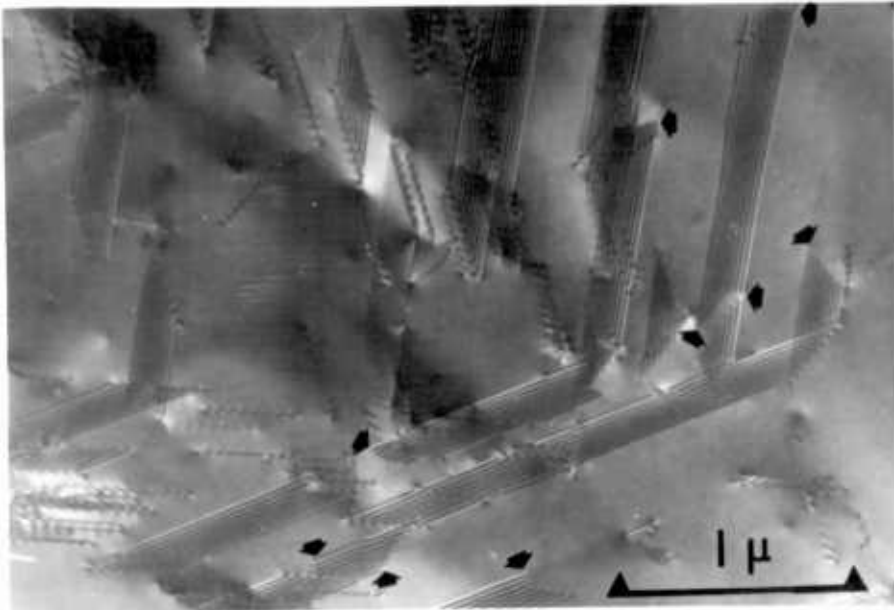
a) TEM micrograph showing general faulted structure



b) Diffraction pattern showing extra (twin) spots



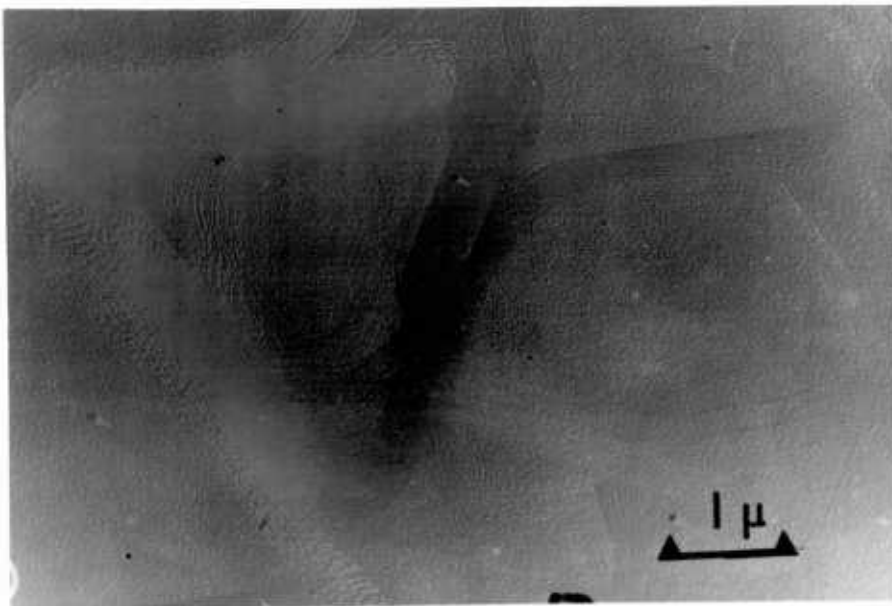
c) Dark field micrograph on twin spot shown ringed in b).



d) TEM micrograph at higher magnification showing details of faulted structures.



e) Pt/C replica showing general features of surface



f) as e) but at higher magnification showing terraced structures around facets.

5.2. Oxygen

Two experiments only were made with oxygen as contaminant gas, using {111} substrates. Details are given in Table 5.2.

TABLE 5.2. OXYGEN EXPERIMENTS

Run No. RB	T°C obs.	T°C corr.	ppm O <sub>2</sub>	Optical		TEM	
				Sirtl etch count cm <sup>-2</sup>	Interference contrast	Defect structure	Surface
52A	800	835	9	3x10 <sup>4</sup>	v.smooth	sf tetra.	v.smooth
52B	"	"	147	7x10 <sup>4</sup>	some pits	no defects obs.	"
53A	915	960	100	10 <sup>4</sup>	v.smooth	"	"
53B	1055	1115	100	10 <sup>4</sup>	"	"	"

No effect due to the presence of oxygen was observed in the 4 layers.

5.3. Water vapour

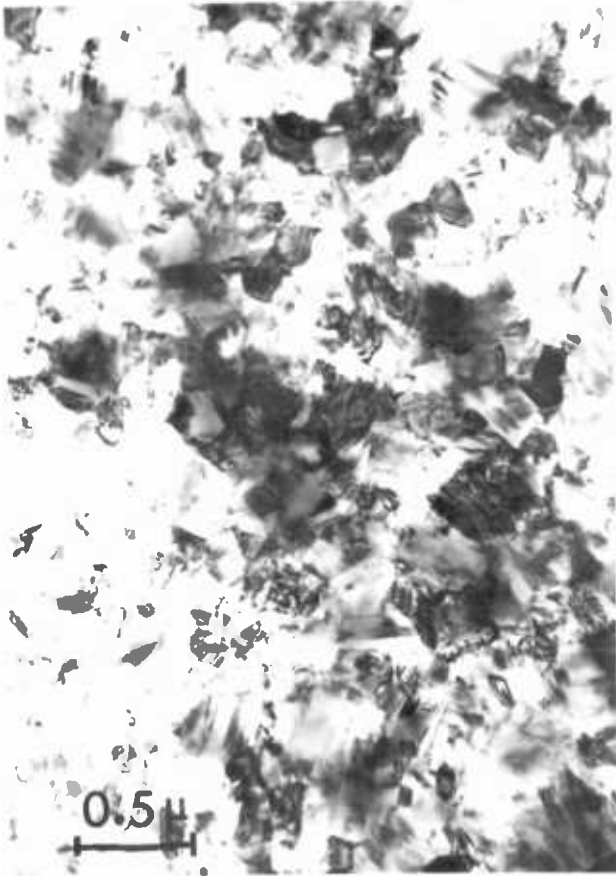
The results of contaminating silane with water vapour are summarised in Table 5.3. There is uncertainty in the contamination levels in runs RB45-47 because of a tendency for the water vapour to ice-up in the gas line. This was prevented in subsequent runs by electrically heating the gas line. Substrates were {111}; or {100} where marked with asterisk \*

TABLE 5.3. WATER VAPOUR EXPERIMENTS

Run No. RB	T°C obs.	T°C corr.	ppm water vapour	Optical		TEM	
				Sirtl pit count cm <sup>-2</sup>	Interference contrast	Defect structure	Surface
47A	825	860	10	5.6x10 <sup>4</sup>	smooth, some saucers	irreg. tetrah.	Saucers, rough patches
*48A	"	"	11	5.3x10 <sup>4</sup>	growth centres	growth centre No defects obs.	Growth centres
45A	"	"	18	1.4x10 <sup>4</sup>	v.smooth	"	V.smooth
46A	"	"	33	3.2x10 <sup>4</sup>	smooth, some saucers	saucers, no defects obs.	V.smooth + 1 rough patch
50A	"	"	100	4.2x10 <sup>4</sup>	small linear growth features	sf tet. & line	V.smooth
45B	"	"	157	8.2x10 <sup>5</sup>	saucers	no defects obs.	Saucers, tri- pyramid.
50B	"	"	515	4.5x10 <sup>5</sup>	"	"	V.smooth, tri- pyramid
46B	"	"	1230	2.8x10 <sup>5</sup>	"	sf pair	V.smooth, some saucers.
*48B	"	"	10 <sup>4</sup>	too high to count	extremely granular	random poly- crystalline	irreg. facets
47B	"	"	1.1x10 <sup>4</sup>	"	"	7x10 <sup>8</sup> cm <sup>-2</sup> s.f complexes, Bands of ppt.	Ridges
49A	900	945	10 <sup>4</sup>	2.7x10 <sup>4</sup>	v.smooth	irreg. tet.	V.smooth
51A	950	1000	10 <sup>4</sup>	1.6x10 <sup>4</sup>	"	no defects obs.	"
49B	1015	1070	10 <sup>4</sup>	5.2x10 <sup>4</sup>	"	"	V.smooth, 1 sf complex.
51B	1105	1170	10 <sup>4</sup>	2.4x10 <sup>5</sup>	"	"	Saucers

Significant effects of water vapour were observed at low growth temperatures when the contamination level was very high. Fig.5.2(a) shows that

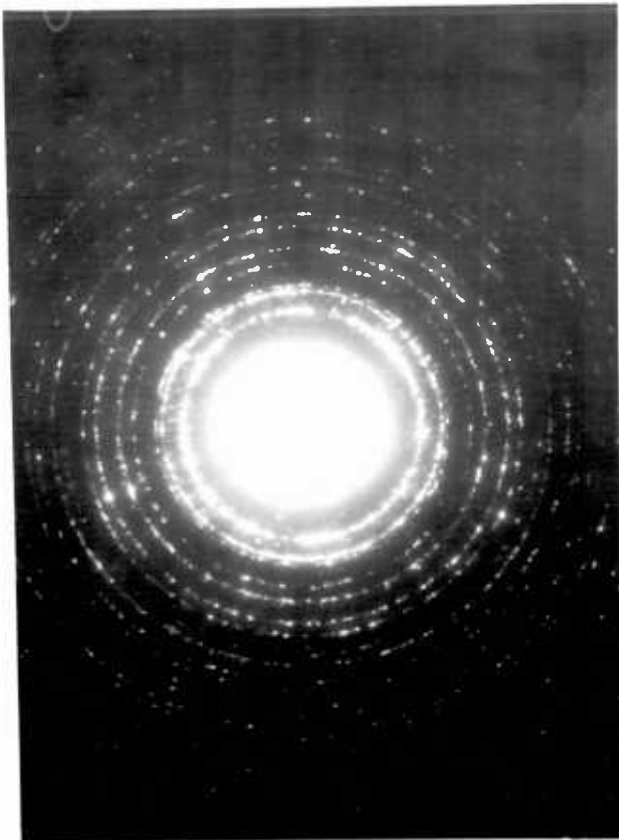
Polycrystalline Si in RE48B grown with water vapour contamination.



a) TEM showing heavily faulted polycrystalline structure



b) Pt/C replica showing growth facets



c) Transmission Electron diffraction pattern of layer



d) Glancing angle electron diffraction pattern of layer.

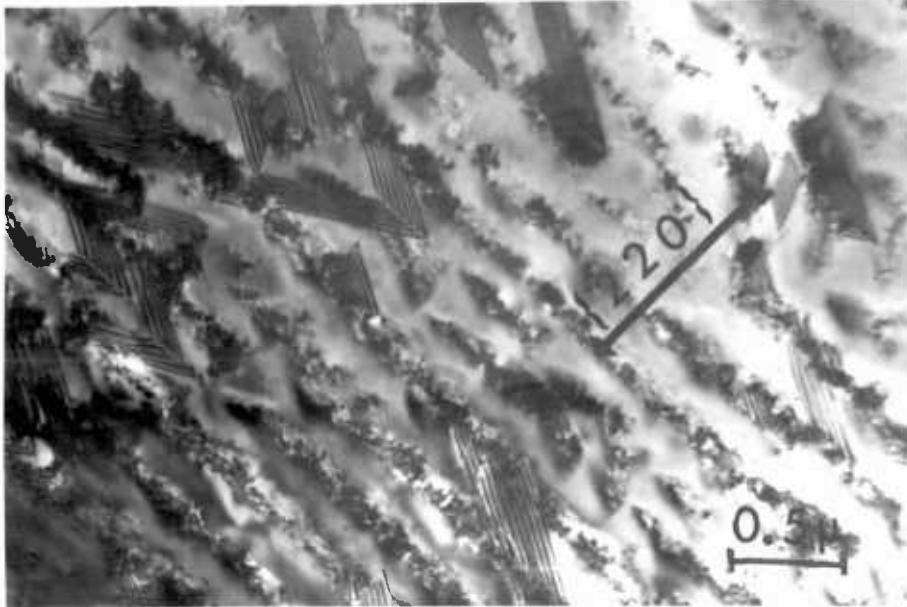
the structure of layer RB48B, grown on a  $\{100\}$  substrate, was polycrystalline with a maximum grain size  $\sim 0.4 \mu\text{m}$ . The replica of the surface, Fig.5.2(b), shows facets corresponding to the upper faces of the crystallites. The similar intensities in transmission electron diffraction and GAED, Figs.5.2c) d) & comparison with ASTM X-ray diffraction data, Table 5.4, shows that the crystallites are randomly orientated.

TABLE 5.4. Si RING PATTERNS FROM Fig.5.2c) d)

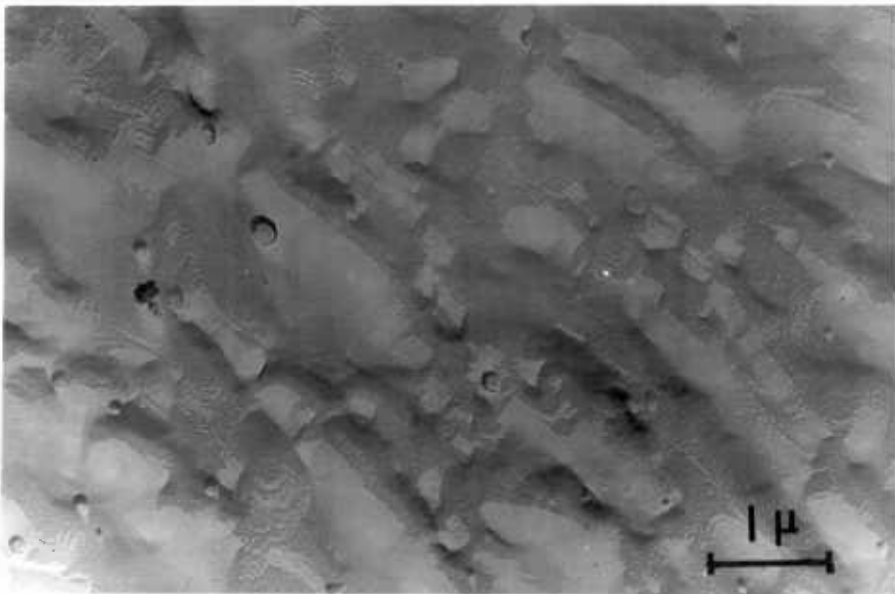
T.E.D			G.A.E.D.			A.S.T.M.		
D cm	d $\overset{\circ}{\text{A}}$	Int.	R cm	d $\overset{\circ}{\text{A}}$	Int.	d $\overset{\circ}{\text{A}}$ Si	hkl	I/I $_0$
1.22	3.12	VS	.67	3.12	VS	3.138	111	1.00
1.98	1.92	S	1.08	1.93	S	1.920	220	.60
2.32	1.64	S	1.27	1.65	S	1.638	311	.35
2.42	1.57	M	1.33	1.57	MW		(222)	
2.80	1.36	M	1.54	1.36	MW	1.357	400	.08
3.05	1.25	MS	1.68	1.24	MS	1.246	331	.13
3.13	1.21	W	-	-			(420)	
3.41	1.11	M	1.88	1.11	M	1.1083	422	.17
3.66	1.04	M	2.01	1.04	M	1.0450	511,333	.09
3.94	.965	W	2.18	.960	W	.9599	440	.05

A similar run on a  $\{111\}$  substrate, RB47B, gave single crystal growth but contained a high density of stacking faults, Fig.5.3(a). Also seen in this micrograph are bands of granular material running roughly parallel to a  $\langle 11\bar{2} \rangle$  direction which appears to be precipitation although the phase was not identified. The bands corresponded to a ridged surface structure, Fig.5.3(b). The stacking faults and saucers observed in other layers was also characteristic of control runs described earlier (Chapter 3.1) and these defects were not attributed to the water vapour contaminant.

FIG. 5.3  
Stacking faults & precipitation in RB47B  
grown with water vapour contamination.



a) TEM showing stacking fault structures & precipitation bands



b) Pt/C replica of layer showing rippled surface.

## CHAPTER 6. DISCUSSION

The major part of this discussion will be concerned with a mechanism for the nucleation and growth of the ribbon stacking faults shown in section 3.2. The occurrence of stacking fault tetrahedra and related structures in  $\{111\}$  layers of Si grown at moderate temperatures, in the presence of ethylene contamination, section 3.3, could have been predicted from the likelihood of SiC formation. However, the observation of ribbon faults in  $\{111\}$  layers grown at low temperatures with ethylene present was unexpected and their analysis as mainly extrinsic Shockley partial dislocation loops has not, to the best of our knowledge, previously been made. As discussed in section 1.3, early TEM work by Finch et al (1963) showed examples of ribbon faults which were not characterised but which were surmised to be bounded by Shockley partials. In view of the present work, their supposition was probably correct. Abrahams & Tietjen (1969) and Chase & Holt (1972) identified Shockley partials bounding intrinsic stacking faults in vapour-deposited III - V compounds and segregation of impurity atoms was suggested as the cause of their nucleation although neither paper explored possible mechanisms in detail.

The proposed model for nucleation of the Shockley loops in the present work is based on the incorporation of carbon impurity atoms in the epitaxial layer and draws on the surface studies outlined in section 1.2. This is followed by a new mechanism for the nucleation of stacking fault tetrahedra based on the results of Burgers vector analyses of observed stacking fault interactions. Implications of the different structures found in carbon-contaminated  $\{110\}$  and  $\{100\}$  layers will then be discussed, as will the largely negative results of contamination with gases other than ethylene. We will commence with a discussion of the tetrahedron-type stacking fault structures observed mainly in  $\{111\}$  layers grown in the presence of ethylene to show how bulk and surface structures are closely related.

### 6.1. Tetrahedron-type Stacking faults

In the absence of ethylene, or at high growth temperatures with ethylene present, the stacking fault density is low ( $\leq 10^4 \text{cm}^{-2}$ ) and the surfaces of the layers are generally very smooth. At moderate growth

temperatures with ethylene present, we observe

- a) stacking fault structures such as tetrahedra and other stair-rod bounded figures (e.g. Fig.3.13(a))
- b) inclusions of  $\beta$ -SiC as filaments (e.g. Fig.3.17(a))
- c) surfaces pitted and terraced (e.g. Fig.3.13(d))

It was pointed out in section 1.3 that particles such as SiC situated on the substrate give rise to stacking fault formation. In the present experiments the simultaneous decomposition of silane and ethylene on the growing layer has led to the continuous formation of SiC particles which become embedded in the layer. Although this does not lead to stacking fault nucleation on a 1 to 1 basis, since Fig.3.13(a) shows several particles which are not associated with stacking fault formation, the configuration ringed in Fig.3.14(a) suggests that this does occur at such particles. Thus, unlike most of the previous work outlined in section 1.3, stacking fault formation is not confined to the substrate:layer interface.

In section 1.2 we reviewed work by Abbink, Broudy & McCarthy (1968) and Cullis & Booker (1971) who attributed surface terraces and pinning sites to SiC formation and showed surface structures very similar to Figs.3.13c) and d). The presence of SiC as filaments in Fig.3.17 rather than as isolated particles is evidence that carbon contamination builds up ahead of the growing terraces in long continuous bands before precipitating as crystallites of SiC. This is in accordance with Frank's (1958) & Cabrera & Vermilyea's (1958) theories on the role of contamination in step propagation as discussed in section 1.2. With no deliberate carbon contamination, the surface is featureless, i.e. growth occurs by the nucleation and propagation of two-dimensional steps and defect densities are low. Similar defects and surface structures were observed at growth temperatures above  $\sim 1100^{\circ}\text{C}$  even with 100 ppm ethylene present. It was found in work by Brown & Watts (1970) that SiC was absent from Si surfaces heated in ethylene at these temperatures. Two possible explanations are

- a) the "sticking" coefficient of ethylene is reduced at these temperatures so that molecules do not reside on the surface long enough to decompose.

- b) increased bulk diffusion of carbon occurs, leading to insufficient surface concentrations to form SiC.

Stacking fault tetrahedra and pinning sites, Fig.3.7(d) were also found at low growth temperatures when the concentration of ethylene was low. This suggests that particles of SiC have formed under these conditions although the  $\beta$ -SiC phase was not identified at the 100 ppm level and we develop the argument in section 6.2 that carbon is incorporated into the layer by a different mechanism.

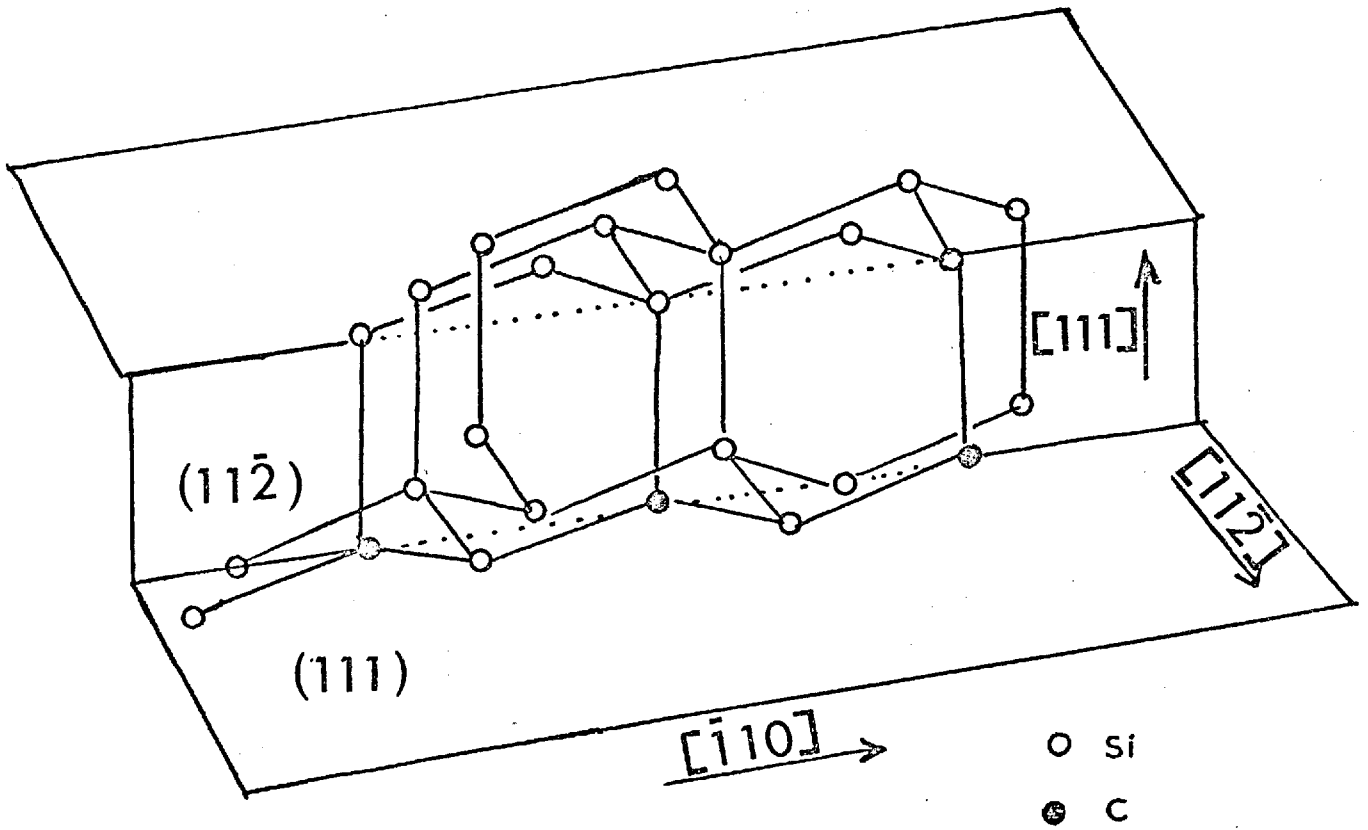
It might have been expected from earlier work by Booker & Joyce (1966) that the SiC particles would have generated tripyramids. These defects were generally only observed by optical means (e.g. Fig.3.1(b)) since their density was low. Substrate preparation and conditions prior to growth were specifically aimed at avoiding SiC formation on the substrate. It seems that simultaneous growth of Si and SiC with ethylene contamination in the silane does not allow the development of the more complex twinning necessary to form a tripyramid.

## 6.2. Nucleation of ribbon stacking faults

At low growth temperatures, under conditions which gave rise to ribbon stacking faults as the dominant defect structure, crystalline SiC was not observed and we believe that carbon enters the layer by an alternative mechanism. The faceted surface structure shown in Figs.3.6a) & b) is similar to that found by Joyce, Neave & Watts (1969) on a similar system and who associated the step pile-up with the accumulation of carbon contamination on the facets (section 1.2). We suggest that carbon is finally incorporated into the step edges in chains or filaments in a random manner. Short range order must be expected so that the chains will consist largely of alternate C and Si atoms:  $C-Si-C-Si-C-Si-C$  as in SiC poly-type structures, with carbon atoms occupying substitutional sites in the lattice. From the orientation of the steps, these chains will lie largely in  $\langle \bar{1}10 \rangle$  directions, Fig.6.1.

Assuming, as in the case of stacking fault tetrahedra, that the ribbon faults are generated at or close to the growing layer surface, then the bounding Shockley partial loops will lie in  $\langle \bar{1}10 \rangle$  directions. It follows from the  $\frac{1}{6} \langle 112 \rangle$  Burgers vectors of the partials that they will be edge in character. Bond configurations of edge Shockley partials bounding intrinsic and extrinsic stacking faults in the diamond-cubic structure

$[\bar{1}10]$  carbon filament on surface step.



BOND CONFIGURATIONS OF EDGE SHOCKLEY DISLOCATIONS BOUNDING INTRINSIC & EXTRINSIC STACKING FAULTS

(after Hornstra (1958)) and Amelinckx (1964)

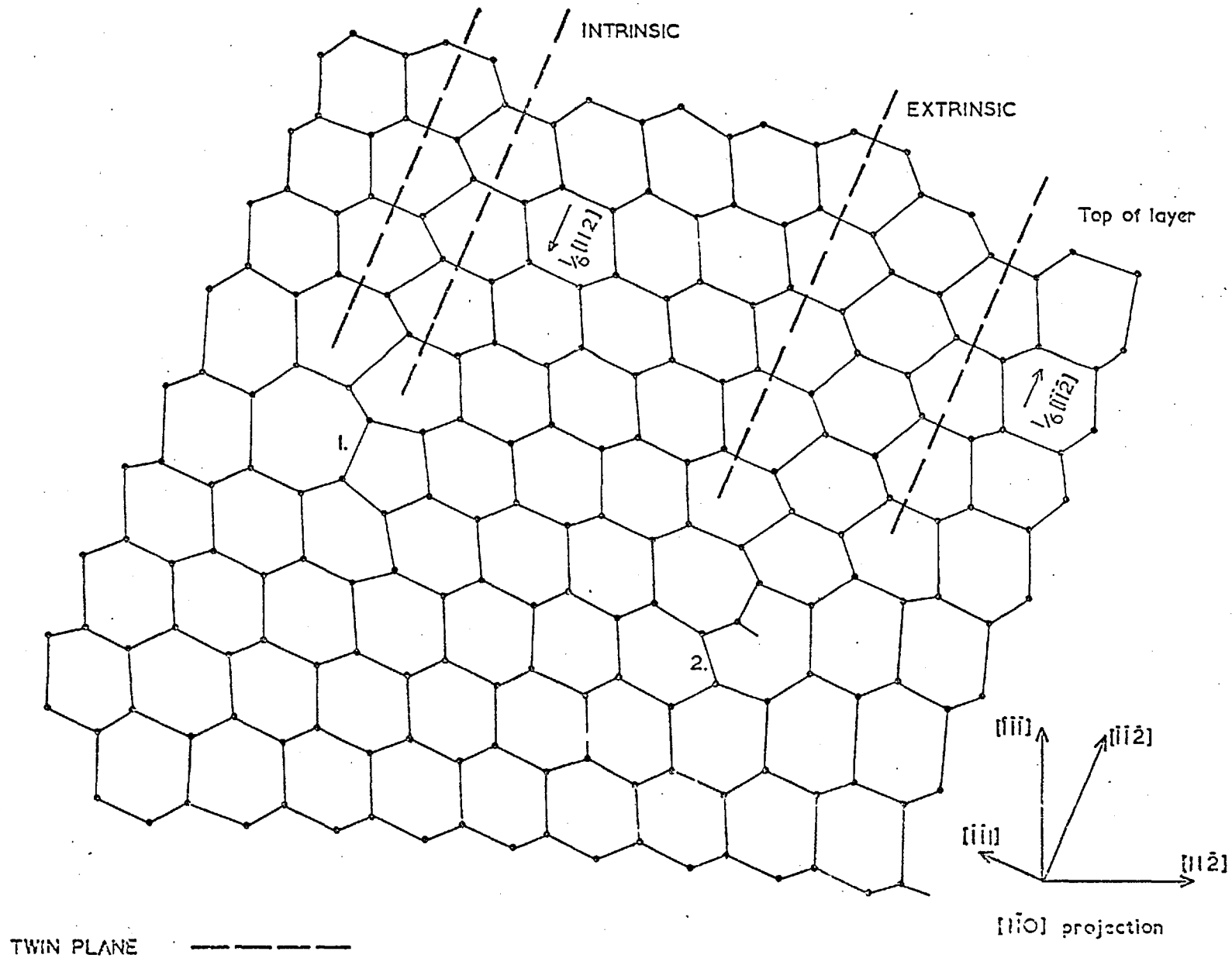


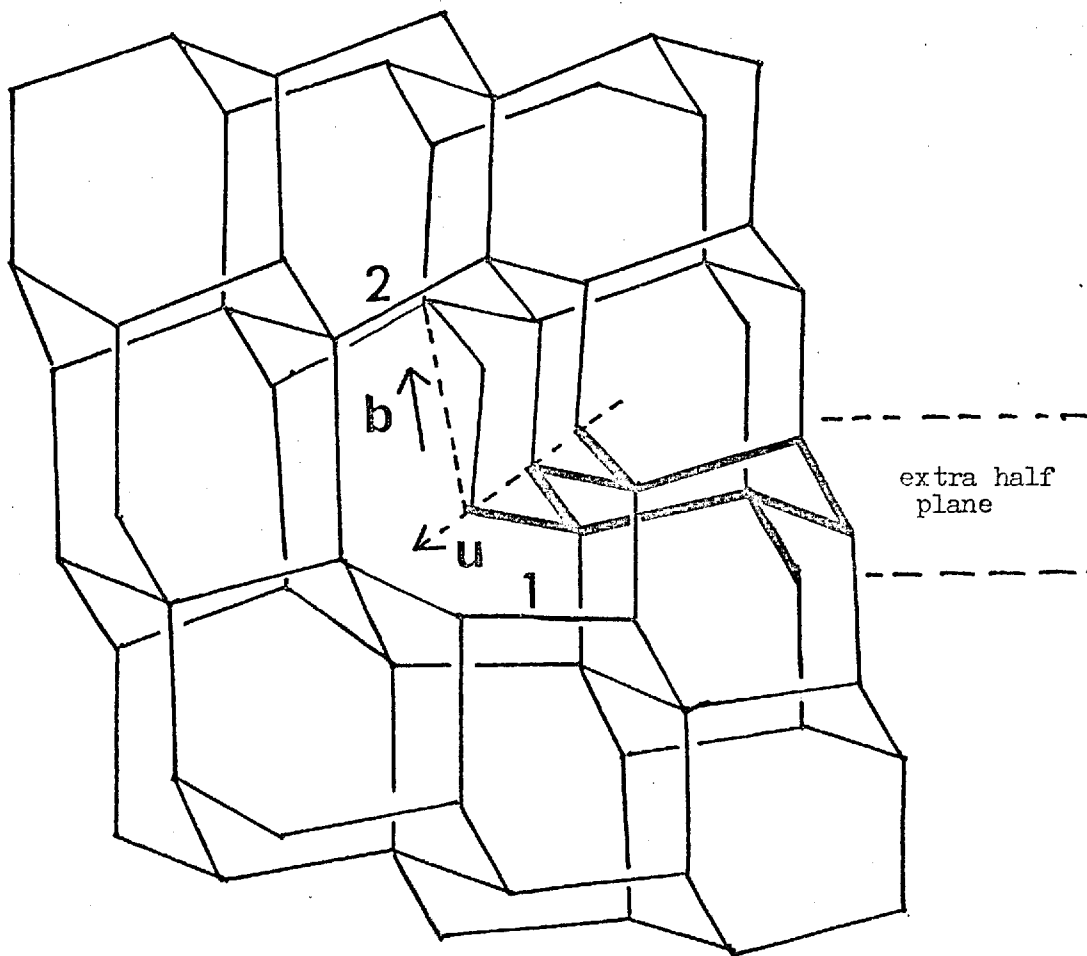
FIG. 6.2.

have been proposed by Hornstra (1958) and by Amelinckx (1964) respectively. The projection onto a  $(\bar{1}10)$  plane of these configurations bounding stacking faults lying on inclined  $(11\bar{1})$  planes is shown in Fig.6.2. The diagram shows that distortion of bonds from the  $[111]$  orientation (i.e. those marked 1 & 2) during epitaxial growth could lead directly to the formation of ribbon faults of each type, if bonds in equivalent sites in  $[\bar{1}10]$  rows perpendicular to the plane of the paper were similarly distorted. We believe that the incorporation of carbon in  $\langle\bar{1}10\rangle$  filaments, as in Fig.6.1, provides this distortion due to the small size of the carbon atoms. The bond length in  $\beta$ -SiC is 20% shorter than in Si. A similar argument can be applied to the formation of undissociated dislocations as shown, for example, in Fig.3.4. Thus these dislocations are also initially formed in  $\langle\bar{1}10\rangle$  directions lying in the  $(111)$  plane of the epitaxial layer and so are  $60^\circ$  dislocations. Fig.6.3 shows the bond configuration of the dislocation core in this situation. The extra  $\frac{1}{2}$ -plane of the dislocation lies in the  $(111)$  plane of the layer. It is apparent from this figure that bond distortion from  $[111]$  orientations is not very great, but bonds marked 1 & 2 suffer the worst distortion and so the dislocation is expected to form with these bonds close to the carbon atoms.

During subsequent epitaxial growth the portions of both the partial and perfect dislocations which intersect the growing surface propagate on the inclined  $\{11\bar{1}\}$  slip planes and have large screw components, i.e. the partials tend to lie in  $\langle 112 \rangle$  orientation and the perfect dislocations take up orientations parallel to their inclined  $\frac{1}{2} \langle 110 \rangle$  Burgers vectors. Dyer (1971) used ball models to explain the formation of twins on  $\{211\}$  and  $\{110\}$  facets in epitaxial Si crystals grown from  $\text{SiHCl}_3$  contaminated with  $\text{CH}_4$ . He suggested that short chains of carbon atoms on substitutional sites caused next and subsequent rows of Si to be deposited on twin positions. However, in the present work, the bond model discussed above seems more appropriate to explain the formation of stacking fault ribbons.

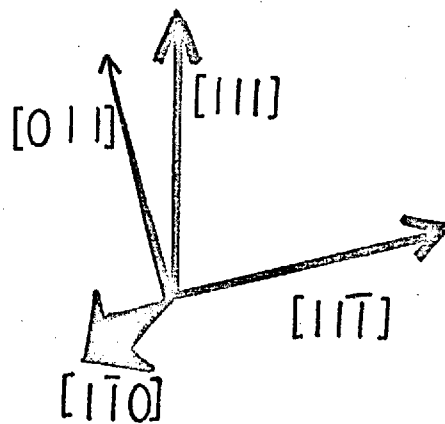
Elastic energy calculations presented in Appendix B show that under certain conditions there can be a net reduction in energy by forming an edge Shockley dislocation in the vicinity of the proposed  $\langle\bar{1}10\rangle$  carbon filaments to relieve the misfit strain. Fig.B1 shows that the elastic energy  $E_1$  due to the misfit of a carbon atom in the Si lattice quickly reaches its maximum value only a few Angstroms below the surface. The same applies to the binding energy  $E_2$  of a carbon atom to an edge Shockley dislocation lying parallel to the layer surface. However, the self energy  $E_3$  of the

CONFIGURATION OF  $60^\circ$  DISLOCATION LYING IN  $[1\bar{1}0]$  orientation in  
(111) SUBSTRATE PLANE, HAVING BURGERS VECTOR OF  $\frac{1}{2}[011]$   
INCLINED TO SUBSTRATE PLANE



$$\underline{b} = \frac{1}{2} [011]$$

$$\underline{u} = \frac{1}{2} [1\bar{1}0]$$



(after Hornstra (1958))

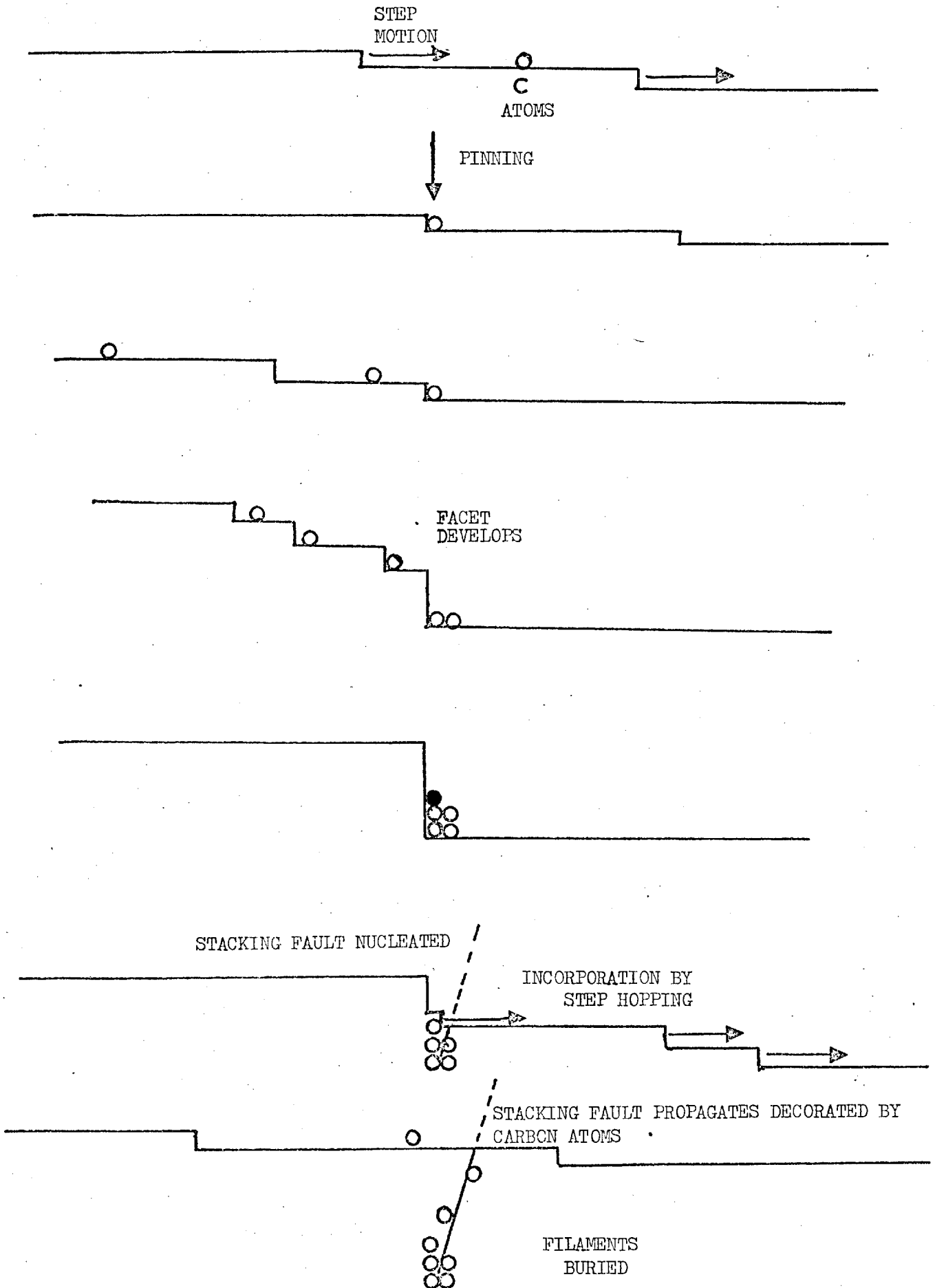
dislocation increases relatively slowly with increasing depth and at distances just below the surface  $E_2 \approx E_3$ . This means that if there is a sufficiently high concentration of carbon atoms, the misfit strain can be relieved by the formation of an edge Shockley dislocation close to the surface of the growing epitaxial layer. An approximate value for this critical carbon level can be derived by balancing the total binding energy of the number  $n$  of carbon atoms in the region of the dislocation with the self-energy per unit length  $E_3$  of the dislocation. We assume that the average binding energy per carbon atom is about half the maximum value, i.e.  $E_2 \sim 0.5\text{eV}$ , since only one carbon atom can occupy the most favourable strain-relieving site near to the core of the dislocation. At a depth  $\sim 8\text{\AA}$ ,  $E_3 \sim 2\text{eV}$  per  $\frac{1}{2} \langle 110 \rangle$  length of dislocation. Thus when  $n \geq 4$  per  $\frac{1}{2} \langle 110 \rangle$  length of dislocation, there is a net reduction in elastic energy on formation of the edge Shockley partial. In other words, if several  $\langle 110 \rangle$  carbon filaments are incorporated in the lattice close together, then the elastic strain energy is reduced by the formation of an edge Shockley dislocation lying parallel to the filaments. The carbon atoms will occupy sites in the compressive regions of the dislocation's strain field. It is not likely that a dislocation would be nucleated at much greater depths within the epitaxial layer because the self-energy of the dislocation would be too high.

It is justifiable to ask why  $\frac{1}{3} \langle 111 \rangle$  Frank loops were not observed since our explanation for the formation of the  $\frac{1}{6} \langle 112 \rangle$  and  $\frac{1}{2} \langle 110 \rangle$  dislocations by bond distortion could also be applied to the Frank dislocation. However, the Shockley and undissociated dislocations form by shear along their inclined  $\{11\bar{1}\}$  slip planes in the direction of the free surface, whereas the Frank dislocation must propagate by climb, i.e. by inserting or removing a  $\{11\bar{1}\}$  double-layer and it appears that this mechanism is not favoured.

### 6.3. Propagation of ribbon faults

The failure of ribbon faults to propagate when the ethylene flow was cut off during epitaxial growth (section 3.2.2.) is taken as evidence that the faults are stabilised by carbon segregation. It is possible that lattice sites where the faults intersect the growing epitaxial layer surface are preferentially occupied by carbon atoms when the contaminated growth steps move across the stacking fault. Fig.6.4 shows a sequence where C filaments accumulate and are 'dumped' in the layer, and generate a stacking fault which

DIAGRAM REPRESENTING GROWTH STEP RETARDATION BY CARBON IMPURITY ATOMS AND THEIR SUBSEQUENT INCORPORATION IN EPITAXIAL LAYER.



then continues to absorb carbon during subsequent step motion. It is significant that the ribbons in Fig.3.4 are not wider than  $\sim 0.4 \mu\text{m}$  which is the maximum length of the straight portions of the surface steps in Figs. 3.6a) & b). The observation of wider faults at lower ethylene levels, Figs. 3.7a) b) is coupled with much less faceted surfaces, Figs. 3.7c) & d) and presumably carbon segregates on long portions of steps before being incorporated in the layer. Competition for carbon atoms from neighbouring faults or changes in surface topography could terminate the carbon supply to a particular fault. During subsequent epitaxial growth, the fault will not propagate but will terminate within the layer, forming a buried loop as the ringed example in Fig.3.5(a). This behaviour is quite different from the propagation of the more usual type of stacking fault structure shown in Figs. 3.13 and 3.14 which, once formed, grow with the epitaxial layer without needing stabilising impurity atoms because of the high stability of the bounding stair-rod dislocations.

The amount of carbon which accumulates at the ribbon faults must be very small since no second phase was detected by electron diffraction and there was no observation of anomalous fringe contrast in TEM. A monolayer of substitutional carbon atoms at a stacking fault would create a maximum strain of  $\sim 30\%$  in the  $\langle 111 \rangle$  direction normal to the fault plane. Since a displacement of  $\Delta R$  of  $2\%$  from  $R = \pm \frac{1}{3} \langle 111 \rangle$  can be taken as a criterion for fringe visibility (Hirsch et al 1965), then  $\geq 10^{14} \text{cm}^{-2}$  carbon atoms at the stacking fault should cause anomalous contrast effects. No direct determination of carbon content in the epitaxial layers was made. Counts were made in layers grown above  $940^\circ\text{C}$  of the numbers of SiC particles found in areas of foil where thickness could be measured from the number of stacking fault fringes, as in Fig.3.13(a), and the total volume of SiC per unit volume of epitaxial layer was estimated from the average size of the particles. These estimates suggest that the amount of C per unit volume in the layer as SiC is of the same order of magnitude as the C : Si ratio in the silane gas stream during growth. Assuming that this result is valid for the low temperature growth runs and that all the carbon segregates at the observed faults, then for the structure shown in Fig.3.4 (total stacking fault area  $\sim 2 \times 10^4 \text{cm}^2$  per  $\text{cm}^3$  of epitaxial layer),  $10^{19} \text{cm}^{-3}$  carbon atoms (100 ppm ethylene) would decorate the faults at  $5 \times 10^{14} \text{cm}^{-2}$ , i.e.  $\sim \frac{1}{3}$  of a monolayer. As discussed above, such amounts though small, should be detectable by TEM. Applications of techniques such

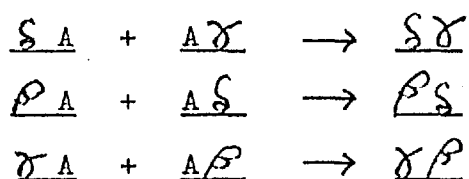
as infra-red adsorption, X-ray lattice parameter measurements, mass spectrometry (Baker et al 1968) and radio-active tracers (Newman & Smith 1969) would be difficult to apply to relatively thin epitaxial layers and tend to give conflicting results. In any case, experiments by Ray & Cockayne (1971) on plastic deformation of bulk crystals of silicon containing unspecified amounts of carbon (possibly  $10^{16} - 10^{17} \text{cm}^{-3}$ ) used the weak beam technique (Cockayne, Ray & Whelan 1969) to resolve partial dislocation separations of  $< 100\text{\AA}$ . Calculation of the stacking fault energy (SFE) from these separations gave an only moderately low value of  $\sim 50 \text{ erg.cm}^{-2}$  and so the total carbon content is probably unimportant compared with its distribution within the lattice. Clearly the Shockley stacking fault loops found in the present study cannot be in equilibrium with the Si lattice since opposite portions of the loop are attractive and do not balance the attractive "surface tension" forces, i.e. the SFE, seeking to reduce the stacking fault area. This indicates that another factor is involved, i.e., carbon as an embryonic SiC phase. The stability of the faults on annealing suggests that the phase is tightly bound to the faults since otherwise carbon in solid solution would be expected to diffuse away from the faults at high temperatures, leading to the disappearance of the faults by glide.

The physical reason for the lowering of the SFE by carbon is speculative. Hirth & Löthe (1968) point out the limitations of theoretical models of SFE. More recently Chen & Falicov (1974) have calculated the SFE of Si and found good agreement with Ray & Cockayne's value, although many assumptions had to be made. The Suzuki effect (1962) of solute segregation to or from stacking faults has been used to explain anomalously low SFE in alloys but is inappropriate for relatively pure crystals of elements. Venables (1970) has shown that extended stacking fault nodes in TiC doped with 100-200 ppm of boron were extremely wide, indicating very low SFE. Using SAED, some of these faults were found to contain a  $\text{TiB}_2$  phase, although the phase was not detected at all faults presumably because it was present in insufficient quantities. A similar situation may exist in oxidised Si (Booker & Tunstall 1966) where extrinsic stacking fault loops bounded by Frank partial dislocations could be associated with an oxide of Si. Precipitation is often observed by TEM near the partials of such faults.

#### 6.4. Model of nucleation of stacking fault tetrahedra

The occurrence of Shockley stacking fault loops with similar Burgers vectors and the production of stair-rod dislocations from the intersection of

ribbons lying on differently inclined  $\{111\}$  planes, Figs. 3.7(e) and 3.12(b) suggest a simple model for the nucleation of stacking fault tetrahedra in  $\{111\}$  epitaxial Si layers. This mechanism is proposed as an alternative to the model of Booker & Stickler (1963), which was based on the decomposition of a Frank loop, as discussed in section 1.3. A drawing of the intrinsic ribbon configuration observed in Fig. 3.12(b) and the Thompson tetrahedron are shown in Fig. 6.5(a). The stair-rod lying parallel to AB has a low energy Burgers vector  $\underline{S\gamma} = \frac{1}{6} \langle 110 \rangle$  and is the direct product of the interaction of the two Shockley partials  $\gamma A$  and  $\delta A$  lying on inclined planes (c) and (d) respectively. Consider three intrinsic Shockley loops lying on inclined planes (b), (c) and (d) having magnitude  $\beta A$ ,  $\gamma A$  and  $\delta A$  respectively, Fig. 6.5(b). If all three mutually intersect at acute angles, then low energy stair-rods  $\underline{S\gamma}$ ,  $\underline{\beta\delta}$  and  $\underline{\gamma\beta}$  form along the inclined  $\langle 110 \rangle$  directions AB, AC and AD respectively. The three reactions can be written as



We suggest that lattice distortion due to small patches of contamination or particles on the substrate/layer interface nucleate Shockley stacking fault loops on inclined  $\{111\}$  planes as discussed in section 6.2. Three loops, each lying on a differently inclined  $\{111\}$  plane, if sufficiently close, will attract those portions of other dislocations nearest to themselves and react to form stair-rod dislocations along the inclined  $\langle 110 \rangle$  directions. Loops which fail to intersect will not continue to grow in the absence of a continuous supply of contaminant as discussed in section 6.3. Other configurations such as intrinsic/extrinsic pairs can be formed by a similar mechanism.

An objection to this model is that formation of extrinsic loops would result in the formation of extrinsic tetrahedra, whereas, as we have noted, tetrahedra are invariably intrinsic. This led Booker & Stickler in their model to propose that their initial Frank loop was extrinsic although this was insufficiently observed. An explanation which answers the above objection can be found in Hirth & L  the's text (1968). This shows that an extrinsic tetrahedron requires the formation of two stair-rod dislocations

ANALYSIS OF RIBBON INTERSECTION SHOWN IN FIG. 3.12.

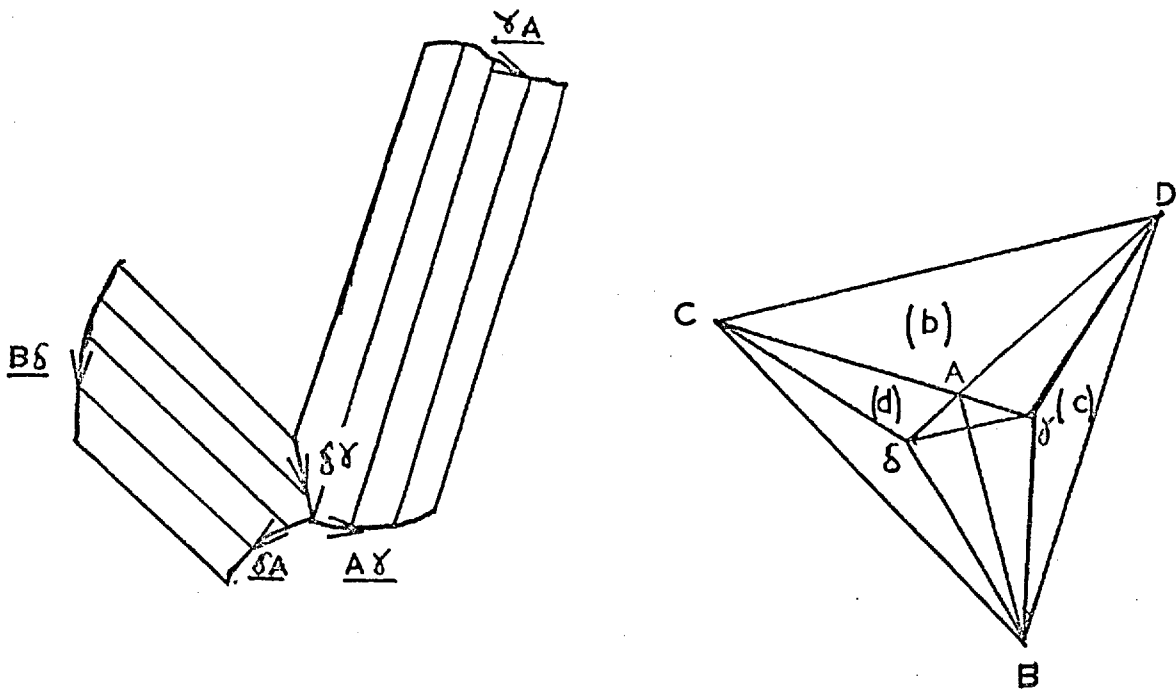
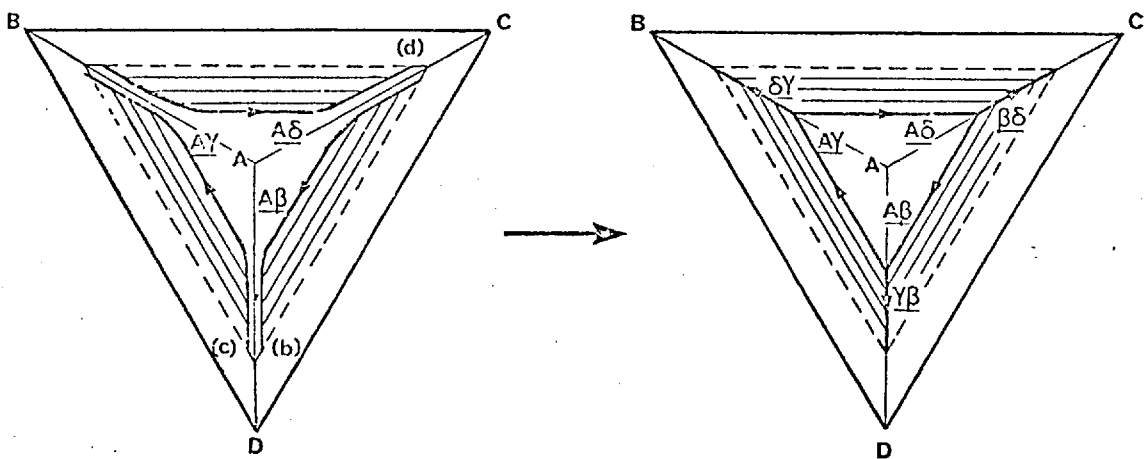


FIG. 6.5(b)

FORMATION OF INTRINSIC STACKING FAULT TETRAHEDRA FROM THREE SHOCKLEY LOOPS. INTERSECTING OF STACKING FAULTS WITH LAYER SURFACE SHOWN 'DASHED'



All Figs.6.5 Thompson tetrahedra drawn apex A pointing up, ribbons viewed from outside tetrahedra.

at each intersection, e.g.  $\underline{S\delta}$  &  $\underline{S D / C\delta}$  of  $\frac{1}{6} \langle 110 \rangle$  &  $\frac{1}{3} \langle 110 \rangle$  type respectively, Fig.6.6, since each extrinsic partial must be regarded as comprising two intrinsic partials e.g.  $\underline{S A} = \underline{B\delta} + \underline{C\delta}$ . The combination of the two stair-rods produces a Burgers vector of  $\underline{\delta\delta}$ , i.e. equal and opposite to the corresponding intrinsic case and with the same elastic energy. But since these double stair-rods are so close together, their core energy is higher than the intrinsic stair-rod and reactions which could lead to the formation of extrinsic tetrahedra are suppressed.

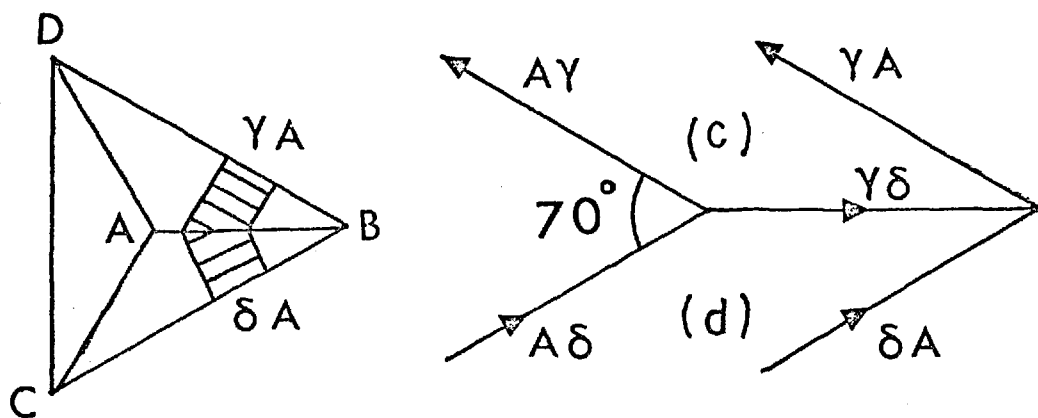
The observation of intrinsic stacking fault pyramids in  $\{100\}$  epitaxial Si layers, as discussed in Appendix A3 adds weight to the proposed mechanism for stacking fault tetrahedra in  $\{111\}$  layers. We show that 4 Shockley loops lying on inclined  $\{111\}$  planes in  $\{100\}$  layers with similar Burgers vectors to those observed in  $\{111\}$  layers could react together via the same mechanism to form the intrinsic pyramids.

#### 6.5. Effect of layer orientation : ethylene contamination

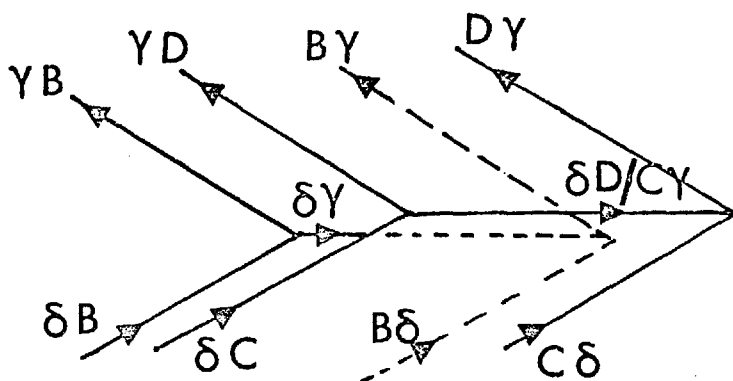
Shockley-bounded ribbon stacking faults were not observed in layers grown on  $\{110\}$  and  $\{100\}$  substrates under similar conditions to which they formed in  $\{111\}$  layers, i.e. low growth temperatures, high ethylene levels. Epitaxial growth on these orientations has not been as intensively studied as growth of  $\{111\}$  layers. It is known in general that stacking fault densities in  $\{100\}$  layers are very low, so that test slices are deliberately scratched prior to growth in conventional systems so that layer thickness can be measured from the resulting stacking faults. Joyce et al (1969(a)) extended their molecular beam work to  $\{100\}$  substrates and showed growth nuclei similar to those observed on  $\{111\}$  substrates, so presumably hydrocarbon contamination resulted in a similar step pile-up. However, our  $\{100\}$  layers were extremely smooth, apart from the larger growth centres, and even those could not be attributed to the presence of ethylene since they were also seen in control run RB5 (section 4.2). Ethylene must decompose on  $\{100\}$  and  $\{111\}$  surfaces in a similar way but faceting and terracing were absent in the  $\{100\}$  layers. We can only suggest that carbon is more easily incorporated into the  $\{100\}$  layer and does not interfere with two-dimensional growth. Thus carbon does not concentrate in SiC filaments as observed on  $\{111\}$  layers and so cannot introduce the localised strain necessary to form stacking faults.

INTERSECTION OF EXTRINSIC STACKING FAULT LOOPS AT ACUTE ANGLE,  
VIEWED FROM OUTSIDE THOMPSON TETRAHEDRON

a) Treatment as single extrinsic loops.



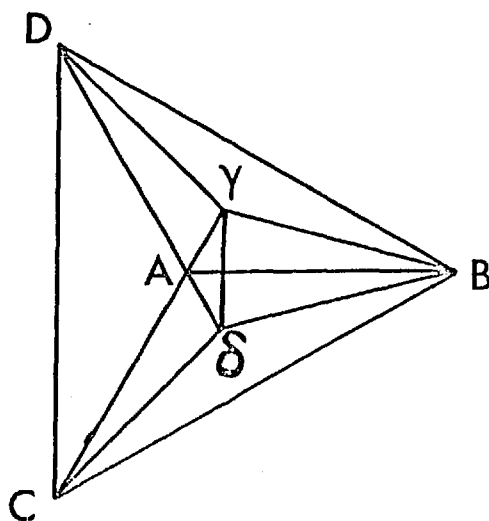
b) Treatment as double intrinsic loops



net Burgers vector of stair-rods

$$\underline{\delta\gamma} + \underline{\delta D/C\gamma} = \underline{\gamma\delta}$$

Thompson tetrahedron  
 apex A pointing up.



Although dislocations were observed in the growth centre in one  $\{100\}$  layer, Figs.4.8b) and c), a mechanism for their formation will not be discussed.

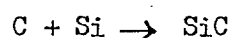
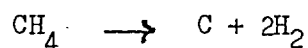
The tangled filaments and pitted surface structure in the  $\{110\}$  layer RB27B show that SiC has formed, and it seems that the crystallites are again associated with the growth of stair-rod bounded stacking fault structures. However, as only two attempts were made to grow on  $\{110\}$  substrates, the results are inconclusive.

## 6.6. The effect of other contaminant gases

### 6.6.1. Methane

Unlike ethylene, no effect of methane contamination on the structural perfection of the epitaxial layers was noted, even at 10% levels in the silane, i.e.  $10^5$  ppm. Methane (heat of formation  $\Delta H = 21.7 \text{ k cal mole}^{-1}$  at  $800^\circ\text{C}$ ) of course, being a saturated hydrocarbon, is more stable than ethylene ( $\Delta H = 8.9$ ). Although, for example, Nakashima et al (1966) grew SiC layers at  $1200\text{--}1300^\circ\text{C}$  on silicon surfaces from methane, Kahn & Summergrad (1967) did not detect SiC growth at temperatures  $< 1000^\circ\text{C}$ .

The rates of the reactions:



must be too slow compared with the silane decomposition rate to produce significant SiC formation and hence to affect Si epitaxial growth.

Dyer (1971) observed a correlation between methane contamination levels and twin formation in Si crystals grown from  $\text{SiHCl}_3$  but the number of defects involved was extremely small ( $< 10^2 \text{ cm}^{-2}$ ).

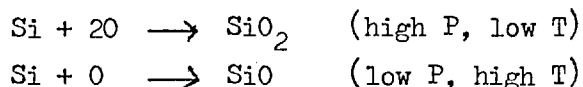
### 6.6.2. Oxygen and water vapour

No structural effects were observed with oxygen contamination levels up to  $\sim 150$  ppm. Water vapour only produced defective epitaxial growth at the 1% level, i.e.  $10^4$  ppm, and low growth temperatures. However, the growth of a polycrystalline film in run RB48B, Fig.5.2, strongly suggests that oxide formation on the substrate occurred prior to silicon growth, and the precipitation in layer RB47B, Fig.5.3(a) is likely to be an oxide.

Lander & Morrison (1962) using LEED in a UHV system investigated the oxidation and reduction of Si at  $600\text{--}1100^\circ\text{C}$ . They found that high

oxygen pressures coupled with low temperatures gave an oxidised surface, but high temperatures and low oxygen pressures gave clean Si surfaces.

The two competing reactions are written as:



The SiO is removed rapidly from the surface as a gas because of its high vapour pressure. More recently Maguire & Augustus (1973) investigated the silicon : water vapour system using Auger spectroscopy. Their experiments gave similar results to the Lander & Morrison work, chief differences being a lower activation energy for oxidation by water vapour and a cross-over below 900°C, indicating a large region of lower pressures where oxidation in O<sub>2</sub> is more favourable than in water vapour.

In the present work, the pyrolysis of silane competes with oxidation reactions in the O<sub>2</sub> and water vapour contamination runs. The high partial pressures of water vapour in runs RB47B & 48B must have resulted in deposition of SiO<sub>2</sub>. Although similar contamination levels were used in runs at higher temperatures (Table 5.3), oxide precipitation did not occur, in accordance with the above oxidation studies, and no structural defects resulted in the epitaxial layers.

## CHAPTER 7. SUMMARY AND CONCLUSIONS

Ethylene contamination, even at extremely low concentrations, has been shown to have a profound effect on the structural perfection of  $\{111\}$  epitaxial layers of silicon grown by the pyrolysis of silane. Examination by TEM has shown that stacking fault structures are formed whose nature depends primarily upon the growth temperature. Ribbon stacking faults bounded by Shockley partials of both intrinsic and extrinsic type occurred at growth temperatures from 830-940°C. These faults could terminate within the epitaxial layer and only propagate with the continuous presence of ethylene during epitaxial growth. We have proposed a model for the nucleation of the ribbons based on the incorporation in the layer, by surface step motion, of carbon impurity atoms lying in  $\langle \bar{1}10 \rangle$  rows. Pt/C replicas showed surface faceting which was thought to be caused by carbon slowing down step motion. The resulting distortion of the lattice can be relieved by the formation of dislocations lying close to the growing surface. Shockley partial dislocations and the observed undissociated dislocations are believed to have been generated in this way. The ribbon faults are stabilised during subsequent epitaxial growth by the continued segregation of carbon atoms to the region of the fault plane.

At temperatures above 940°C the more usual stacking fault tetrahedra and related configurations were predominant. These structures are associated with the presence of  $\beta$ -SiC crystallites. Consideration of ribbon fault interactions has led to a new model for the nucleation of stacking fault tetrahedra. Analysis of stacking fault pyramids occurring in  $\{100\}$  epitaxial Si suggests that these defects can be generated by a similar mechanism.

No effect of ethylene was observed on  $\{100\}$  epitaxial layers. It is believed that carbon contamination did not accumulate on  $\{100\}$  surfaces since these surfaces were shown to be extremely smooth and so did not generate stacking faults. Insufficient work on  $\{110\}$  layers was performed to fully characterise the effect of ethylene contamination. Limited results indicated that only stair-rod bounded stacking fault configurations were formed.

Methane was shown to have no effect on the structural quality of the Si epitaxial layers even at extremely high levels in the silane. The decomposition of methane to form SiC proceeds very slowly in the range of Si growth temperatures used and so methane is quite different from the case of ethylene. Oxygen and water vapour also showed no effects at low levels of contamination tested. Oxidation is presumed to be the cause of polycrystalline growth in one layer and highly faulted growth in another layer at high water vapour levels and low growth temperatures.

It is stressed that it was only by employing UHV techniques that the effect of small amounts of gaseous impurities could be studied. Even with no deliberate contamination, stacking fault densities were not negligible. This suggests that contamination or mechanical damage of the substrates still occurs even with the elaborate procedure adopted. The ion etch technique of Henderson & Helm (1972) as discussed in section 1.2, seems an interesting direction to avoid high temperature pre-growth anneals.

Low temperature epitaxial Si has not yet been exploited commercially to any extent, in spite of the general trend, mentioned in Chapter 1, towards lower deposition temperatures. The technology would be adopted if device designers find applications which would emphatically need the fabrication of very abrupt junctions. Much has been written on the causes of structural imperfections in epitaxial layers. Now that these are understood in some detail, and hence can be controlled, it remains to be seen if the industry can exploit the possibilities of low temperature epitaxial growth.

PART II

DEFECT AND ELECTRICAL STUDIES IN A SILICON DEVICE

CHAPTER 8. INTRODUCTION

Part I of this thesis was concerned with a particular aspect of Si device technology: the epitaxial growth of silicon. Intensive study of the effect of ethylene contamination on the defect structure of epilayers as revealed by Transmission Electron Microscopy (TEM) led to proposed mechanisms for stacking fault generation. In industrial terms the work can be regarded as fairly "pure" research. It was part of a long term research programme which was flexible enough to be directed along interesting avenues without much immediate commercial significance. Much more of concern to semiconductor device manufacturers are problems of yield and electrical 'defects' of devices. Whilst many problems can be treated successfully by a production engineering approach, e.g. by improving cleanliness or by tighter control of processing parameters, there exists an extensive and persistent literature on the role of crystal imperfections such as stacking faults and dislocations in the electrical behaviour of devices. The much cited reviews by John (1967) and by Schwuttke (1970) provide a useful introduction to studies in silicon devices.

The characterisation of crystal imperfections has been achieved principally by the use of TEM diffraction contrast techniques such as those detailed in Part I. Meieran and Cass (1972) have reviewed the application of electron microscopy to semiconductor device manufacture. Mechanisms for the generation of these defects have been proposed over the years and this field continues to attract interest. It is beyond the scope of the present work to attempt to review this subject but Table 8.1. lists the main imperfections found in starting material and processed Si device slices. The defects observed in the present study will be described in Chapter 10.

TABLE 8.1. CRYSTAL IMPERFECTIONS IN SEMICONDUCTOR Si.

<u>Crystal imperfection</u>	<u>Character</u>	<u>Process</u>	<u>Mechanisms</u>	<u>Observation technique</u>	<u>Reference</u>
<u>Starting Material</u>					
Dislocations		ingot growth	thermal gradients during pulling and dislocations in seed.	etching & optical microscopy (OM)	virtually absent today
Swirls	dislocation loops & precipitates	" "	point defect clustering & O <sub>2</sub> segregation due to fluctuations in micro growth rate.	XRT on Cu decorated slices TEM	de Kock (1973) Petroff & de Kock (1975)
Banding/ striations	impurity segregation	" "	fluctuations in microgrowth rate.	spreading resistance Xray lattice parameter Vidicon SEM with BEVE	Vieweg-Gutberlet (1974) Yoshikawa & Chikawa (1973) Celotti et al (1974) Ravi & Varker (1974)
<u>Process induced</u>					
cracks	faceted cleavage steps, dislocation arrays, massive elastic strain	slice sawing, lapping, polishing, indentation	not understood. poss. quantum mechanical tunneling of dislocations	TEM	Hill & Rowcliffe (1974)
dislocations	screw, 60°	a) annealing indent damage	glide due to stress field	"	" "
"	inclined $\mu$ in plane of slice	b) high temp. processing	temperature grads. produce stress, relieved by slip	XRT	Miltat & Bowen (1970)
"	60°	c) epitaxy on mismatched substrate	relief of stress due to lattice mismatch due to dopant differences between layer & substrate.	TEM	Tamura & Sugita (1970)
"	edge dislocatn. networks	d) diffusion	climb. Mechanisms not well understood	"	Levine, Washburn & Thomas (1967)

TABLE 8.1. CRYSTAL IMPERFECTIONS IN SEMICONDUCTOR Si. (continued)

Crystal imperfections	Character	Process	Mechanisms	Observation technique	Reference
<u>Process induced (contd)</u>					
dislocations	prismatic loops	e) ion implantation	amorphous layer recrystallises to loops, grow & escape.	TEM	Bicknell (1972)
stacking faults	closed configuration, stair-rod bound. line, Shockley bound.	a) epitaxy	nucleated by damage, impurity	"	Thesis Part I
		Frank bound, often decorated	b) oxidation	vacancy release ahead of growing SF allows oxide precipitation	"
<u>Precipitates</u>					
	SiO <sub>2</sub> spheres	oxidation	exceed solid solubility, precipitates on dislocations	"	Bialas & Hess (1969)
	FeSi <sub>2</sub> rods	boron deposn.	Fe impurity picked up from BN source	TEM, electron microprobe Xray analysis	Cullis & Katz (1974)
	Si P rods	phosphorus deposition	exceed solid solubility, rod precipitates in $\langle 110 \rangle$ directions	"	Servidori & Armigliato (1975)

## 8.1. Effect of imperfections on electrical properties

8.1.1. Dislocations. Much careful work has been done by a team at Gottingen University on the effect of dislocations on the bulk electrical properties of Si and Ge, as summarised by Haasen & Schroter (1970). Read's (1954) model of a charged dislocation which formed a mid-gap energy level has been replaced by an energy band whose position depends on the occupancy of charge on the dislocation and on dislocation density. However, significant effects on mobility and conductivity due to dislocations were only noted at low temperatures and low doping levels where phonon and ionisation scattering were reduced. Figielski's work on photo-conductivity in Ge (e.g. Jastrzebska & Figielski (1966)) shows that dislocations act as recombination centres and so affect minority carrier lifetimes. In the above work dislocation densities were controlled by plastically deforming bars of material at high temperature and assessed by etching and optical microscopy. However, the theory of imperfections penetrating pn junctions has not been treated in detail. Although workers in industrial laboratories have demonstrated general correlations between the electrical properties of devices and heavy dislocation densities (e.g. Schwuttke 1970), the establishing of one-to-one relationships has been far from straightforward. Experimental results on similar device structures can be contradictory. For example, Plantinga (1969) using anodic etching and optical microscopy, demonstrated an exact correlation between dislocation etch pits and 'pipes', i.e. low collector/emitter (C/E) breakdown ( $BV_{CEO}$ ) in a multiemitter transistor structure. The dislocations were generated by high temperature processing, i.e. thermal slip. Later, Tice, Lange & Shasteen (1973) combined TEM with Plantinga's etching technique to observe dislocations in transistors with C/E pipes. However, Juleff (1973), examining a similar device structure, found no harmful effects of thermal slip. He observed a linear defect running between the emitter/base and base/collector junctions which appeared to be responsible for pipes although this defect was not characterised.

8.1.2. Current leakage and precipitates. Some notable successes have been achieved recently in demonstrating current leakage due to precipitation extending across pn junctions. Ravi, Varker & Volk (1973) grew extrinsic stacking faults by mechanical damage followed by thermal oxidation in Si and showed, using Scanning Electron Microscopy (SEM) with the conductive mode, that above a certain threshold voltage the stacking

faults could become sites for current leakage in diode structures. TEM showed that the stacking faults were decorated with precipitation at their bounding Frank partials. Cullis & Katz (1974) using a combination of TEM and SEM with in-situ electron probe microanalyser proved that rod-like precipitates found in leaky devices were crystalline  $\text{FeSi}_2$ . Also there was evidence that oxidation stacking faults were decorated with copper.

### 8.2. Outline of present investigation.

It was a premise of the present work that to reach a deeper understanding of the role of crystal defects in device performance it was necessary to employ a number of different techniques of microscopy to ensure that all types of defects were detected. In addition, techniques were needed to determine which crystal defects were electrically active in each case and to measure the electrical properties of those defects. The work is mainly concerned with the detailed study of two commercially-processed Si slices which contained large numbers of discrete phototransistor devices. X-ray topography (XRT) was used to establish a strong correlation between slip, i.e. heavy dislocation densities, and low emitter/collector breakdown voltages ( $BV_{\text{CEO}}$ ). The correlation, however, was far from 1 to 1 and other microscopy techniques, i.e. SEM and TEM, were employed to examine the devices in more detail. In particular, the conductive mode of SEM was found to be useful in revealing dislocations in the junction region of devices. The results of this aspect of the work were first reported by Ogden & Holt (1974) and published by Holt and Ogden (1976). Whilst the dislocations do not appear to contribute directly to premature breakdown, SEM showed that photoengraving faults can result in very low breakdown voltages. The high resolution of TEM revealed the detailed structure of dislocations and other defects and has led to some insight into the role of defects in the degradation of the electrical properties of the devices.

## CHAPTER 9. EXPERIMENTAL

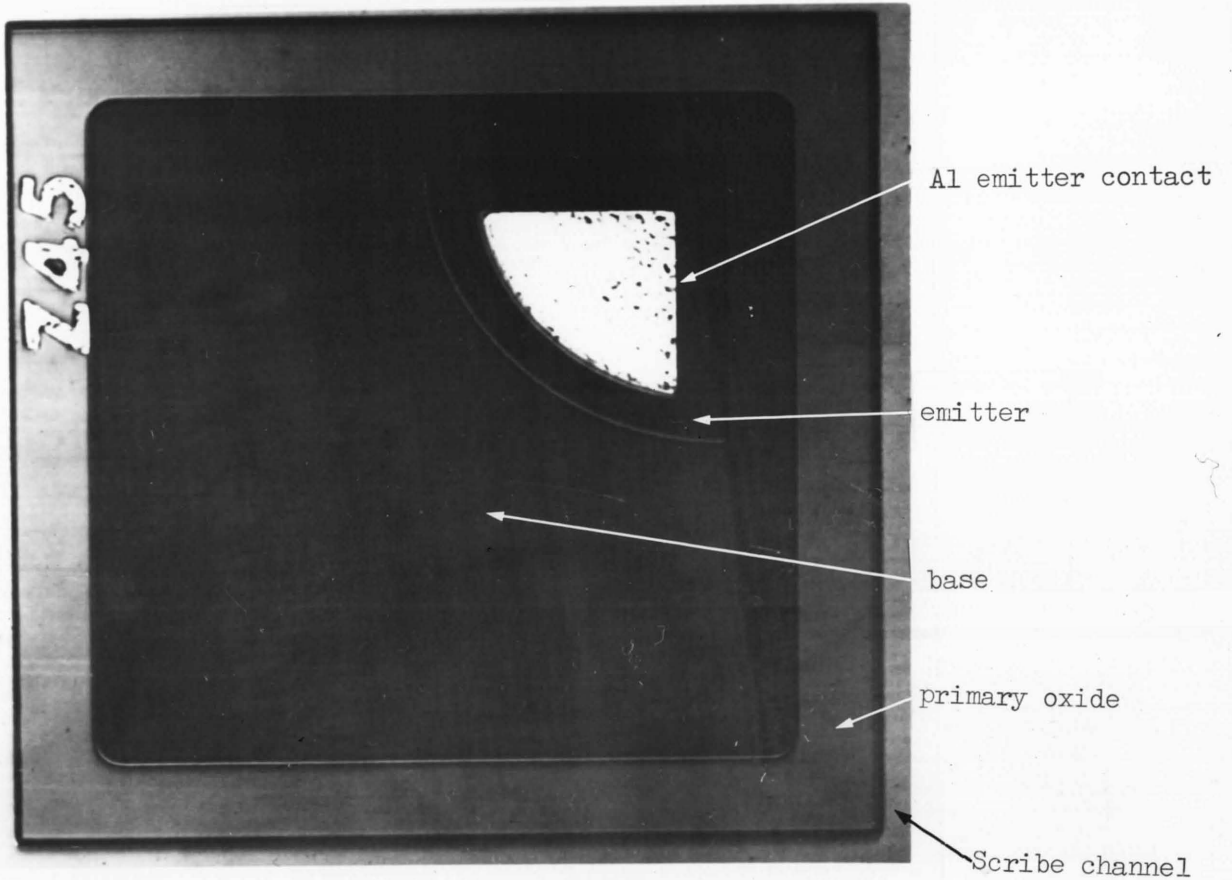
### 9.1. Operation of Phototransistor

Fig.9.1(a) shows a micrograph of the device used in this study. The  $n^+pn$  structure was achieved by a boron (p) base diffusion into n-type starting slice followed by a heavy phosphorus ( $n^+$ ) emitter diffusion. Fig.9.1(b) shows a section through the device. In a phototransistor, photocurrent amplification is achieved by the injection of carriers into the base. Light falling on the reverse biased base/collector region creates electron/hole pairs. The minority carriers generated in or near the depletion region diffuse across the junction, i.e. holes into the p-type base and electrons into the n-type collector, Fig. 9.1(b). The hole current  $I_B$  flowing into the base causes electron injection from the  $n^+$  emitter through the forward-biased emitter/base junction to compensate for the charge imbalance. The emitter/collector current  $I_C = \beta I_B$ , where  $\beta$  is the gain of the device (typically 30), is thus much higher than the light current achieved from a photo diode. Fig. 9.1(c) shows the equivalent circuit of the device.

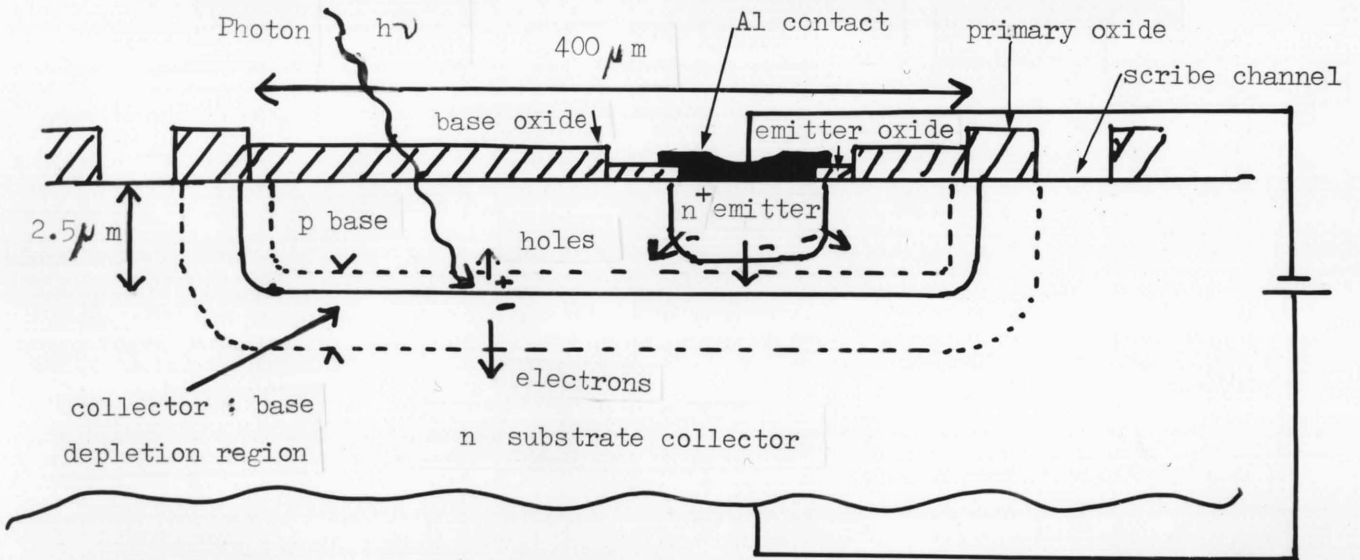
The phototransistor shown in Fig.9.1(a) is from the Plessey OPT 500 range, coded Z45. The chief application of the device is in conjunction with a gallium phosphide light emitting diode (LED) as an optical isolator.

Fig. 9.1

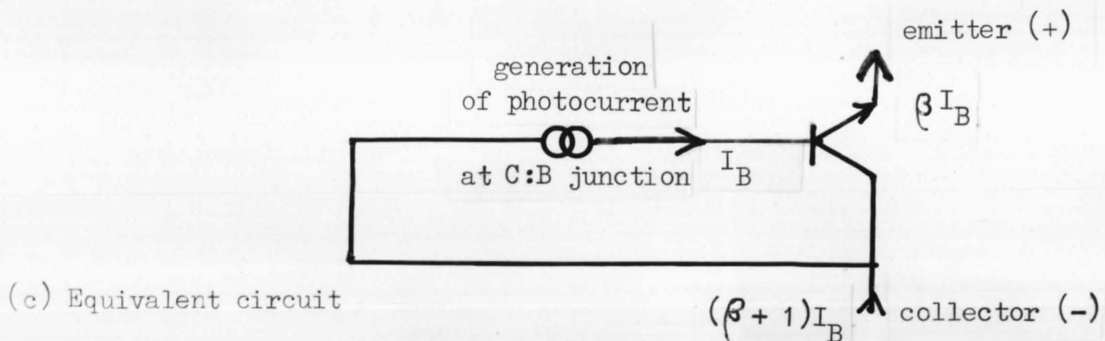
Z45 Phototransistor



(a) Optical micrograph of fully-processed chip.



(b) Section through device showing operation



(c) Equivalent circuit

## 9.2. Fabrication of phototransistor

Initial interest arose because of differences in the characteristics of two Z45 slices from different suppliers (Dow Corning and Texas Instruments) which were processed together. The substrates were  $1\frac{1}{4}$ " diameter {111}  $8\ \Omega\text{cm}$  n-type Si slices. Table 9.1. shows the processing schedule.

TABLE 9.1.  
PROCESS SCHEDULE FOR PHOTOTRANSISTOR DEVICES

PROCESS	AMBIENT	TEMPERATURE (°C)	TIME (Min)
1. Gas Polish	HCl	1200	10
2. Oxidation ( $1\frac{1}{2}\mu$ )	Steam	1100	300
3. Photo engrave base window	—	—	—
4. Boron deposition	B N	925	17
5. Boron drive-in	O <sub>2</sub> { dry wet	1100 "	90 45
6. Photo engrave emitter window	—	—	—
7. Emitter deposition and drive-in	POCl <sub>3</sub>	1050	24
8. Photoengrave emitter contact. evap. Al.	—	—	—
9. Photoengrave Al contact to emitter, float off Al	—	—	—
10. Sinter contacts	—	450	—

Modification to fabrication procedure is a fact of life in the semiconductor device industry and so there will be some differences between the processing schedule used for the two slices and current schedules.

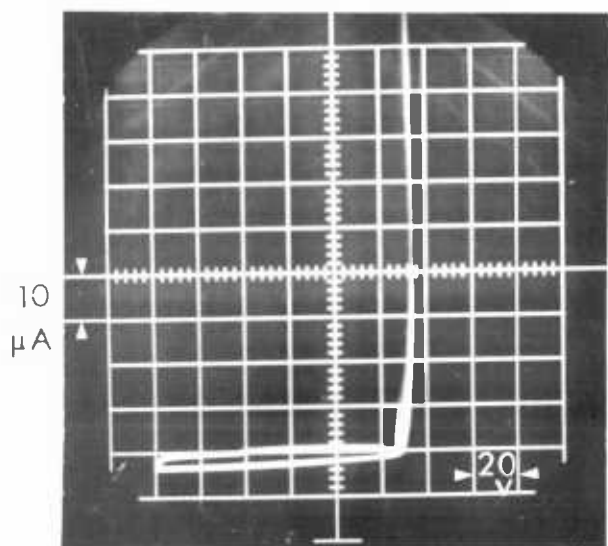
## 9.3. Examination Techniques

9.3.1. Electrical. The Z45 slices were manually probe-tested on a Textronic 723 Curve Tracer using a single probe for the emitter contact and the back of the slice as collector contact. A positive potential was applied to the collector so that the emitter/base junction was forward biased and the base/collector junction reverse biased as in the normal operating condition. The reverse voltage  $V_{CEO}$  required to give 10  $\mu\text{A}$  current

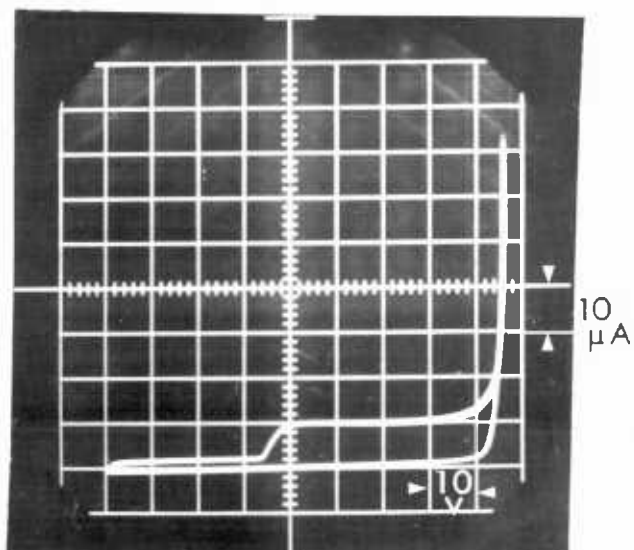
• was recorded. Specimen photographs of the curve tracer screen display were taken using a Polaroid Land camera mounted on the screen and are shown in Fig.9.2. About 1800 devices were probed on each slice; a very tedious procedure. The results on a portion of a slice are shown in Fig.9.3.

Fig. 9.2.

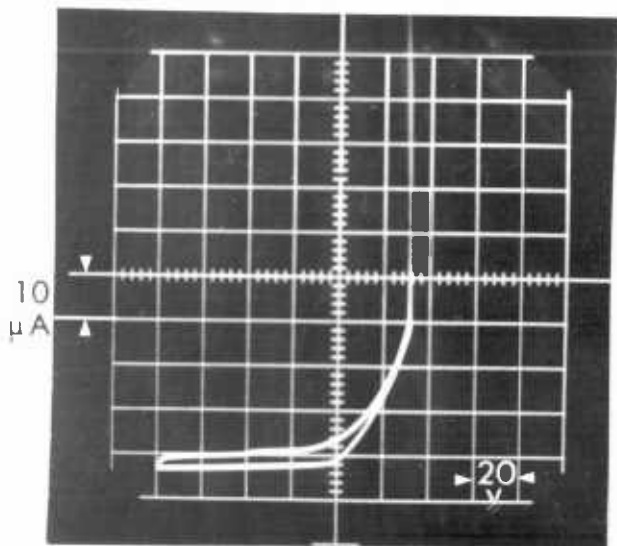
Curve traces showing various breakdown characteristics of Z45 devices



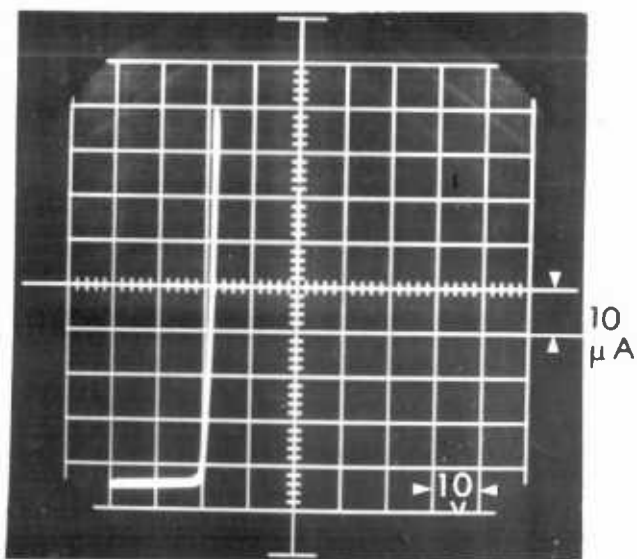
(a) Dow Corning



(b) Texas Instruments



(c) D.C. going 'soft'



(d) T.I. Catastrophic failure

FIG. 9.3. BREAKDOWN VOLTAGES  $BV_{CEO}$

Results on portion of Dow Corning Z45 slice.

COLUMN	1	2	3	4	5	6	7	8	9	10	11	12	13	14	15	16	17	18	19
ROW 10		85 <sub>1</sub> 97	94	94	97	94	45 <sub>1</sub> 55	95	98	96	93	96	102	96	96	96	98	92	97
11		94	104	83	94	98	24	96	98	92	102	98	96	95	97	94	11	96	98
12	93	94	100	85	96	94	96	95	93	101	98	96	94	98	95	96	97	96	93
13	92	96	95	25	94	96	96	93	34	96	95	96	98	94	98	96	92	94	96
14	91	35	94	93	96	95	79 <sub>1</sub> 92	96	96	96	96	96	96	94	93	93	96	97	97
15	37	36	93	96	4	91	94	95	93	96	93	96	98	12	96	93	95	*98	93
16	93	16	94	12	88 <sub>1</sub> 95	94	95	94	100	93	48	93	91	95	93	97	93	*92	95
17	91	26	93	13	92	93	94	96	13	95	93	91	97	97	97	93	94	96	94
18	86	95	95	92	84	61 <sub>1</sub> 72	97	97	93	94	91	93	96	95	93	94	*4	92	92
19	84	93	84	91	93	45	93	93	90	94	93	94	93	93	99	92	32	91	95
20	79	9	93	96	93	89	94	86	93	91	89	90	90	92	89	*2	87	90	87
21	72 <sub>1</sub> 77	87	91	90	92	93	88	90	92	88	88	88	95	90	88	*87	88	92	86
22	10	85	95	93	90	91	87	93	8	87	93	88	92	87	87	*90	8	88	92
23	59 <sub>1</sub> 26	86	93	72	87	90	89	90	95	95	90	84 <sub>1</sub> 91	79	88	88	93	88	86	95
24		89	92	93	95	88	3	2	94	90	93	93	90	87	92	91	88	93	93
25		93	48	94	88	86	95	88	88	92	93	92	88	91	2	90	94	96	97
26			94	91	94	88	88	94	88	92	93	90	94	91	89	88	96	93	88
27			92	88	88	8	8	88	87	88	92	95	89	89	19	93	94	93	94
28				92	87	89	85	90	88	92	91	90	86	90	88	96	93	92	93
29				89	88	91	86	82 <sub>1</sub> 88	88	95	92	50 <sub>1</sub> 85	92	87	87	92	92	91	92
30					85	96	97	92	92	93	11	93	97	89	90	79 <sub>1</sub> 85	93	85	94
31					87	86	85	*92	96	92	87	95	95	92	91	93	90	96	95
32						88	83	91	92	93	92	92	96	*1	94	89	93	94	95
33							85	89	87	90	93	90	95	90	92	92	92	92	92
34								90	88	89	96	91	92	96	92	95	96	96	92
35									87	9	87	61	95	94	87	94	7	93	91
36										87	89	93	92	92	90	24	92	73 <sub>1</sub> 88	93
37											90	18	93	90	28	92	97	93	94

edge of slice

\* denotes photo-engraving fault.

Note (1) where two numbers appear, 1st is  $V_{CEO}$  at 10 $\mu$ A, 2nd is  $BV_{CEO}$  at avalanche

Note (2) 2 x 2 chips framed with heavy lines were packaged for SEM.

Selected devices were packaged and retested for  $V_{CEO}$ . Their photo current response was measured on an optical bench using a 50W, 8V tungsten lamp powered by a variac. The filament was set to a colour temperature of 2870°K and a calibrated photodiode was used to obtain an irradiance of 10 mW/cm<sup>2</sup> at the device. The light current was measured at  $V_{CEO} = 5V$  and was typically about 0.3mA for 'good' devices.

9.3.2. X-ray topography (XRT). Fig.9.4(a) is a photograph of the Lang (1959) X-ray topography camera operating in the transmission mode. This is a recent photograph and considerable design modification was made to the camera after most of the topographs presented here were taken.

Figs.9.4(b) and (c) show the geometries of transmission and surface reflection arrangements respectively. In both cases a well-collimated ribbon beam of X-rays is incident on the specimen crystal C at angle  $\theta$  to the chosen set of planes (hkl) of spacing  $d_{hkl}$  to satisfy the Bragg relation

$$n \lambda = 2 d_{hkl} \sin \theta$$

where n is the order of the reflection (= 1 for XRT) and  $\lambda$  is a characteristic wavelength of the X-ray source, usually  $K\alpha_1$ . For transmission topographs in Si, Mo radiation is usually employed and for surface topographs, Cu radiation. The slits  $S_1$  and  $S_2$  mounted at the end of the collimator A are narrow enough to permit resolution of the  $\alpha_1$  and  $\alpha_2$  components of even hard (low  $\lambda$ ) radiations such as Ag  $K\alpha \sim 0.5\text{\AA}$ .

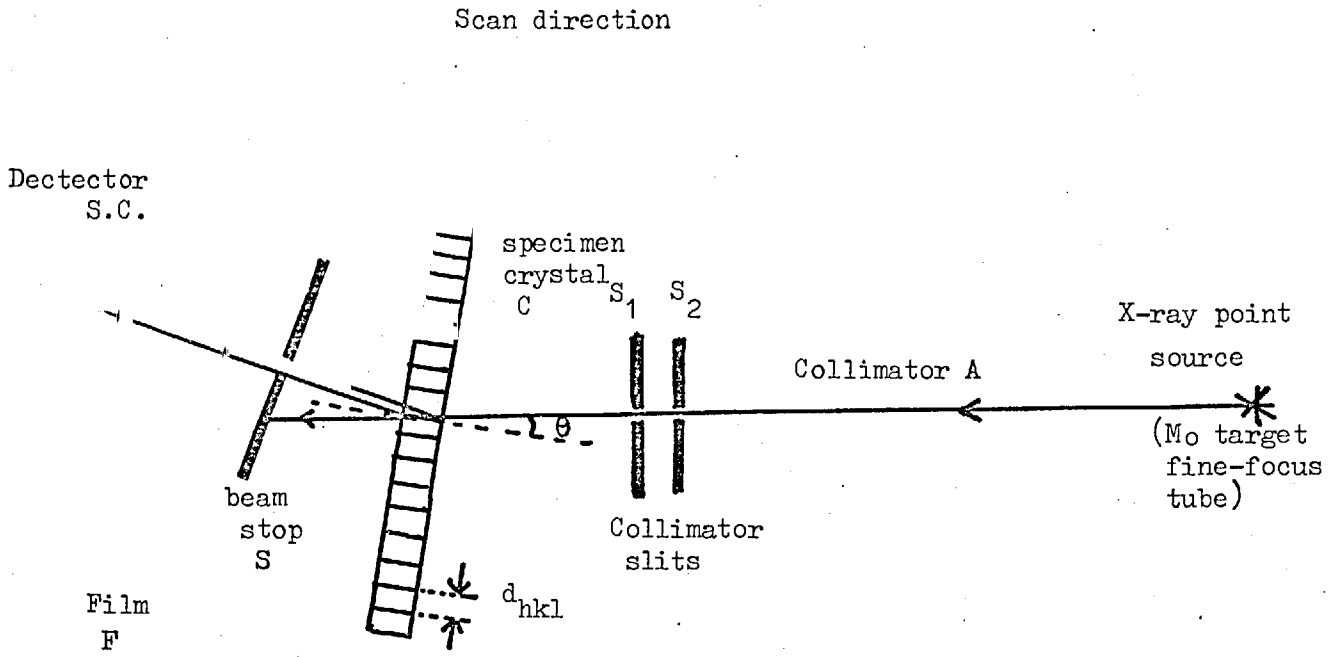
The diffracted beam forms a projected image on the film F of the portion of the crystal slice through which it has passed and so to image the whole slice, it must be scanned together with the film across the X-ray beam. Images are usually recorded for best resolution on Ilford I4 nuclear emulsions which require several hours exposures. The beam stop S is a set of slits which prevent the main beam from fogging the film and allows only the diffracted beam to reach the film. However, in the reflection mode, the geometry is usually such that slots are inessential. The present instrument's resolution in either mode is about 5 $\mu$ m and is set by the spot size of the source and the vertical divergence of the beam. The maximum magnification of the nuclear emulsion plates which can be usefully employed is about X100 and is limited by the graininess of the emulsion. The crystal is mounted on the goniometer head fixed in the centre of a table which travels on linear bearings. The drive cord D winds onto a winch W connected to a gearbox and reversible motor unit M. The length of scan is set by traverse stops  $L_1$  and  $L_2$  which operate a microswitch B.

(a) The Lang X-ray Tomography Camera

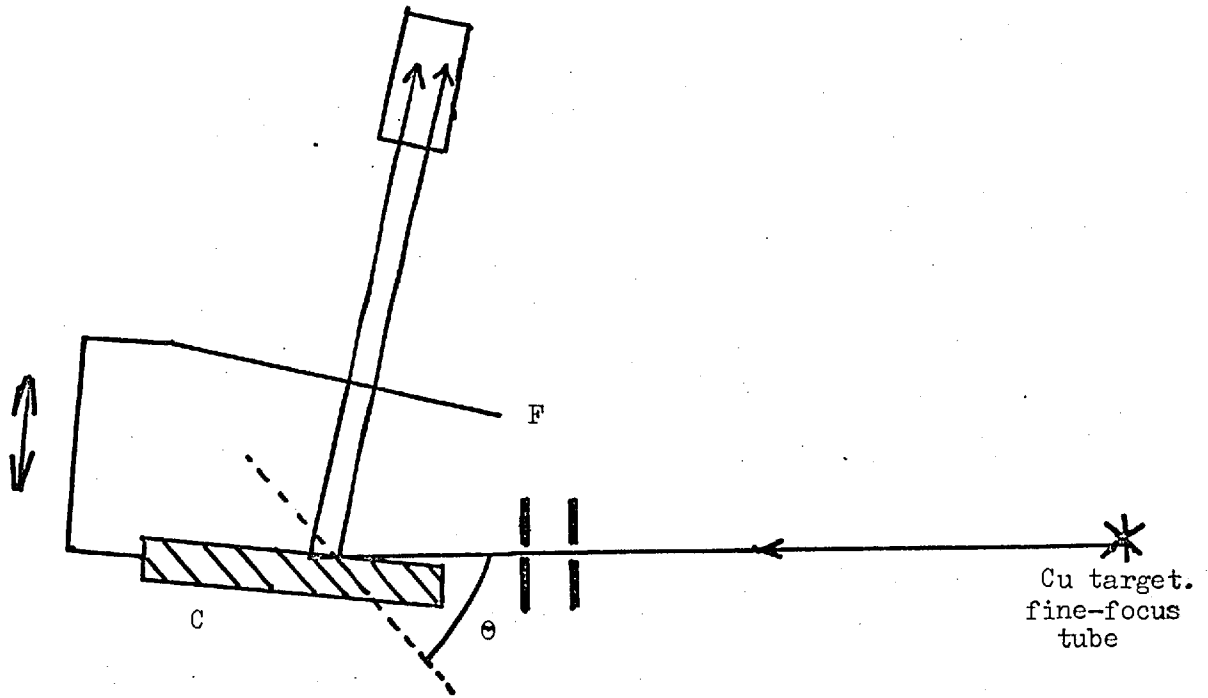


Fig. 9.4

(b) Geometry of transmission mode Lang XRT



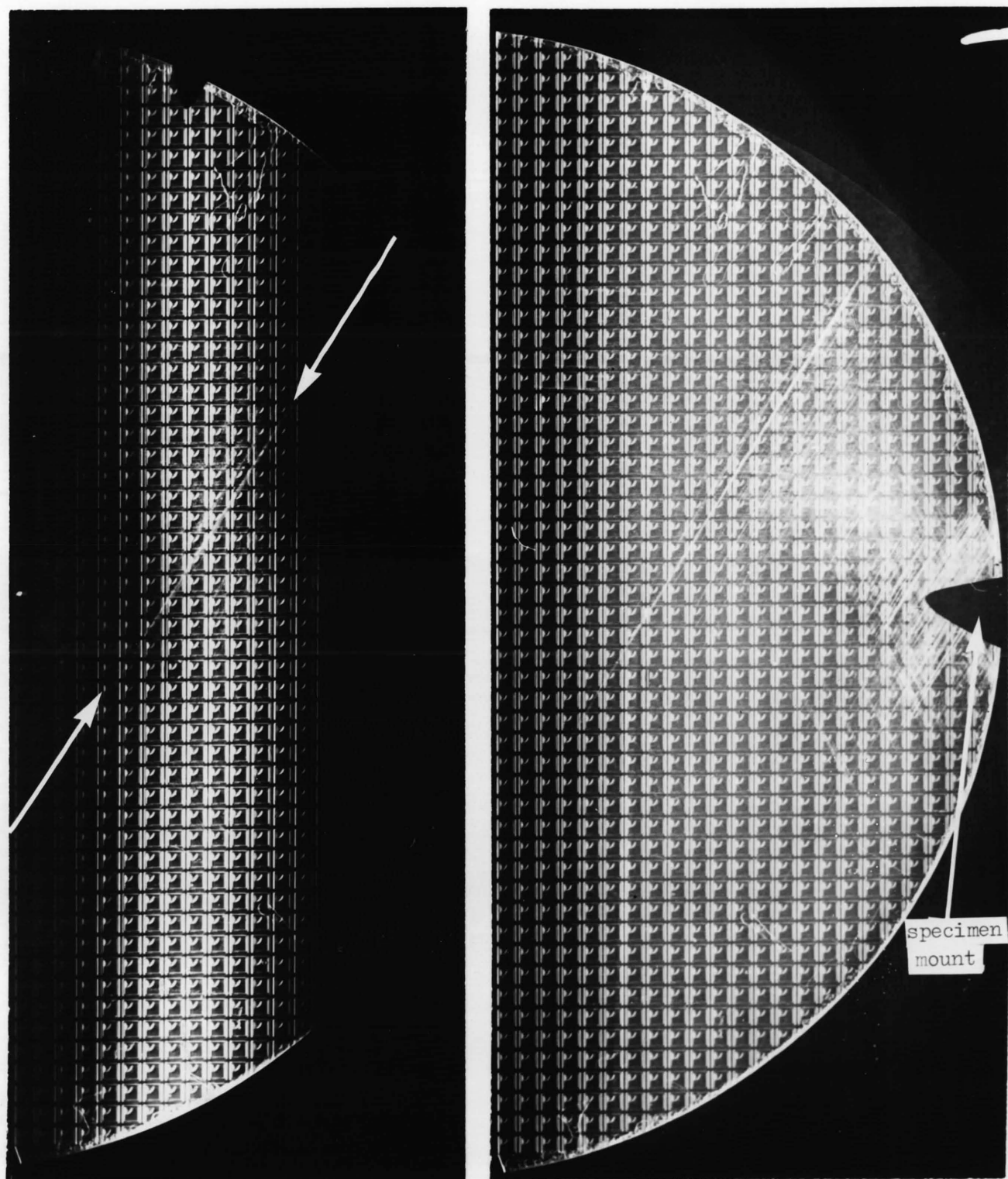
(c) Geometry of surface reflection mode Lang XRT



Details of setting up a crystal, running a topograph and the subsequent development of the nuclear emulsion plates are omitted but the technique of XRT is straightforward and has been widely used for semiconductor material evaluation, e.g. Schwuttke (1970). Defects such as dislocations and precipitates show contrast on the topographs for the same reason as in TEM, i.e. lattice strain in the crystal but X-ray diffraction contrast due to dislocations is more difficult to interpret (e.g. Authier (1966), Ishida et al (1976)) Although similar invisibility criteria apply for dislocations, in practice analysis is limited to very low densities, say  $\leq 10^3 \text{ cm}^{-2}$ . This is because the XRT image width of a dislocation is several microns compared to a few hundred angstroms for TEM images. Thus projected densities of  $> 10^4 \text{ cm}^{-2}$  dislocations tend to produce unresolvable regions of contrast. However, XRT is a non-destructive technique which is particularly useful in locating low densities of defects where TEM would be of little use on its own because of its very small sampling volume.

Due to manufacturers' routine procedure, the present phototransistor slices were cut in half along a  $\langle 110 \rangle$  cleavage direction to remove a central row of transistors for packaging and testing. Thus each half of the slice was topographed separately. The half slice with its cleavage edge vertical was mounted using a blob of wax on a Pb prong which was then clamped on the goniometer head of the Lang Camera set in the transmission mode as in Fig.9.4(a). (220) reflections from planes parallel to the cleavage direction were used with Mo  $K\alpha$  radiation. The chief problem in the resulting topographs was that strong contrast only extended across a few rows of devices, as shown in Fig.9.5(a). The devices are visible on the topograph due to the strain fields caused by the oxide windows and diffusions. There is a narrow slip band, arrowed crossing this portion of the slice, but otherwise few dislocations are observed. Dislocations scatter radiation more intensely than regions of perfect material (under conditions of kinematic contrast which obtain in this experiment). This contrast is observed when the criterion  $\mu t < 1$  applies, where  $\mu$  is the linear absorption coefficient for the crystal whose thickness is  $t$ .  $\mu$  is very low for Si using Mo  $K\alpha$  radiation, i.e.  $\sim 14 \text{ cm}^{-1}$  and so for normal slice thicknesses kinematic contrast always applies.

Fig. 9.5 Transmission XRT micrographs of Dow Corning half-slice



(a) Normal scan XRT

(b) Scanned oscillating topograph (SOT)

0.25 cm

MoK $\alpha$ , radiation

{220} reflection

**g**

The fall-off in contrast in Fig.9.5(a) is caused by elastic bending of the slice, probably due to stresses in the oxide film and diffused regions on the front of the slice. Outside the regions of contrast, the wafer has been presented to the X-ray beam at an angle greater or smaller than the Bragg angle. This problem is quite common in processed semiconductor slices and was overcome in the present case by taking several topographs, each at a slightly different  $\theta$  setting, in order to obtain strong contrast from each portion of the slice. A montage of the prints from the XRT plates was prepared. As will be seen in the next section, this was not wholly successful.

A variant technique was to oscillate the specimen table about its own axis of rotation by means of a small reversible motor and gearbox. This unit is marked 'O' in Fig. 9.4(a). Manual drive to this gearbox provides the fine  $\theta$  control in setting up the crystal for XRT. The method is known as the Scanning Oscillator Technique (SOT) and was devised by Schwuttke (1965). Fig.9.5(b) shows the result of SOT applied to the same half-slice as in Fig. 9.5(a). Although overall contrast is much improved, detailed examination of the XRT plates shows that the SOT image is blurred due to a combination of mechanical instability and overlapping of images from the  $K\alpha_1$  and  $K\alpha_2$  components of the incident X-ray beam. However, the region near the specimen mount on the wafer shows many overlapping slip bands. Since each portion of the crystal is only in the correct Bragg condition over very small angular positions during oscillation, SOT requires several times the exposure needed for conventional XRT.

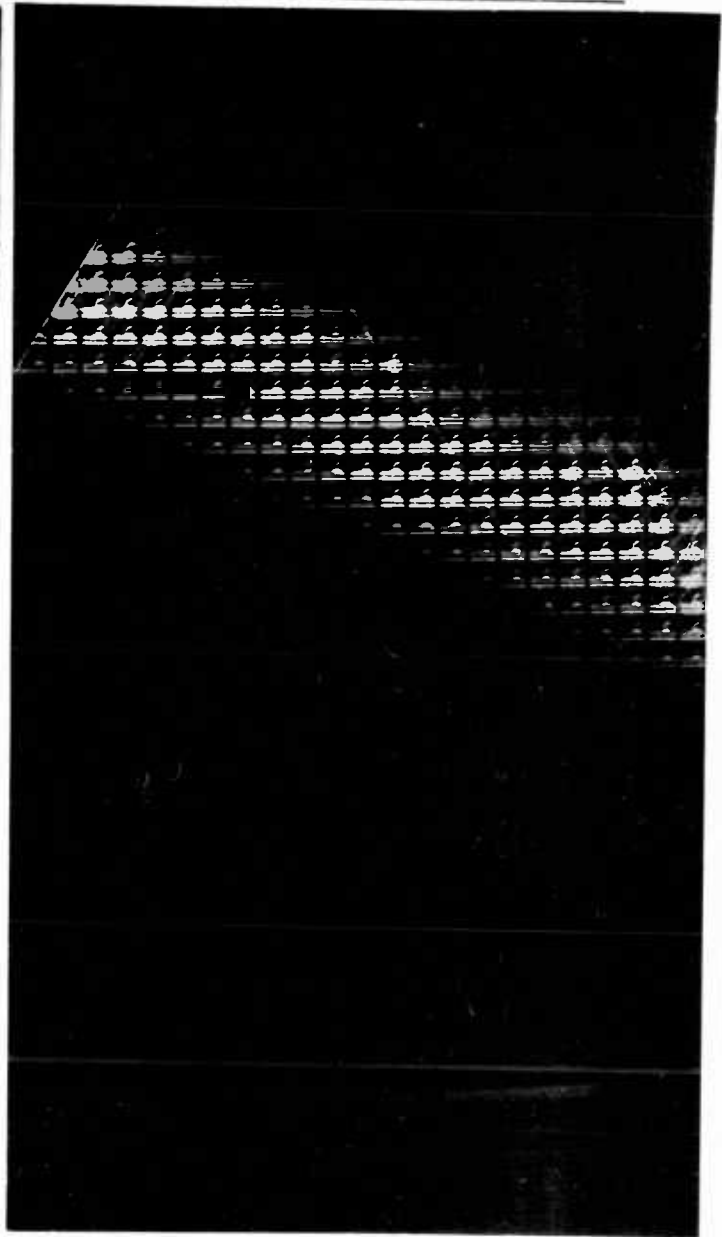
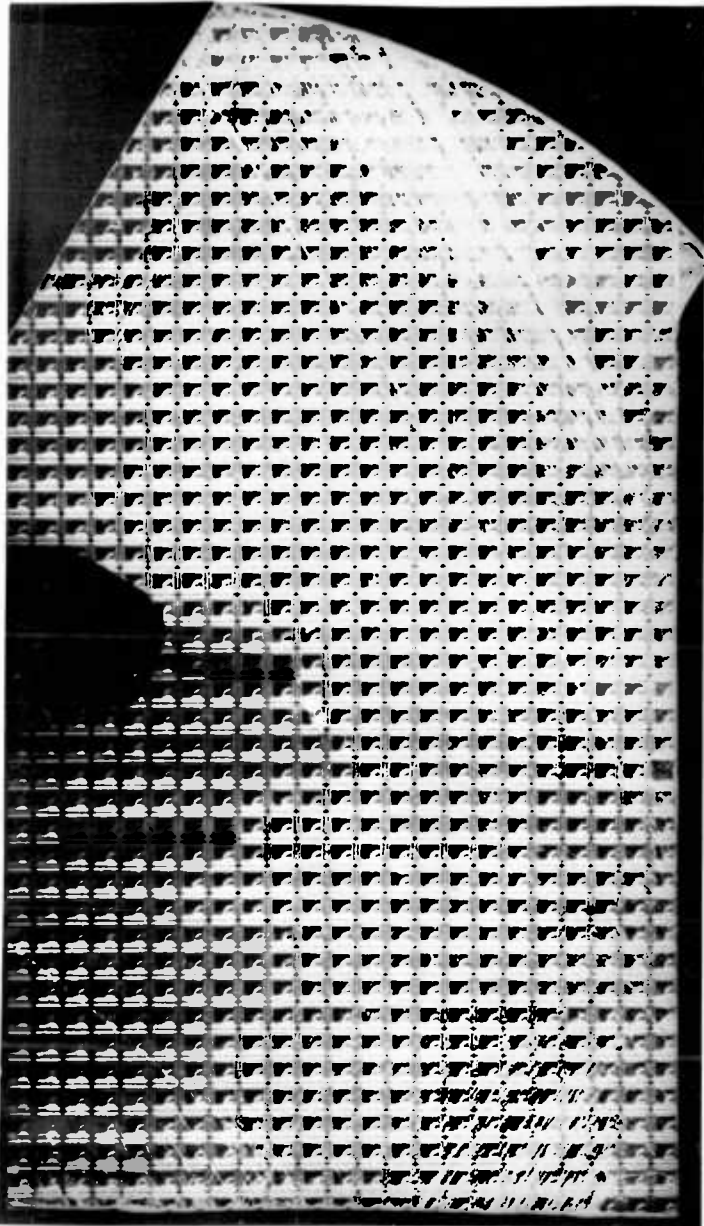
More recently there has become available commercially\* an Automatic Bragg Angle Controller (ABAC) which, as the name implies, locks the crystal to the Bragg position throughout the scan period. Such a unit has recently been brought into operation at Caswell. Bragg angle control is achieved by mounting the crystal on a transducer, marked 'T' in Fig.9.4(a) which causes a small variation  $\Delta \theta$  in  $\theta$ . A scintillation counter (marked 'S.C' in Fig. 9.4(a)) and Scalar ratemeter \*\* detects the resulting variation in intensity of the diffracted beam and feeds a servo unit which rotates the crystal to maximise the beam intensity by means of a similar motor and gearbox to those used in SOT (marked 'D' in Fig.9.4(a)).

Figs. 9.6(a) and (b) show XRT micrographs of a T.I. half-slice with and without ABAC respectively. Exposure times for each run were the

\* "The Bristol ABAC" supplied by Precision Instruments Ltd. Malvern.

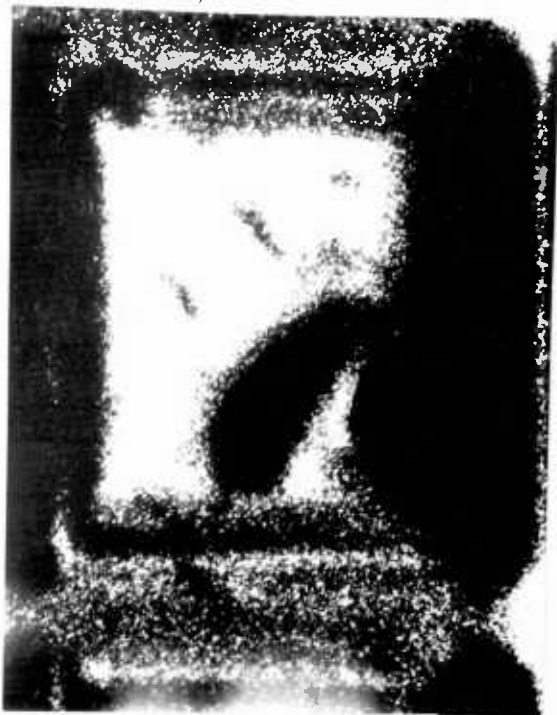
\*\* NaI thin crystal scintillation counter with integral head amplifier, SR5 scaler ratemeter both supplied by Nuclear Enterprises Ltd.

Demonstration of Automatic Bragg Angle Control (ABAC) on T I half-slice



(a) With ABAC, G5 nuclear plate

(b) without ABAC, L4 nuclear plate



(c) enlargement of chip on (a)



(d) enlargement on (b) of same chip as (c)

same. Enlargements of the same area on each topograph, Figs.9.6(c) and (d) show that resolution is unimpaired using ABAC.

9.3.3. Optical Microscopy. During probe testing, processing faults were observed using a low magnification stereo-viewer. Devices marked with an asterisk in Fig.9.3 are examples where linear features or "scratches" ran wholly or part way across the surface of the device. Fig.9.7 is an optical micrograph of a "scratch" which crosses two devices. The upper device recorded a  $BV_{CEO}$  value of 4V when tested. All devices where the "scratches" were located in the emitter region of the device showed similar catastrophic failures. The mark made by the single probe is seen on the A1 emitter contact pad of each phototransistor.

9.3.4. Scanning electron microscopy (SEM). Like the other techniques XRT and TEM used in this study, SEM has been widely applied to semiconductor device manufacture. Thornton et al (1969) have considered in detail the application of SEM to device failure analysis. SEM is as well established now as TEM was a decade ago and several reference texts on the technique are available, e.g. Thornton (1968), Holt et al (1974).

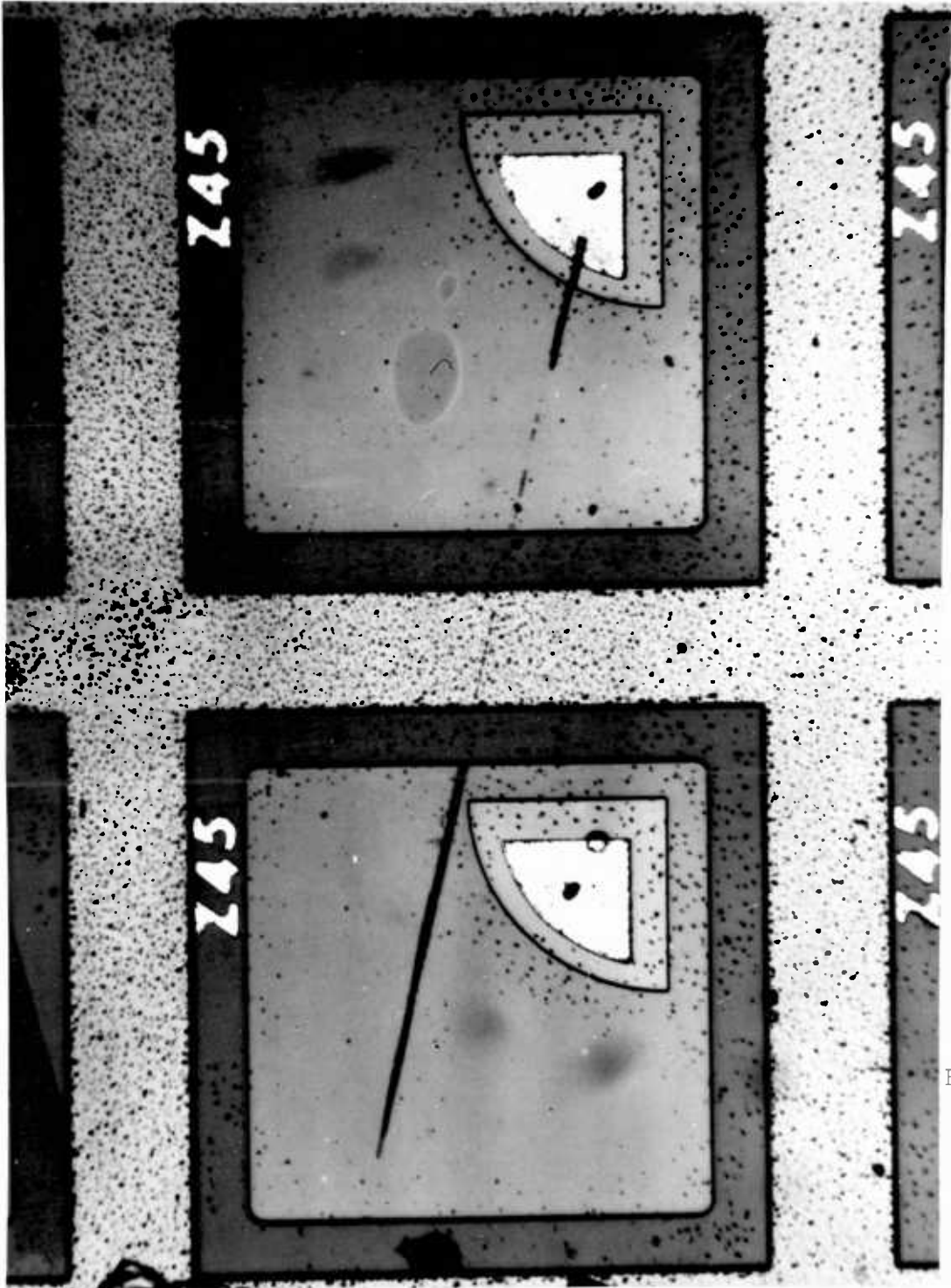
Of the several available modes of operation of the SEM, the conduction mode employing the barrier electron voltaic effect (BEVE) currents as video signal was extensively used in the present study. The barrier here was the collector : base pn junction of the phototransistor which covers the whole active area of the device. Contrast is observed from defects in or near the junction which are electrically active and information relevant to the role of the defect in device behaviour can be obtained.

Selected devices were wired to the specimen current amplifier (SCA) of a Cambridge Instruments Mk.IIA SEM located in the Metallurgy Dept. at Imperial College. The BEVE is analogous to the barrier photovoltaic effect and it produces a signal due to the separation of electron-hole pairs by the built-in field such as a pn junction. The magnitude of the resultant "charge collection current" is dependent on the charge collection efficiency  $\eta_{cc}$  of the barrier. The electron : hole pairs generated by electron bombardment in the region of the junction are separated by the depletion region : holes to the p-type material and electrons to the n-type material. Holt (1974) has shown that the short circuit current  $I_{SC}$  used as video signal is given by

$$I_{SC} = \eta_{cc} G I_b/q$$

Fig. 9.7

Optical Micrograph of "scratch" on probe-tested Dow Corning Z45 Slice



where  $G$  is the generation factor, i.e. the number of hole-electron pairs generated per incident electron,  $I_b$  is the electron beam current and  $q$  is the charge on an electron. Contrast arises at defects due to local variation in  $\eta_{cc}$ . Mid-gap energy bands can be caused by dislocations, as discussed in Section 8.1.1, and these are expected to act as recombination : generation centres to reduce  $\eta_{cc}$  and give dark spots on the BEVE micrographs. However, most of the present work used a.c. coupling to the SCA and the resulting differentiated signal produces black/white images. Fig.9.8. shows the circuit used which is very similar to that used by Ravi and co-workers (1973) for the examination of diodes. However, the zero bias condition used by them produced no output signal from the phototransistor here because the emitter : base junction must be forward biased for the device to function, as explained in Section 9.1. All BEVE mode micrographs were taken with at least  $1\frac{1}{2}$ V applied between the emitter and collector.

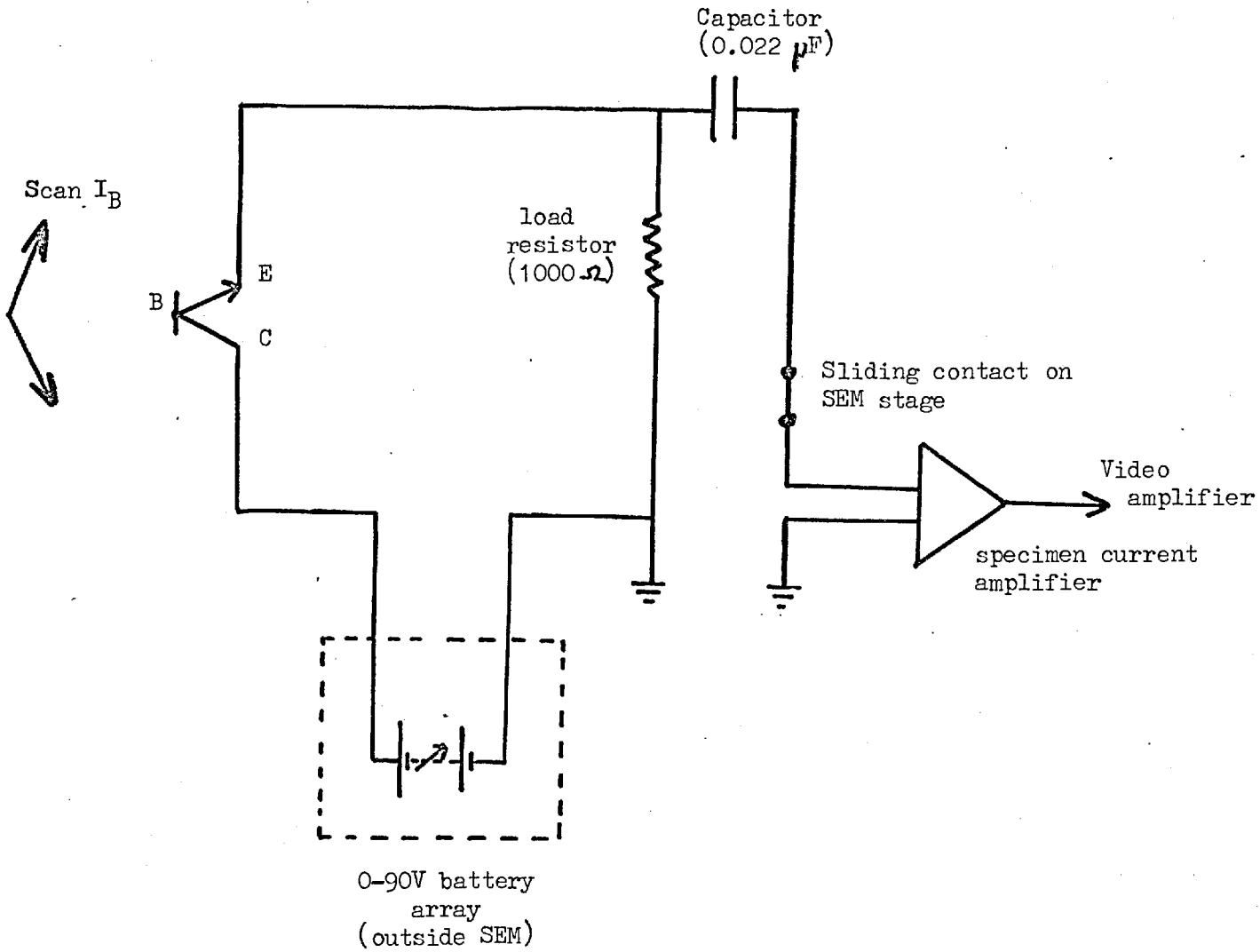
The BEVE current was displayed as video signal on a CRT screen scanned in synchronism with the scanning of the SEM electron beam over the surface of the phototransistor. In addition the signal was recorded graphically as a Y-modulation line scan trace. This was done for a line scan passing through the electrically active defects.

9.3.5. Transmission Electron Microscopy (TEM). The techniques of thin foil preparation of Si and examination by TEM have been described in detail in Part I of this thesis. Only slight modification was needed to prepare specimens from device slices. Oxide and metallisation were removed by soaking the specimen chips in hydrofluoric acid prior to jet thinning. This was done partly to improve visibility in TEM but also to obtain good taper sections during jet thinning. Another difficulty not encountered in Part I was that specimen chips were only 1 mm across and were difficult to handle and to perforate in the desired region. This was made easier by using a rotating specimen stud. Perforation occurred about the centre of rotation and the specimen chip was centred by carefully sliding the chip in the mounting grease. Specimens were glued to slotted copper grids for mounting in the TEM tilt cartridge.

Problems of identifying areas under observation were overcome using very low magnifications (a few hundred times) in the electron microscope. This was achieved by using only the condenser and objective lenses.

FIG. 9.8

Circuit diagram showing a.c. coupling on phototransistor to specimen current amplifier



(following Ravi et al 1973)

Areas of Si under metallised regions were pitted due to alloying with Al. Edges of diffused regions and scribing channels were identified by thickness variations.

#### 9.4. Examination Procedure

Each of the 4 half-slices was probe tested for  $BV_{CEO}$  in turn and specimen curve traces of the collector/emitter breakdown recorded. Several X-ray topographs of each slice were taken as detailed in Section 9.3.2. One half of each slice was scribed and diced into squares each containing 4 devices, mounting the slice on PTFE tape to prevent scrambling. Selected devices for SEM observation were mounted on an 8 lead T05 header with a common collector post and the 4 emitters wired to separate posts. The chips were chosen to represent each electrical and structural type encountered on probing and by XRT respectively, i.e. 'hard', 'soft' and catastrophic breakdowns occurring in slipped and non slipped areas and scratched devices. Some examples of selected devices were shown in Fig.9.3. Enlargements were made of the XRT plates corresponding to each dice selected for SEM using a Reichert optical microscope in transmission mode. Polaroid prints were used for convenience. After preliminary SEM observations on some of the devices had been made, the light currents of packaged devices were measured.

The blank end-strips of the slices were put to good use. These regions had been given a blanket base diffusion, followed by the emitter diffusion and were monitored by 4 point probes for sheet resistivity during fabrication as a process control check. A portion of each end-strip was cut up for TEM specimens and the remaining portions were bevelled and stained to check the diffusion depth.

## CHAPTER 10. RESULTS

### 10.1. Electrical failure correlation with slip

$BV_{CEO}$  data from a portion of a device slice was shown in Fig.9.3. The overall trend of results is best seen from yield maps of the slices, Figs. 10.1(a) and 10.2(a) where each dot represents a failed device. The criterion for passing a device was that  $V_{CEO}$  at 10 uA should exceed 90V for the Dow Corning (D.C.) slice and 80V for the Texas Instruments (T.I) slice. The difference between the criteria was due to the overall lower voltage breakdowns on the latter slice.

The yield maps have been printed on film so that the correlation with the dislocation structure of the device slices can be judged. Figs. 10.1(b) and 10.2(b) are montages of the XRT micrographs and clearly show the presence of slip bands along  $\langle 110 \rangle$  directions, i.e. regions of high dislocation density. Visual correlation between slip and device failure is very strong for the T.I. slice but it can be shown that there is a statistically significant correlation for both slices by applying the  $\chi^2$  test (e.g. Moroney (1951)). First, a contingency table is constructed for each slice, Tables 10.1(a) and 10.2(a) by counting the number of 'bad' devices in heavily slipped regions. These slipped regions are contained within the white lines drawn in Figs. 10.1(b) and 10.2(b). The other boxes in the tables, e.g. the number of 'good' devices in slipped regions, were deduced from the population of 'bad' devices and slipped devices and the total population of the slice.

TABLE 10.1

#### Dow Corning Slice

		(a) experimental distribution (n)				(b) Theoretical distribution (v)			
		good	bad			good	bad		
slip	slip	210	140	350	slip	262	88	350	
	non-slip	1169	320	1189		non-slip	1117	372	1489
		1379	460	1839			1379	460	1839

Devices which had failed because of obvious photoengraving errors or which had portions missing at the edge of the slice were not included in the analysis. From the population of good and bad, slipped and non-slipped devices, a theoretical distribution can be calculated based on random probability of finding a 'bad' device in a slipped region, etc, Table 10.1(b) and 10.2(b).

TABLE 10.2  
Texas Instruments Slice

	(a) <u>experimental distribution (n)</u>			(b) <u>Theoretical distribution (v)</u>		
	good	bad		good	bad	
slip	362	366	728	515	213	728
non-slip	941	172	1113	788	325	1113
	1303	538	1841	1303	538	1841

For example, in Table 10.1(b), the probability of finding a device in a slipped region is 350/1839 and the probability of finding a 'bad' device is 460/1839. Thus the probability of finding a 'bad' device in a slipped region is

$$\frac{350}{1839} \times \frac{460}{1839}$$

and the theoretical expected number (v) of these devices is

$$\frac{350}{1839} \times \frac{460}{1839} \times 1839 = 88$$

This number is far fewer than the experimental number  $n = 140$  but we have to decide whether the difference is significant. The next step is to tabulate  $n_s$  and  $v_s$  values for each box as in Tables 10.3 and 10.4.

TABLE 10.3  
D.C. Slice (data from Table 10.1)

$n_s$	$v_s$	$v_s - n_s$	$\frac{(v_s - n_s)^2}{v_s}$
210	262	52	10.4
140	88	-52	31
1169	1117	-52	2.3
320	372	52	7.3
			$\chi^2 = \sum \frac{(v_s - n_s)^2}{v_s} = 49.$

TABLE 10.4.  
T.I. Slice (data from Table 10.2)

$n_s$	$v_s$	$v_s - n_s$	$\frac{(v_s - n_s)^2}{v_s}$
362	515	153	45
366	213	-153	110
941	788	-153	30
172	325	153	72
			$\chi^2 = \sum \frac{(v_s - n_s)^2}{v_s} = 257$

FIG. 10.1(a)

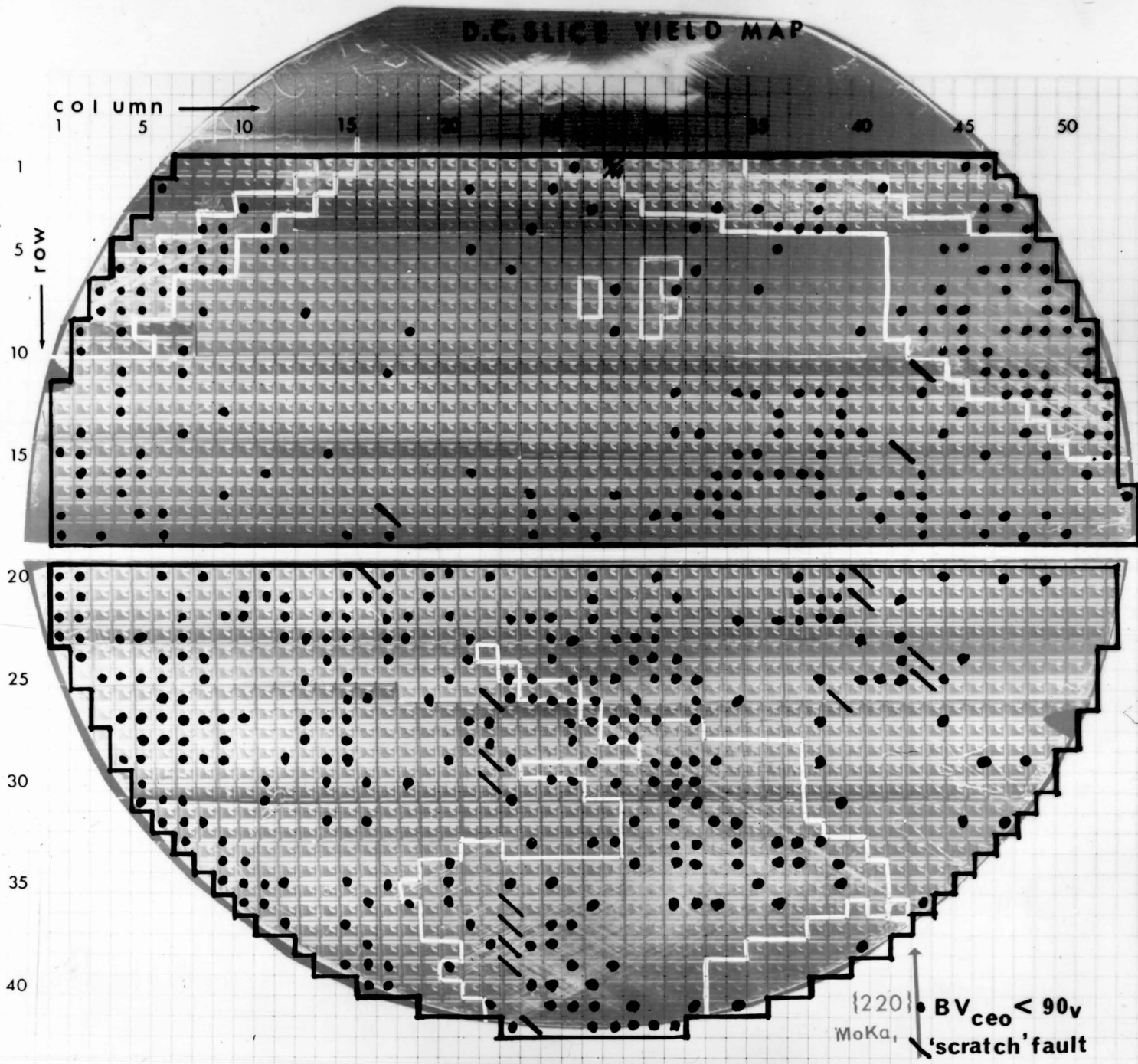


FIG. 10.1(b)

Dow Corning Slice XRT MONTAGE

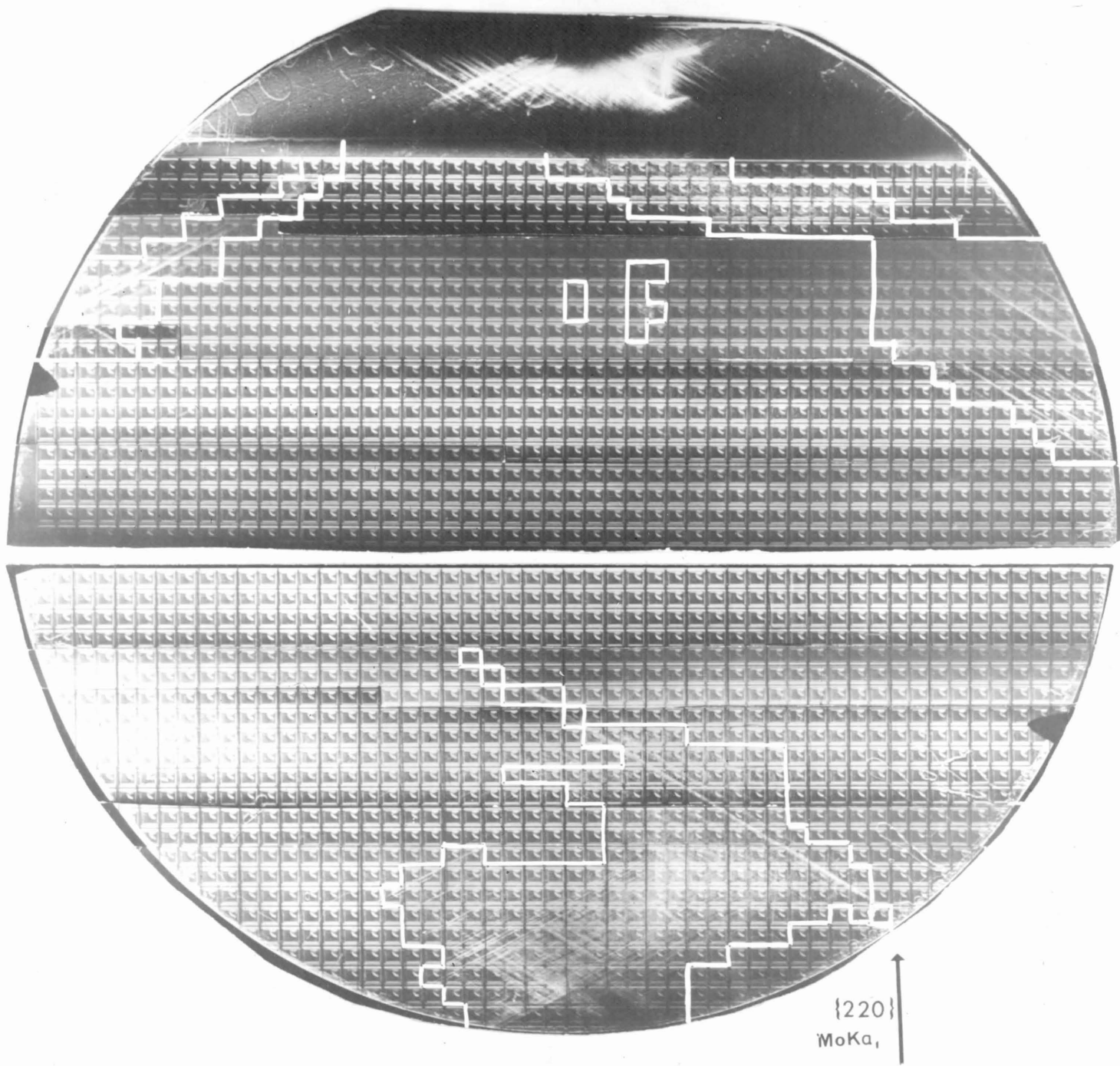


FIG. 10.1(b)

**Dow Corning Slice XRT MONTAGE**

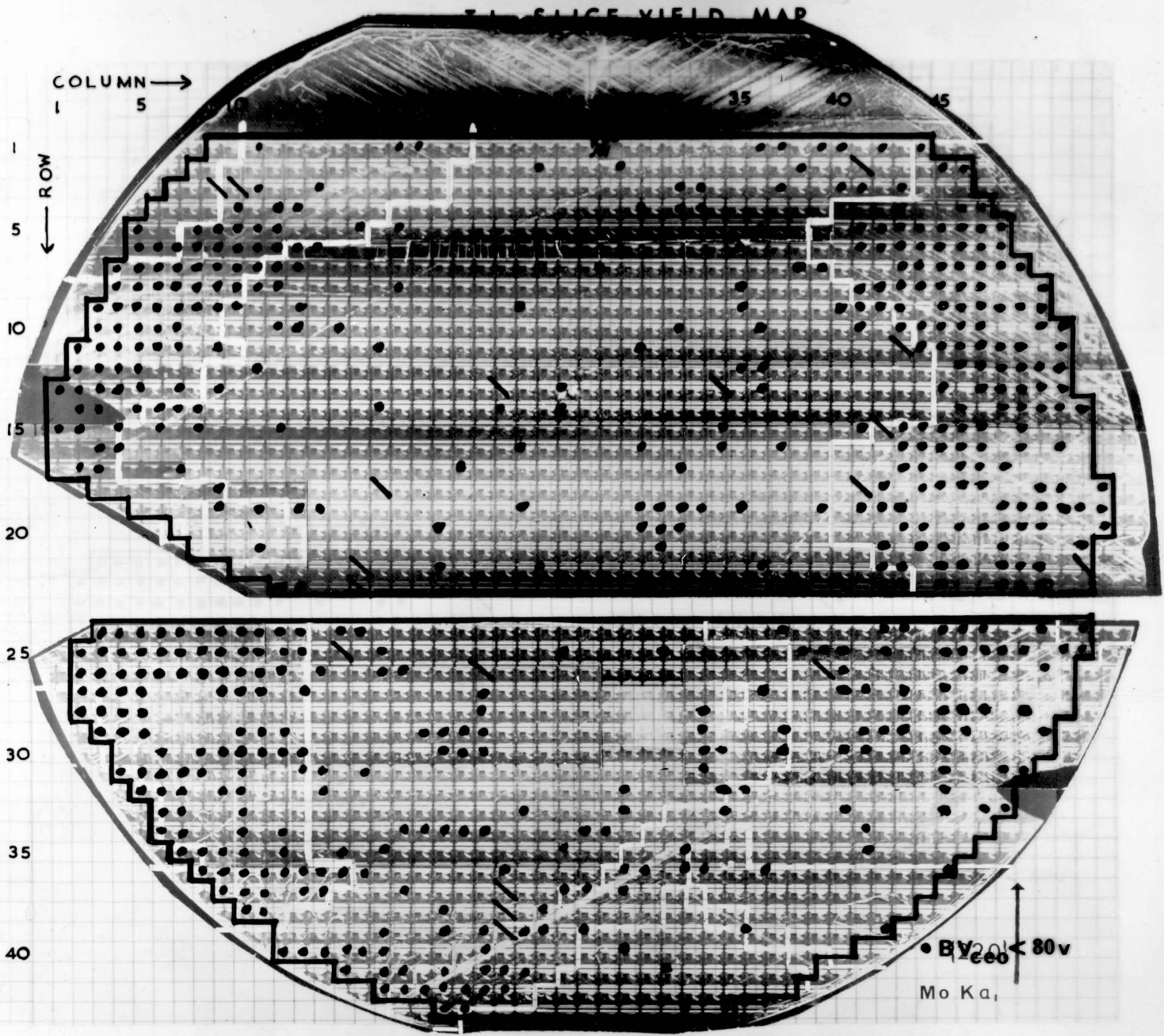


FIG. 10.2(b)

T.I. Slice XRT MONTAGE

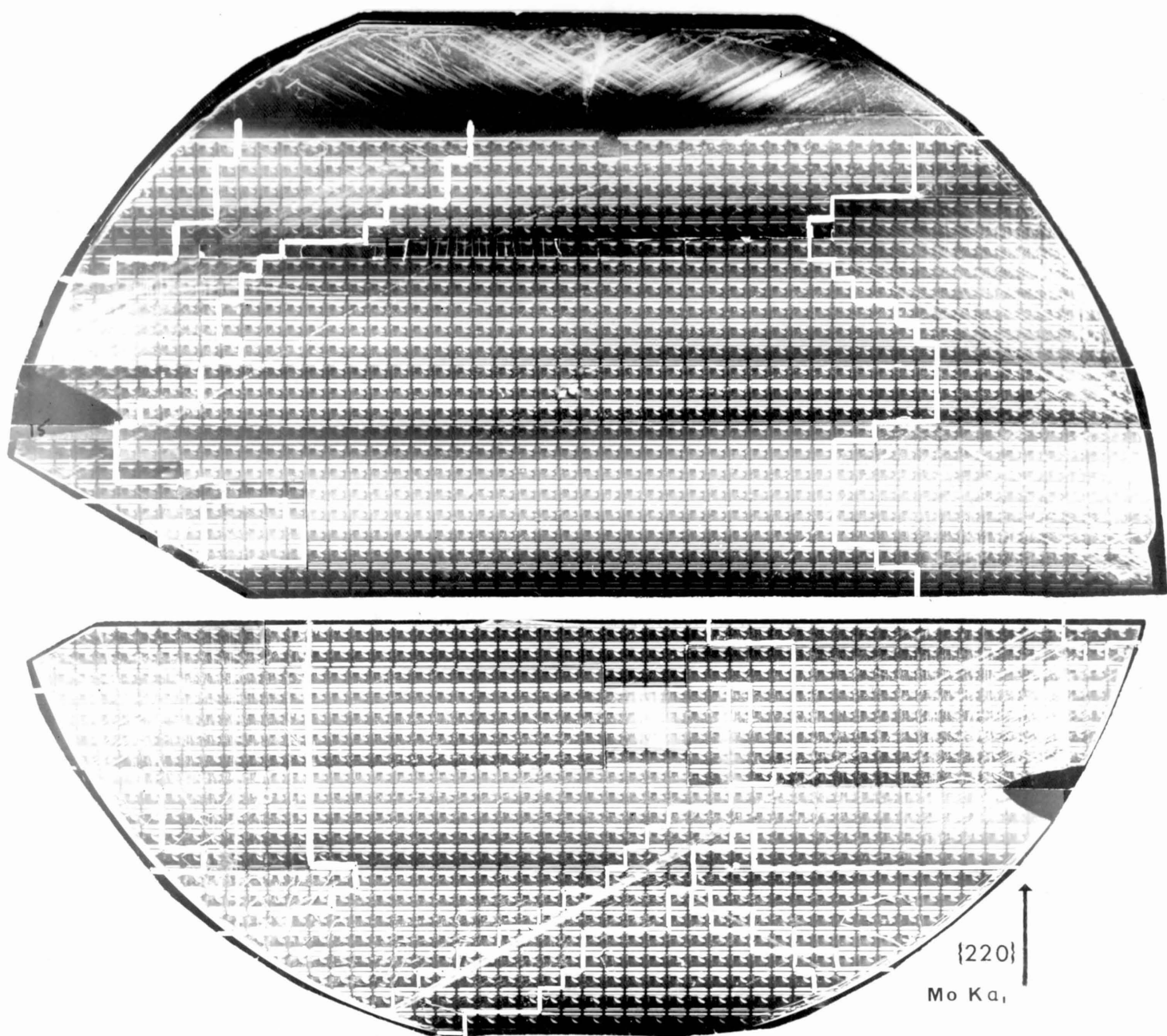


FIG. 10.2(b)

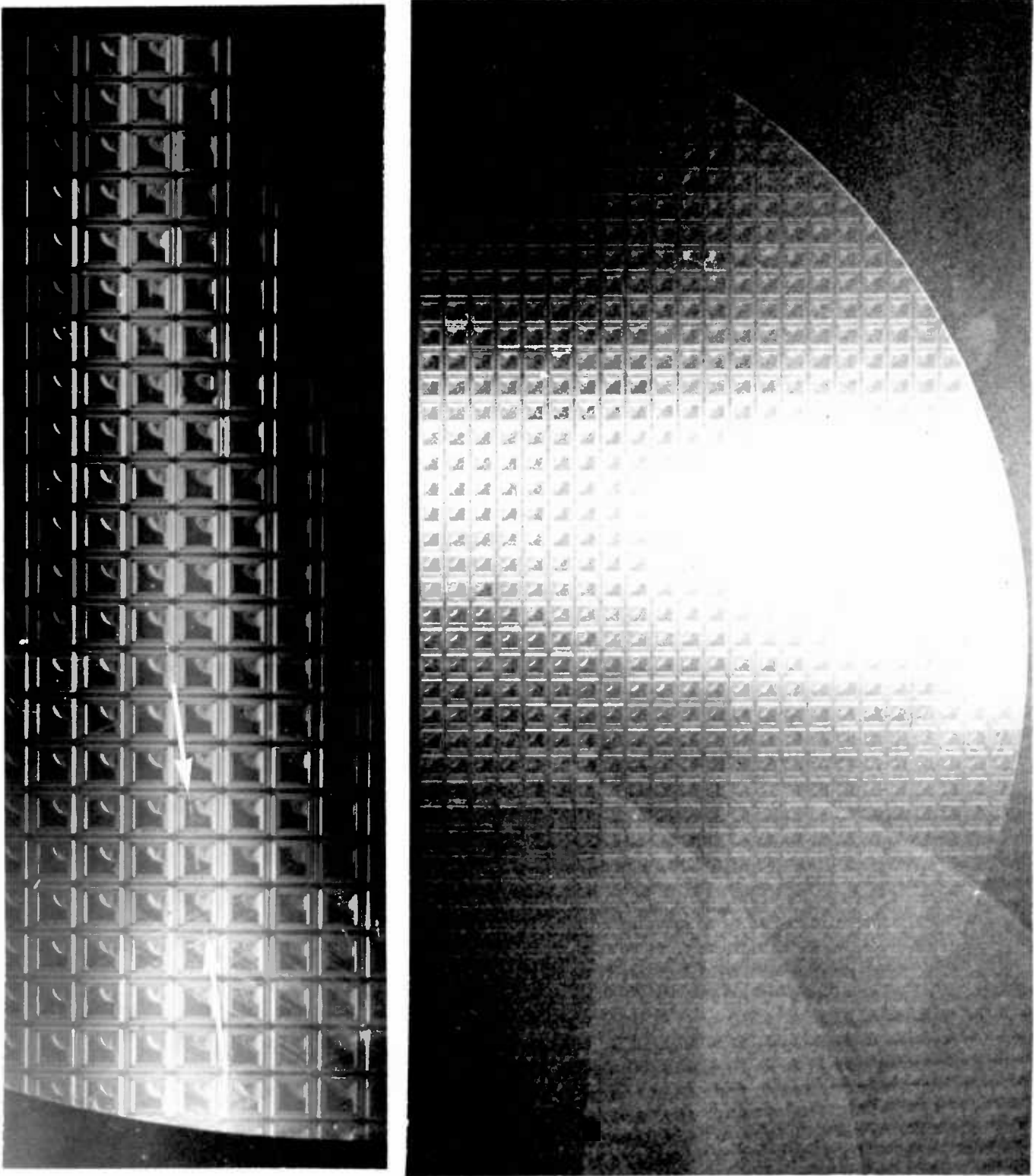
T.I. Slice XRT MONTAGE

These high values of  $\chi^2$  mean that there is little probability that the failed devices are distributed randomly across the slice. A  $\chi^2$  value of only 15 corresponds to a probability of 0.01% that the distribution is random. By inspecting Tables 10.1 and 10.2 we can say that there is a strong correlation for each slice between the slipped regions and soft phototransistors. However, two points should be noted:

- 1) Detailed comparison of the yield maps and X-ray topographs shows that the correlation is far from 1 to 1, i.e. many good devices are located in heavily slipped areas and conversely failed devices are by no means confined to these areas.
- 2) Designating the slipped areas in Figs.10.1(b) and 10.2(b) is somewhat arbitrary. In spite of several topographs being taken of each half-slice, there are several regions of the montage, e.g. D.C. Slice rows 4-6, Fig.10.1(b), where contrast is poor due to insufficient overlap between "peaked" areas of adjacent topographs. As shown in Fig.9.5(b) SOT gives better overall contrast but because of the resolution and very long exposure time the technique was not applied to the other half-slices. Also the topographs were taken in transmission mode and dislocations lying in the whole bulk of the slice are imaged. Although projected dislocation densities of  $\sim 10^4 \text{ cm}^{-2}$  give the appearance of heavily slipped regions, the actual number of dislocations lying within the top few microns of the slice, i.e. in the active regions of the devices, may be very low. Surface XRT using the geometry shown in Fig.9.4(c) is useful since the X-ray beam forms an image of only a few microns depth of crystal when a suitable set of planes and radiation are used. Fig.10.3(a) shows an XRT micrograph of the bottom half of the D.C. slice taken using  $\text{Cu K}\alpha_1$  radiation and  $\{511\}$  planes. For this topograph the crystal and photographic plate were not scanned across the beam. Because of the low angle of incidence to the slice surface ( $\sim 9^\circ$ ) a large area of the slice was exposed. Beam penetration for kinematic contrast is limited to about  $10 \mu\text{m}$  for this case. Individual dislocations can now be resolved in regions of heavy slip near the circular perimeter of the slice where resolution was impossible in transmission, Fig.10.1(b). The corresponding scanned topograph using these conditions produced overlapped images due to strong reflections yet still did not give complete coverage due to slice bowing, Fig.10.3(b). Further attempts were not made to obtain surface X-ray topographs.

Fig. 10.3

Surface XRT Micrographs of DC half slice.



(a) Stationary XRT, showing individual dislocations and 'scratch' features.

(b) Scanned XRT of slice shown in (a), showing multiple reflections.

Cu  $K\alpha_1$  radiation  $\{511\}$  reflection

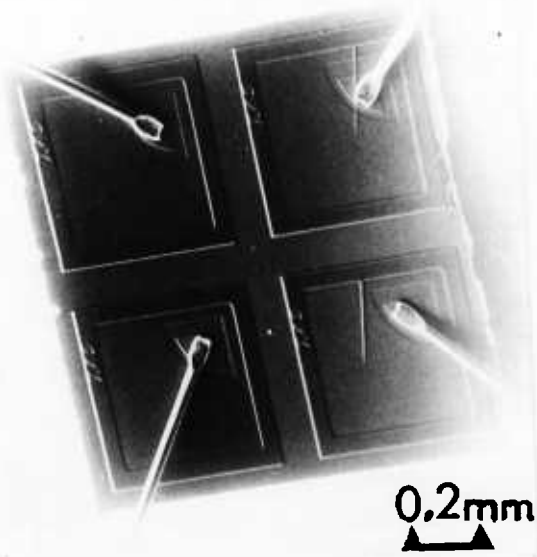
Also visible in Fig.10.3(a) are examples of "scratches" (arrowed) which were similar to those shown optically in Fig.9.7. These features are visible in XRT because strain is produced in the underlying Si crystal. The explanation of the scratches is given in the following section.

## 10.2. SEM Observations

10.2.1. Photoengraving faults. Examination of a chip containing scratch features similar to those shown in Fig.9.7 showed that the features were actually bars of oxide left inside the base window regions cut after the initial oxidation of the slice, Fig.10.4. Device C16R21 contains an oxide bar wholly within the base region, Fig.10.4(d) and has a relatively high breakdown voltage but in device C16R20, the bar crosses the emitter region and the device registered almost a dead short. Figs. 10.4(e,f,g) are SEM micrographs using the BEVE mode which show that the device is breaking down along the bar. It is evident that the oxide bars are due to photoengraving faults and their origin and effect on device performance will be discussed in Section 11.3.

Fig.10.4

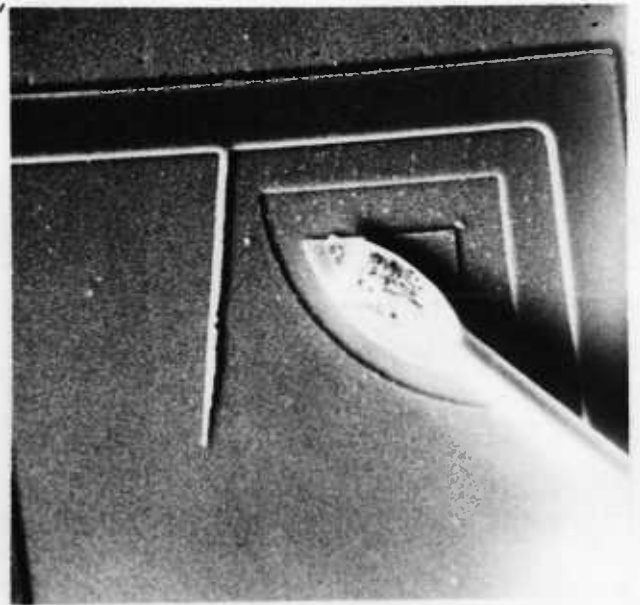
SEM Micrographs of 'scratch' features on DC slice



	C15	C16
R 20	89	2
R 21	88	87

(a) Secondary electron emissive mode micrograph showing chip and emitter bonding wires.

(b)  $V_{CEO}$  values of devices on chip



(c) enlargement of C16 R20 device

(d) enlargement of C16 R21 device



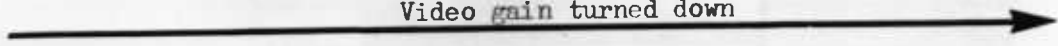
(e)

(f)

(g)

area (c), BEVE mode d.c. coupled to SCA showing breakdown at 'scratch'

Video gain turned down

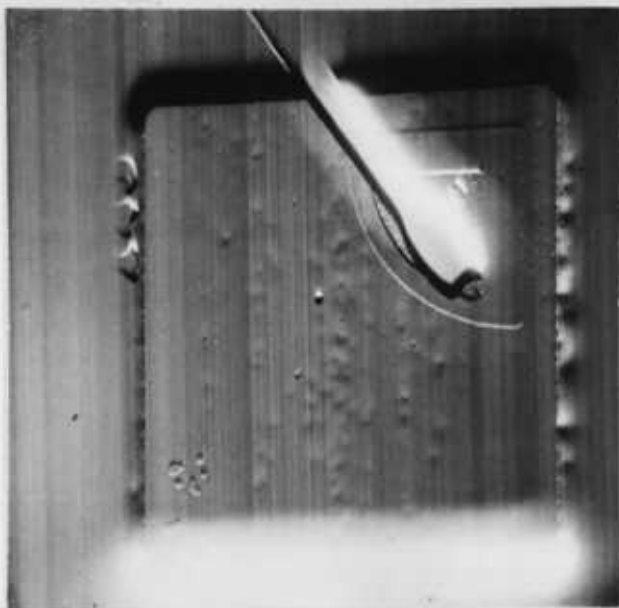


10.2.2. Dislocation imaging using the BEVE mode. The most important single result of Part II of this thesis was observing spots of contrast in the base regions of devices using the BEVE mode in the SEM which coincided with positions at which dislocations emerged at the device surface. The dislocations were mapped using XRT and contrast due to dislocations was first noted in devices fabricated in heavily slipped regions. Figs. 10.5(a) and (b) show the secondary electron and conductive mode SEM micrographs respectively of a T.I. device crossed from top to bottom by a heavy slip band as shown in X-ray topograph, Fig. 10.5(c). The central band of black/white spots in Fig.10.5(b) does not correspond to any surface features seen in Fig.10.5(a), but does lie in the slip band shown in Fig.10.5(c). A patch of debris in the bottom-left corner of the device shows contrast in both Figs.10.5(a) and (b). Particles are visible in BEVE mode because they absorb part of the primary electron beam and so locally reduce the number of carrier pairs generated. Similarly the top and bottom edges of the base show strong contrast due to sudden changes in current delivered to the SCA when the scanning beam moved into and out of the base junction area. A.C coupling enhances the effect because the signal is differentiated.

The BEVE mode was able to resolve individual dislocation images in devices fabricated in regions so heavily slipped that the window contrast from the devices was reduced and dislocation densities were too high to measure from the XRT micrographs. Fig.10.6(a) shows a topograph of a device containing an unresolvable mass of dislocations. The corresponding BEVE micrograph, Fig.10.6(b) shows an average dislocation density of  $6 \times 10^4 \text{ cm}^{-2}$ . From the size of the dislocation image point-to-point resolution is limited to about  $20 \mu\text{m}$  so that the maximum density of dislocations which could be resolved by the technique is  $\sim 2.5 \times 10^5 \text{ cm}^{-2}$ . We note that with a high dislocation density, the device shown in Fig.10.6 still recorded a breakdown at 97V. Figs.10.5(b) and 10.6(b) clearly show that dislocation contrast in the BEVE mode is confined to the active area of the device since a pn junction is necessary to separate the carriers generated by the scanning primary electron beam. This eliminates any possibility of explaining the effect by any non-barrier mechanism.

Because of the size of the BEVE mode "spots" and the large image width of dislocations in XRT, convincing correlations were only possible in regions of low dislocation density. A device containing a few dislocations distributed in a narrow slip band is shown in Fig.10.7(a) In the corresponding BEVE micrograph, Fig.10.7(b), some but not all of

First observation of SEM contrast at dislocations in photo transistor



(a) Secondary emissive mode of T I device C10 R28,  $V_{CEO} = 80V$  showing surface debris

(b) Conductive mode using BEVE  $V_{app.} = 1.5V$

(c) XRT of same device taken from topograph of half-slice.

$MoK\alpha_1$ , {220} reflection

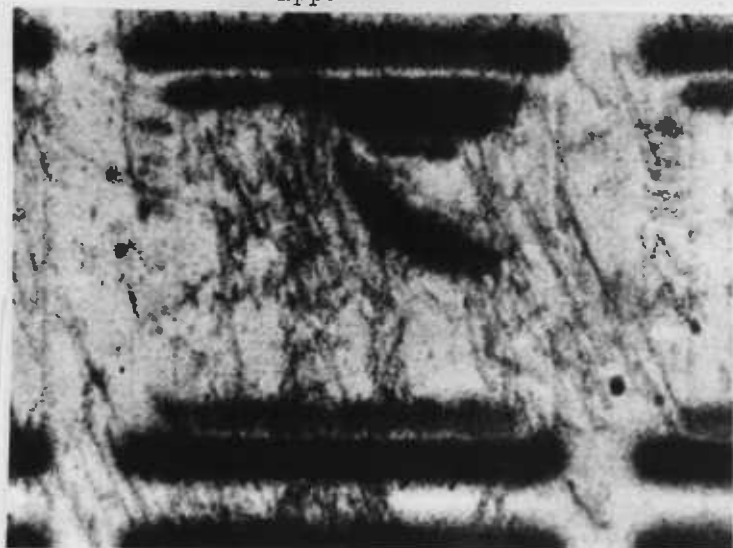
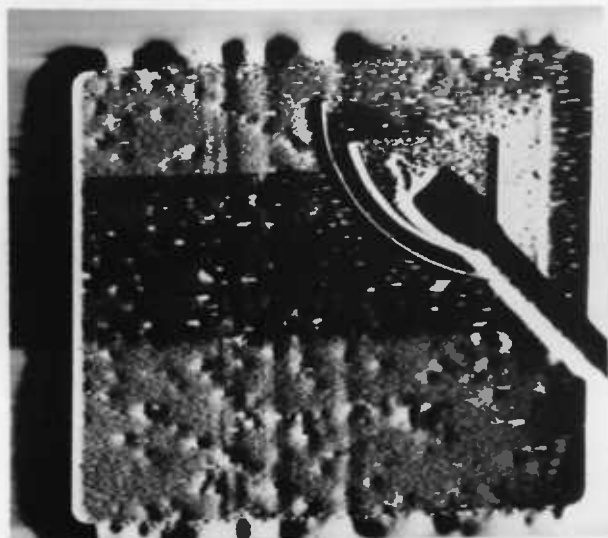
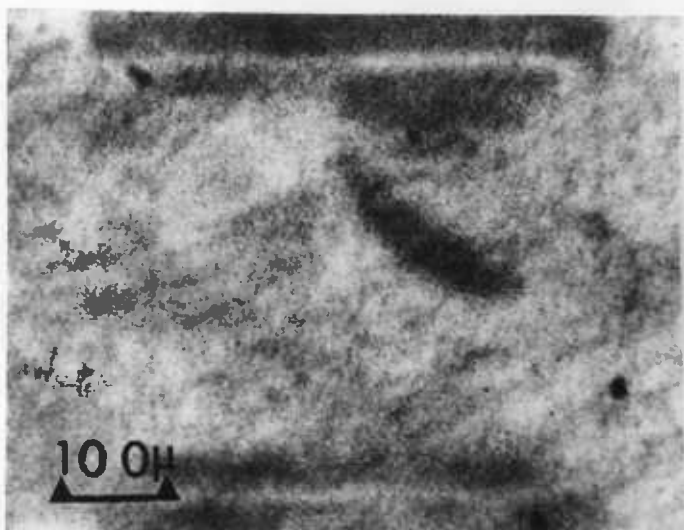


Fig.10.6

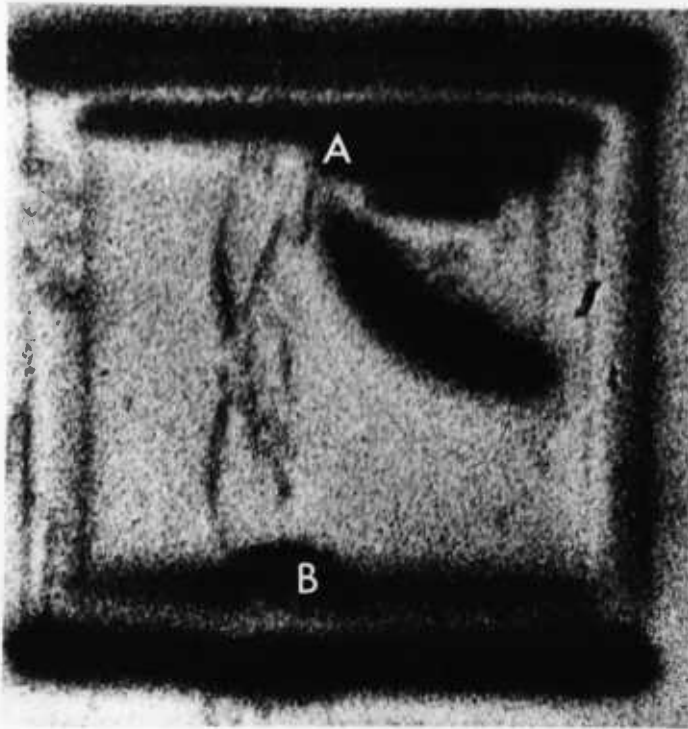
Comparison of XRT and BEVE mode SEM in heavily slipped device.



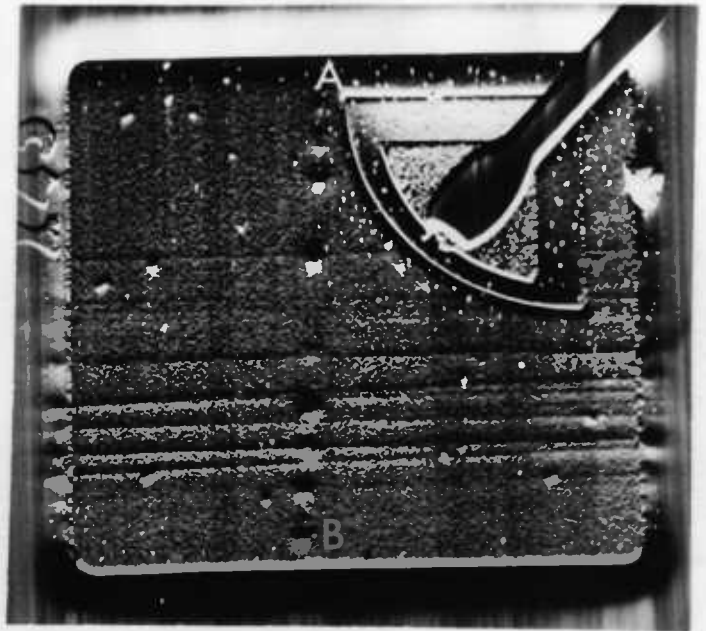
(a) Transmission XRT micrograph of DC device C28 R37

(b) BEVE mode SEM micrograph with  $V_{app} = 6V$

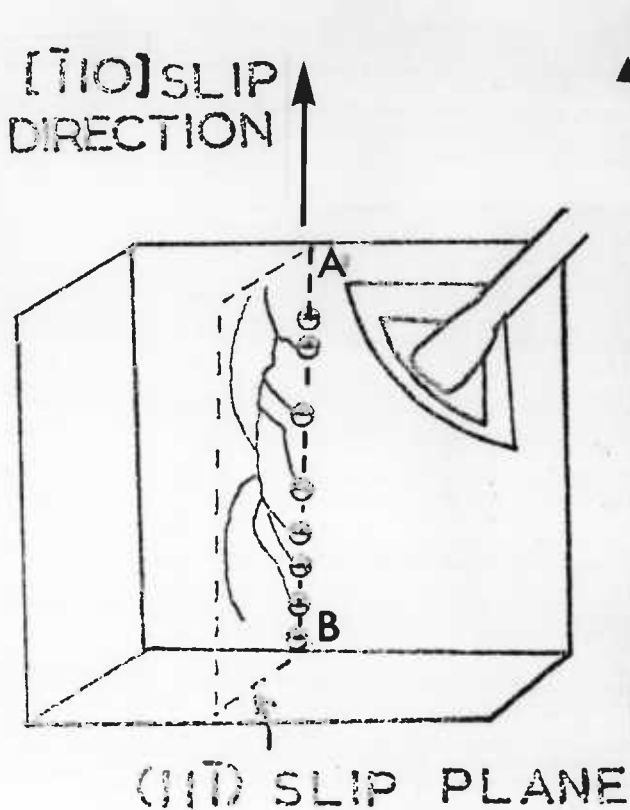
DC device C8 R26 ( $BV_{CEO} = 94V$ ) crossed by narrow slip band



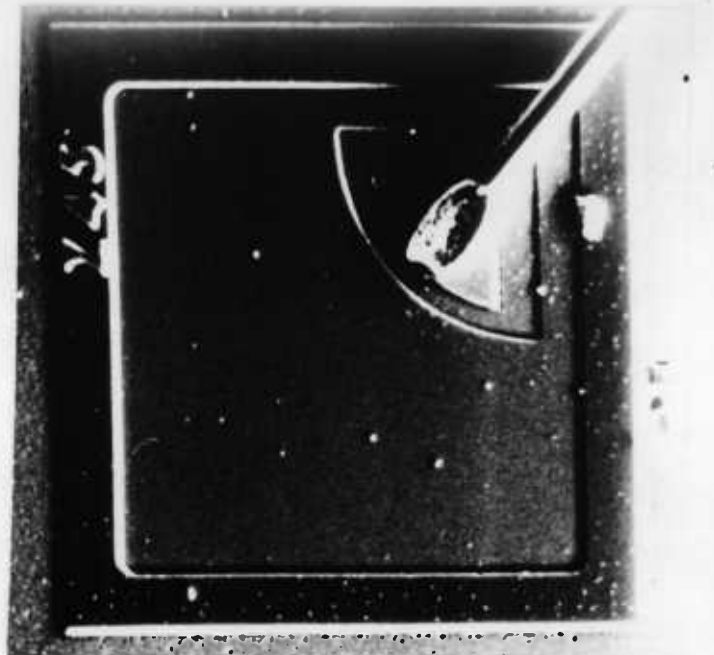
(a) XRT, transmission



(b) BEVE mode SEM,  $V_{app} = 1.5V$



(c) Geometry of slip plane containing dislocations in this device



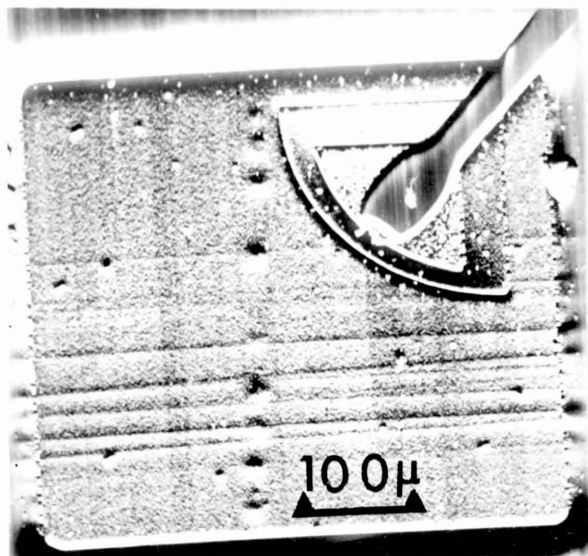
(d) Secondary electron SEM micrograph showing surface topography of photo transistor

the dislocations display contrast. The row of point contrast features running along line B - A in Fig.10.7(b) corresponds to the ends of dislocations lying along the top edge of the band of slip visible on Fig.10.7(a). Since the XRT transmission technique reveals dislocations throughout the entire 200  $\mu\text{m}$  thickness of the slice, it is clear that along most of their lengths, most dislocations will lie well below the depletion region of the junction and hence will not contribute to the image. The considerable projected length of some of the dislocations shows that they run approximately parallel to the (111) plane of the slice. The geometry of the slip plane is indicated in Fig.10.7(c). This diagram was produced by superimposing tracings of identical sized prints of Figs. 10.7(a) and (b). It can be seen that dislocations, visible in Fig.10.7(a) were found to end in each of the point contact features along the line B - A except for the two outermost ones. These each occur in regions in which visibility is lost in the X-ray topograph in the large dark bars due to the elastic strain fields arising at the edges of the emitter and base regions. It was established from the geometry of the slice in setting up the asymmetric reflection topographs shown in Fig.10.3 that the  $(11\bar{1})$  plane is inclined as shown in Fig.10.7(c) and therefore the ends of dislocations which give rise to BEVE contrast are specifically those at the top of the slice, i.e. those which come up through the base-collector junction. Again the smaller, more sharply defined spots in Fig.10.7(b) are due to surface debris which is also visible in the secondary emissive mode micrograph, Fig.10.7(d)

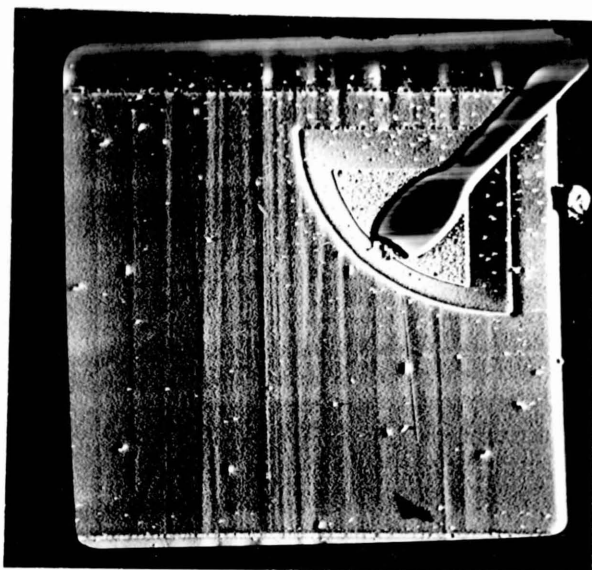
BEVE contrast due to dislocations diminishes with increasing junction reverse bias. Fig.10.8 was taken on the same device as shown in Fig.10.7. At 15V, Fig.10.8(b) the dislocations are no longer visible.

Fig.10.8

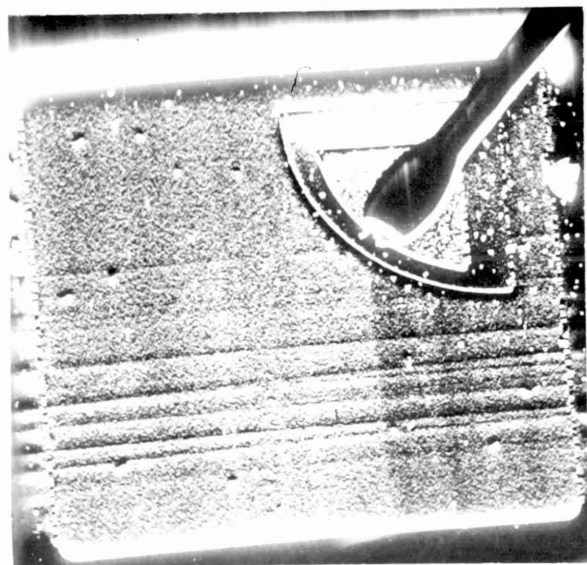
Effect of increased reverse bias on collector/base junction of device shown on Fig.10.7.



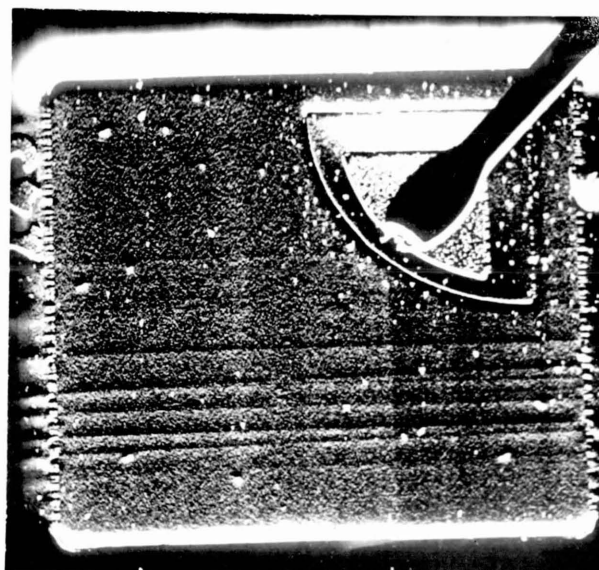
(a) 1.5V



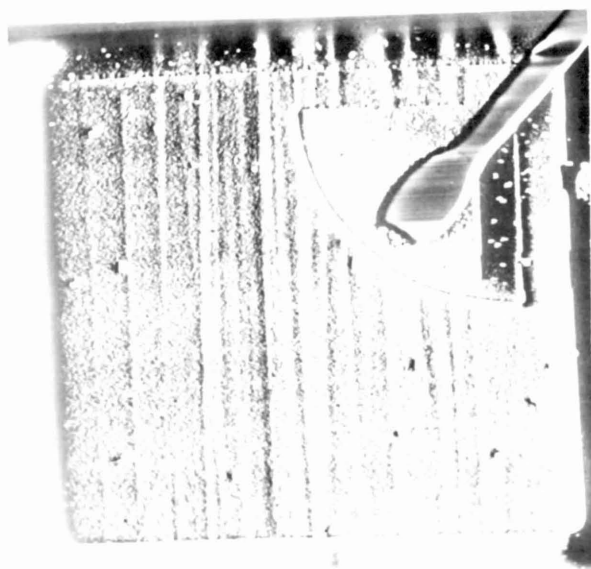
(b) 15V



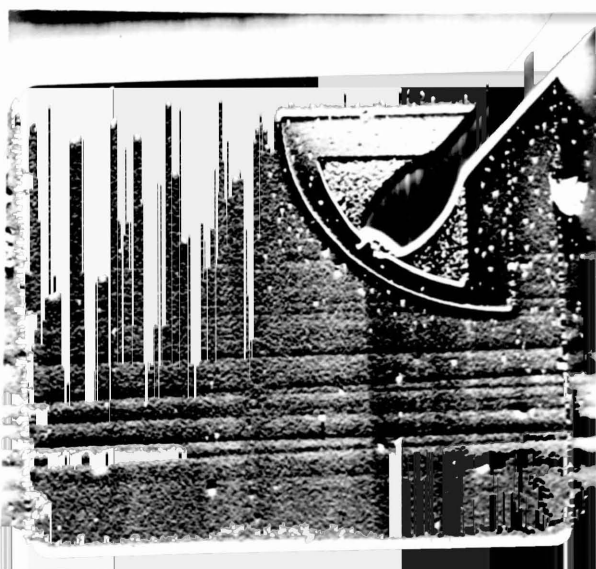
(c) 30V



(d) 60V



(e) 30V, line scan →



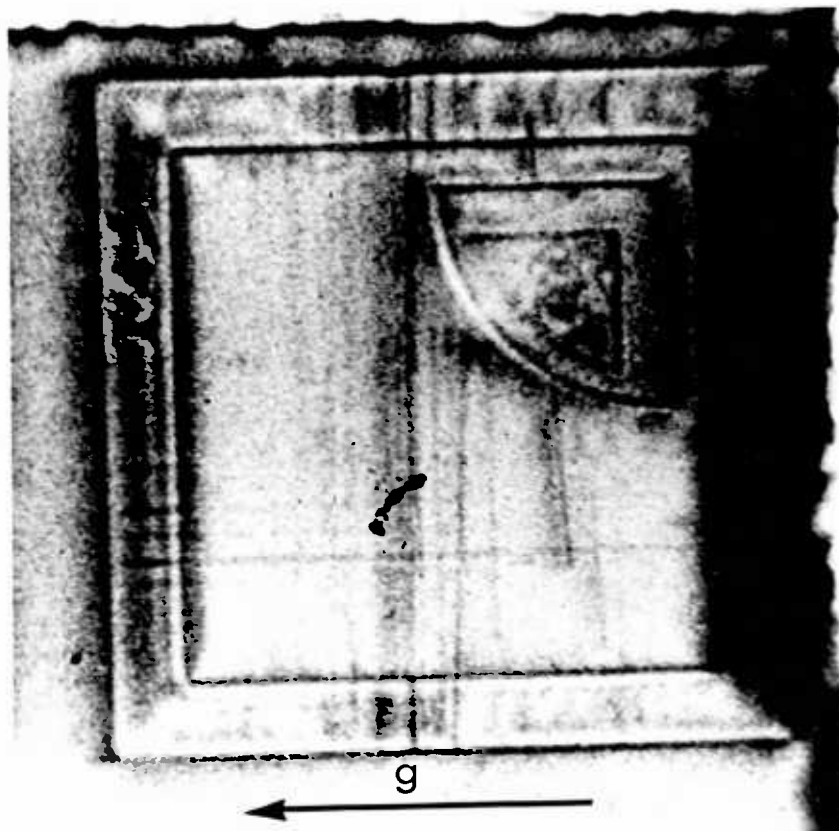
(f) 90V, line scan

Another significant observation appears in Fig.10.8: the sets of prominent horizontal and vertical lines across the device. These were produced on prolonged scanning of the lines concerned and are parallel to the scan directions employed. Due to the capacitive coupling of the amplifier, constant enhanced signal strength during the scanning of a line (i.e. a raised or lowered d.c. signal) does not appear in the video display. Thus for horizontal or vertical scanning only the lines of contrast in the orthogonal direction appear as can be seen in Figs. 10.8(e) and (f). At this stage the chip was removed from its header and mounted in the XRT camera. Using the same geometry as employed to obtain Fig.10.3, a surface topograph was obtained of the chip. This was not accomplished without considerable difficulty owing to the small dimensions of the chip ( $\sim 1$ mm square). The same scan lines are visible on the topograph as shown in Fig.10.9(a), in particular the central vertical band which contained the dislocations shown in Fig.10.7(a). Many stationary Y modulation line scans were used in this region to study the profiles of the dislocation "spots" shown in Fig.10.7(b). Both sets of scan lines were also revealed by optical microscopy using Nomarski interference contrast, Fig.10.9(b). This shows that steps have been created on the oxide surface at the position of the line scans. These steps could be contamination build-up due to electron beam cracking of pump vapours in the SEM. Such depositions could cause elastic strain fields in the underlying Si and give rise to the contrast visible in Fig.10.9(a). The contamination stripes would also reduce the effective beam intensity  $I_B$  locally and so lead to lower specimen currents  $I_{SC}$  which would give contrast in BEVE mode, Fig. 10.8.

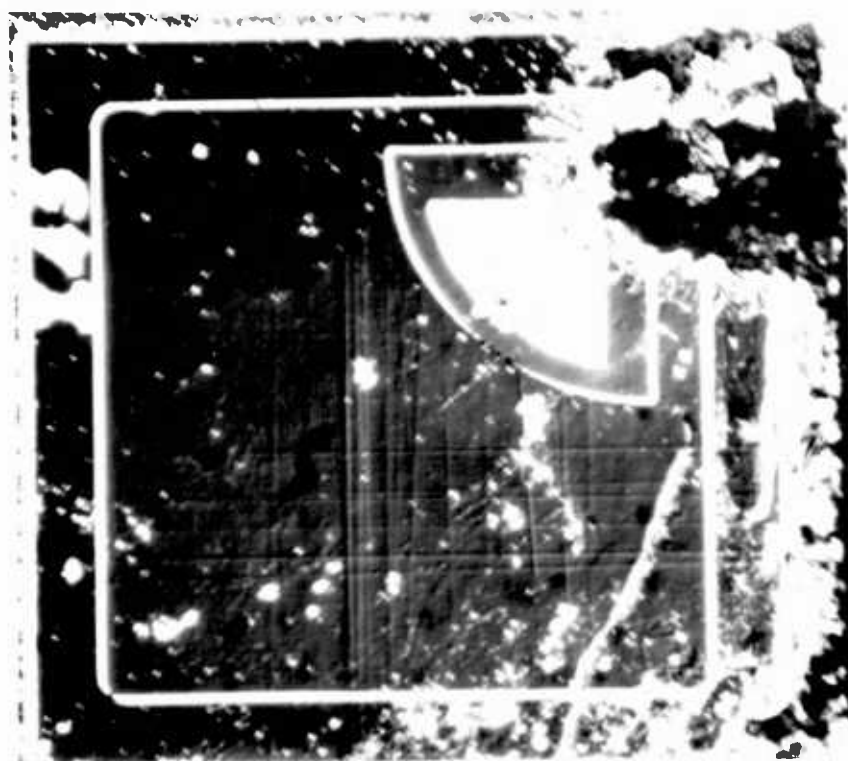
Returning to the observation of diminishing contrast at dislocations using the BEVE mode on increasing the applied voltage, the effect can also be demonstrated using Y modulation line scans recorded where the line intersects a dislocation image. Figs.10.10(a) to (f) show that the amplitude of the Y modulation signal as it crosses three dislocations diminished with increasing bias. The line scan position is marked by arrows in Fig.10.10(g). There was a surface particle almost coincident with the centre dislocation. This particle was responsible for the deep narrow minimum occurring within the broader central trough in the  $1\frac{1}{2}$ V trace, Fig.10.10(a). It can be seen that this narrow minimum in the BEVE signal was still readily distinguished in the trace recorded with an applied bias of 18V whereas the BEVE point contrast minima due to the dislocations were virtually eliminated, Fig.10.10(f).

Fig.10.9

Comparison of XRT and optical microscopy of device shown in Figs. 10.7 and 10.8 after prolonged examination by SEM



(a) Surface XRT,  $\alpha_1$  {511} reflection

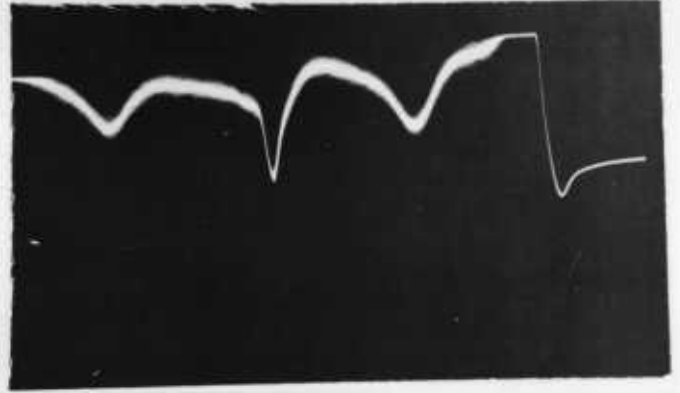


(b) Optical micrograph, Nomarski interference contrast

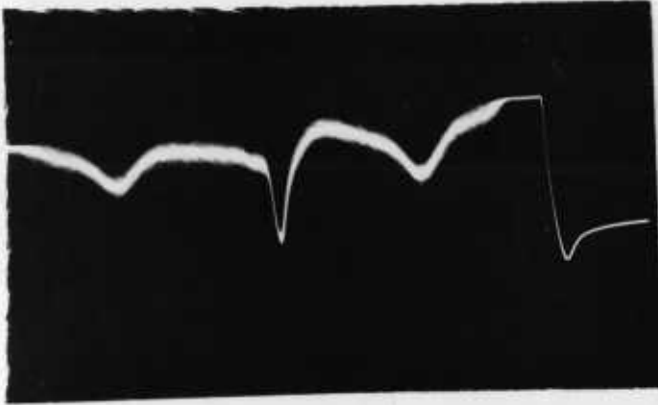
Y-modulation line scan traces of a row of 3 dislocations



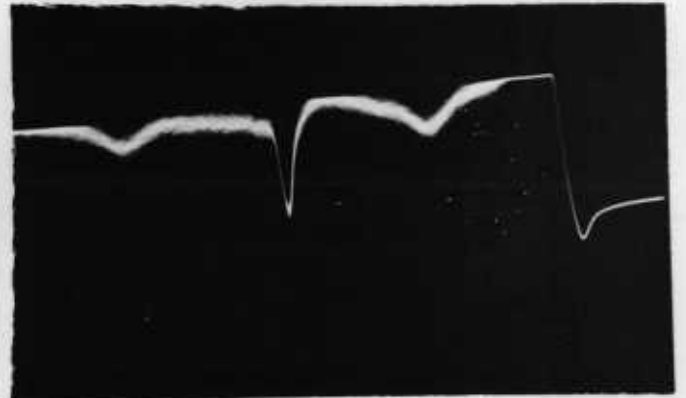
(a)  $V_{app} = 1.5V$



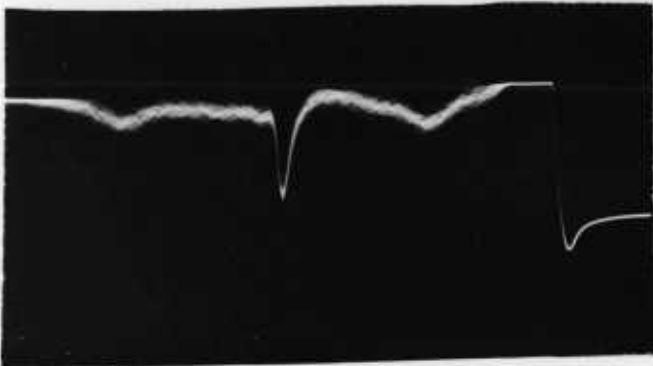
(b)  $V_{app} = 4.5V$



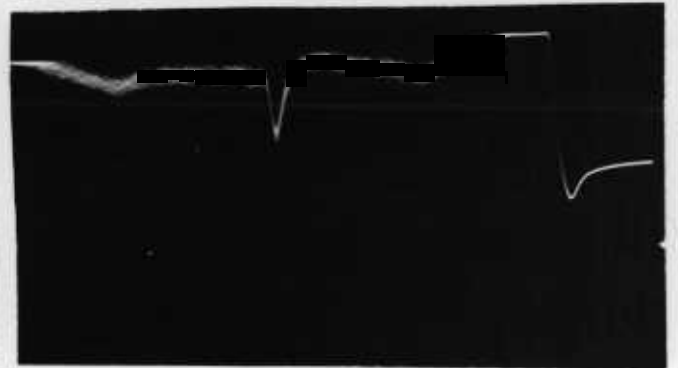
(c)  $V_{app} = 7.5V$



(d)  $V_{app} = 12V$



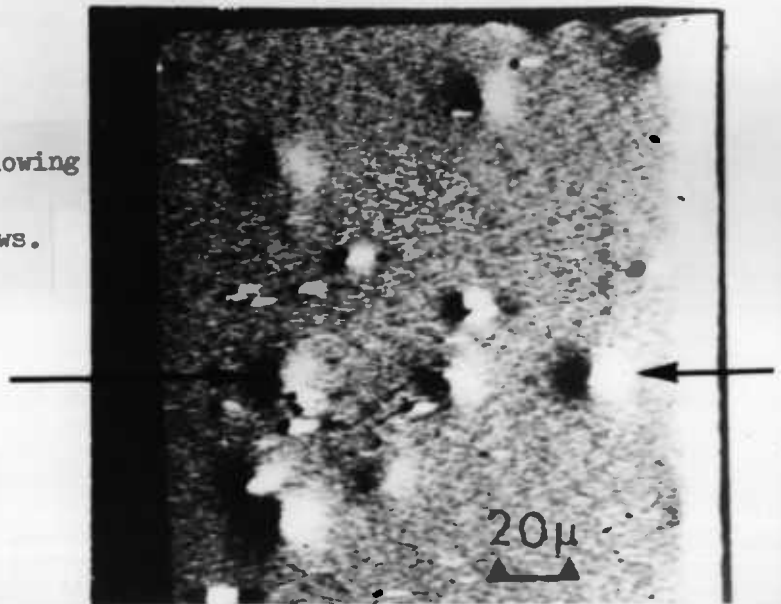
(e)  $V_{app} = 15V$



(f)  $V_{app} = 18V$

(g) BEVE mode micrograph at  $V_{app} = 15V$  showing position of line scan marked by arrows.

Scan spot moves from left to right.



Replacing the usual a.c. coupling to the SCA with d.c. coupling, i.e. by shorting out the capacitor, showed dark spots in the positions of the black/white images at dislocations, Figs. 10.11(a) and (b). This demonstrates that dislocations locally reduce the BEVE signal, probably by reducing the charge collection efficiency  $\eta_{cc}$ . Note that although this device contains a photoengraving "scratch" across the emitter, its breakdown was at 3V and so normal images were obtained in BEVE mode using  $V_{app} = 1\frac{1}{2}V$ .

10.2.3. Metallisation pits. The areas between devices, the scribe channels, are stripped of oxide towards the end of fabrication, just prior to metallisation. The edges of these channels were often decorated with small, triangular shaped pits, Fig.10.12(a). Similar pits were observed at the edges of the Al contact to the emitter, Fig.10.12(b). The pits are due to alloying of Al with silicon during the sintering stage after Al is evaporated onto the slice.

### 10.3. TEM Observations

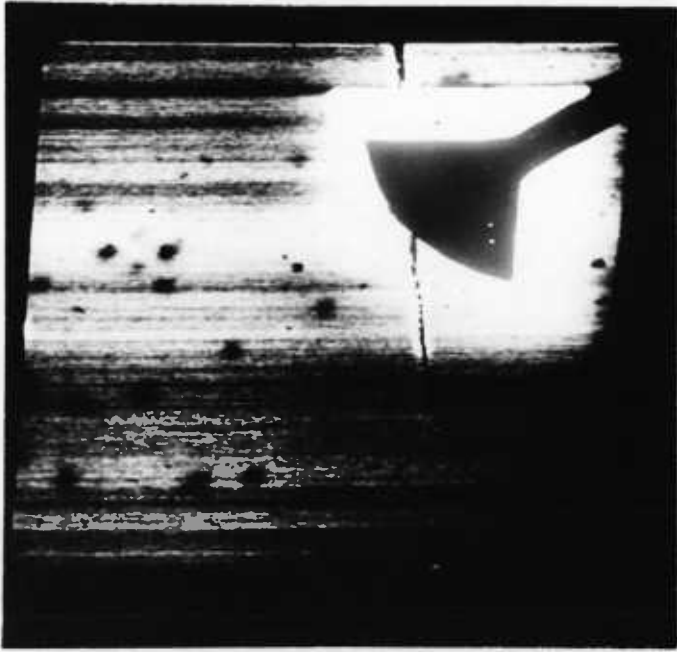
10.3.1. Pitting. The above SEM observations of pitting in scribe channel and emitter contacts was also seen by TEM. Figs.10.13(a) and (b) show examples of scribe channel pits in a region of the Dow Corning slices which showed heavy slip on the XRT micrograph.

Severe pitting also occurred in the end strip double-diffused regions which were also metallised, Fig.10.14. The presence of metallisation pits could lead to short circuiting of the device (collector/emitter pipes) if their depth approaches the base diffusion depth ( $2\frac{1}{2} \mu m$ ).

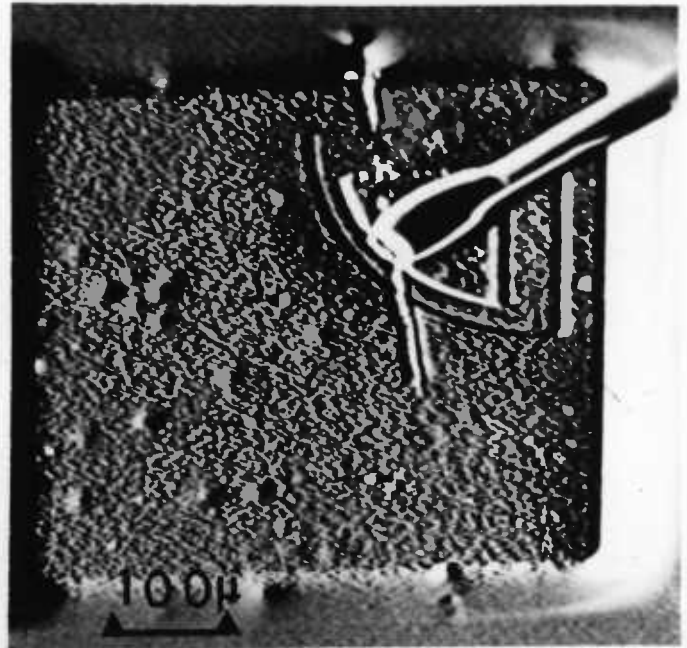
10.3.2. Dislocations. Careful examination of Fig.10.13(a) shows two dislocations, arrowed, but none at all are visible in Fig.10.13(b). Even so this corresponds to an average dislocation density of  $10^5 cm^{-2}$  and it is surprising that XRT could not resolve individual dislocations. Note that pits are not associated with the dislocations, which are steeply inclined to the foil surface.

Fig.10.11

Comparison of d.c. and a.c. coupling to SCA of device containing dislocations



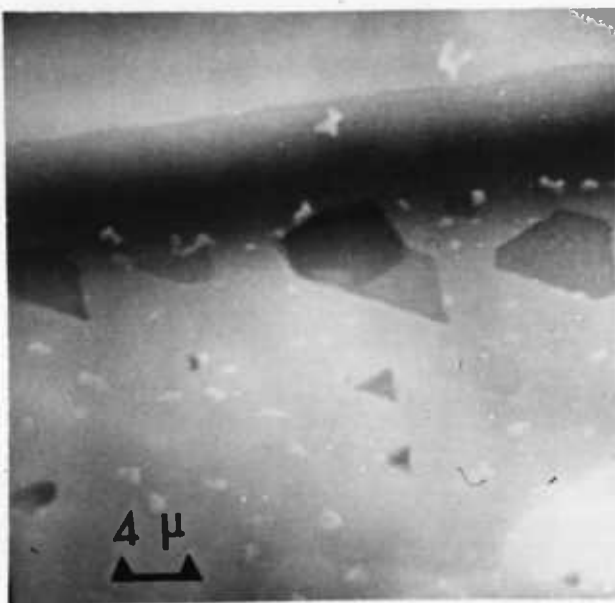
(a) BEVE mode d.c. coupling,  $V_{app} = 1.5V$   
T.I. chip C23 R38 ( $BV_{CEO} = 3V$ )



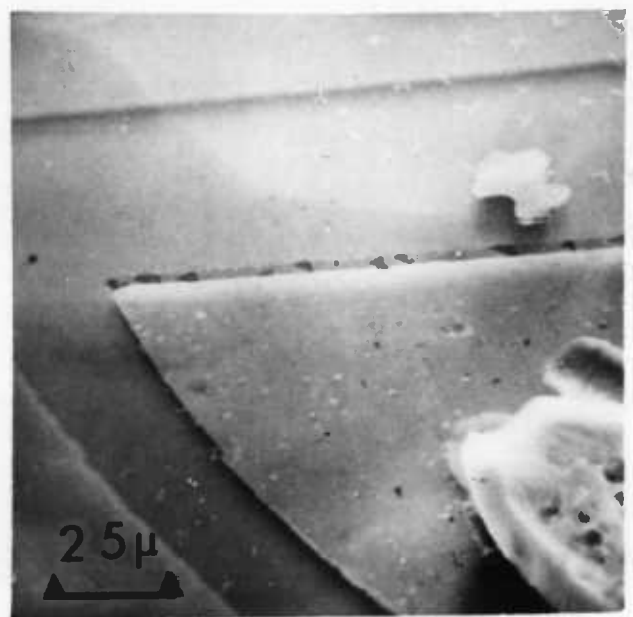
(b) Same chip as (a), a.c. coupling  
 $V_{app} = 1.5V$

Fig.10.12

SEM micrograph of metallisation pits in Al coated regions of device slice

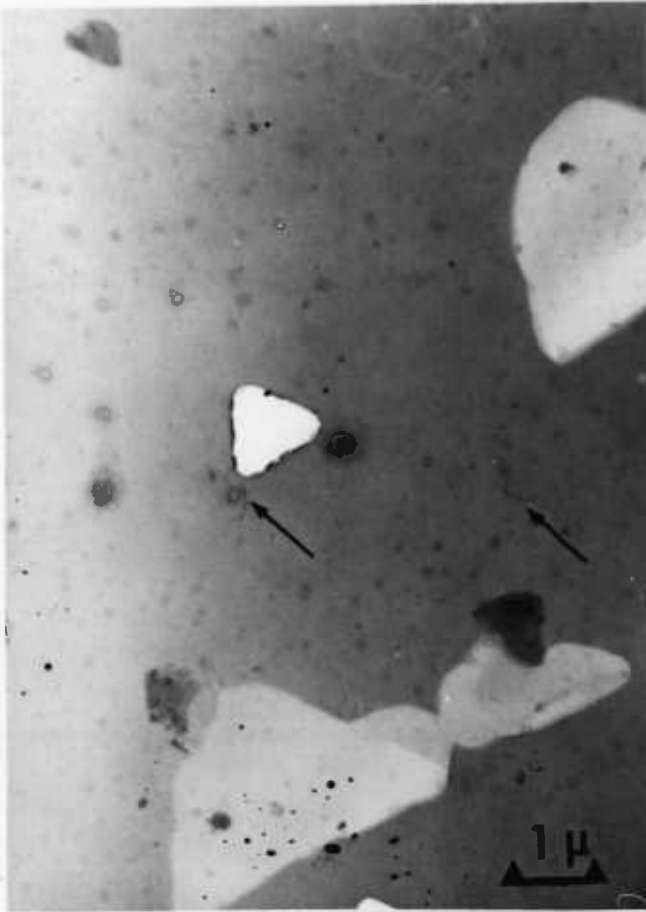


(a) Scribe channel

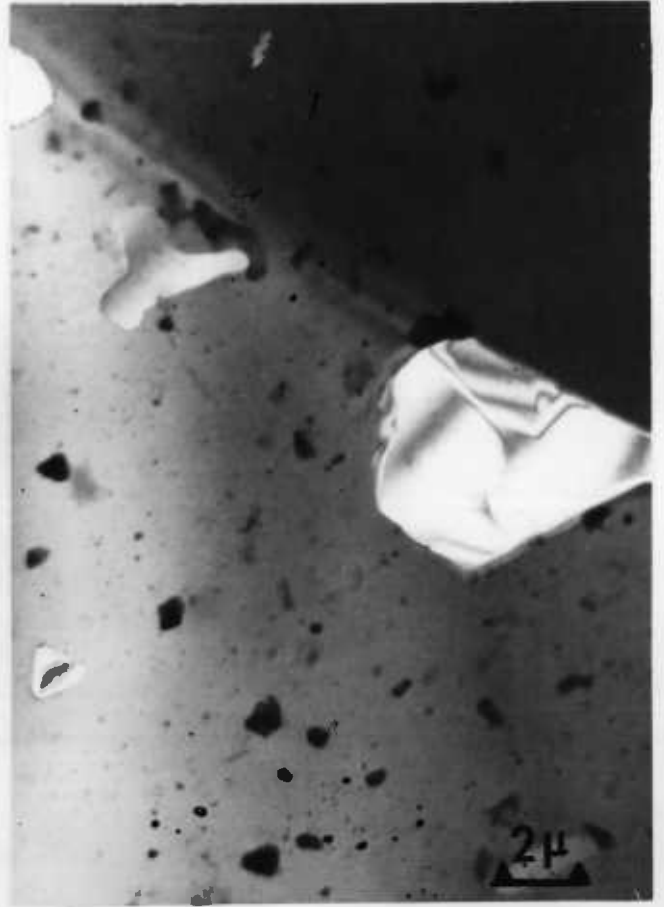


(b) emitter contact

Fig.10.13 Pits in scribe channel of D.C. device



(a) pitted area containing dislocations



(b) edge of scribe channel

Fig.10.14 Pitting in end strip of T.I. slice

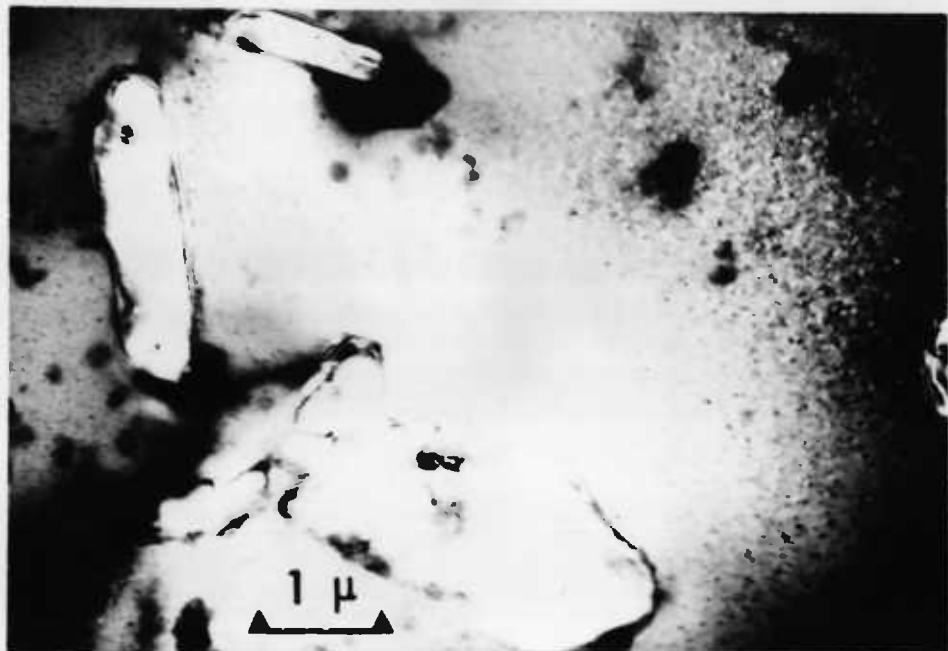


Fig.10.14 was taken from an end strip region showing heavy slip in XRT. This region had been subjected to a boron diffusion followed by a phosphorous diffusion. A band of dislocations about 10  $\mu\text{m}$  across was found in this specimen. The dislocations were lying largely in the (111) substrate plane and formed long chains of helices. Small dislocation loops and isolated segments were also present, Fig.10.15. Diffraction contrast analysis in the electron microscope, Figs. 10.16(a) to (f), Table 10.5, proves that the dislocation arrays are in fact helices with  $\frac{1}{2} [0\bar{1}1]$  Burgers vectors lying parallel to their axis. The dislocation loops, formed by pinched-off turns of the helices have the same  $\frac{1}{2} [0\bar{1}1]$  Burgers vectors. The significance of these results will be discussed later. The crystalline debris observed on the foil was not identified but is possibly a silicate.

TABLE 10.5

Zero Values of  $\underline{g}\cdot\underline{b}$  for  $\frac{1}{2} \langle 110 \rangle$  type dislocations for reflections used in Fig. 10.16.

$\underline{g} \backslash \underline{b}$	110	101	011	$\bar{1}10$	$\bar{1}01$	$0\bar{1}1$
$\bar{2}20$	0					
022						0
$\bar{2}02$		0				
$\bar{1}3\bar{1}$					0	
$3\bar{1}\bar{1}$						0
$\bar{1}\bar{1}3$				0		

Examination of base areas of devices in heavily-slipped areas showed narrow slip bands where dislocations had strongly interacted, Fig.10.17(a). Fig.10.17(b) is a drawing of the dislocation array showing analysed Burgers vectors of some of the dislocations. Dislocations were found with five out of a possible six  $\frac{1}{2} \langle 110 \rangle$  Burgers vectors. Helical dislocations and loops were not observed in base or scribe channel regions.

Fig. 10.15

Helical dislocations in double-diffused end strip region of T.I. slice

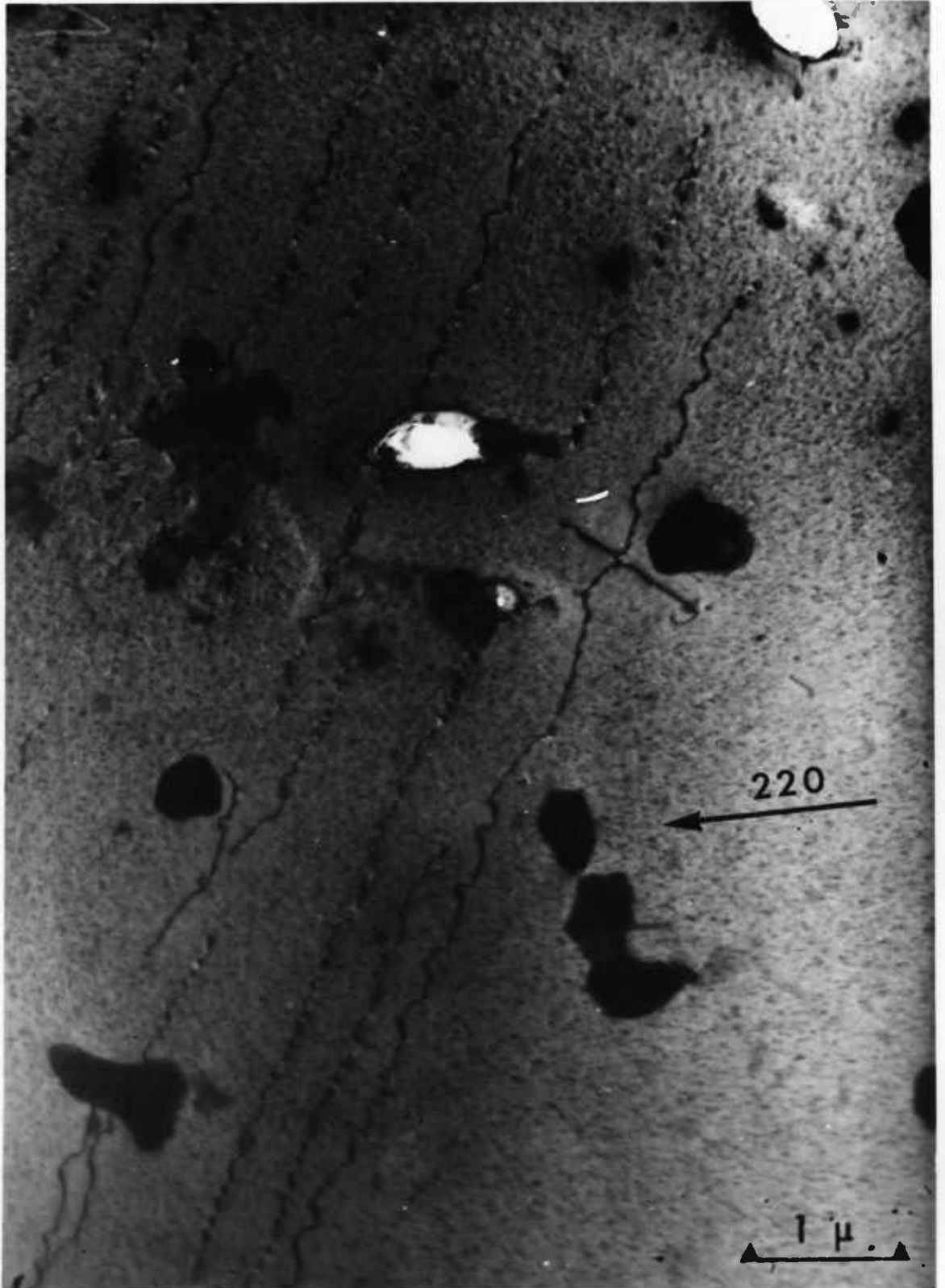


Fig. 10.16

## Analysis of dislocation band in T.I. end strip

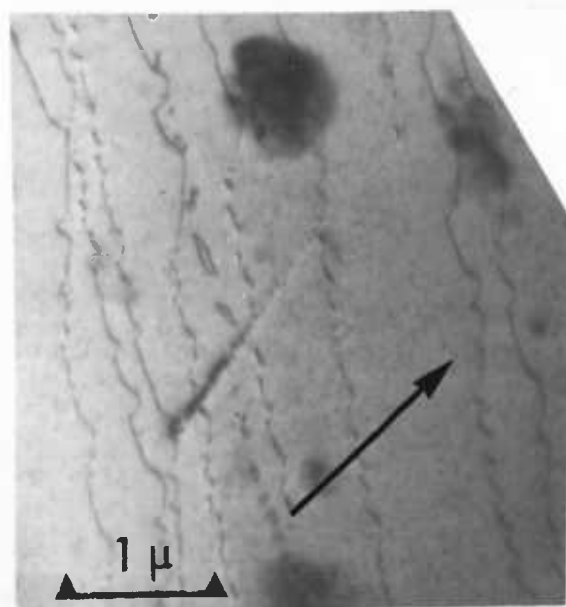
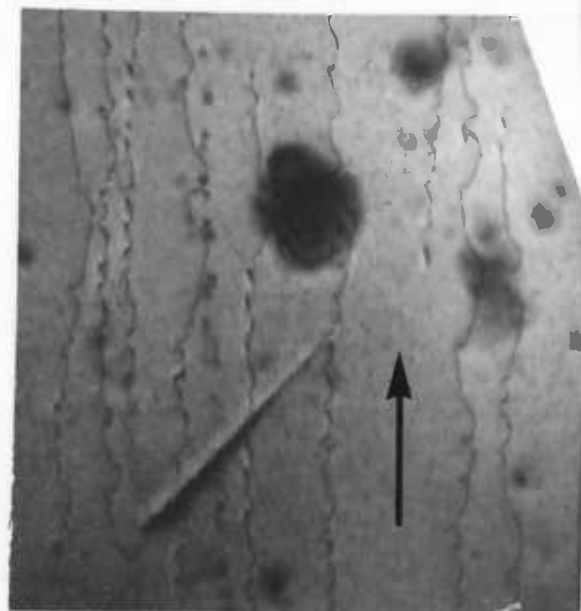
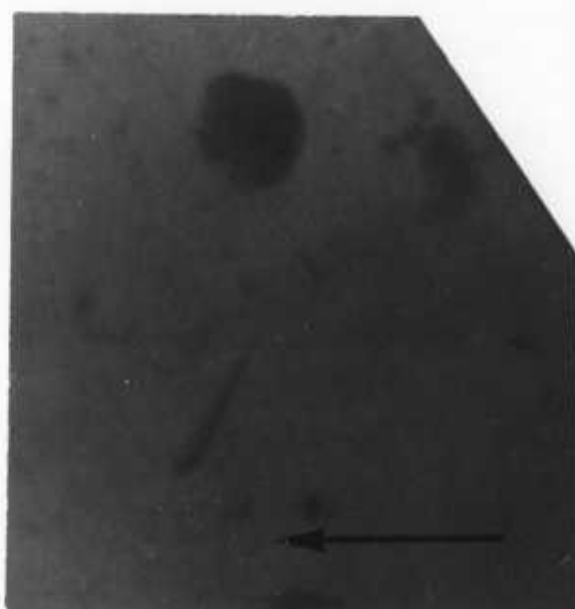
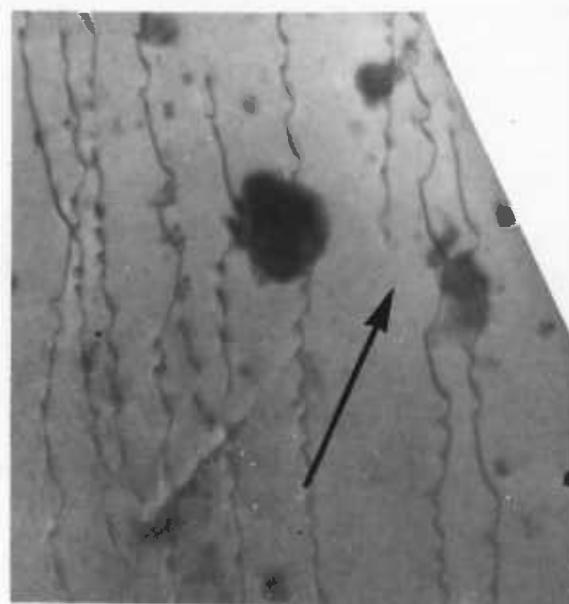
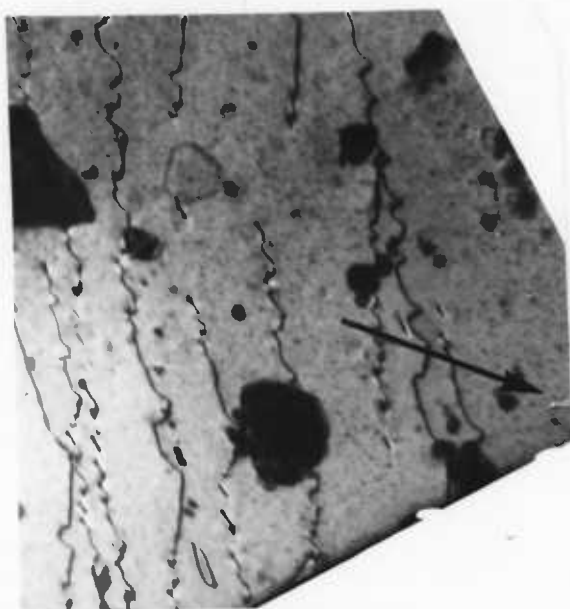
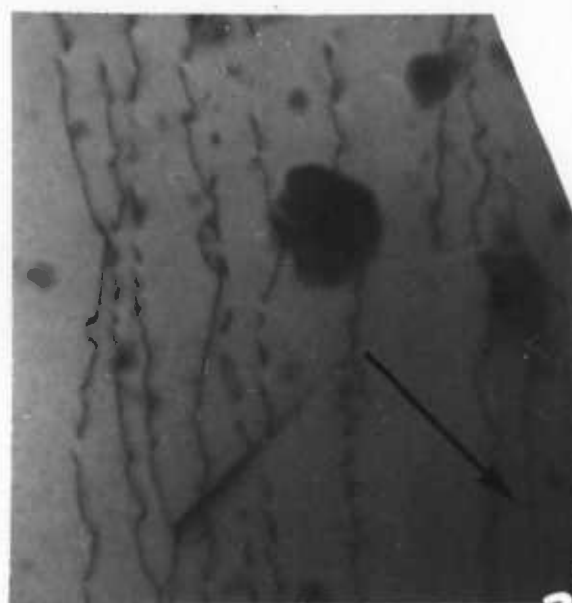
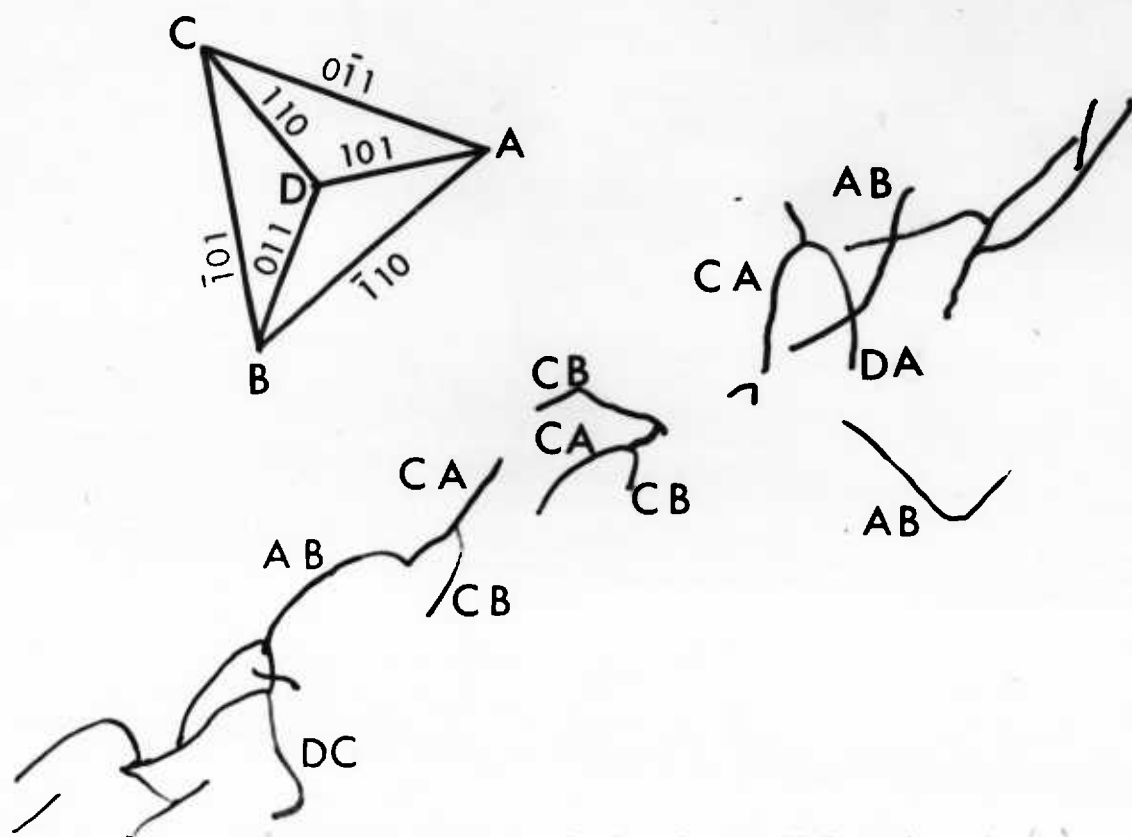
(a)  $\bar{2}20$ (b)  $02\bar{2}$ (e)  $3\bar{1}\bar{1}$ (f)  $\bar{1}\bar{1}3$

Fig.10.17 Dislocation band in base area of T.I. device



(a) TEM micrograph



(b) Burgers vector analysis of some dislocations in (a)

Examples of glide dislocations were found in scribe channel regions in heavily slipped areas. The Burgers vectors of the dislocations were in the  $(111)$  plane of the substrate. Fig.10.18(a) shows a long dislocation which appears to have been pinned so that a kink occurs. The dislocation has a large screw component. Interacted dislocations were also found in scribe channels, Fig.10.18(b).

10.3.3. Oxidation-induced stacking faults. Fig.10.19 shows an example of an extrinsic stacking fault bounded by a Frank partial dislocation in an end strip region. Clusters of small dislocation loops are visible forming a band in the same slip plane at the stacking fault. This could be precipitation left behind by the collapse of the stacking fault. Few stacking faults were observed by TEM, and so the density can be considered to be  $< 10^4 \text{cm}^{-2}$ .

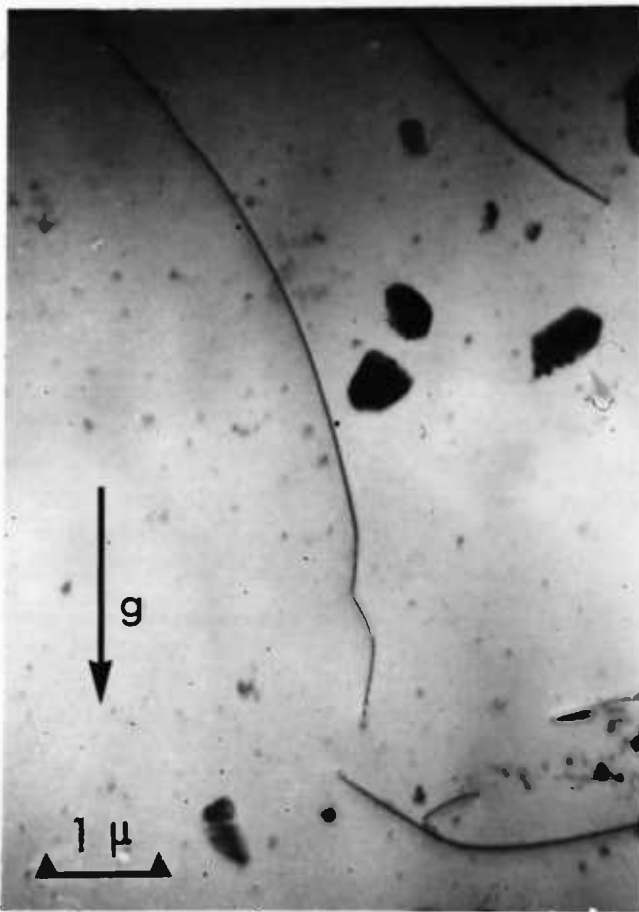
10.3.4. Emitter edge dislocations. Networks of dislocations were observed at the edge of emitter regions in some devices, Fig.10.20. These are believed to be due to stress gradients introduced during the emitter diffusion owing to the size difference between the substitutional phosphorus atoms and the Si host, Fairfield and Schwuttke (1968). The defects were not observed using XRT because the high elastic strain field around the diffused windows gave enhanced contrast and so masked the dislocations. Also the density of the dislocations, as shown in Fig.10.20, is far too high to be resolved using XRT.

In some devices, networks of  $60^\circ$  dislocations, some extremely long, are found in the emitter region. A portion of such a dislocation, which is over  $100 \mu\text{m}$  long, is shown arrowed in Fig.10.21.

A systematic attempt to examine 'good' and 'bad' device chips by TEM was not made.

Fig.10.18

Dislocations in Scribe channel



(a) long dislocation segments,  
largely lying in  $\{111\}$  substrate plane

(b) Interacted dislocations similar  
to band in Fig.10.17.

Fig.10.19 Extrinsic stacking fault and decoration in end strip region of T.I.slice

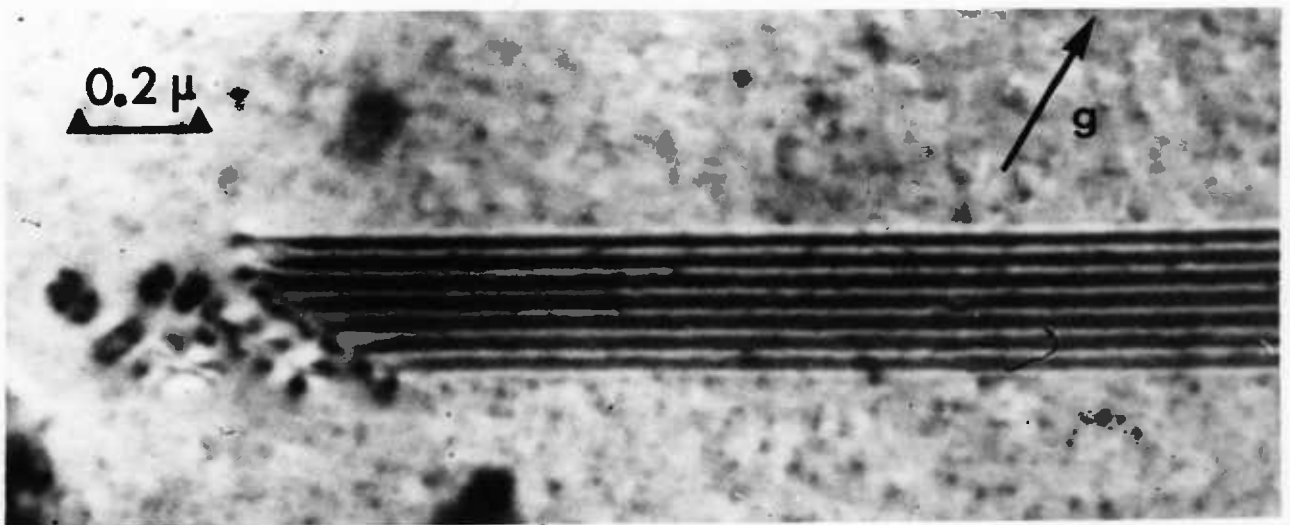
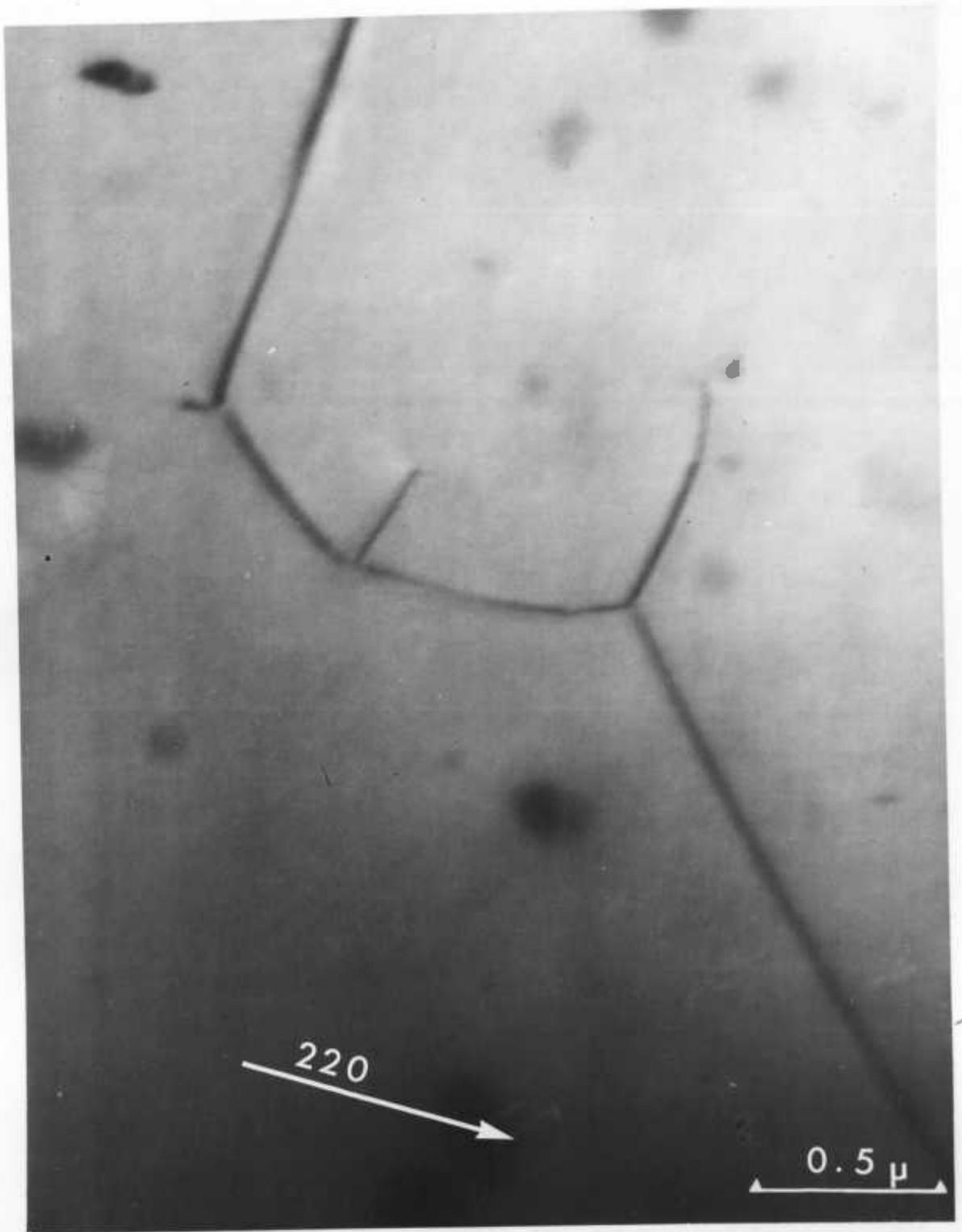


Fig. 10.20

Dislocation network at edge of emitter region





2 μ

12201 ←

TEM Micrographs of dislocations in emitter region of P-I device

Fig. 10.21

#### 10.4. Miscellaneous results

10.4.1. Bevel and Stain. As described in Section 9.4, portions of the end strips of the slices were bevelled by hand to a  $1^\circ$  taper and stained with  $\text{CuNO}_3$  solution to measure the depths of the boron and phosphorous diffusion. The specimens were first given a thick coat of oxide using the Silox process ( $\text{SiH}_4 + \text{O}_2$  at  $400^\circ\text{C}$ ) prior to bevelling to protect the surface and to give a built-in calibration from the oxide fringes. Figs.10.22(a) and (b) show the results on the D.C and T.I. slices respectively. The  $n^+$  emitter regions are strongly stained and the n substrate lightly stained. The base region is unstained and is thus outlined between these two regions. Although the base widths are identical to within experimental error, the T.I. slice gave better staining than the D.C. slice.

10.4.2. Sheet resistance results. Sheet resistances were measured using a 4-point probe on 2mm discs as cut for TEM from the end strips. Four measurements were taken on each specimen, by reversing polarities and interchanging current and voltage points. The technique is a routine procedure in quality control in the semiconductor industry. The "points" are usually tungsten styli loaded with typically 5 gm. wts. in a square array. A constant current source and digital voltmeter complete the required apparatus. A calibration factor is used which is a function of the geometry of the probes and the current, size and shape of the specimen. Four specimens from each slice were measured and the results are shown in Table 10.6.

TABLE 10.6  
Sheet resistances of double-diffused slice regions

Slice	Specimen	Voltages ( $\mu\text{V}$ )				Sheet resistances 'ohms per square'
D.C	1	48	48	49	48	4.95
	2	47	48	50	50	5.00
	3 *	39	42	60	62	5.21
	4	44	47	56	59	5.29
T.I.	1	52	53	46	47	5.08
	2	48	48	50	50	5.02
	3	50	50	48	49	5.03
	4 *	63	63	37	38	5.15

\* denotes chipped specimen

Fig. 10.22

Sections of double-diffused regions obtained by the bevel & stain technique

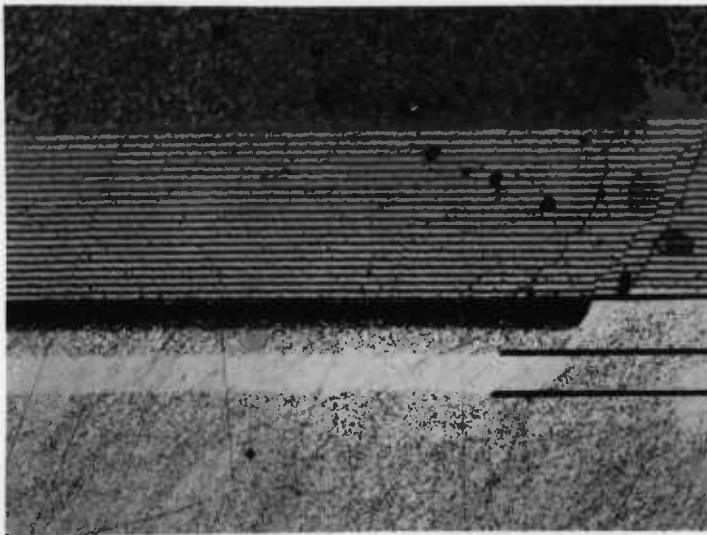


1 oxide fringe =  $2068\text{\AA}$

emitter  $1.23\mu\text{m}$

base  $1.03\mu\text{m}$

(a) D.C. slice



emitter  $1.30\mu\text{m}$

base  $1.05\mu\text{m}$

(b) T.I. slice

Sheet resistances were similar for each slice. Calculations are set out in Appendix C to give the expected profile of the base diffusion based on data such as sheet resistances. Depletion widths of the collector/base junction are then calculated as a function of reverse bias.

10.4.3. Photo current measurements. Packaged devices were tested for photo current output as described in Section 9.3.1. Seven D.C. 2 x 2 chips and eight T.I. 2 x 2 chips were measured, a total of 60 devices and the results are given in Tables 10.7(a) and (b). Devices marked with an asterisk had previously been examined by S.E.M. There is no correlation between photo current and dislocation density, but as noted earlier, the T.I. devices show a lower  $V_{CEO}$  than D.C. devices. It is immediately obvious that devices which had been viewed in SEM were badly degraded as far as photo current is concerned. In every case, currents were only a fraction of non-examined devices, typically  $\sim 10\%$  of a 'good' device.

TABLE 10.7(a)

Photo current measurements on Dow Corning Devices

Device	Photo current mA	$V_{CEO}$ for 10 uA	Dislocation structure
C5R26	0.31	94	none
C5R27	0.34	88	"
C6R26	0.34	88	"
C6R27	0.38	8	"
C51R24	0.29	98	"
C51R25	0.27	96	"
C52R24	-	-	edge of slice
C52R25	-	-	"
C39R20	-	-	$< 10^3 \text{ cm}^{-2}$
C39R21	0	74	$< 10^3$
C40R20	-	2	none, emitter "scratch" (es)
C40R21	-	2	" " "
C7R26	0.40	88	none
C7R27	0.38	87	"
C8R26	0.36	94	narrow slip band
C8R27	0.36	88	" " "
*C29R20	0.04	96	none
*C29R21	0.04	93	"
*C30R20	0	86	1 in emitter
*C30R21	0.085	98	none

Device	Photocurrent mA	$V_{CEO}$ for 10 uA	Dislocation structure
*C27R40	0.021	89	Very heavy slip $> 10^4$
*C27R41	0.013	68	" "
*C28R40	0.021	100	" "
*C28R41	0.019	100	" "
*C15R20	0.022	89	none
*C15R21	0.025	88	"
*C16R20	-	2	" , es
*C16R21	0.036	87	"

TABLE 10.7(b)

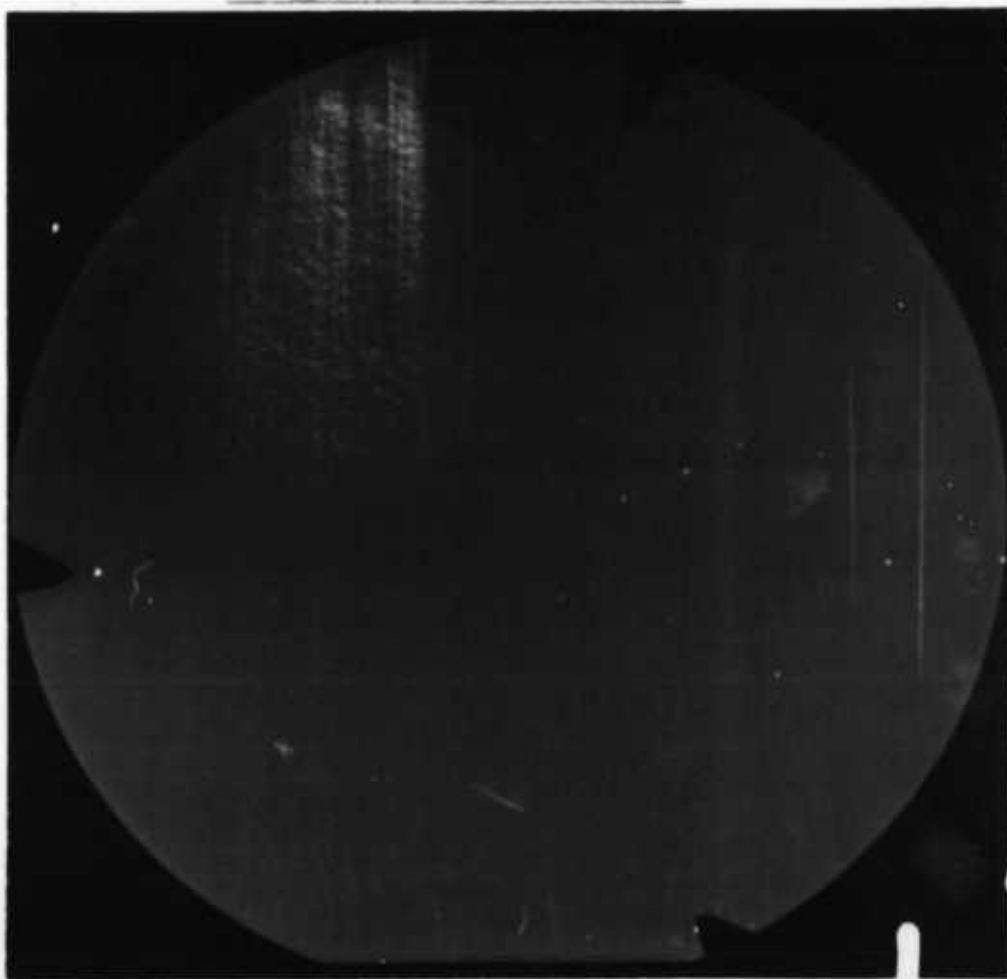
Photocurrent measurements on Texas Instruments Devices

Device	Photocurrent mA	$V_{CEO}$ for 10 uA	Dislocation structure
C8R32	0.47	80	Narrow slip band
C8R33	0.46	80	slip band across emitter
C9R32	0.47	35	medium dislocation density
C9R33	0.50	80	" " "
C22R38	0.36	88	med. dislocations close emitter
C22R39	0.35	53	med./low dislocn. density
C23R38	-	3	" " " , emitter scratch(es)
C23R39	-	3	heavy dislocn. band es
C26R26	0.34	87	med/low density $\sim 10^3$
C26R27	0	90	" "
C27R26	0.33	92	" "
C27R27	0.33	90	" "
C26R24	0.38	90	$\sim 10^3$
C26R25	0.36	10	"
C27R24	0.40	85	"
C27R25	0.36	88	"
C46R26	0.36	45	heavy, $5 \times 10^3$
C46R27	0.34	45	"
C47R26	0.36	90	"
C47R27	0.34	90	"
*C40R24	0	80	$\sim 5 \times 10^3$ in some areas
*C40R25	0.059	25	$\sim 10^4$ density in base
*C41R24	0.050	81	$5 \times 10^3$ in some areas
*C41R25	0	93	$10^4$ in emitter
*C24R42	0.036	87	$6 \times 10^3$
*C24R43	0.033	88	$< 10^3$
*C25R42	0.017	92	$3 \times 10^3$
*C25R43	0.039	86	$< 10^3$
*C30R24	0.178	88	$< 10^3$
*C30R25	0.090	88	"
*C31R24	0.160	90	"
*C31R25	0.190	57	"

10.4.4. Cause of slip in device slices. Examination by XRT of a slice of starting material which had been gas polished in HCl at 1150°C showed a large amount of slip in one region of the slice, Fig.10.23(a). For comparison a starting slice is shown in Fig.10.23(b). No dislocations are present in this slice: a general feature of current Si material. It is generally believed that slip is induced by thermal gradients during heating and cooling and also by point to point variations in the steady state. Slices for gas polishing lay on a SiC coated graphite susceptor which was RF heated in a cold walled furnace. Optical pyrometer sightings on slices during several runs were taken and a typical time/temperature schedule is shown in Fig.10.24. It is seen that the slices are subjected to severe thermal shock during the heating and cooling cycle, especially on cooling. Temperature variation in the steady state up to 70°C were observed by sighting on different portions of the slice. Slices examined under a bright light after gas polishing showed heavy regions of slip visible to the naked eye.

During subsequent <sup>high</sup>temperature processing, the region of slip increases in area. Fig.10.25 shows the progress of a square { 100 } D.C. slice from gas polish and through two blanket diffusions under conditions similar to those used to process Z45 slices. An increase in dislocation density is very marked comparing the slice after boron diffusion with the gas polished condition.

XRD micrographs of D.C. alicon

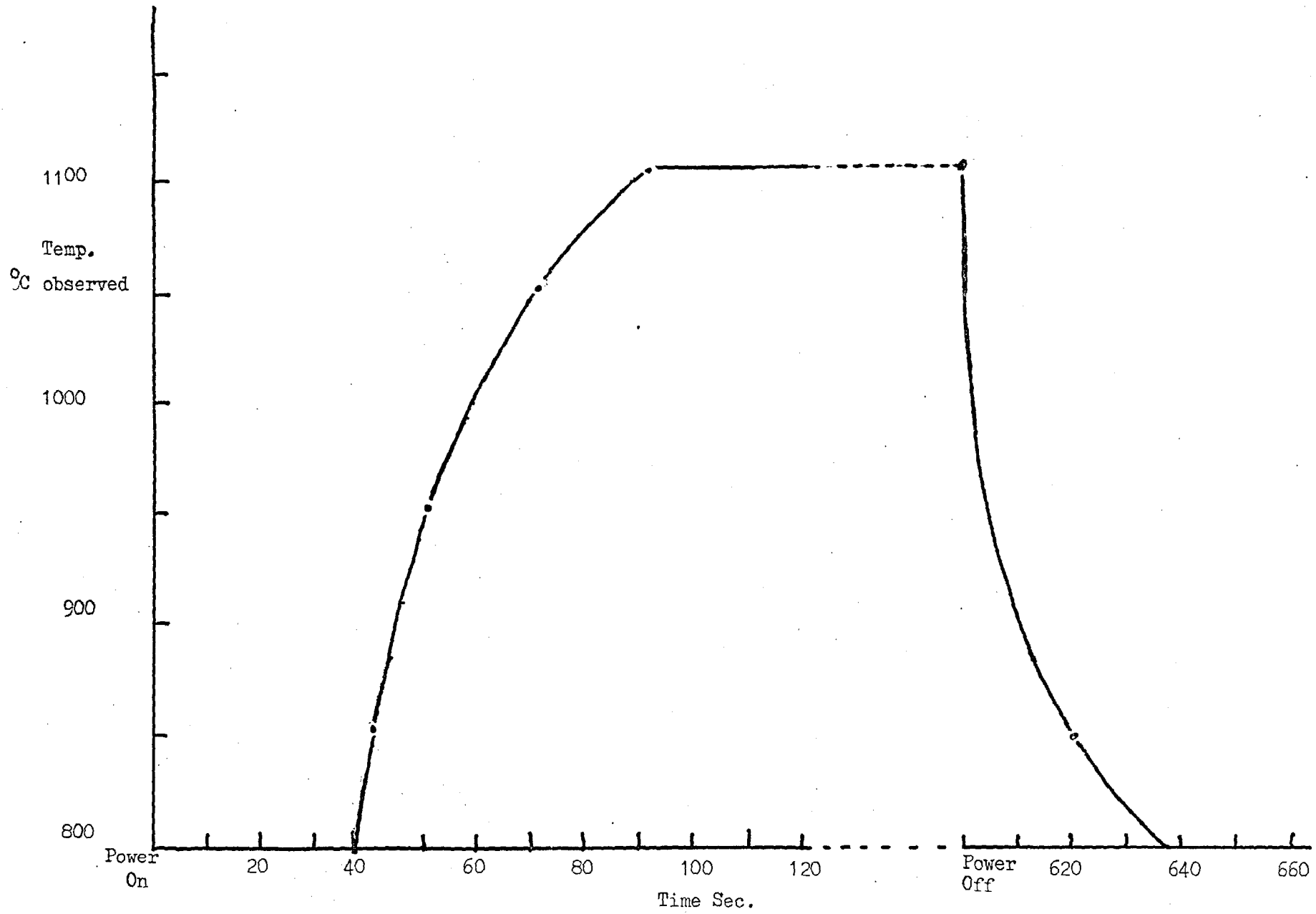


(a) gas polished

MoK $\alpha$ , radiation, {220} reflections



(b) as received



Typical observed temperature cycle of Si slice on IR heated susceptor during gas polishing.

TABLE 10.24

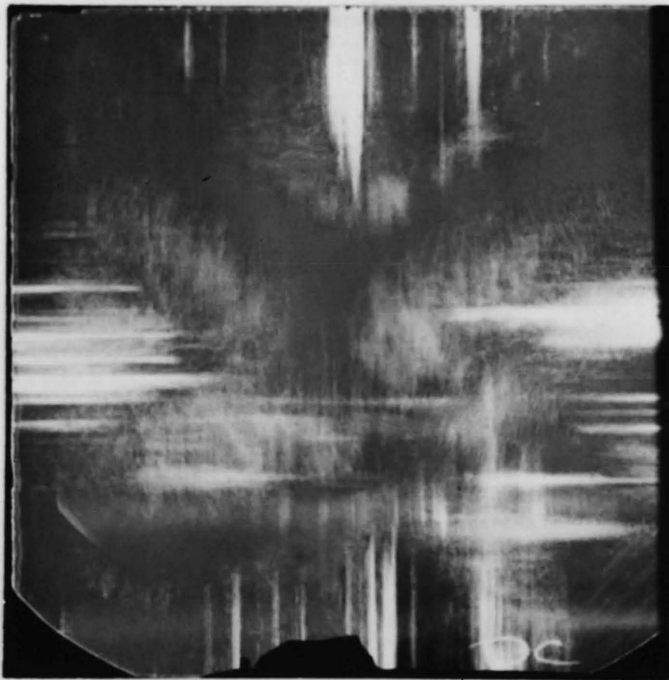
Dislocation generation during successive heat treatments.



XRT transmission mode,

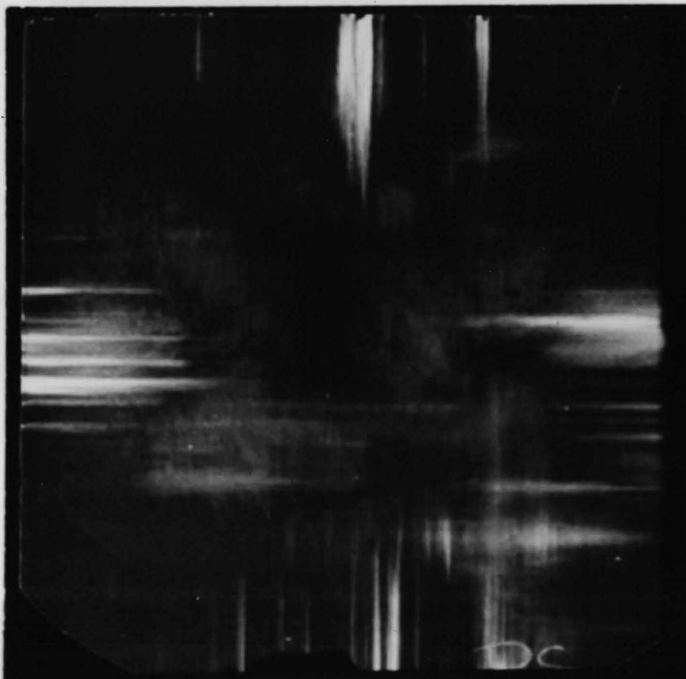
$\{111\}$  reflections

(a) gas polished



(b) as (a) + Boron diffusion

(see Table 9.1)



(c) as (b) + Phosphorus diffusion

(see Table 9.1)

## CHAPTER 11. DISCUSSION

### 11.1 First observation of individual dislocations by BEVE contrast

This is believed to be the first unambiguous observation of dislocations by means of BEVE contrast in conductive mode SEM micrographs. Lander et al (1963) and Czaja and co-workers (1964,5,6) showed BEVE mode micrographs where Si p-n junctions were crossed by dark lines thought to be diffusion induced dislocations. It is now clear that these lines are slip planes containing many dislocations rather than individual dislocations. The high resolution of TEM is needed to resolve this high density of dislocations, as shown in Figs.10.15 and 10.17. Czaja & Patel (1965) observed dark lines around indentations in Si diodes after annealing. It was subsequently shown by Neve & Thornton (1966) in a similar experiment supported by etching studies, that cracks as well as dislocations could give rise to the observed contrast.

As discussed in Part I of this thesis, etching is not generally capable of distinguishing one type of defect from another. This doubt applied also to the recent report by Stringfellow et al (1974) of dark spots seen on BEVE micrographs of GaP diodes. In the present case, XRT applied to devices containing low densities of dislocations does unambiguously show that the spot contrast features as seen in Fig.10.7(b) do correlate with individual dislocations, Fig.10.7(a) to within the limits of resolution of both techniques. However, the TEM study of the narrow slip band in the base region of a device, Fig.10.17, shows that interactions leading to complex dislocation configurations have occurred that could certainly not be resolved by XRT or BEVE mode SEM. Armigliato & Servidori (1974) examined phosphorus diffused Si wafers using both XRT and TEM. Similar micrographs were shown of long dislocations lying in the plane of the wafer but XRT did not resolve the node structures where two such dislocations were intersected by a third, inclined dislocation.

The ideal solution would be to prepare the chip shown in Fig.10.7 for TEM after SEM had been performed. Then we could establish that single dislocations are located at each of the points of contrast in Fig.10.7(b). This was not attempted. Section 9.3.5. gave details of the preparation of thin foils for TEM. The success rate for chemically thinning a particular specimen so that a large selected area is viewable in TEM operated at 100kV (i.e.  $< 1 \mu\text{m}$  thick) is not high. Currently

available preparation techniques involving polishing specimens to about 15  $\mu\text{m}$  thick prior to ion-beam thinning would greatly improve the chance of success.

### 11.2. Electrical behaviour of dislocations

The reason for the fading contrast with increasing bias in BEVE mode SEM at dislocations as in Figs.10.8 and 10.10, is not clear. The calculation in Appendix C shows that the collector/base depletion width increases significantly with reverse bias. Thus the volume of region which separates the carrier pairs generated by the scanning electron beam increases. Since dislocations inclined to the surface pass through the junction region, the length of dislocation which could affect the charge collection efficiency will also increase. However, the result seems to indicate that the dislocations do not directly cause leakage paths through junctions. Their behaviour is quite different from that of the highly decorated stacking faults of Ravi et al (1973); discussed in Section 8.1.2, where contrast at the faults reversed at a threshold voltage associated with the onset of leakage. Examination of several devices at their breakdown voltage  $BV_{\text{CEO}}$  did not show enhanced contrast at any particular site although the edge of the base region generally showed bright spots along its edge at all voltages as in Fig.10.8.

Section 10.1 established a strong correlation between high dislocation density and low  $BV_{\text{CEO}}$ . The correlation was not absolute and the absence of contrast due to leakage at dislocation sites in BEVE mode SEM shows that the cause of correlation is subtle. Two explanations based on earlier ideas could be employed to fit these observations:

1. Ragged junction (after Queisser (1961) model of grain boundary enhanced diffusion)

From Figs. 10.15 and 10.16 it is seen that the primary dislocations formed during gas polishing due to thermal stress have been transformed by climb during the diffusion processes into helical dislocation arrays. Such arrays have been observed by Dash & Joshi (1968) in arsenic-diffused Si. Helical dislocations were not observed in undiffused regions in the present work. The reciprocal effect could be locally enhanced diffusion of dopant, especially phosphorous which is present in much higher surface concentrations ( $\sim 10^{21} \text{cm}^{-2}$ ) than the boron ( $4 \times 10^{18} \text{cm}^{-2}$ ). This leads to ragged emitter:base junction regions which in places could produce very thin base widths. The result of locally enhanced emitter diffusion is often termed an "emitter spike".

2. Decorated dislocation (after Goetzberger & Shockley (1960) and Queisser & Goetzberger (1965) model of metallic decoration of dislocations)

Differences between the D.C. and T.I. slices can be summarised as

- a) The T.I. slice gave a better visual correlation between slip and premature breakdown, and a higher  $\chi^2$  value than did the D.C. slice.
- b) The softer breakdown characteristics and lower  $BV_{CEO}$  values of the T.I. slice c.f. to D.C. slice - compare Figs.9.2(a) and (b).
- c) Although the base widths were the same, the T.I. slice gave much higher Cu plating levels during bevel and staining - compare Figs. 10.22(a) and (b).

These results suggest that the T.I. slice may be more heavily contaminated with impurities than the D.C. slice. There is some evidence that crystal defects are only troublesome electrically if decorated with impurity atoms. The bad effect of fast diffusing metal contaminants such as Fe, Cu and Au has been known for some time. Impurities can be present in the starting material or on the surface, or can be introduced during device fabrication. The importance of "gettering" techniques to remove impurities is well-established, e.g. Meek, Seidel & Cullis (1975). Impurity atoms are attracted to dislocations, i.e. they have binding energies up to 1eV (Bullough & Newman 1963). Thus dislocations may only be important electrically because of the cloud of impurities which could be associated with them. It has been noted in Section 8.1.1. that the effect of "clean" dislocations on conductivity in bulk Si is small and that the most convincing correlations established to date between device failure and defects have involved precipitation (section 8.1.2). Unfortunately, no precipitation at dislocations on either slice was detected by TEM and no significant differences in BEVE mode SEM were noted between T.I. and D.C. chips. The junction depths (Fig.10.22) and the sheet resistances (Table 10.6) of both slices were similar and the differences outlined above are relatively small.

No benefit will be achieved by further speculation on these points. Until techniques are developed which can (a) identify small numbers of atoms at any position in a crystal or (b) determine by diffraction contrast analysis whether a defect is "decorated" with sub-precipitate levels of impurity, the answers to these and similar problems will remain unsolved.

Perhaps the most promising technique currently available is in-situ energy-dispersive X-ray analysis in TEM. Here X-ray energy spectrum of the specimen, generated by the incident electron beam, is analysed by comparison with the standard spectra of elements. Such facilities are available as bolt-on attachments to the current generation of both scanning and transmission electron microscopes, but the detection sensitivity of the technique is not at present sufficient for the detection at Cottrell atmospheres of impurities at dislocations.

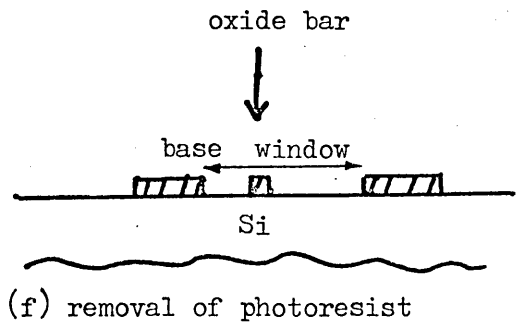
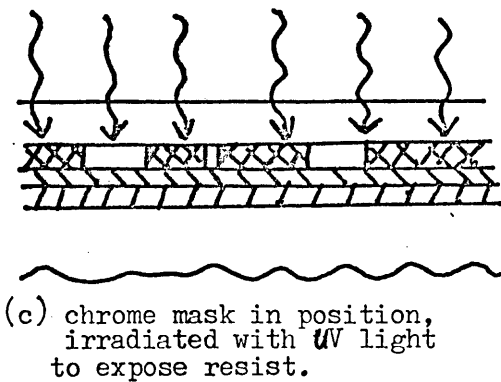
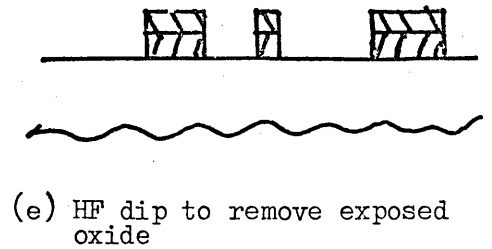
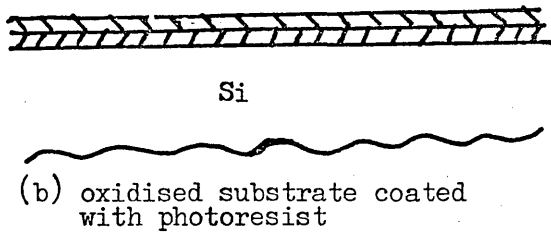
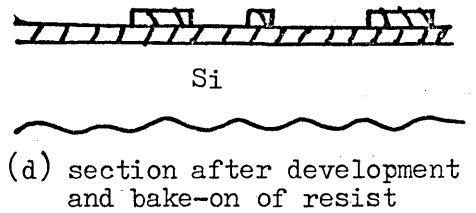
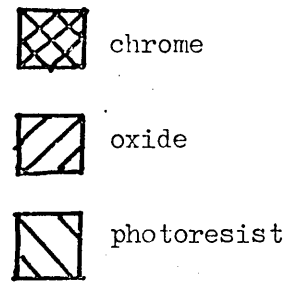
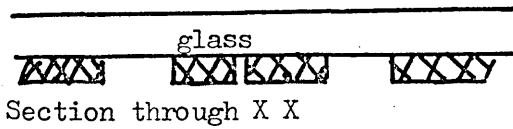
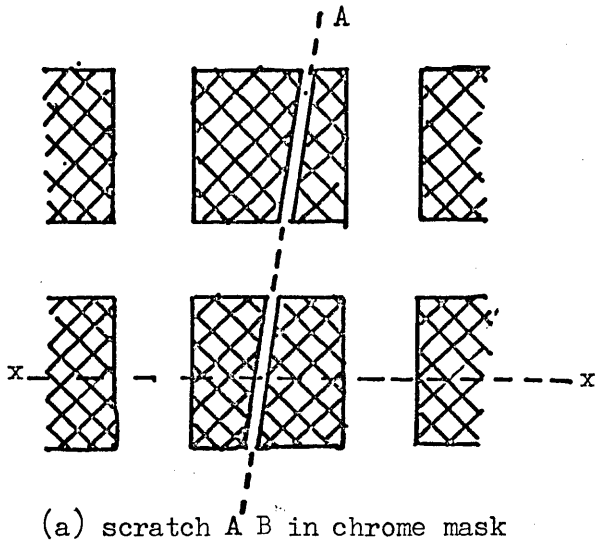
### 11.3. Photoengraving faults.

The origin of the oxide bar faults in base regions of phototransistors as shown in Figs. 9.6 and 10.4. will now be explained. They are caused by scratch damage on the chrome mask used for the photoengraving step to cut the base windows in the initial thick oxide layer grown on the slice. This results in photoresist being exposed in the scratch regions, e.g. along line AB, Fig.11.1(a) and so the photoresist remains behind when the photoresist is developed. During subsequent immersions in HF to remove oxide from the unexposed (i.e. chrome-masked) areas which are designated as the base regions of the devices, the "scratched" regions remain as bars of oxide, Figs. 11.1(b) to (f) show the fabrication steps.

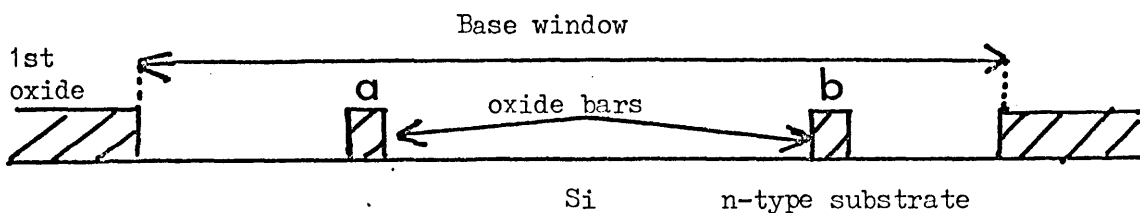
Identifying the "scratch" features as oxide immediately explains why they cause catastrophic failure when located in the emitter regions of the device. Fig.11.2 shows cross sections through a device which contains oxide bars which lie (a) in the region which becomes the emitter (b) within the base region, during subsequent diffusion steps. During each diffusion the oxide bars protect the underlying Si from dopants. In case (b) where the bar is contained within the base region this merely reduced the area of the base: collector junction but in the case (a) where the bar lies in the emitter, the region below its edge provides contact between the  $n^+$  emitter and the  $n^-$  substrate which comes to the surface here with no intervening p-type base region.

Of course, device failure due to this photoengraving fault will always occur at the same position on the slice when the same chrome mask is used for the initial cutting of the base windows. The lesson to be learnt then is that masks must be handled with extreme care to avoid damage or contamination. Replacement, depending on the complexity of the device, can be costly.

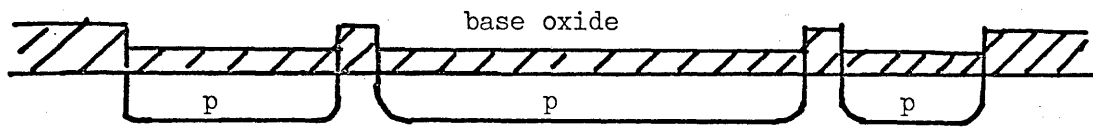
Formation of oxide bar photoengraving faults in base window



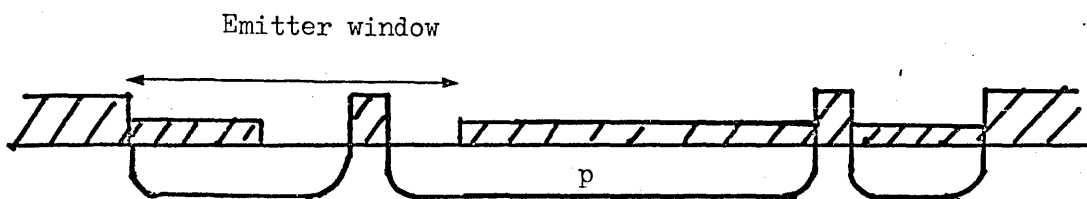
Effect of oxide bars on diffusion fronts



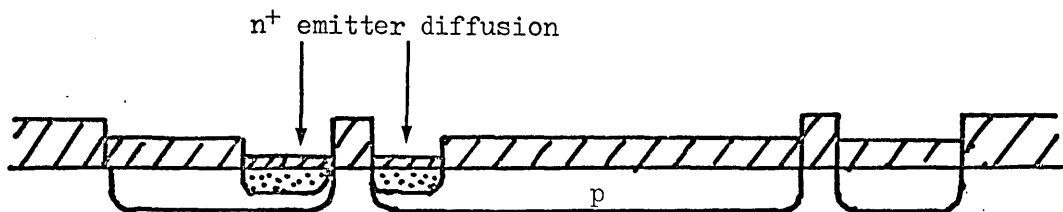
(a) base window cut in initial oxide



(b) boron base diffusion



(c) Emitter window cut



(d) Phosphorous emitter diffusion

The above explanation raises an interesting point. If dust or contamination patches are present in the base window during base diffusion, they could cause a similar effect to residual oxide, i.e. the absence or very low concentrations of dopant. The following emitter diffusion at a much higher concentration may penetrate to the substrate even if these contaminants were not removed during cleaning and cutting emitter windows. Thus as in the case of oxide "scratches" dead shorts or collector : emitter pipes will occur if these contaminants lie in regions designated to become the emitter. Another possible cause of C : E pipes, as noted in Section 10.3.1. is alloying of the Al contacts into the emitter region.

#### 11.4. Photo current and defects

No correlation was found between slip and photocurrent response as noted in Section 10.4.3. Dislocations locally reduce the BEVE current, i.e. carrier pairs created by the SEM beam and so could be expected to have a similar effect on photo-voltaic currents. If the effect is present, it seems to be quite small. However, calculation of the total area occupied by spot contrast in BEVE mode even in a heavily slipped size shows that there is only about 10% coverage. Thus if the effectiveness of the dislocation sites as recombination centres is similar for the barrier photo and electron voltaic effects, photocurrents may be relatively unaffected by slip. Certainly much more important is the damaging effect of SEM examination on photocurrents as shown in Section 10.4.3. Traps created by the scanning electron beam at the oxide : silicon interface are believed to be responsible for the degradation. Because of the strong absorption of visible light in Si, most of the carrier pairs will be generated by incident photons close to the Si surface and so traps here will be very efficient at recombination.

Pease & Galloway (1974) have noted a degradation in gain  $\beta$  of bipolar transistors during SEM examination. The effect was enhanced by biasing the device during SEM viewing. Gains as low as 20% of un-irradiated specimen gains were recorded. Current leakage was increased by a factor of 10 after prolonged SEM examination.

#### 11.5. Summary

Dislocations were observed in active areas of a Si device using BEVE contrast in SEM. A 1 to 1 correlation was established, to the limits of resolution of each technique, between contrast spots in conductive mode SEM and individual dislocations as revealed by XRT. The high

resolution of TEM, however, has shown that dislocations usually form interacted structures. Both thermally - and diffusion - induced dislocations were observed in the processed slices and there is evidence that the former dislocations can transform into helices during the diffusion process. Significant correlations between heavily slipped areas and device leakage were found but the reasons remain speculative. Differences in electrical behaviour between devices from the two wafers examined could not be explained by the structural work in this study. Photocurrent response did not appear to be affected by slip, although it was badly degraded by SEM examination.

Oxide bars, characterised by SEM, were shown to cause catastrophic device failure when located in the emitter region. These artefacts were thought to be caused by scratched photoengraving masks - the mechanism proposed for their effect on the  $p^+ n p$  device structure suggests that contamination of the slice surface could have a similar effect.

CHAPTER 12. CONCLUSIONS

Part I of the thesis was concerned with a rather narrow subject : the growth of Si epilayers under closely specified conditions. The contract under which the work was carried out terminated when interest in obtaining hyper-abrupt junctions by low temperature epitaxial deposition lost priority to competing problems. However, with the introduction of ion implanted substrates, defects in epilayers again have become a serious problem. Experience gained with the earlier work has been valuable in dealing with this new challenge. Recent publications by the author (Ogden (1975, 1976), Baker & Ogden (1975)) underlies the continuing interest in this subject at Caswell.

The multitechnique approach used in Part II yielded much information on the electrical and structural defects in two phototransistor device slices. Some indication was given of the continual improvement to the microscopy techniques: TEM, XRT & SEM. A current investigation involved a combination of XRT, TEM and optical microscopy to observe stacking faults and dislocations at leakage sites in charge-coupled devices (CCDs). In these devices minute leakage currents can be detected and calculation shows that only a few picoamps leakage current is associated with each stacking fault (Ogden & Wilkinson 1977). This is about three orders of magnitude lower than currents associated with the diodes of Ravi and co-workers (1973). Greater emphasis must now be given to the detection and assessment of chemical impurities associated with defects.

As an exercise in obtaining results which could be directly applied to yield improvement, the present study underlined two points which are well-recognised in general terms in the industry.

1. Thermal slip correlates with device leakage and should be minimised.
2. Good care must be taken of photoengraving masks as scratch damage is a yield hazard. Device yields in excess of 70% obtained on the slices in this study were considered acceptable for discrete transistors as the required production target was relatively low. Consequently no major effort was undertaken to improve processing.

Shortly after the present investigation was concluded, slip was shown to correlate with failure in integrated circuits (I.Cs) incorporating high frequency bipolar transistors at Caswell. The technique of comparing yield maps with XRT micrographs used in the present study was applied with similar success. Serious efforts are now being made to reduce slip. It cannot be claimed that this effort comes solely as a result of the present study but it helped. Improvements to device processing, especially in cleanliness and tighter process control, have eliminated several yield hazards which were not structure dependent. The manufacture of I.Cs involves many more process steps and is very exacting compared with the fabrication of phototransistors and hence, potentially, more problems are created. Even so, it is becoming clear to production personnel that in the absence of "cosmetic" defects such as photoengraving errors and process steps outside of specification, crystal imperfections such as dislocations, stacking faults and precipitates must be given serious consideration. To this advance, work like that reported here, has made a useful contribution.

APPENDIX A

DIFFRACTION CONTRAST ANALYSIS IN TEM

Defects, in general, introduce strain fields or phase boundaries in the lattice which perturb the interaction between transmitted and diffracted electron beams, i.e. bright or dark field respectively. Comparison of images of defects formed using different Bragg reflections, i.e. different diffraction vectors ( $\underline{g}$ ) makes possible the characterisation of the defects. The standard reference for this diffraction contrast analysis is Hirsch et al (1965). Computer generation of theoretical intensity profiles of a given defect in a single crystal foil under specific viewing conditions is employed. For a perfect dislocation with Burgers vector  $\underline{b}$  this leads to the invisibility criteria,

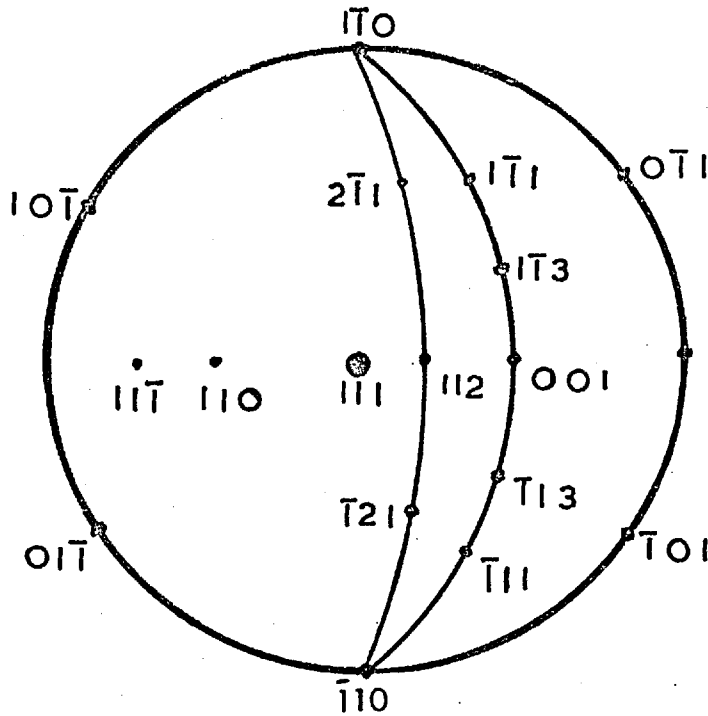
$$\left. \begin{array}{l} \underline{g} \cdot \underline{b} = 0 \\ m \leq 0.08 \end{array} \right\}$$

where  $m = \frac{1}{8} (\underline{g} \cdot \underline{b} \wedge \underline{u})$ , and  $\underline{u}$  is unit vector along the direction of the dislocation line. Extension of the theory to account for the contrast at partial dislocations, i.e. dislocations which formed stacking faults, added the invisibility criterion  $\underline{g} \cdot \underline{b} = \pm \frac{1}{3}$ , whereas in the cases of  $\underline{g} \cdot \underline{b} = \pm \frac{2}{3}$  or  $\pm \frac{4}{3}$  the partial dislocations were visible, provided the deviation  $s$  from the exact 2 beam Bragg reflection condition was small (Silcock & Tunstall 1964).

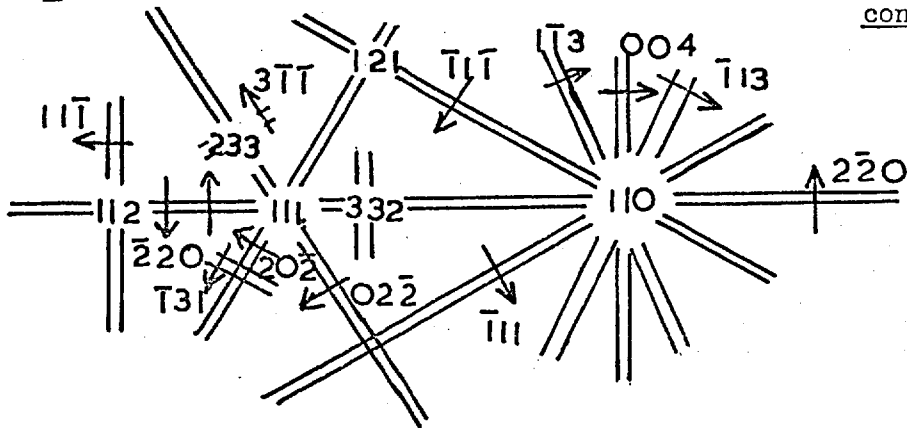
A.1 . STACKING FAULT RIBBONS

The analysis of Frank extrinsic loops in  $\{110\}$  oxidised Si by Booker & Tunstall (1966) has been closely followed in the first part of the present analysis of the type of stacking fault structures shown in Fig.3.4. For this purpose, the specimen was wedged at an angle in the cartridge so that the  $[110]$  zone could be reached using the tilt available. Fig.A1(a) is a  $[111]$  stereogram for a cubic crystal showing the great circles of the  $[11\bar{1}]$  and  $[110]$  poles and Fig.A1(b) is the Kikuchi map of this region. Fig.A1(c) shows the Thompson tetrahedron, which consists of  $\{111\}$  planes bounded by  $\langle 110 \rangle$  directions, in the same orientation as the stereogram. The concept of the Thompson tetrahedron is developed in section A1.2.3. Care was taken to select faults for analysis which were not overlapping, e.g. faults marked D in Fig.A3(a) and it was attempted to take all micrographs in the exact 2 beam  $s = 0$  position.

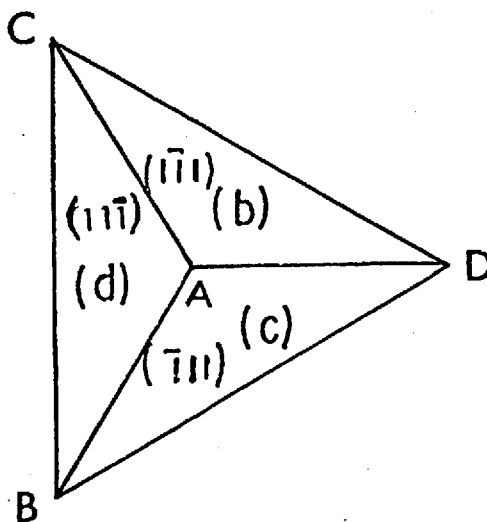
a)  $[11\bar{1}]$  Stereogram of cubic crystal, showing great circles of  $(11\bar{1})$  and  $(110)$  planes.



b) Kikuchi map of 110/111/112 poles showing reflections used in diffraction contrast analysis.



c) Thompson tetrahedron correctly oriented with respect to a), apex A pointing up.



### A.1.1. NATURE OF THE FAULTS

The stacking faults were shown to lie on inclined  $\{111\}$  planes by simple trace analysis. The specimen was tilted in turn to the three  $\langle 211 \rangle$  poles which lie at  $\sim 19^\circ$  from  $[111]$  and micrographs were taken using  $\{111\}$  reflections. For each 111 reflection, one set of faults appeared as edge-on traces perpendicular to  $g$ , for example, faults marked A in Fig.A3(c) lying on  $(11\bar{1})$  become short lines using  $g = [11\bar{1}]$ , arrowed in Fig.A3(g). The  $\langle 111 \rangle$  directions are thus shown to be the normals to the planes on which the faults lie. The two stacking faults chosen for analysis in the  $[110]$  zone are shown in Fig.A2. The reflections have been indexed so that the faults lie on  $(11\bar{1})$  planes, and this also applied to the faults marked A shown in Fig.A3. The faults showed fringe contrast for  $\bar{1}1\bar{1}$ ,  $\bar{1}11$ , and 004 reflections, but fringe contrast was absent for  $2\bar{2}0$ ,  $1\bar{1}\bar{3}$  and  $\bar{1}13$  reflections. Fringe contrast is due to a phase change  $\phi = 2\pi g \cdot R$  occurring when the electron beam traverses a stacking fault which is inclined to the plane of the foil.  $R$  is the displacement of the crystal below the fault, upwards for an intrinsic and downwards for an extrinsic fault. No fringes will occur when  $g \cdot R$  is zero or an integer and it follows from the absence of fringes in Figs.A2e and f) that  $R = \pm \frac{1}{3} [11\bar{1}]$ , the sign depending on the intrinsic (+) or extrinsic (-) nature of the fault. A lattice translation vector of  $\frac{1}{2} \langle 110 \rangle$  can be added to  $R$  for a stacking fault produced by slip in the  $(11\bar{1})$  plane. This does not alter the observed fringe contrast and means that the displacements  $\frac{1}{3} [11\bar{1}]$ ,  $\frac{1}{6} [112]$ ,  $\frac{1}{6} [1\bar{2}1]$  and  $\frac{1}{6} [\bar{2}1\bar{1}]$  are indistinguishable except by analysis of the bounding partial dislocations. The absence of residual fringe contrast in Figs. A2e), f) is evidence that little precipitation could have occurred to modify the displacement from the ideal stacking fault case, i.e.  $\leq 2\%$  of  $R$ . The intrinsic or extrinsic nature of the faults follows from the contrast of the outer fringes of the stacking faults. Contrast is symmetrical in bright field, i.e. both the outer fringes are white or both are black corresponding to  $\phi = + \frac{2\pi}{3}$  or  $- \frac{2\pi}{3}$  respectively. When the inclination of the faults is established, i.e. top and bottom with respect to the electron beam, the intrinsic or extrinsic nature of the fault can be determined. The fault inclination can be found using 3 methods:

ANALYSIS USING SEPARATIONS IN  $[110]$  ZONE

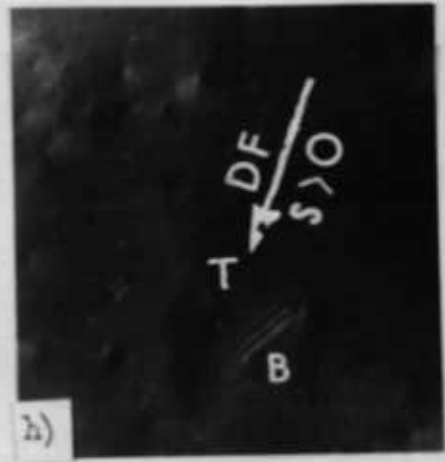
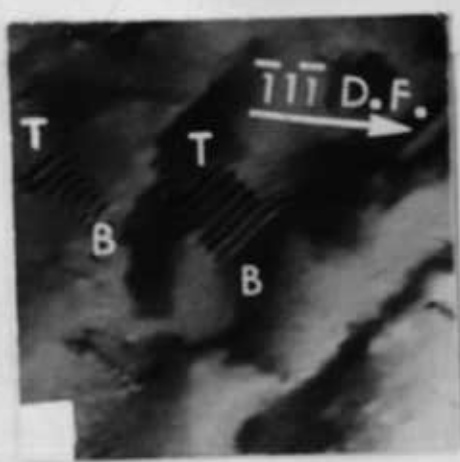
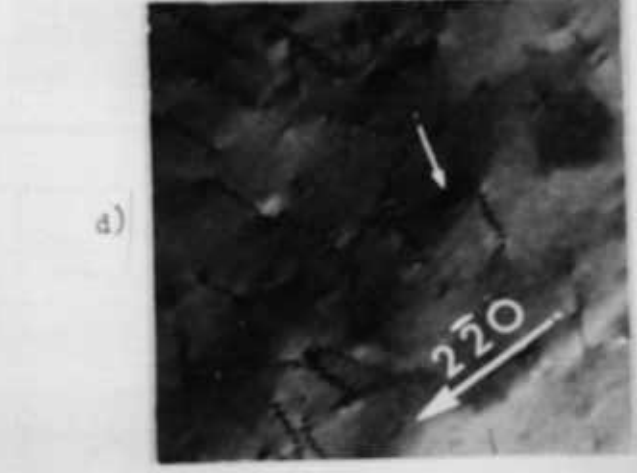
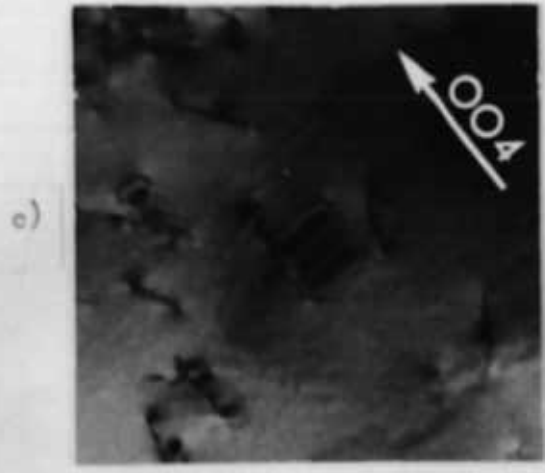
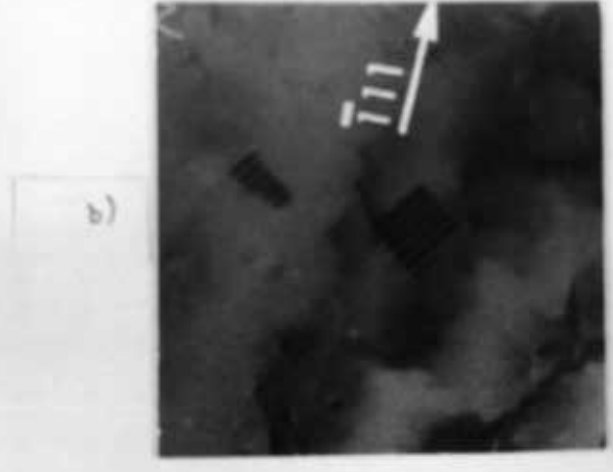
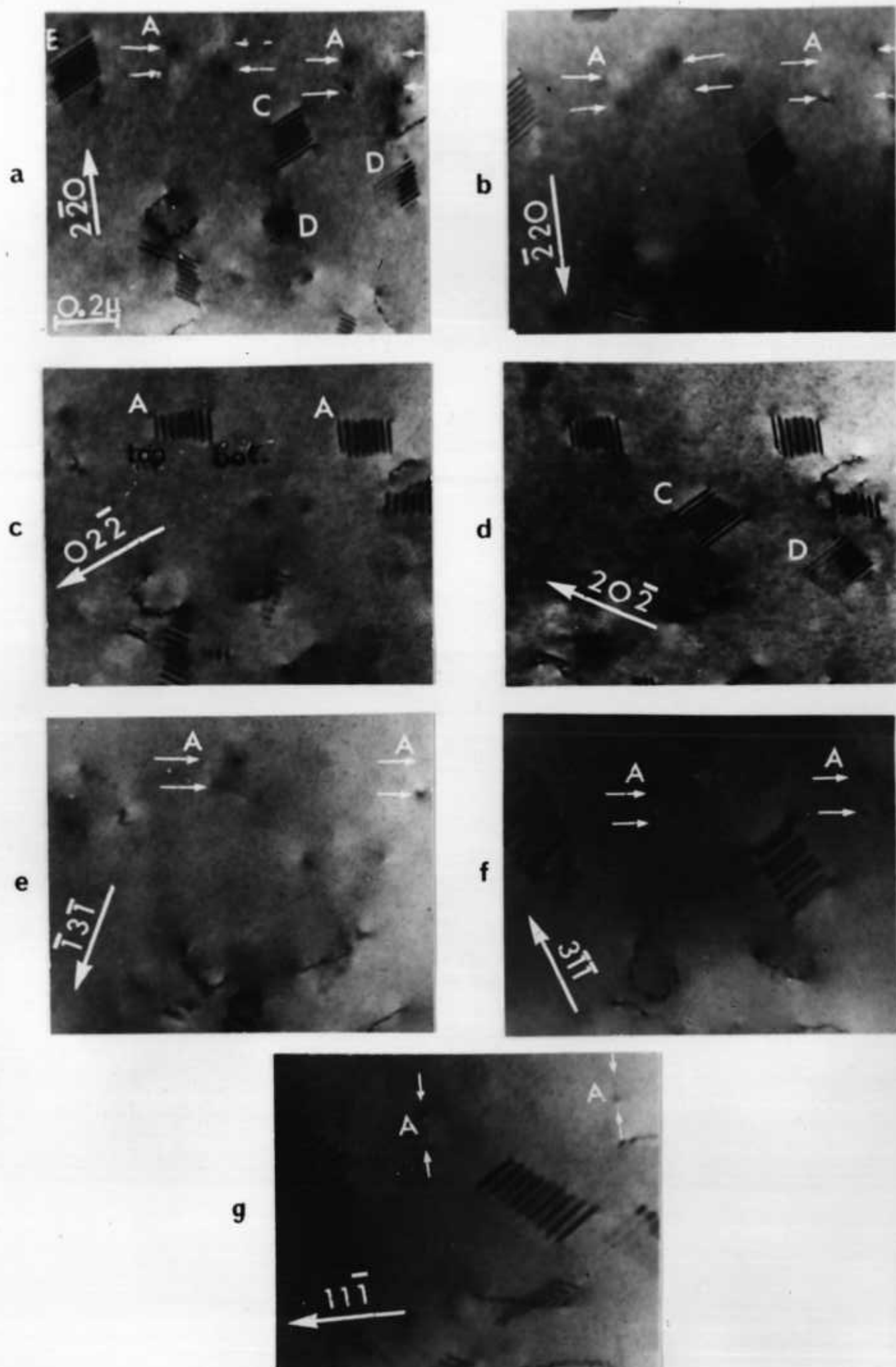


FIG. A3  
ANALYSIS USING REFLECTIONS IN OR NEAR  $[111]$  ZONE



a) The Kikuchi map, Fig.A1b), can be plotted by tilting the specimen in the diffraction mode, and the stereogram orientation can be fixed with respect to the crystal, Fig.A1a). This gives the direction of the upward normals to the  $\{111\}$  planes and enables the Thompson tetrahedron to be drawn, Fig.A1(c). Note that the (111) spot pattern alone cannot be used since it shows six-fold, not three-fold symmetry.

b) In dark field, the outer fringe contrast is asymmetric, i.e. one fringe is black and the other fringe is white and the fringe which changes contrast on going from bright to dark field is located at the bottom of the foil with respect to the beam. Thus comparing Figs.A2a) & g) shows that the RH fringe is at the bottom of the foil.

c) Deviation from the  $s = 0$  condition in dark field enhances the contrast at the top ( $s < 0$ ) or bottom ( $s > 0$ ) of the foil. (Bell & Thomas 1965). Thus Figs.A2h) and i) show stronger fringe contrast at the bottom and top of the foil, marked B and T respectively.

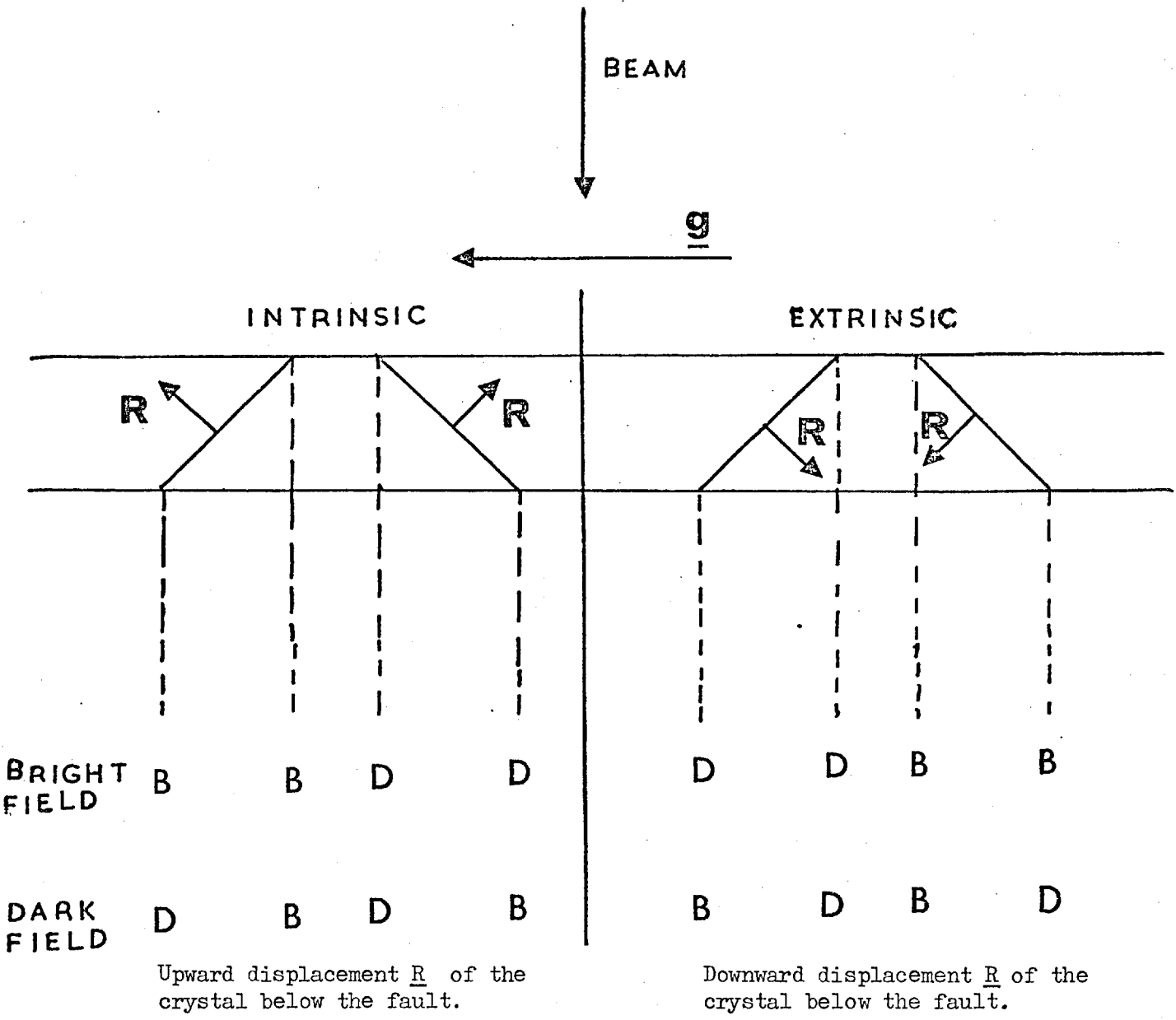
The intrinsic or extrinsic nature of the faults can then be deduced from the sense of  $g$  across the faults. Fig.A4 shows how bright (B) or dark (D) outer fringes result from each type of fault. Examination of fringe contrast in Figs.A2(a), g), h) and i) show that both stacking faults are extrinsic. Similar micrographs, not shown in Fig.A3, established that the faults marked A were also extrinsic. The extrinsic nature of the faults can be deduced from the dark field image alone when the direction of  $g$  is known, using the rule of Gevers, Art & Amelinckx (1963). Thus for both 111 and 220 type reflections, the bright leading fringe in the sense of  $g$  (Fig.A2g) means the fault is extrinsic, irrespective of the slope of the fault.

#### A.1.2. BOUNDING PARTIAL DISLOCATION ANALYSIS

The series of micrographs shown in Figs.A2 and A3 are presented as proof that the stacking faults are bounded by Shockley partials. Table A1 gives  $g \cdot b$  values of the possible Burgers vectors of the partials.

[110] zone. The partials show strong contrast for 004,  $\bar{1}\bar{1}\bar{3}$  and  $\bar{1}\bar{1}3$  reflections, but are invisible for  $\bar{1}\bar{1}\bar{1}$  and  $\bar{1}\bar{1}1$  reflections, Fig.A2. Reference to Table A1 eliminates the Shockley partials  $\pm \frac{1}{6} [\bar{1}21]$  and  $\pm \frac{1}{6} [2\bar{1}1]$  since each of these partials should be visible for one set of  $\{111\}$  and  $\{311\}$  reflections when  $g \cdot b = \pm 1$  or  $\pm \frac{2}{3}$  and invisible for the other set where  $g \cdot b = 0$  or  $\pm \frac{1}{3}$ .

Outer fringe contrast of intrinsic and extrinsic stacking faults using  
2 beam,  $s = 0$  diffraction conditions



B = bright outer fringe  
 D = dark outer fringe

TABLE A1

g.b values of possible partials bounding stacking faults on (111) planes

$\frac{b}{g}$	$\pm \frac{1}{3} [11\bar{1}]$	$\pm \frac{1}{6} [\bar{1}\bar{1}2]$	$\pm \frac{1}{6} [\bar{1}21]$	$\pm \frac{1}{6} [2\bar{1}1]$
$\bar{1}\bar{1}\bar{1}$	$\pm \frac{1}{3}$	$\pm \frac{1}{3}$	$\pm \frac{1}{3}$	$\pm \frac{2}{3}$
$\bar{1}11$	$\pm \frac{1}{3}$	$\pm \frac{1}{3}$	$\pm \frac{2}{3}$	$\pm \frac{1}{3}$
004	$\pm \frac{4}{3}$	$\pm \frac{4}{3}$	$\pm \frac{2}{3}$	$\pm \frac{2}{3}$
$1\bar{1}\bar{3}$	$\pm 1$	$\pm 1$	0	$\pm 1$
$\bar{1}13$	$\pm 1$	$\pm 1$	$\pm 1$	0
$2\bar{2}0$	0	0	$\pm 1$	$\pm 1$
$02\bar{2}$	$\pm \frac{4}{3}$	$\pm \frac{1}{3}$	$\pm \frac{1}{3}$	$\pm \frac{2}{3}$
$20\bar{2}$	$\pm \frac{4}{3}$	$\pm \frac{1}{3}$	$\pm \frac{2}{3}$	$\pm \frac{1}{3}$
$\bar{1}\bar{3}\bar{1}$	$\pm 1$	0	$\pm 1$	$\pm 1$
$3\bar{1}\bar{1}$	$\pm 1$	0	$\pm 1$	$\pm 1$
$11\bar{1}$	$\pm 1$	0	0	0

accessible from  
 $[110]$  zone

accessible  
 $[111]$  zone

### $\bar{2}20$ reflection

The  $\frac{1}{3}$   $[11\bar{1}]$  Frank partial is eliminated using the  $\bar{2}20$  reflection, Fig.A2(d). Booker & Tunstall (1966) and later Laister & Jenkins (1969) working on GaAs, used this reflection to identify Frank partials, where for this case  $m$  has a large value, approaching the maximum of  $\sim 0.2$  when  $g$ ,  $b$  &  $u$  are mutually perpendicular. But  $m$  is zero for the three Shockleys since  $g$ ,  $b$  and  $u$  are coplanar, i.e. all lie on  $(11\bar{1})$ . 'm' term contrast is strongest where the leading partial in the sense of  $g$  intersects the top surface of the foil and where the trailing partial intersects the bottom surface of the foil. Thus image contrast reversal occurs when  $g$  is reversed from  $\bar{2}20$  to  $2\bar{2}0$ . In the present analysis, although  $u$  is generally favourable for strong 'm' term contrast for a Frank partial, i.e.  $u$  lies near to  $[112]$ , very little contrast is observed. The black patch, arrowed in Fig.A2(d) at one end of a partial, is the only contrast observed. On reversing  $g$  (not shown), no contrast at all was detected.

### $[11\bar{1}]$ zone

Examples where patchy contrast at the partials is stronger using  $\bar{2}20$  and  $2\bar{2}0$  reflections is shown arrowed in Fig. A 3a) & b). It can be seen that, at least for the fault on the left, the patchy contrast reverses with  $g$  reversal, but knowing the fault inclination, the black contrast is at the opposite surface to that expected from a Frank partial, i.e. the leading partial shows a black patch at the bottom surface. Thus the partials are not Franks and it is probable that the residual contrast is caused by surface relaxation effects. Tunstall, Hirsch & Steeds (1964) have shown that screw dislocations in silver perpendicular to the foil, i.e. lying parallel to the beam, give strong black and white patches at their intersection with the foil surface. As in that case, the remaining  $\frac{1}{6}$   $[112]$  Shockley partials are largely in screw orientation and are also steeply inclined to the foil surface. Although there is a line of zero contrast parallel to  $g$ , the patches in Figs. A 3a) & b) would be more accurately described as black/black or white/white. Head (1967) has shown that inclined dislocations in  $\beta$ -brass can produce patchy contrast even when  $g \cdot b$  and  $m$  are both zero. His technique of computer-generated imaging, an extension of the earlier profiling technique

of Howie & Whelan (1962), is being increasingly adopted. He was able to predict subtle contrast variations of dislocations observed under closely defined tilt conditions. Undoubtedly, application of this imaging technique to the present work would have been useful, but was not attempted. At the time when the analysis was being performed, suitable computer programmes were not generally available and it was felt to be beyond the scope of the project.

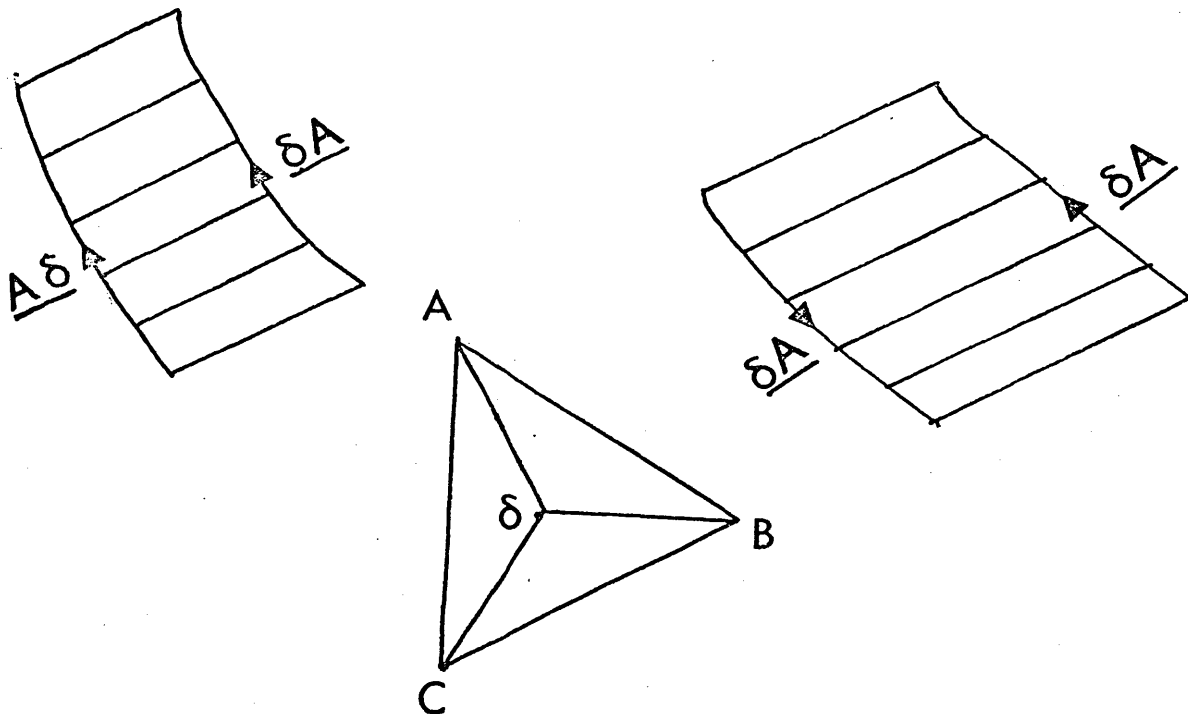
The series of micrographs Figs A3c) to g) confirms the  $\frac{1}{6} [112]$  Shockley partial since in no case is dislocation contrast observed at the faults, although faint lines, possibly due to decoration, are visible along part of the bounding partials in Fig.A3e) (arrowed). Table A1 shows that the Frank partial should be visible in all of these micrographs and the previously eliminated Shockley partials should also be visible in most of them. Clareborough (1971) has pointed out that partials may be invisible for  $g \cdot b = \pm \frac{2}{3}$  under certain conditions, but Table A1 shows that there are sufficient cases where  $g \cdot b$  is zero or an integer to establish the Burgers vectors of the partials without using this value.

#### A.1.2.3. THE THOMPSON TETRAHEDRON

Figs.A5a) & b) represent the stacking fault ribbons shown in Figs.A2 and A3 respectively, using the Thompson notation for the Burgers vectors of the Shockley partials. The Thompson tetrahedron (Thompson 1953, Hirth & L othe 1968) Fig.A6 has  $\{111\}$  glide plane faces and the edges AB, CD etc. are in  $\langle 110 \rangle$  orientation and have length  $\frac{1}{2} \langle 110 \rangle$ , thus representing the Burgers vectors of perfect dislocations in diamond-cubic crystals. The mid-points of the faces opposite A,B,C & D are labelled  $\alpha, \beta, \gamma$  &  $\delta$  respectively and the plane ABC is denoted by (d) etc. on the outside surface and ( $\bar{d}$ ) etc. on the inside surface. Shockley partial dislocations have Burgers vectors of  $\frac{1}{6} \langle 211 \rangle$  and are represented by vectors such as  $\underline{\delta B}$  whilst Frank partial dislocations have Burgers vectors of  $\frac{1}{3} \langle 111 \rangle$  and are represented by vectors such as  $\underline{\delta D}$ . An extension to the normal FS/RH Burgers circuit definition (Fig.A7(a)) is required to distinguish between intrinsic and extrinsic stacking faults. Consider a perfect dislocation lying in glide plane (d) with Burgers vector  $\underline{AB}$  which splits into two partial dislocations separated by an

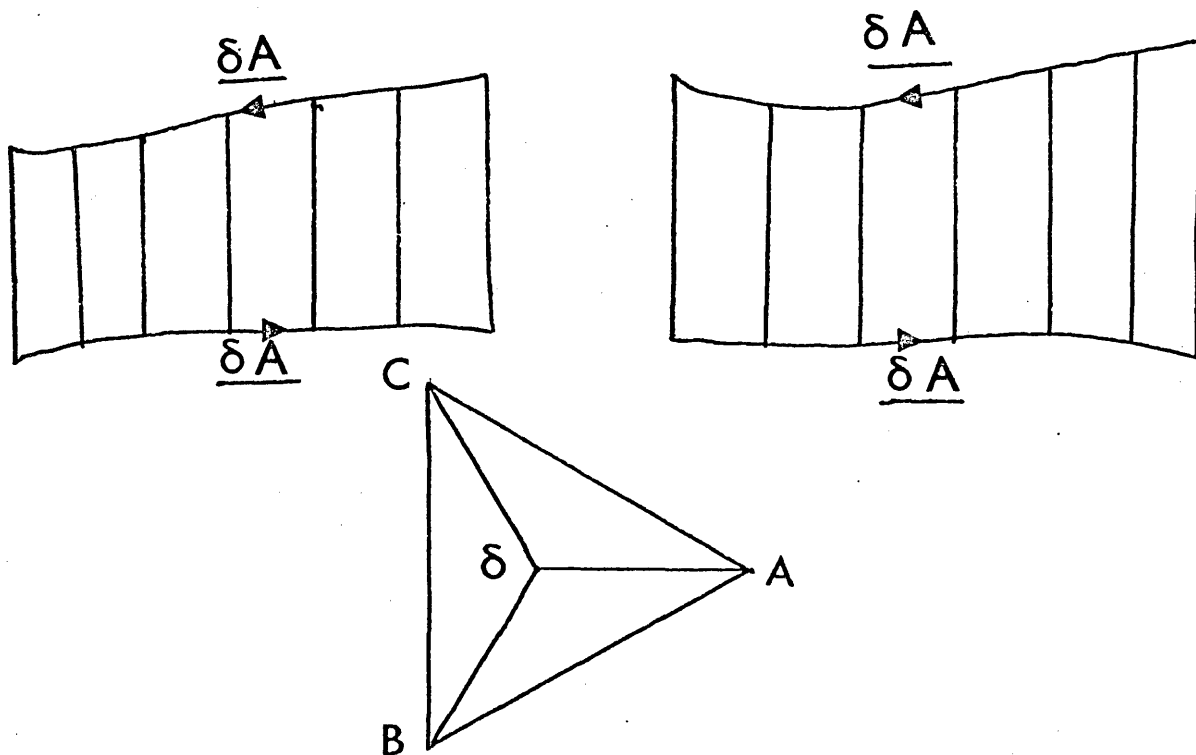
a) Stacking fault ribbons  
in Fig. A2

Burgers vectors of Shockley  
partials. Direction of dis-  
location line u shown by arrows.



$\underline{BC} = \frac{1}{2} [1\bar{1}0]$	$\underline{\delta A} = \frac{1}{6} [112]$
$\underline{CA} = \frac{1}{2} [011]$	$\underline{\delta C} = \frac{1}{6} [1\bar{2}1]$
$\underline{BA} = \frac{1}{2} [101]$	$\underline{\delta B} = \frac{1}{6} [\bar{2}11]$

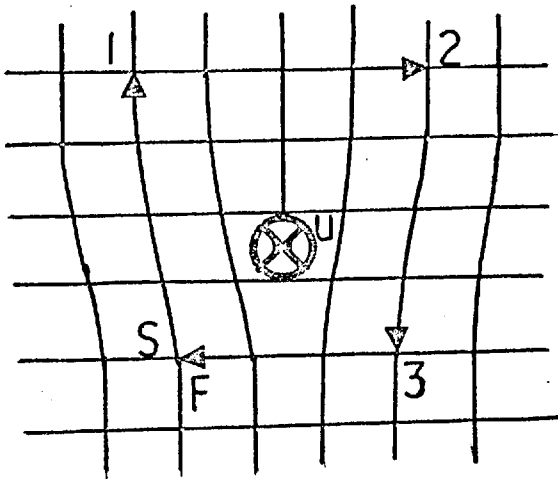
b) Stacking fault ribbons  
marked A in Fig. A3



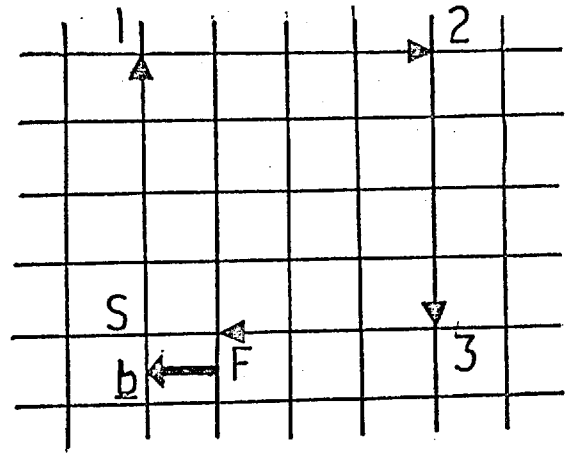
Viewed from outside Thompson tetrahedron.



- a) Finish/Start, Right Hand (FS/RH) (perfect crystal) convention for Burgers circuit to define the Burgers Vector of a dislocation.

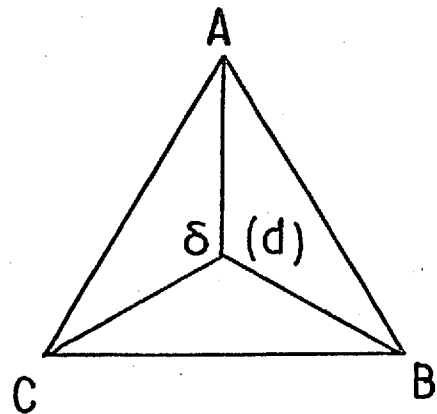
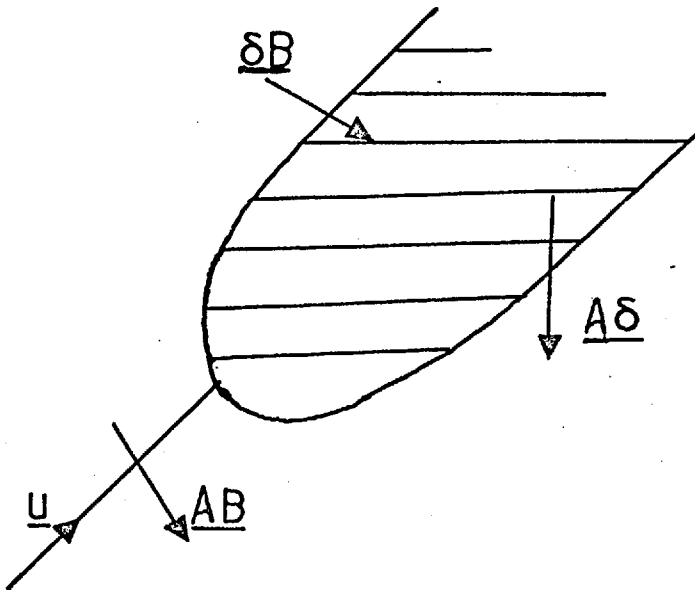


edge dislocation,  
direction u into paper



perfect crystal

- b) Extended dislocation  $AB = A\delta + \delta B$  on glide plane (d) enclosing an intrinsic stacking fault.



intrinsic stacking fault, Fig.A7(b), i.e. forms an extended dislocation. The dislocation is viewed from outside the tetrahedron along the positive direction u of the dislocation line. Then if the directions of partials are defined in a similar way to the perfect dislocation, their Burgers vectors have Roman/Greek letters for the right-hand partial, i.e. A $\delta$ , and Greek/Roman letters for the left-hand partial, i.e.  $\delta$ B. Reversal of any one of these conditions would define an extrinsic stacking fault. Care must be taken to define all conditions when considering the interaction of stacking faults on adjacent planes to ensure that the stair-rod product is correct. Referring back to Fig.A5, the ribbon faults can be regarded as being bounded by Shockley partials having equal but opposite Burgers vectors A $\delta$  and  $\delta$ A as in the fault on the left in Fig.A5(a), or alternatively as loops with Burgers vectors  $\delta$ A truncated by the foil surfaces as shown the remaining stacking faults in Fig.A5. As can be seen from the diagram, the partial dislocations lie largely in screw orientations, i.e.  $\delta$ A//u.

#### A2 INCLINED DISLOCATIONS

The high density of undissociated dislocations in layers grown with ethylene contamination at low temperatures, in addition to ribbon faults, has been noted in section 3.2. There are two prominent dislocations close to the stacking fault on the right in Fig.A2. Unfortunately these dislocations are only extinguished by the  $\bar{1}\bar{1}\bar{1}$  reflection and reference to Table A2 shows that of the 6 possible  $\frac{1}{2}\langle 110 \rangle$  Burgers vectors, only 4 can be eliminated and a choice cannot be made between  $\pm \frac{1}{2} [10\bar{1}]$  and  $\pm \frac{1}{2} [01\bar{1}]$ .

TABLE A2

g.b. VALUES OF PERFECT DISLOCATIONS FOR  $[110]$  ZONE REFLECTIONS, Fig.A2

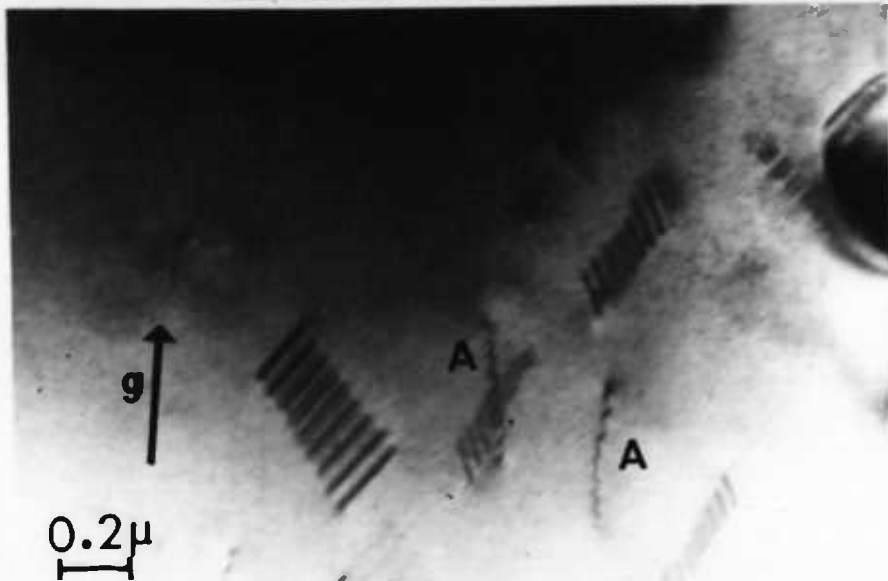
g	Observed contrast. Visible (v) Invis. (i)	b					
		$\pm \frac{1}{2}[110]$	$\pm \frac{1}{2}[\bar{1}\bar{1}0]$	$\pm \frac{1}{2}[\bar{1}0\bar{1}]$	$\pm \frac{1}{2}[10\bar{1}]$	$\pm \frac{1}{2}[01\bar{1}]$	$\pm \frac{1}{2}[0\bar{1}\bar{1}]$
$\bar{1}\bar{1}\bar{1}$	i	0	$\pm 1$	$\pm 1$	0	0	$\pm 1$
$\bar{1}11$	v	0	$\pm 1$	0	$\pm 1$	$\pm 1$	0
004	v	0	0	$\pm 2$	$\pm 2$	$\pm 2$	$\pm 2$
$2\bar{2}0$	v	0	$\pm 2$	$\pm 1$	$\pm 1$	$\pm 1$	$\pm 1$
$1\bar{1}\bar{3}$	v	0	$\pm 1$	$\pm 2$	$\pm 1$	$\pm 1$	$\pm 2$
$\bar{1}13$	v	0	$\pm 1$	$\pm 1$	$\pm 2$	$\pm 2$	$\pm 1$
$11\bar{1}$	-	$\pm 1$	0	0	$\pm 1$	0	$\pm 1$

The simplest way of analysing perfect dislocations is to use the three  $\{111\}$  reflections which lie in the  $\langle 211 \rangle$  zones at  $\sim 19^\circ$  to  $[111]$ . Extending the field of view of Fig.A3(g) shows the zig-zag contrast of several inclined dislocations, Fig.A8(a). Dislocations marked A in Fig.A8(a) and marked C in Fig.A8(c) are only visible in these particular micrographs. Thus from Table A2, dislocations A have  $\underline{b} = \pm \frac{1}{2} [110]$  and dislocations C have  $\underline{b} = \pm \frac{1}{2} [10\bar{1}]$ . Reference to the Thompson tetrahedron, Fig.A6, shows that these Burgers vectors are inclined to the  $(111)$  layer.

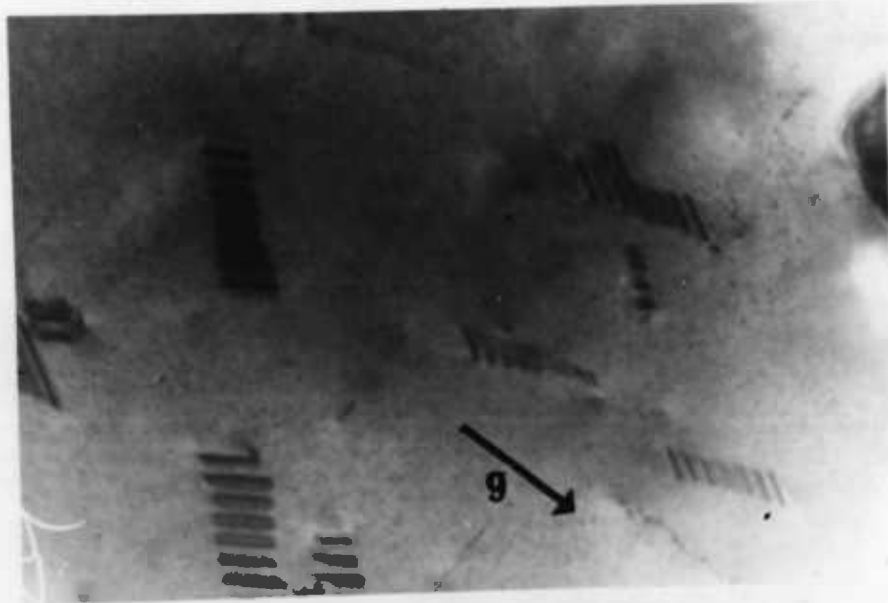
From their positions the dislocations appear to be largely screw in character. Similar analyses were performed on several sets of dislocations with the same result. Burgers vectors in the  $(111)$  epitaxial layer plane were not observed.

#### A3 STACKING FAULT PYRAMIDS IN $\{100\}$ EPITAXIAL Si

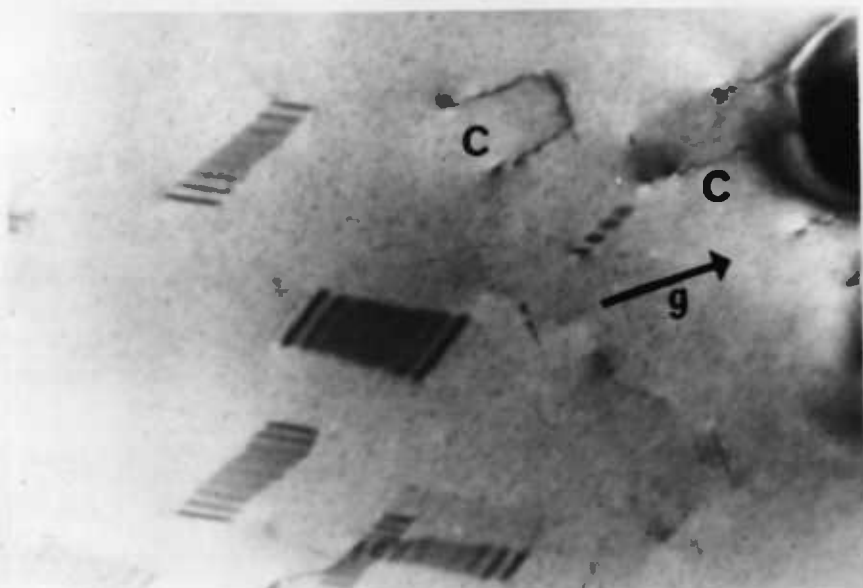
A most interesting postscript to the carbon contamination work has been a recent TEM investigation of thin epitaxial layers grown on  $\{100\}$  substrates which had been ion-implanted and oxidised (Ogden 1975, Baker & Ogden 1975). Stacking fault pyramids have been found which are different from the generally accepted view of alternate intrinsic and extrinsic faults. Analysis of the pyramids yields a result which is relevant to the present study and so is included here as an appendix.



a) Bright field ( $\bar{1}\bar{1}1$ ) reflection



b) Bright field ( $\bar{1}11$ ) reflection



c) Bright field ( $\bar{1}1\bar{1}$ ) reflection

A total dose of  $\sim 10^{16}$  arsenic ions/cm<sup>2</sup> was implanted with 100kV, 1 mA beam (at A.E.R.E. Harwell) in a 5- $\Omega$  p-type slice which was then oxidised at 1200°C for 2 hours. After removal of the oxide, an epitaxial layer  $\sim 0.5 \mu\text{m}$  thick was grown from silane at 1050°C in a conventional gas flow system. The stacking faults lie on all four inclined  $\{111\}$  planes and nucleate at the apex of the pyramid which is usually located at or near the substrate : epitaxial layer interface, and they intersect the surface of the layer to form a square base. Booker (1966) observing stacking fault fringe contrast using TEM, found that the pyramids consisted of alternate intrinsic:extrinsic stacking faults. It was pointed out that with this arrangement, low energy stair-rod dislocations with Burgers vectors  $\underline{b} = \frac{1}{6}\langle 110 \rangle$  formed at the inclined  $\langle \bar{1}10 \rangle$  intercepts, and a parallel was drawn with the intrinsic stacking fault tetrahedra formed in  $\{111\}$  epitaxial Si layers (Booker & Stickler 1963). We have found the occurrence of pyramids in  $\{100\}$  epitaxial Si layers, consisting of stacking faults which were all intrinsic.

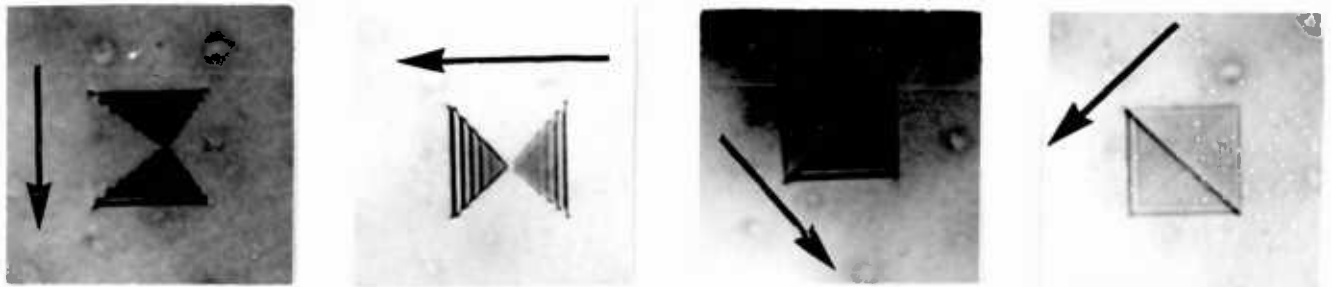
Figs.A9(a) and (b) show TEM micrographs of a stacking fault pyramid taken using bright field 220 type reflections in the 2 beam  $s = 0$  condition. It can be seen that the outer fringe contrast for each pair of stacking faults is identical when compared with the direction of the diffraction vector  $g$ . This means (from Section A1) that all four stacking faults must be of the same type. The intrinsic nature of the faults is established from the outer fringe contrast in dark field, Fig.A9(c), i.e. bright outer fringe away from the sense of  $g$ . Diffraction contrast analysis was then made to determine the Burgers vectors of the four stair-rod dislocations using reflections from  $[001]$ ,  $[11\bar{4}]$  &  $[\bar{1}\bar{1}4]$  zones in the  $s \gg 0$  condition. The series micrographs shown in Figs.A10(a) to (h) confirms that the stair-rods have  $\underline{b} = \frac{1}{3}\langle 100 \rangle$ . Table A3 gives  $g \cdot \underline{b}$  values of low energy stair-rods of  $\underline{b} = \frac{1}{6}\langle 110 \rangle$  and  $\frac{1}{3}\langle 100 \rangle$  type for the reflections used. Since partial dislocations show strong contrast for  $g \cdot \underline{b}$  values of  $\frac{4}{3}$ ,  $\pm \frac{2}{3}$  and  $\pm 1$ , it can be seen from the Table that one pair of stair-rods lying on  $[011]$  &  $[0\bar{1}1]$  has  $\underline{b} = \pm \frac{1}{3}[100]$  and the other pair lying on  $[101]$  &  $[\bar{1}01]$  has  $\underline{b} = \pm \frac{1}{3}[010]$ . Fig.A11 shows the crystallography of the pyramid and the Burgers vectors of the stair-rods. The energy of the partial dislocations is twice that of the

FIG.A9  
 Analysis of stacking fault pyramid in  $\{100\}$  epitaxial Si

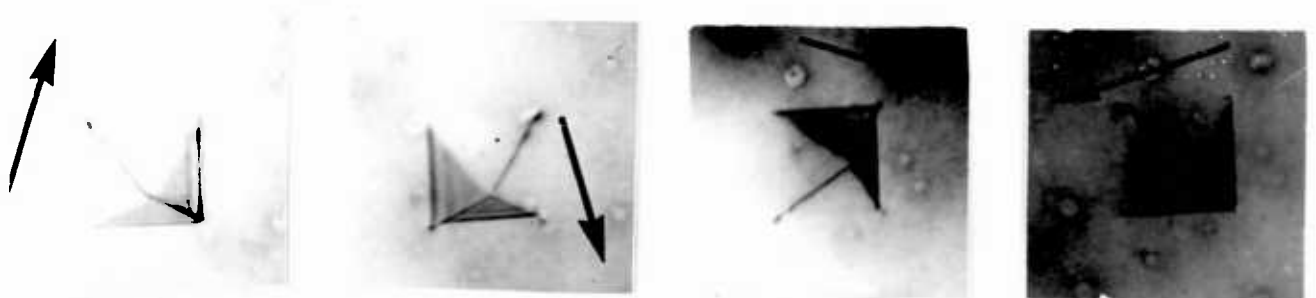
a)  $\bar{2}\bar{2}0$  B.Fb)  $\bar{2}\bar{2}0$  B.Fc)  $\bar{2}\bar{2}0$  D.F

FIG.A10

Analysis of stair-rod dislocations in stacking fault pyramid,  
 all micrographs bright field,  $s > 0$  condition.

a)  $\bar{2}\bar{2}0$ b)  $\bar{2}\bar{2}0$ 

c) 400

d)  $0\bar{4}0$ e)  $\bar{1}\bar{3}1$ f)  $3\bar{1}\bar{1}$ g)  $3\bar{1}\bar{1}$ h)  $\bar{1}\bar{3}1$



$\frac{1}{6} \langle 110 \rangle$  type but is still comparatively low.

Consideration of the dislocation reactions which could nucleate the pyramids yields an interesting result. Four Shockley partial dislocation loops, with  $\underline{b} = \frac{1}{6} \langle 211 \rangle$  lying on different inclined  $\{111\}$  planes and formed by shear in the direction of the epitaxial layer surface, could interact directly to form the stacking fault pyramid. In Thompson notation the loops, Fig.A12(a), have Burgers vectors  $\underline{\alpha D}$ ,  $\underline{\beta C}$ ,  $\underline{\gamma B}$  &  $\underline{\delta A}$  lying on planes a), b), c) & d) respectively. Fig.A12(b) shows the Thompson tetrahedron orientated with respect to the pyramid. The reactions between these loops are:

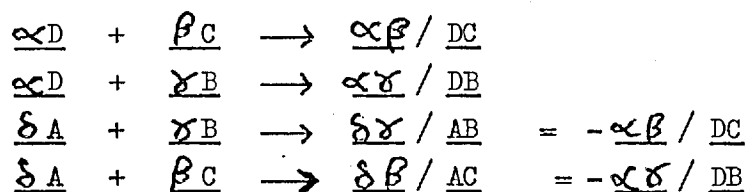


TABLE A3

g. b Value of possible low energy stair-rod dislocations

$\underline{g} \backslash \underline{b}$	$\pm 1/6$ [101]	$\pm 1/6$ [101]	$\pm 1/6$ [011]	$\pm 1/6$ [011]	$\pm 1/3$ [100]	$\pm 1/3$ [010]
$\bar{2}\bar{2}0$	$\pm 1/3$	$\pm 1/3$	$\pm 1/3$	$\pm 1/3$	$\pm 2/3$	$\pm 2/3$
$\bar{2}\bar{2}0$	$\pm 1/3$	$\pm 1/3$	$\pm 1/3$	$\pm 1/3$	$\pm 2/3$	$\pm 2/3$
400	$\pm 2/3$	$\pm 2/3$	$\pm 0$	0	$\pm 4/3$	0
040	0	0	$\pm 2/3$	$\pm 2/3$	0	$\pm 4/3$
$\bar{1}\bar{3}1$	0	$\pm 1/3$	$\pm 1/3$	$\pm 2/3$	$\pm 1/3$	$\pm 1$
$3\bar{1}\bar{1}$	$\pm 1/3$	$\pm 2/3$	$\pm 0$	$\pm 1/3$	$\pm 1$	$\pm 1/3$
$3\bar{1}\bar{1}$	$\pm 1/3$	$\pm 2/3$	$\pm 1/3$	$\pm 0$	$\pm 1$	$\pm 1/3$
$\bar{1}\bar{3}1$	0	$\pm 1/3$	$\pm 2/3$	$\pm 1/3$	$\pm 1/3$	$\pm 1$

and the stair-rod products are both  $1/3 \langle 100 \rangle$  type. We have shown in section A1 that Shockley loops lying on inclined  $\{111\}$  planes and having Burgers vectors in the direction of the surface exist in carbon-contaminated  $\{111\}$  epitaxial Si layers grown at low temperatures. This led (section 6.4) to a proposed mechanism for the nucleation of stacking fault tetrahedra in  $\{111\}$  layers based on the intersection of three of these loops. The present work is evidence that our mechanism may be more general.

Intrinsic Shockley loops which could form observed stair-rods, apex of pyramid pointing up, also showing each projected face of Thompson tetrahedron against appropriate loop.

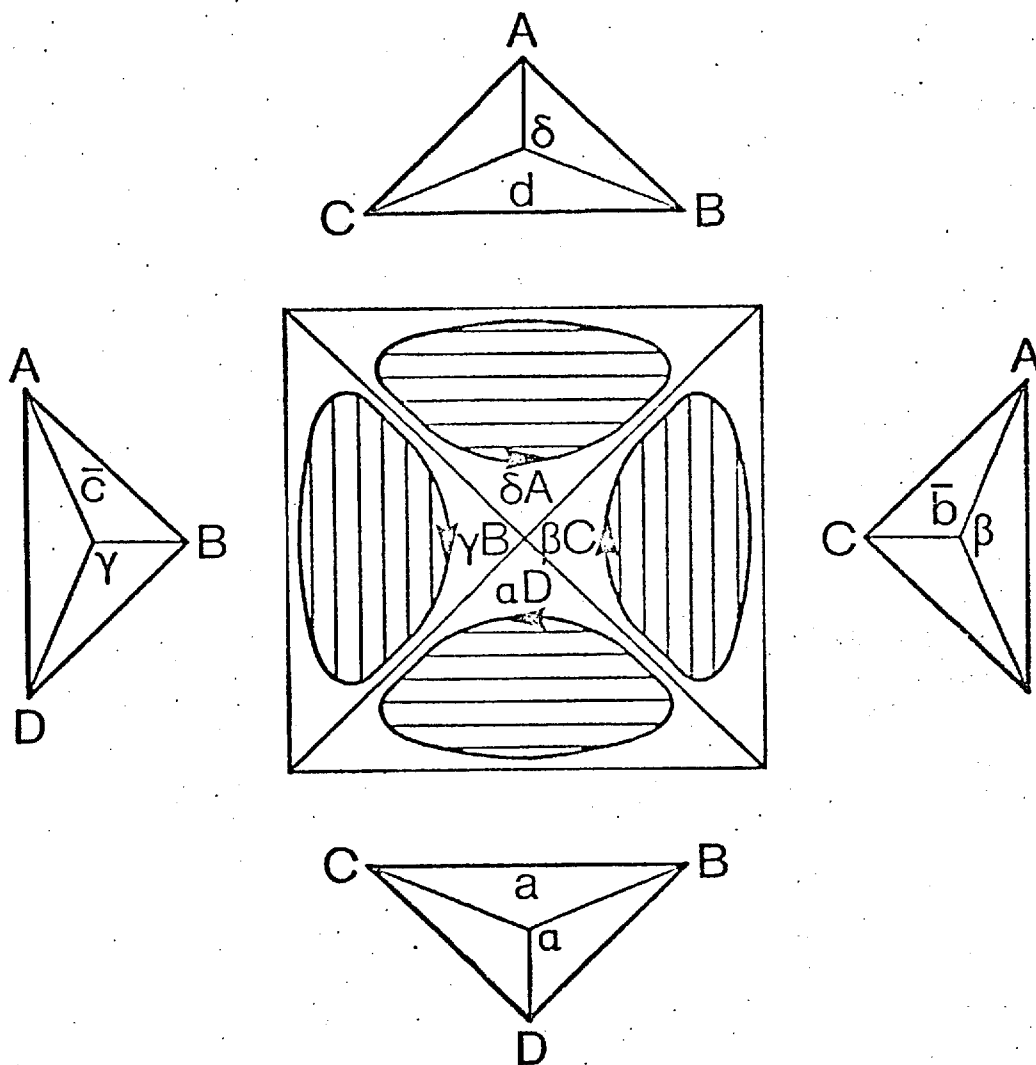
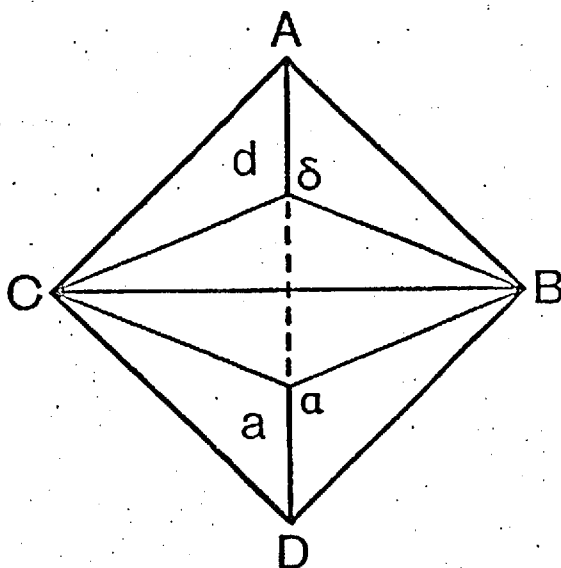


FIG. A12(b)

Completed Thompson tetrahedron viewed from above



Similar consideration of possible dislocation reactions leading to the arrangement of alternate intrinsic : extrinsic stacking faults in pyramidal formation in  $\{100\}$  layers show that four perfect dislocations with inclined  $1/2\langle 110\rangle$  Burgers vectors could dissociate into Shockley partials which then react to form  $1/6\langle 110\rangle$  type stair-rods. However, we have not to date observed this type of defect.

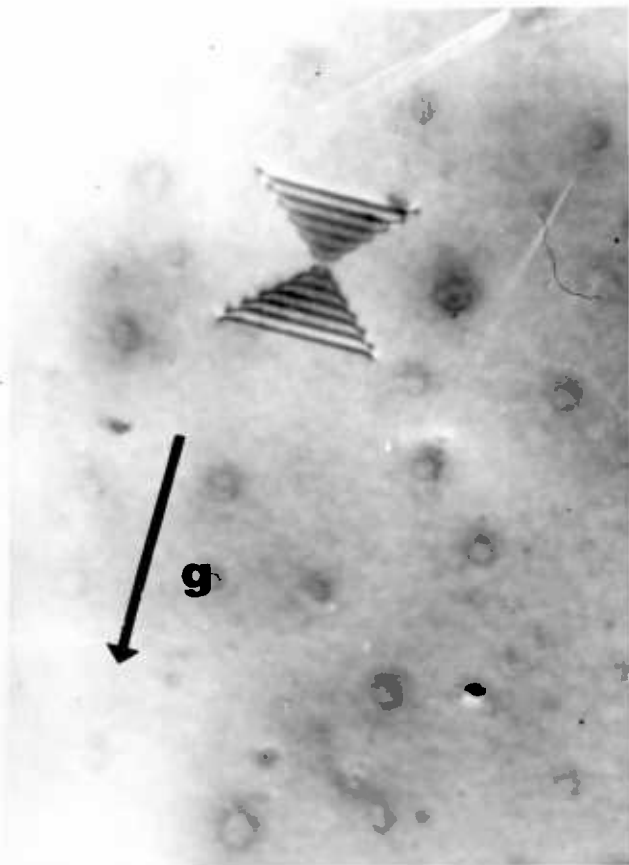
In addition to the stacking fault pyramids, dislocation half loops were found in the layer, Fig.A13(a), which lie on the vertically inclined  $\{110\}$  planes. Since they are extinguished by  $g$  parallel to their projection on (100), Fig.A13(b), they are edge in nature with Burgers vectors in the plane of the layer. The dark field micrograph Fig.A13(c) shows that the dislocations emerge at the top of the epitaxial layer and Fig.A13(d), obtained by tilting  $\sim 20^\circ$  from  $[100]$  shows that it penetrates about  $0.6 \mu\text{m}$  below the epitaxial surface. Examination of substrate materials reveals similar dislocations which evidently propagate with the epitaxial layer.

FIG. A13

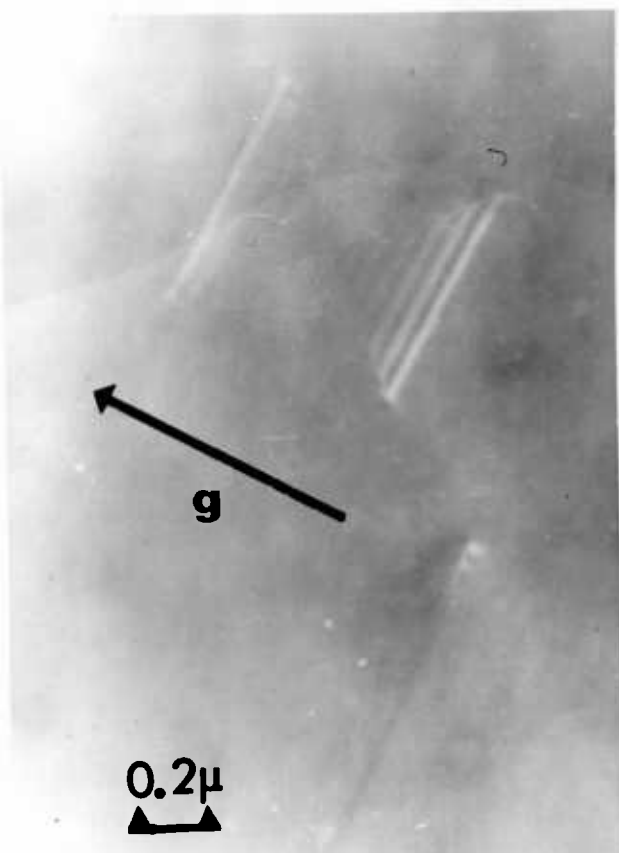
Series showing pyramid & dislocation half-loop in  $\{100\}$  epilayer



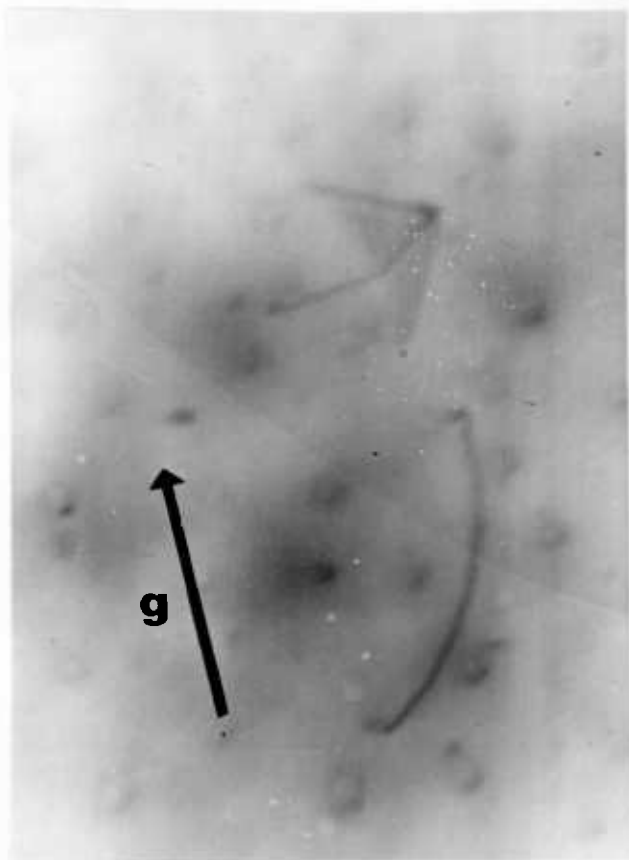
a)  $\bar{2}20$  reflection



b)  $220$  reflection



c)  $\bar{2}20$  reflection, D.F.  $s \ll 0$



d)  $1\bar{3}1$  reflection

APPENDIX B

ELASTIC ENERGY CALCULATIONS

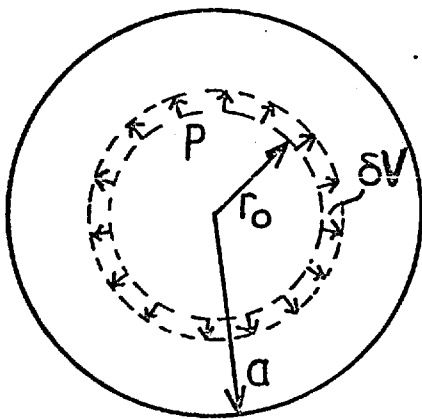
Simplified cases only are presented but the variation of elastic energies of defects with depth below the Si crystal surface can be seen at least semi-quantitatively. Where appropriate, references to the original equations are given. The sources used were

- Hirth & L the (1968) (hereafter H & L)
- Head (1953) (hereafter H)
- Bullough & Newman (1963) (hereafter B & N)

B1. The Shear Modulus  $\mu$  at the growth temperature

Nikanorov et al (1972) have given values of the elastic constants for Si at temperatures up to 600 C. Extrapolation of their values at a typical low temperature epitaxial growth run at 850 C enabled the Voigt average shear modulus  $\mu$  to be calculated at 6.4 x 10<sup>11</sup> dyne cm<sup>-2</sup>, compared to a room temperature value of 6.8 x 10<sup>11</sup> dyne cm<sup>-2</sup>. In view of the approximations to be made in the following calculations, the difference is not significant.

B2. Elastic energy of a carbon atom in a Si crystal



Consider a sphere of elastic material of radius  $a$  with a concentric spherical hole of radius  $r_0$ . Apply an internal pressure  $P$  to the surface of the hole that opens it by volume  $\delta V$ . Then fill the hole with the same material as the sphere. It has been shown that when  $r_0 \ll a$

$$P = \frac{\mu \delta V}{\pi r_0^3} \quad (\text{H \& L 2-91})$$

However, we require the case of an inclusion near a free surface. It can be easily shown (by fully solving H & L 2-86) that

$$P = \frac{\mu \delta V}{\pi r_0^3} \left( 1 - \frac{r_0^3}{a^3} \right)$$

We take  $r_0$  covalent radius of Si atom = 1.17 .  $\delta V$  is given by the difference between the volume occupied by a Si atom and the volume occupied by a substitutional carbon atom, covalent radius  $r_c = 0.77$  .

$$\delta V = \frac{4}{3} \pi (r_0^3 - r_c^3) = 4.8 \times 10^{-24} \text{ cm}^3$$

The elastic strain energy  $E_1$  in the crystal due to the carbon atom is

P§ V. Thus

$$E_1 = \frac{\mu(\delta v)^2}{\pi r_0^3} \left(1 - \frac{r_0^3}{a^3}\right) = 1.83 \left(1 - \frac{1.6}{a^3}\right) \text{ eV}$$

where  $a$  is the depth in Å of the C atom below the surface.

### B3. The Binding energy of a carbon atom to an edge Shockley dislocation.

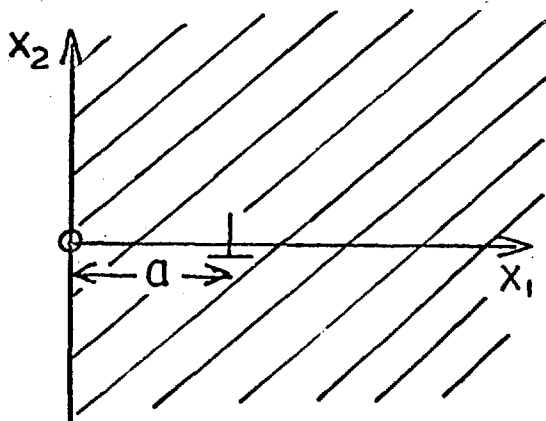
The interaction energy  $E_2$  of an impurity atom with the strain field of an edge dislocation due to the size effect has been shown (B & N 7, 9, 11) to be

$$E_2 = -4\pi\epsilon r_0^3 \left(\frac{1-\nu}{1+\nu}\right) (\sigma_{11} + \sigma_{22} + \sigma_{33})$$

where  $\epsilon = \frac{r_0 - r_c}{r_0} = -0.34$ ,  $\nu$  = Poissons ratio = 0.215 and  $\sigma_{11}$  is the stress component along the  $x_1$ , axis acting on the plane  $x_1 = 0$  etc. i.e. the hydrostatic component of the stress field. B & N only considered the case of an infinite medium, but we need to take surface relaxation into account. Expressions for the stress field of an edge dislocation with Burgers vector  $b$  perpendicular to a free surface  $x = 0$  and distance  $x = a$  from the surface is given by (H13, H & L 2-50).

$$\sigma_{11} = \frac{\mu b}{2\pi(1-\nu)} \left[ \frac{-y \{(x-a)^2 + y^2\}}{\{(x-a)^2 + y^2\}^2} + \frac{y \{3(x+a)^2 + y^2\}}{\{(x+a)^2 + y^2\}^2} + 4a x y \cdot \frac{3 \{(x+a)^2 - y^2\}}{\{(x+a)^2 + y^2\}^3} \right]$$

$$\sigma_{22} = \frac{\mu b}{2\pi(1-\nu)} \left[ \frac{y \{(x-a)^2 - y^2\}}{\{(x-a)^2 + y^2\}^2} - \frac{y \{(x+a)^2 - y^2\}}{\{(x+a)^2 + y^2\}^2} + 4a y \frac{(2a-x)(x+a)^2 + (3x+2a)y^2}{\{(x+a)^2 + y^2\}^3} \right]$$



Where  $x, y$  are co-ordinates along the  $x_1, x_2$  axes respectively. There is no displacement along the  $x_3$  axis (plane strain) which means, for an isotropic medium that (H & L 2-51)

$$\sigma_{33} = \nu(\sigma_{11} + \sigma_{22})$$

adding these 3 expressions and simplifying we get:

$$\sigma_{11} + \sigma_{22} + \sigma_{33} = \frac{4\mu b(1+\nu)}{\pi(1-\nu)} \frac{ay}{\{(x+a)^2 + y^2\}^3} \left[ \frac{-x\{(x+a)^2 + y^2\}^2}{(x-a)^2 + y^2} + (x+a)^3 + ay^2 \right]$$

Solving at  $x = a, y = b$ , i.e. near the dislocation core in the region of highest strain gives

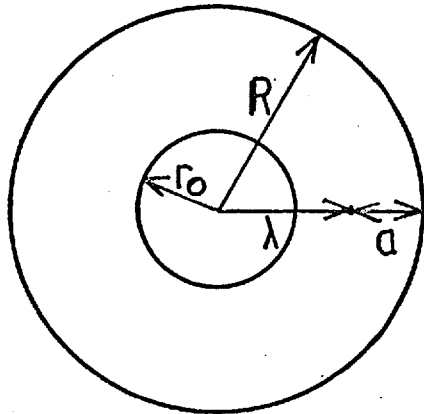
$$E_2 = 4r_0^3 \epsilon \mu \left[ 1 + \frac{3}{4} \frac{b^2}{a^2} + \frac{3}{16} \frac{b^4}{a^4} + \frac{b^6}{64a^6} \right]^{-1}$$

$$= 4r_0^3 \epsilon \mu \left( 1 - \frac{3}{4} \frac{b^2}{a^2} \right) \quad \text{for } b \ll a$$

As a check on this result, the value of  $E_2$  at this position given by B & N (10,11) is  $E_{\max} = 4r_0^3 \epsilon \mu = 0.88\text{eV}$ .

The Binding energy  $E_2 = 0.88 \left( 1 - \frac{3b^2}{4a^2} \right) \text{eV}$  for a carbon impurity atom at an edge Shockley partial dislocation.

B4. The Self energy of an edge Shockley dislocation



Consider a hollow edge dislocation along the axis of a right circular cylinder with inner and outer radii  $r_0$  &  $R$  respectively. The energy per unit length  $E_e$  is given by (H & L 3-49)

$$E_e \sim \frac{\mu b^2}{4\pi(1-\nu)} \ln \frac{R}{r_0}$$

$r_0$  is used to account for the core energy and is usually taken as  $\sim b/4$ . The corresponding energy for a screw dis-

location  $E_s$  is identical except for the factor  $(1-\nu)$ . H & L also consider the more useful case of a non-coaxial screw dislocation distance  $\lambda$  from the centre of the cylinder and include image forces. The energy per unit length is given by (H & L 3-31)

$$E_{s,\lambda} \sim \frac{\mu b^2}{4\pi} \left[ \frac{R^2 - \lambda^2}{r_0 R} - \frac{(R^2 - \lambda^2)^2}{R^4} \right]$$

For the case of a dislocation close to the surface of a crystal at a depth  $a$  where  $R - \lambda = a, R \approx \lambda$ , then the above equation approximates to  $E_{s,\lambda} \sim \frac{\mu b^2}{4\pi} \ln \left( \frac{2a}{r_0} \right) - \frac{4a^2}{R^2}$

The last term is negligible since  $a \ll R$ .

The corresponding case for an edge dislocation  $E_{e,\lambda}$  is more complicated but it seems likely, because of the similarity between  $E_e$  and  $E_s$ , that it will show a similar variation with depth to  $E_{s,\lambda}$ . Suppose then that

$$E_{e,\lambda} \sim \frac{E_{s,\lambda}}{(1-\nu)}$$

Then the self energy of an edge Shockley dislocation at a distance  $a$  below the surface  $E_3$  is given by

$$E_3 \sim \frac{\mu b^2}{4\pi(1-\nu)} \ln \frac{2a}{r_0}$$

$$\sim 1.73 \log(3.6a) \text{ eV per } \frac{1}{2} \langle 110 \rangle \text{ length of dislocation line}$$

### B3. SUMMARY

1. Carbon atom  $E_1 = 1.83 \left(1 - \frac{1.6}{a^2}\right)$
2. Binding energy of c atom to edge Shockley dislocation

$$E_2 = 0.88 \left(1 - \frac{3.6}{a^2}\right)$$

3. Self-energy of edge Shockley dislocation

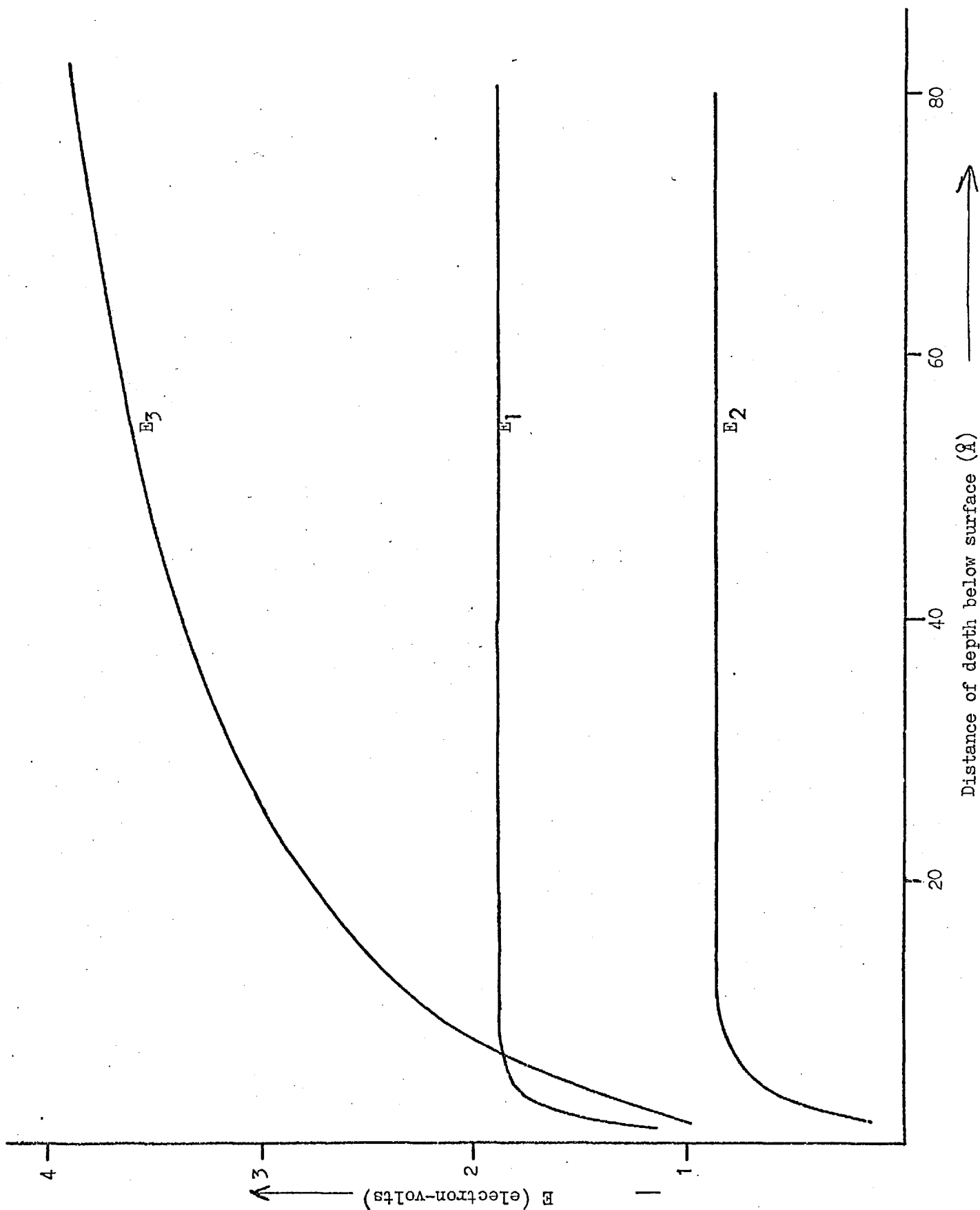
$$E_3 = 1.73 \log(3.6a)$$

Values of these energies are tabulated below and are plotted in Fig.B1 for defects sited at depth  $a$  below the crystal surface

depth a A	Elastic Energy (eV)		
	$E_1$	$E_2$	$E_3$
2	1.46	.09	1.48
4	1.78	.68	2.00
10	1.82	.85	2.69
20	1.83	.87	3.22
50	1.83	.88	3.90
100	1.83	.88	4.42
1000	1.83	.88	6.15
10000	1.83	.88	7.90

FIG. B1

Elastic energy variation of carbon atom, & edge Shockley partial dislocation close to Si surface.  $E_2$  = binding energy of carbon atom to Shockley partial;  $E_1$  = elastic energy of carbon atom in substitutional site due to size difference.  $E_3$  = self-energy of edge Shockley partial per  $\frac{1}{2}$   $\langle 110 \rangle$  unit length of dislocation.



APPENDIX C

THE DEPLETION WIDTH OF Z45 BASE : COLLECTOR JUNCTION

C1. Estimation of boron diffusion profile

Sectioning techniques involving 4 point probing and the removal of equal small increments from the specimen surface are available which accurately measure carrier concentrations as a function of depth below the diffused surface. Anodic etching can remove say  $400\text{\AA}$ , but the oxide so formed has to be removed in HF between each anodisation. Also when the junction is approached, the efficiency of the process falls and estimates of the thickness of the oxide film usually have to be made. However, the bevel and stain technique has shown that the base junction depth  $x_j \sim 2.5 \mu\text{m}$ , Fig.10.22, and so the required number of anodisations would be at least 60, making even a single profile determination very time consuming. Etching methods using very low concentrations of HF in  $\text{HNO}_3$  are faster but are more suitable for whole slice sectioning where the slice can be weighed, rather than the small areas of blanket diffusions on the test slices.

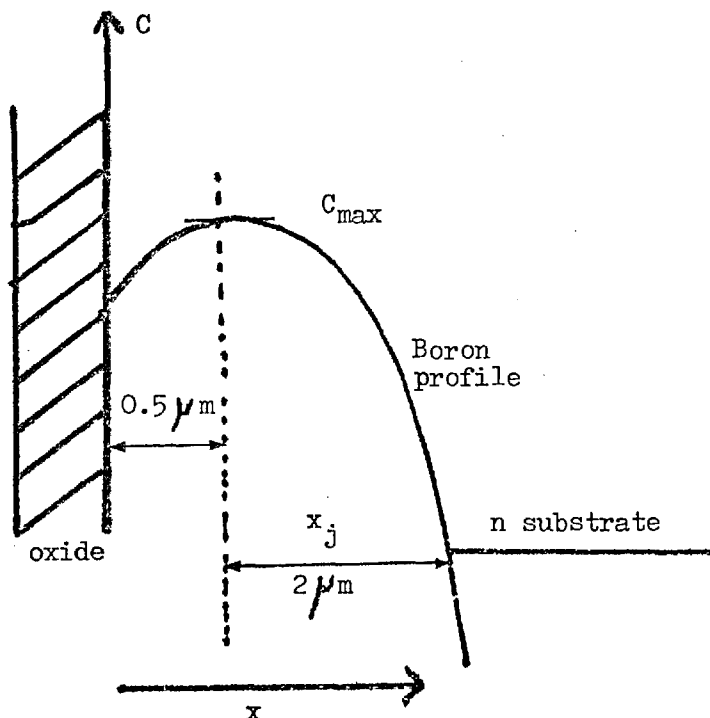
If certain assumptions are made concerning the shape of the profile, the carrier concentration C, due to the diffused boron dopant, atoms can be calculated at each depth  $x$  below the surface. Boron is known to "leach" into the drive-in oxide, leading to lower surface concentrations than just inside the Si surface. Thus we assume the effective  $x_j \approx 2.0 \mu\text{m}$  and we neglect 'run-on', i.e. base extension into Si due to subsequent emitter diffusion. Assuming a gaussian profile

$$C = C_{\text{max}} \exp\left(\frac{-x^2}{4Dt}\right) \dots(1)$$

Where  $C_{\text{max}}$  is the maximum (surface) concentration

$D$  = Diffusion coefficient ( $\text{cm}^2\text{sec}^{-1}$ )

$t$  = time (sec)



Now average conductivity  $\bar{\sigma} = \frac{1}{\rho_s x_j}$  where  $\rho_s =$  surface sheet resistance  $\sim 300 \Omega/\text{sq.}$

$$\therefore \bar{\sigma} = \frac{10^4}{300 \times 2} = 16.7 \Omega^{-1} \text{cm}^{-1}$$

Published graphs can be used giving  $C_{\text{max}}$  from  $\bar{\sigma}$  (Irvin (1962)), gives

$$C_{\text{max}} = 4 \times 10^{18} \text{cm}^{-3}$$

The n-type substrate has a resistivity of  $8 \Omega \text{cm}$ , and again from Irvin's data, this corresponds to a carrier concentration of  $7 \times 10^{14} \text{cm}^{-3}$ . Solving (1) at  $x_j$

$$7 \times 10^{14} = 4 \times 10^{18} \exp\left(\frac{-4}{4 Dt}\right)$$

gives

$$4 Dt = 0.464$$

$$C = 4 \times 10^{18} \exp\left(\frac{-x^2}{.464}\right) \dots\dots\dots(2)$$

Where  $x$  is in  $\mu\text{m}$ .

Table C1 shows calculated values of  $C$  as a function of depth  $x$ . The calculation was done quite quickly using an HP45 electronic pocket calculator. Values for  $(N_D - N_A)$  in substrate and  $N_A - N_D$  in base account for compensation in each region and gives fixed charge levels in depletion region calculations.

TABLE C1.  
Estimated Carrier Concentrations versus depth for boron diffusion

$x \mu\text{m}$	$x$ (from surface)	$C$	$N_A - N_D$	$N_D - N_A$
.1	.6	$3.91 \times 10^{18}$		
.2	.7	3.67		
.3	.8	3.30		
.4	.9	2.83		
.5	1.0	2.33		
.6	1.1	1.84		
.7	1.2	1.39		
.8	1.3	1.00		
.9	1.4	$6.98 \times 10^{17}$		
1.0	1.5	4.63		
1.1	1.6	2.95		
1.2	1.7	1.80		
1.3	1.8	1.04		
1.4	1.9	$5.85 \times 10^{16}$		
1.5	2.0	3.13		
1.6	2.1	1.61		
1.7	2.2	$7.89 \times 10^{15}$	$7.2 \times 10^{15}$	
1.8	2.3	3.71	3.0	
1.9	2.4	1.67	$9.0 \times 10^{14}$	
2.0	2.5	$7.21 \times 10^{14}$	Junction	
2.1	2.6	2.98		$4.2 \times 10^{14}$
2.2	2.7	1.18		6.0
2.3	2.8	4.47		6.8
2.4	2.9	1.62		7.0

Values in Table C1 are plotted on log/linear graph paper in Fig.C1 and close to the junction on linear/linear graph paper in Fig.C2.

C2. Calculation of Depletion width W

The depletion width W of a step or abrupt junction in reverse bias is given by

$$W = \frac{2 \epsilon \epsilon_0 (V_r + \phi_B)}{q N_A} \dots \dots \dots (3) \text{ (Grove. 1967)}$$

Where  $\epsilon$  = permittivity of Si = 11.7

$\epsilon_0$  = permittivity of free space =  $8.86 \times 10^{-14}$  Farad  $\text{cm}^{-1}$

q = electronic charge =  $1.6 \times 10^{-19}$  coulomb

$V_r$  = applied reverse bias in volts

$\phi_B$  = built-in voltage of p-n junction

$$= \frac{kT}{q} \ln \left( \frac{N_A N_D}{n_i^2} \right) \dots \dots \dots (4)$$

Where k = Boltzmann's constant  $\frac{kT}{q} = 0.0259V$  at R.T.

T = absolute temperature in  $^{\circ}K$

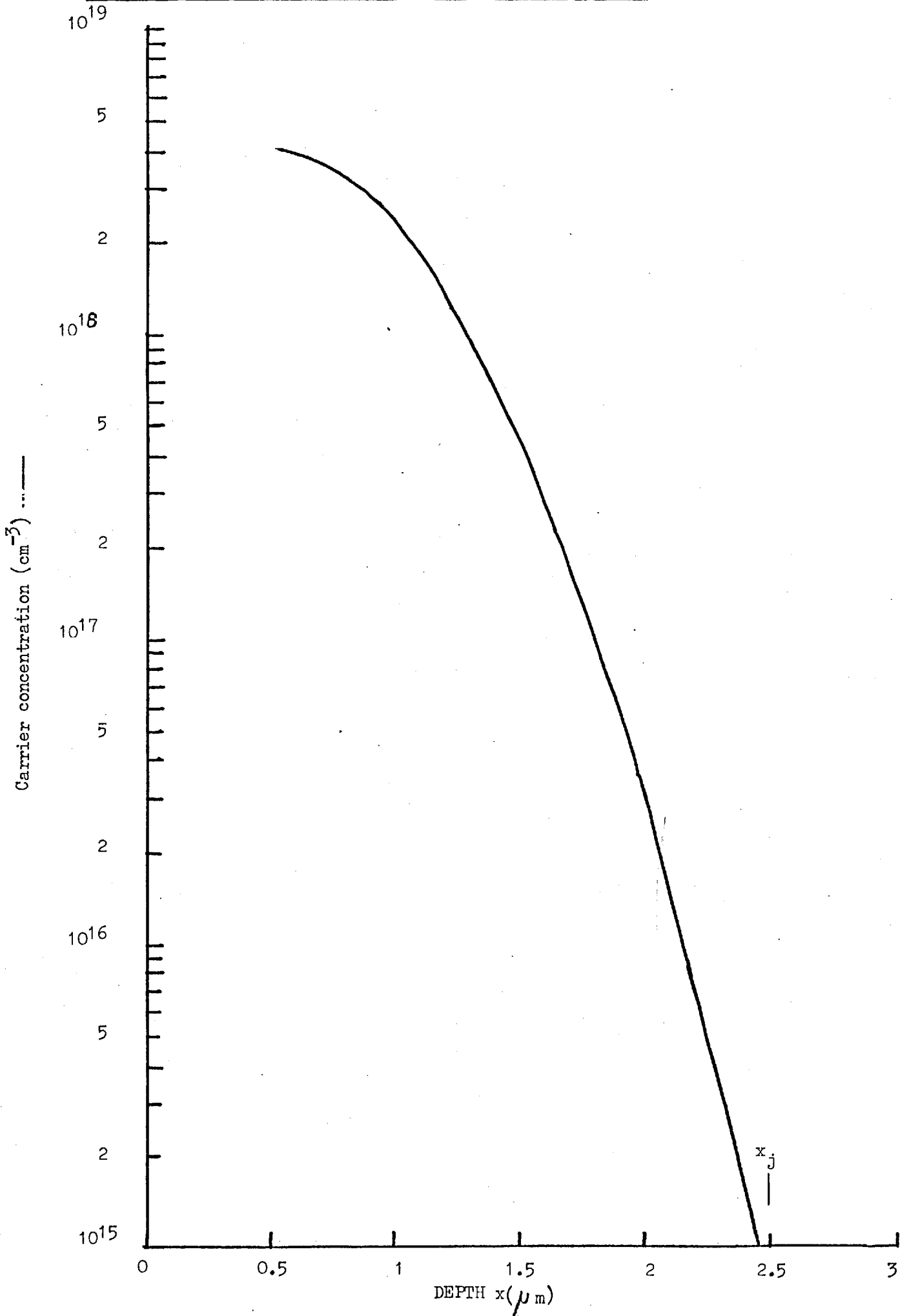
$N_A$  = accepted impurity concentration on p side

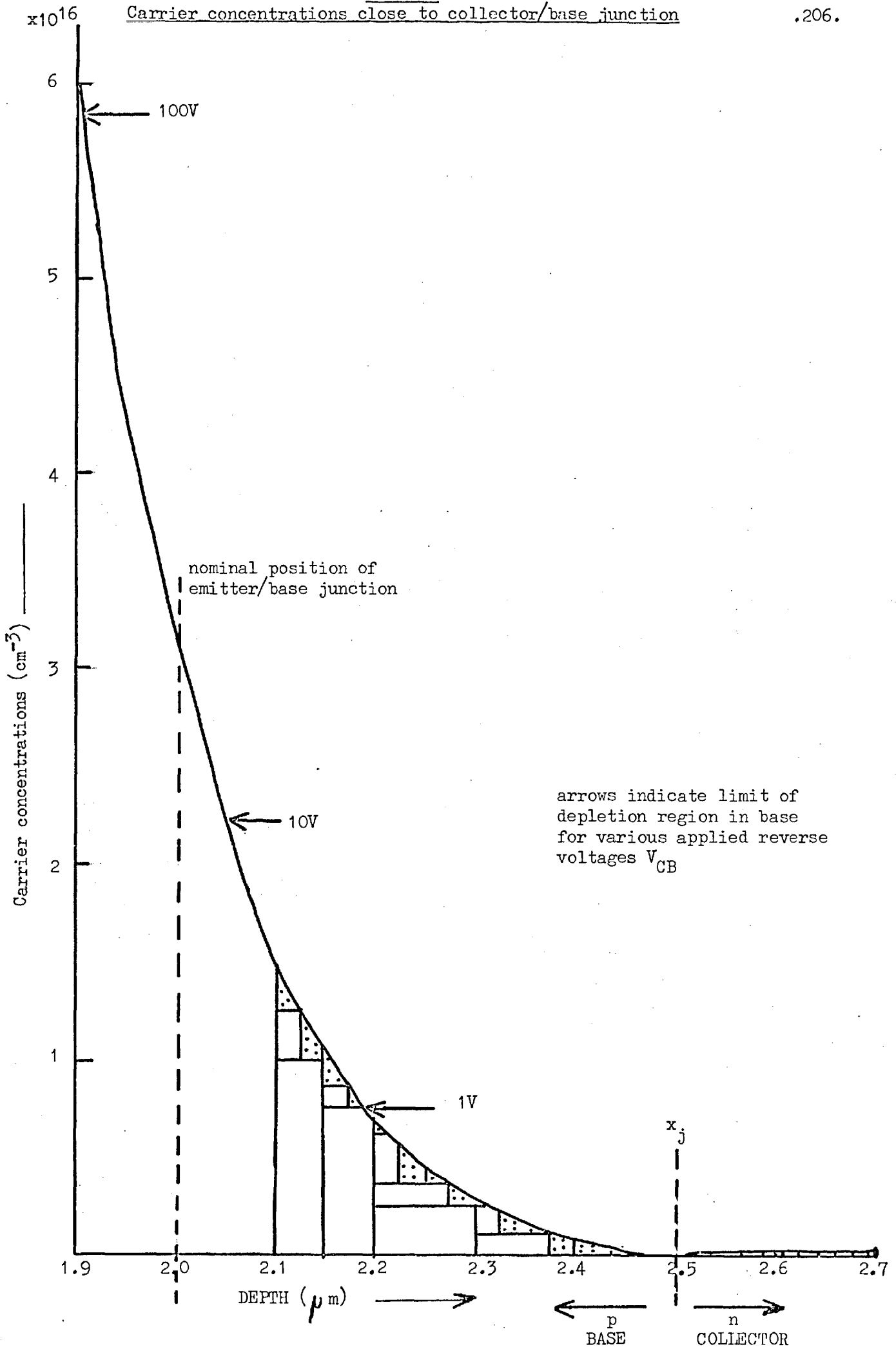
$N_D$  = donor impurity concentration on n side

$n_i$  = intrinsic hole or electron concentration for Si at temperature T  $^{\circ}K = 1.45 \times 10^{10} \text{cm}^{-3}$  at R.T.

$N_D = 7 \times 10^{14} \text{cm}^{-3}$  i.e. substrate donor concentration

but which value of  $N_A$  in boron profile? Solving equation (4) gives:







e.g.  $V_r = 1V, \quad W = 1.7 \mu m$

try  $1.7 = W_p + W_n$   
 $0.2 + 1.5$

Squares	124	145
	75	840
	<u>50</u>	<u>      </u>
	249	985

$\therefore$  try  $1.7 = 0.3 + 1.4$

Squares	249	145
	195	770
	<u>300</u>	<u>      </u>
	744	915

try  $1.7 = 0.4 + 1.3$

Squares	974	145
	<u>744</u>	<u>700</u>
	1718	845

$\therefore$  Best fit for  $V_r = 1V$  is

$$\underline{W_p = 0.3 \mu m}$$

$$\underline{W_n = 1.4 \mu m}$$

e.g.  $V_r = 100V, \quad W = 13.6 \mu m$

try  $13.6 = 0.5 + 13.1$

Squares	4000	86
		<u>9030</u>
		9116

try  $0.55 + 13.05$

Squares	5791	86
		<u>8995</u>
		9081

try  $13.6 = 0.6 + 13.0$

Squares	5791	86
	<u>2430</u>	<u>8960</u>
	8221	9046

Best fit

$$W_p = 0.6 \mu m$$

$$W_n = 13.0 \mu m$$

To summarise we have

$V_r$	$W_p$	$W_n$	$W_{tot}$
1	0.3	1.4	1.7
10	0.45	3.85	4.3
100	0.6	13.0	13.6

These values are indicated on Fig.C2.

Since the width of the base is only  $\sim 1\mu\text{m}$ , this explains why  $BV_{CEO} \sim 100\text{V}$ .

The above table gives an idealised view of the depletion region. In practice corners of the emitter diffused region and inhomogeneities in substrate material and dopant profiles will mean that the depletion region on the base side will 'punch-through' to the emitter causing breakdown. Note that the depletion region only extends a very short extent into the substrate collector region.

### C3. Diffusion length calculations

In p-type base, minority carrier diffusion length  $L_e = \sqrt{D_e \tau_e}$   
 where  $D_e$  is the electron diffusion constant  
 and  $\tau_e$  is minority (electron) carrier lifetime.

In n-type substrate,  $L_n = \sqrt{D_n \tau_n}$

Since  $D_e = \frac{kT}{q} \mu_e$  Einstein relation

and  $\mu_e$  can be found from Irvin's data for base  $D_e \sim 8$   
 for substrate  $D_h \sim 11$

By experiment at Caswell on similar materials,

$$\begin{aligned} \tau_e &= 25 \text{ nS} = 2.5 \times 10^{-8} \text{ s} \\ \tau_h &= 4 \mu\text{s} = 4 \times 10^{-6} \text{ s} \end{aligned}$$

$$\begin{aligned} \therefore L_e &\sim 4.5 \mu\text{m} \\ L_h &\sim 70 \mu\text{m} \end{aligned}$$

This important result shows that the surface of the device is within a diffusion length of the base/collector junction and so explains why electron beam surface damage or contamination during SEM examination could have such a powerful effect on the photocurrent values. Recombination centres at the surface in sufficient number could virtually quench the carrier pair generation created by incident photons.

## REFERENCES

- Abbink, H.A., Broudy, R.M., McCarthy, G.P., (1968). *J.App.Phys*, 39, 4673
- Abrahams, M.S., Tietjen, J.J., (1969), *J.Phys.Chem.Solids*, 30, 2491
- Alexander, H., and Haasen, P. (1968), *Solid State Physics*, 22, 27.
- Allen, F.G., (1957), *J.Appl.Phys*, 28, 1510
- Amelinckx, S., (1964), *Solid State Phys. (Supp.)* 6, 279
- Armigliato, A. & Servidori, M. (1974) *Phys.Stat.Sol(a)* 25, K1
- Authier, A. (1966), *adv. X-ray anal* 10, Plenum Press, p9
- Baker, J.A., Tucker, T.N., Mayer, N.E., Buschert, R.C. (1968) *J.App.Phys*, 39, 4365
- Baker, J.F.C., Ogden, R. (1975) *J.Mat.Sci.* 10, 1259
- Bell, W.L., Thomas, G. (1965) *Phys. Stat. Sol.* 12, 843
- Bialas, D. & Hesse, J. (1969) *J.Mat.Sci.*, 4, 779
- Bicknell, R.W. (1972) *Phil. Mag.* 26, 273
- Bicknell, R.W. (1973) "Ion Implantation in Semiconductors", Ph.D. Thesis, University of London
- Bloem, J. 1973) in "Semiconductor Silicon 1973", Eds. Huff, H.R., Burgess, R.R., The Electrochem Soc. p.180.
- Bloem, J. and Goemans, A.H. (1972) *J.App.Phys*, 43, 1281.
- Booker, G.R. (1964), *Disc. Farad Soc.* 38, 298.
- Booker, G.R. (1965), *Phil. Mag.* 11, 1007
- Booker, G.R. (1966), *J. App. Phys.* 37, 441.
- Booker, G.R., and Joyce, B.A. (1966) *Phil. Mag.* 14, 301
- Booker, G.R., Joyce, B.A., Bradley, R.R. (1964) *Phil.Mag.* 10, 1087
- Booker, G.R., Stickler, R. (1962(a)), *Brit.J. App. Phys*, 13, 446.
- Booker, G.R., Stickler, R. (1962(b)), *J. App. Phys*, 33, 3281
- Booker, G.R., Stickler, R. (1963), *App. Phys. Lett.*, 3, 158
- Booker, G.R., Tunstall, E.J. (1966), *Phil. Mag.* 13, 71.
- Booker, G.R., Unvala, B.A. (1965), *Phil. Mag.* 11, 11.
- Bradley, D.E. (1959), *Brit. J. App. Phys.* 10, 198
- Bradley, D.E. (1960) *ibid*, 11, 506
- Brown, A.S., Watts, B.E. (1970) *J.App. Cryst.* 3, 172
- Bullough, R., Newman, R.C. (1963), *Progress in Semiconductors*, 7, 100
- Burton, W.J., Cabrera, N., Frank, F.C. (1951), *Phil. Trans. Roy Soc.* 243A, 299
- Cabrera, N., Vermilyea, D.A. (1958) in "Growth & Perfection of Crystals" Ed. Doremus, R.H., et al, J. Wiley, 393
- Celotti, G., Nobili, D., & Ostoja, P. (1974) *J.Mat. Sci.* 9, 821
- Charig, J.M., Joyce, B.A., Stirland, D.J., Bicknell, R.W. (1962), *Phil. Mag*, 7, 1847
- Charig, J.M., Skinner, D.K. (1969). *Surf. Sci.* 15, 277
- Chase, B.D., Holt, D.B. (1972), *J.Mat. Sci.* 7, 265
- Chen, L.J., Falicov, L.M. (1974), *Phil. Mag.* 29, 1.
- Chu, T.L., Gavalier, J.R. (1963), *J. Electrochem.Soc.* 110, 388
- Clareborough, L. (1971) *Austral. J. Phys.*, 24, 79.
- Cockayne, D.J.H., Ray, I.L.F., Whelan, M.J. (1969) *Phil.Mag.* 20, 1265
- Cullis, A.G., Booker, G.R. (1971), *J. Cryst.Growth*, 9, 132
- Cullis, A.G., & Katz, L.E. (1974) *Phil. Mag.* 30, 1419
- Czaja, W. (1966), *J. App. Phys.* 37, 4236
- Czaja, W., & Patel, J.R. (1965) *J.App. Phys*, 35, 1476
- Czaja, W., & Wheatley, G.H. (1964) *J. App. Phys*, 35, 2782
- Dash, S., & Joshi, M.L. (1968), *Phys.Stat.Sol.* 26, 159
- Ditchfield, R.W., Cullis, A.G., (1970) 7th International Conference on Electron Microscopy, Grenoble, p.125.
- Drum, C.M., Clark, C.A. (1968) *J. Electrochem. Soc.* 115, 664
- Dyer, L.D. (1969) in "Semiconductor Silicon 1969", Ed.Haberecht, R.R., & Kern, E.L, *Electrochem.Soc.* p.132.
- Dyer, L.D. (1971), *J. Electrochem. Soc.* 118, 957
- Fairfield, J.H., & Schwuttke, G.H. (1968) *J.Electrochem.Soc.* 115, 415
- Finch, R.H., Queiser, H.J., Thomas, G., Washburn, J. (1963) *J.App.Phys*, 34, 406
- Frank, F.C. (1958) in "Growth & Perfection of Crystals", Ed.Doremus, R.H., et al J.Wiley, p.411

- Gevers, R., Art. A., Amelinckx, S. (1963), Phys.Stat.Sol. 3, 1563
- Glang, R., Wajda, E.S. (1962) in Met.Soc.Conf. 15, Ed.Schroeder, J.B. Intersci, p.25
- Goetzberger A. & Shockley, W. (1960), J.App.Phys. 31, 1821.
- Grove, A.S. "Phys. & Techng. of Semiconductor Devices". Wiley (1967)
- Haase, O. (1962) in Met. Soc.Conf. 15, ed. Schroeder, J.B., Intersia. p.159
- Haasen, P., & Schroter, W. (1970) in "Fundamental Aspects of Dislocation Theory, ed. J.A.Simmons, R.de Wit, & R.Bullough, Nat. B stand. spec. Publ. 11, 317.
- Head, A.K., (1953), Proc. Phys. Soc. B66, 793
- Head, A.K., (1967), Austral. J. Phys.Soc. 20, 557
- Henderson, R.C., Helm, R.F., (1972), Surf.Sci. 30, 310
- Hill, M.J., & Rowcliffe, D.J.(1974), J.Mat.Sci. 2, 1569
- Hirsch, P.B., Howie,A., Nicholson, R.B., Pashley, D.W., Whelan, M.J. (1965) "Electron Microscopy of Thin Crystals" Butterworths (London)
- Hirth, J.P., Lothe, J. (1968) "Theory of Dislocations", McGraw Hill Series in Mat. Sci. & Engineering.
- Holt, D.B. (1974) in "Quantitative S.E.M." ed D.B. Holt, M.D.Muir, P.R.Grant & I.M. Boswarva, acad. Press, Ch.8.
- Holt, D.B., & Ogden, R. (1976) Solid State Electronics, 19, 37.
- Hornstra, J. (1958), J. Phys. Chem. Solids, 5, 129
- Howie, A., and Whelan, M.J. (1962) Proc. Roy. Soc. A267, 206
- Humble, P. (1968), Phys. Stat. Sol. 30, 183
- Irvin, J.C. (1962) Bell Syst. Tech. J. 41, 387
- Ishida, H., Miyamoto, N., Kohra, K. (1976) J.App.Cryst. 9, 240
- Jaccodine, R.J., (1963) App. Phys. Lett. 2, 201.
- Jastrzebska, M., Figielski, T. (1966), Phys.Stat. Sol. 14, 381
- John, H.F., (1967) Proc. IEEE 55, 1249
- Joyce, B.A., Bradley, R.R. (1963) J. Electrochem. Soc. 110, 1235
- Joyce, B.A., Bradley, R.R. (1966) Phil. Mag. 14, 289
- Joyce, B.A., Bradley, R.R., Booker, G.R., (1967) Phil.Mag. 15, 1167
- Joyce, B.A., Bradley, R.R., Watts, B.E., Booker, G.R.,(1969(a)), Phil. Mag.19, 403
- Joyce, B.A., Neave, J.H., Watts, B.E. (1969(b)),Surf.Sci. 15, 1.
- Juleff, E.M. (1973) Solid State Electronics, 16, 1173
- Kahn, I.H., Summergrad, R.N. (1967), App. Phys.Lett, 11, 12.
- de Kock, A.J.R., (1973) Phillips Res. Rep. Supp. No.1.
- de Kock, A.J.R., Roksnoer, P.J., Boonen, P.G.T. (1975) J.Cryst.Growth, 30, 279
- Laister, D., Jenkins, G.M. (1969), Phil. Mag. 20, 361
- Lander, J.J., Morrison, J. (1962) J. App. Phys. 33, 2089
- Lander, J.J., Schreiber, H., Buck, T.M. & Matthews, J.R. (1963) App.Phys.Lett 3, 206
- Lang, A.R. (1959) J. App. Phys. 30, 1748
- Levine, E., Washburn, J., & Thomas, G. (1967) J.App. Phys, 38, 81.
- Lewis, B. (1974) J. Crystl.Growth, 21, 29
- Light, T.B. (1962) in Met.Soc.Conf. 15, Ed.Schroeder, J.B. Intersci. p. 137
- Maguire, H.G., Augustus, P.D. (1973), Phys. Stat. Sol. (a), 17, 101
- Meek, R.L., Seidel, T.E. & Cullis, A.G. (1975), J.Electrochem.Soc. 122, 786
- Meieran, E.S., Blech, I.A. (1967), J. App. Phys. 38, 3495
- Meieran, E.S., Cass, T.R. (1972) in "Electron Microscopy and Structure of Materials", ed. G. Thomas, R.M. Fulrath, and R.M. Fischer, U. of Calif. Press, p.1027. Proc. 5th Internl.Mat.Symposium,U.C.B.(1971)
- Mendelson, S. (1964), J. App. Phys, 35, 1570.
- Mendelson, S. (1965), J. App. Phys, 36, 2525
- Mendelson, S. (1967)(a), ibid, 38, 1573
- Mendelson, S. (1967(b)), Surf. Sci. 6, 233
- Mendelson, S. (1968), J. App. Phys., 39, 2477
- Mendelson, S. (1970), in Electrochem. Soc. Spring Meeting (Los Angeles) Extended Abstracts, p.753.
- Miller, D.P., Watelski, S.B., Moore, C.R. (1963), J.App. Phys. 34, 2813
- Miltat, J.E.A., & Bowen, D.E. (1970) Phys.Stat. Sol. (a) 3, 431
- Moroney, M.J. (1951), "Facts from Figures", Pelican Original, Ch.15.

- Nakashima, H., Sugano, T., Yanai, H. (1966) Jap. J. App. Phys., 5, 874  
 Neve, N.F.B., & Thornton, P.R. (1966), Solid State Electronics, 9, 900  
 Newman, R.C., Smith, H.S. (1969), J. Phys. Chem. Soc. 30, 1493  
 Nikanorov, S.P., Burenkov, Yu.A., Stepanov, A.V. (1972), Sov. Phys. Solid State, 13, 2516  
 Ogden, R. (1972) Phys. Stat. Sol. (a), 14, K101  
 Ogden, R. (1975), *ibid*, (a), 28, K97  
 Ogden, R. (1976), First European Conference on Crystal Growth, ECCGI Zurich. September 12-18. paper D10.  
 Ogden, R., Bradley, R.R., Watts, B.E. (1971), Institute of Physics 5th Thin Film Conference, Southampton  
 Ogden, R., Bradley, R.R., Watts, B.E. (1974) Phys. Stat. Sol. (a), 26, 135  
 Ogden, R., & Holt, D.B. (1974), 4th European Solid State Physics Device Research Conference (ESSDERC), Univ. of Nottingham, paper B6.7.  
 Ogden, R., & Wilkinson, J.M. (1977), J. App. Phys. (in Press)  
 Pashley, D.W., Stowell, M.J. (1963) Phil. Mag. 8, 1605.  
 Pease, R.L., and Galloway, K.F. (1974) Microelectr. & rel. 13, 549  
 Petroff, P.M., and de Kock, A.J.R., (1975) J. Cryst. Growth, 30, 117  
 Plantinga, G.H. (1969), IEEE Trans. on Electron Devices ED-16, 394  
 Queisser, H.J. (1961) IEEE Trans. Electron Dev. ED-8, 429  
 Queisser, H.J. & Goetzberger, A. (1963) Phil. Mag. 8, 1063  
 Ray, I.L.F., Cockayne, D.J.H. (1971), Proc. Roy. Soc. London A325, 543  
 Ravi, K.V., Varker, C.J., & Volk, C.E. (1973) J. Electrochem. Soc. 120, 533  
 Ravi, K.V., Varker, C.J. (1974), App. Phys. Lett. 25, 69  
 Read, W.T. (1954). Phil. Mag. 45, 775 and 1119  
 Schwoebel, R.L., Shipsey, E.J. (1966) J. App. Phys. 37, 3682  
 Schwuttke, G.H. (1965) J. App. Phys. 36, 2712  
 Schwuttke, G.H. (1970) Microelect. & rel. 9, 397  
 Schwuttke, G.H., and Sils, V. (1963) J. App. Phys. 34, 3127  
 Servidori, M. & Armigliato, A. (1975), J. Mat. Sci. 10, 306  
 Silcock, J.M. Tunstall, W.J., (1964), Phil. Mag. 10, 361  
 Silcox, J., Hirsch, P.B. (1959) Phil. Mag. 4, 72  
 Stringfellow, G.B., Lindquist, P.F., Cass, T.R., Burmeister, J. (1974) J. Electron. Mat. 3, 497  
 Suzuki, H. (1962), J. Phys. Soc. Jap., 17, 322.  
 Tamura, M., Sugita, Y. (1970), Japan, J. App. Phys, 9, 368  
 Thomas, R.N., Francombe, M.H. (1967) App. Phys. Lett. 11, 134  
 Thomas, R.N., Francombe, M.H. (1971) Surf. Sci. 25, 357  
 Thompson, N. (1953), Proc. Phys. Soc. 366, 481  
 Thornton, P.R. (1968) "S.E.M. Applications to Mat. & Device Sci." Chapman & Hall, London.  
 Thornton, P.R., Davies, I.G., Shaw, D.A., Sulway, D.V., & Wayte, R.C. (1969), Microelectron. & rel. 8, 33.  
 Tice, W.K., Lange, R.C., Shasten, R.B. (1973) in "Semiconductor Si 1973", ed. H.R. Huff and R.R. Burgess, Electrochem. Soc. p.639  
 Tunstall, W.J., Hirsch, P.B., Steeds, J. (1964) Phil. Mag. 9, 99  
 Unvala, B.A., Booker, G.R. (1964), Phil. Mag. 9, 691  
 Varker, C.J., & Ravi, K.V. (1974), J. App. Phys, 45, 272  
 Venables, J.D., (1970) Met. Trans. 1, 2471  
 Vieweg - Gutberlet, F.G. (1974) N.B.S. spec. publ. 400-10, 185  
 Watts, B.E. (1973), Thin Solid Films, 18, 1.  
 Widmer, H. (1964), App. Phys. Lett, 5, 108

LIST OF PUBLICATIONS

1. Ogden, R. (1972) Shockley Loops in Epitaxial Silicon, Phys. Stat. Sol. (a) 14, K101
2. Ogden, R., Bradley, R.R, and Watts, B.E. (1974) Stacking Fault Structures in carbon-contaminated low-temperature Epitaxial Silicon. Phys. Stat. Sol. (a) 26, 135
3. Ogden, R. (1975). The Nature of Stacking Fault Pyramids in  $\{100\}$  Epitaxial Silicon, Phys. Stat. Sol. (a), 28, K97
4. Baker, J.F.C., & Ogden, R. (1975), Crystal imperfections in Si epitaxial layers grown on ion implanted substrates, J.Mat.Sci.10, 1259
5. Holt, D.B., & Ogden, R. (1976). Observation of dislocations in a silicon phototransistor by scanning electron microscopy using the barrier electron voltaic effect, Solid State Electron, 19, 37
6. Ogden, R. (1976). Defects in Epitaxial Si grown on As<sup>+</sup> ion-implanted substrates, ECCGI, Zurich, paper D.10.
7. Ogden, R., & Wilkinson, J.M. (1977). Characterisation of crystal defects at leakage sites in charge-coupled devices, J. App. Phys. (in press).



FIRST EUROPEAN CONFERENCE ON CRYSTAL GROWTH  
ECCG-1 ZÜRICH SEPTEMBER 12 - 18, 1976

THIRD CIRCULAR

PROGRAM AND INFORMATION

TO PARTICIPANTS

- X D 1 M. Balarin (Acad. Sciences, Dresden, GDR)  
EFFECTS OF IMPURITIES ON METAL PROPERTIES
- X D 2 J.J. Gilman (Allied Chemical, Morristown N.J., USA)  
METALLIC GLASSES
- X D 3 C.H.L. Goodman (STL, Harlow/Essex, UK)  
CONTROL OF STRUCTURE IN SEMICONDUCTOR DEVICES
- D 4 R.F. Belt, R. Uhrin, D. Dentz (Airtron, Morris Plains N.J., USA)  
PRODUCTION PROBLEMS OF 5 CM DIAMETER SINGLE CRYSTALS AND  
WAFERS OF GADOLINIUM GALLIUM GARNET
- D 5 W. Schmidt, W. Stählin (Swiss Aluminium, Neuhausen, Switzerland)  
CRYSTAL GROWTH AND CHARACTERISATION OF GGG
- W. Schmidt, R. Weiss (Swiss Aluminium, Neuhausen, Switzerland)  
DISLOCATION PROPAGATION IN CZOCHRALSKI-GROWN GGG CRYSTALS
- X D 6 A. Authier (Univ. Paris, France)  
X-RAY AND NEUTRON TOPOGRAPHY OF SOLUTION-GROWN CRYSTALS
- X D 7 A.J.R. de Kock (Philips, Eindhoven, Netherland)  
EFFECT OF GROWTH CONDITIONS ON SEMICONDUCTOR CRYSTAL QUALITY
- D 8 P.J. Roksnoer (Philips, Eindhoven, Netherlands)  
INFLUENCE OF COOLING RATE AND CARBON CONCENTRATION ON MICRO-  
DEFECTS IN DISLOCATION-FREE SILICON CRYSTALS
- D 9 B. Jakowlew, W. Jeske (ONPMP, Warsaw, Poland)  
A COMPARISON BETWEEN THE "SWIRLS" DEFECTS OCCURRING IN  
FLOAT-ZONE AND CZOCHRALSKI SILICON SINGLE CRYSTALS
- 
- D10 R. Ogden (Plessey, Caswell/Towcester, UK)  
DEFECTS IN EPITAXIAL Si GROWN ON As<sup>+</sup> ION-IMPLANTED SUBSTRATES
- 
- D11 P. van der Putte, L.J. Giling, J. Bloem (Univ. Nijmegen, Netherlands)  
ETCHPIT FORMATION ON SILICON DURING ETCHING WITH HCl
- D12 R. Kruse (Techn. Univ. Braunschweig, FRG)  
MISFIT DISLOCATIONS IN CELLULAR SUBSTRUCTURES OF Sb-Bi  
ALLOY SINGLE CRYSTALS
- D13 A. Chevy, A. Kuhn, M.-S. Martin (Univ. Paris, France)  
BIG InSe MONOCRYSTALS GROWN FROM A NON-STOICHIOMETRIC MELT
- D14 A.A. Chernov, S.S. Stoyanov (Acad. Sciences, Moscow, USSR and  
Sofia, Bulgaria):  
IMPURITY TRANSPORT DURING MOLECULAR BEAM CONDENSATION
- X D15 V.P. Skripov (Acad. Sciences, Sverdlovsk, USSR)  
HOMOGENEOUS NUCLEATION IN MELTS AND AMORPHOUS FILMS
- D16 A. Räuber (IAF, Freiburg, FRG)  
SEGREGATION OF IMPURITIES in  $\text{LiNbO}_3$  UNDER THE INFLUENCE OF  
ELECTRIC FIELDS
- D17 J.C. Brice (Mullard, Redhill/Surrey, UK)  
TRENDS IN LIQUID PHASE EPITAXY
- D18 E. Andre (RTC, Caen, France)  
ELECTRIC CURRENT INDUCED LIQUID PHASE EPITAXY

DEFECTS IN EPITAXIAL Si GROWN ON

As<sup>+</sup> ION-IMPLANTED SUBSTRATES

RAYMOND OGDEN

ALLEN CLARK RESEARCH CENTRE

THE PLESSEY COMPANY LIMITED

CASWELL, TOWCESTER

NORTHANTS, ENGLAND.

## INTRODUCTION

THE CHEMICAL VAPOUR DEPOSITION (CVD) OF EPITAXIAL LAYERS OF Si WAS BROUGHT INTO LARGE SCALE PRODUCTION IN THE EARLY 1960s FOR THE FABRICATION OF BIPOLAR TRANSISTORS. THE MAJOR CRYSTAL IMPERFECTIONS FOUND IN EPILAYERS WERE STACKING FAULTS (SFs) WHICH WERE STUDIED INTENSIVELY FOR A NUMBER OF YEARS USING A VARIETY OF TECHNIQUES.

BECAUSE OF ITS HIGH RESOLUTION AND POWERFUL ANALYTICAL FACILITY, TRANSMISSION ELECTRON MICROSCOPY (TEM) WAS SOON ESTABLISHED AS THE PRIMARY TOOL FOR THE CHARACTERISATION OF SFs. SFs LIE ON  $\{111\}$  PLANES AND USUALLY FORM STRUCTURES OF CLOSED CONFIGURATION TERMINATING IN STAIR ROD DISLOCATIONS LYING IN  $\langle 110 \rangle$  DIRECTIONS.

NUCLEATION OF SF STRUCTURES USUALLY OCCURRED AT THE SUBSTRATE:EPILAYER INTERFACE AND TWO CHIEF SOURCES WERE IDENTIFIED: MECHANICAL DAMAGE AND CONTAMINATION ON THE SUBSTRATE. VARIOUS MODELS OF SF NUCLEATION WERE ADVANCED: BOOKER AND STICKLER (1962, 3), FINCH ET AL (1963), MENDELSON (1965), THOMAS AND FRANCOME (1967).

AS CVD TECHNIQUES WERE IMPROVED AND LOW DEFECT DENSITIES AND CONTROLLED DOPANT LEVELS WERE ROUTINELY ACHIEVED, INTEREST IN SFs LESSENERED. HOWEVER IN THE LAST 3 YEARS WITH THE INTRODUCTION OF ION-IMPLANTATION TO DOPE SUBSTRATE SURFACES, DEFECTS IN

EPILAYERS ONCE AGAIN BECAME A PROBLEM (MOLINE ET AL 1974). GROWTH ON ARSENIC IMPLANTED  $\{100\}$  Si SUBSTRATES (OGDEN (1975), BAKER AND OGDEN (1975)) RESULTED IN

1. DISLOCATIONS IN THE SUBSTRATE WHICH PROPAGATE WITH THE EPILAYER.
2. SF PYRAMIDS WHICH NUCLEATED CLOSE TO THE SUBSTRATE:LAYER INTERFACE.

THE PRESENT WORK CONCERNS THE CONTROL OF SFs IN EPILAYERS GROWN ON  $As^+$  IMPLANTED  $\{111\}$  SUBSTRATES BY THE CHOICE OF AMBIENT DURING THE POST-IMPLANT OXIDATION DRIVE-IN TREATMENT.

## PERIMENTAL

SUBSTRATES USED WERE LOW DISLOCATION DENSITY ( $< 500 \text{ cm}^{-2}$ ) MONSANTO CZ MATERIAL,  $\Omega \text{ CM.P-TYPE}$ . A DOSE OF  $9 \times 10^{15} \text{ cm}^{-2}$  ARSENIC IONS WAS IMPLANTED THROUGH A STANDARD DEVICE OXIDE MASK PRODUCING A BURIED PATTERN SO THAT EPITAXIAL GROWTH OVER IMPLANTED AND NON-IMPLANTED REGIONS COULD BE COMPARED ON EACH SLICE. THE SUBSTRATES WERE OXIDISED FOR 16H AT  $1200^\circ\text{C}$  IN VARIOUS  $\text{O}_2/\text{N}_2$  MIXTURES. THE SCHEDULE WAS DESIGNED TO GIVE A JUNCTION DEPTH OF  $8 \mu\text{m}$  WITH A SHEET RESISTANCE OF  $8 \Omega$  PER SQ. AFTER REMOVAL OF OXIDE, THE SUBSTRATES WERE PREFIRED IN  $\text{H}_2$  AT  $1240^\circ\text{C}$  FOR 10M PRIOR TO EPITAXIAL GROWTH. LAYERS  $10 \mu\text{m}$  THICK WERE DEPOSITED AT  $1240^\circ\text{C}$  USING  $\text{SiCl}_4$ .

EPITAXIAL LAYERS WERE FIRST EXAMINED BY OPTICAL MICROSCOPY USING NORMARSKI INTERFERENCE CONTRAST. SPECIMENS WERE PREPARED FOR TEM BY ULTRASONICALLY CUTTING 2MM DISCS AND JET THINNING FROM THE SUBSTRATE SIDE USING AN  $\text{HF}/\text{HNO}_3$  MIXTURE. SUBSTRATES BOTH AFTER THE OXIDATION AND THE  $\text{H}_2$  PREFIRE TREATMENTS WERE ALSO EXAMINED BY TEM AND IN THE LATTER CASE GLANCING ANGLE ELECTRON DIFFRACTION (GAED) AND Pt/C REPLICES WERE ALSO EMPLOYED.

## RESULTS

TABLE 1 SUMMARISES THE RESULTS OF THIS WORK.

### (A) EPILAYERS

IT WAS FOUND THAT AT LOW CONCENTRATIONS OF  $O_2$  IN THE DRIVE-IN OXIDATION AMBIENT, THE RESULTING EPITAXIAL LAYERS CONTAINED HIGH DENSITIES ( $10^6 - 10^7 \text{ CM}^{-2}$ ) OF SFs IN REGIONS GROWN OVER ION-IMPLANTED AREAS (FIG. 1(A)). SF DENSITIES OUTSIDE THESE AREAS WERE LOW ( $10^2 - 10^3 \text{ CM}^{-2}$ ) ALTHOUGH DENSITIES WERE HIGHER CLOSE TO THE IMPLANTED AREAS. THE VARYING SIZE OF THE TRIANGLES IN FIGURE 1(A) (SF TETRAHEDRA) SHOWS THAT NUCLEATION WAS NOT CONFINED TO THE SUBSTRATE:LAYER INTERFACE. THIS IS SHOWN MORE CLEARLY BY TEM, FIG. 2(A). THE CLOSING SIDES OF THE SF TETRAHEDRA ARE INVISIBLE DUE TO THE DIFFRACTION CONDITIONS USED. MEASUREMENT OF THE TETRAHEDRA IN THIS MICROGRAPH SHOWS THAT THEY HAVE BEEN NUCLEATED IN THE RANGE  $1.6 - 6.3 \mu\text{m}$  BELOW THE TOP OF THE LAYER. FRINGE CONTRAST AT THE STACKING FAULTS IS SHOWN IN FIG. 2(B), OBTAINED USING THE 2 BEAM  $s = 0$  CONDITION.

IN ADDITION TO SFs, DISLOCATIONS WERE ALSO FOUND IN LARGE NUMBERS, FIG. 2(C). DIFFRACTION CONTRAST ANALYSIS OF A GROUP OF INTERACTING DISLOCATIONS IS SHOWN IN FIG. 3. BURGERS VECTORS ARE DEDUCED FROM TABLE 2 USING THE INVISIBILITY CRITERION

$\underline{g} \cdot \underline{b} = 0$ . A STACKING FAULT RIBBON WHICH DOES NOT TERMINATE IN A STAIR ROD DISLOCATION AT ONE END IS MARKED A.

AS THE PERCENTAGE OF  $O_2$  IN THE AMBIENT DURING DRIVE IN WAS INCREASED, SF DENSITIES FELL IN THE EPILAYERS UNTIL AT ABOVE 20%  $O_2$  DENSITIES COMPARABLE WITH THE NON-IMPLANTED AREAS WERE ACHIEVED, FIG. 1(B).

### (B) SUBSTRATES

PREFIRED SUBSTRATES WERE SPECIFICALLY EXAMINED FOR SiC PRECIPITATION BY GAED AND BY ELECTRON DIFFRACTION OF PARTICLES EXTRACTED BY Pt/C REPLICA, BUT THIS PHASE WAS NOT DETECTED. ALL SUBSTRATES WERE VERY SMOOTH. DETAILED EXAMINATION OF BOTH OXIDISED AND PREFIRED SUBSTRATES BY TEM SHOWED THAT THE LIGHTLY OXIDISED SUBSTRATES WERE FREE OF DISLOCATIONS AND PRECIPITATES, BUT THESE DEFECTS WERE OBSERVED AS DECORATED DISLOCATION NETWORKS ON HEAVILY OXIDISED SUBSTRATES IN ION-IMPLANTED REGIONS FIGS. 4 (A) AND (B) SHOW BRIGHT FIELD AND WEAK BEAM IMAGES RESPECTIVELY OF A DECORATED DISLOCATION FORMING ONE ARM OF A DISLOCATION NODE IN THE PREFIRED, 20%  $O_2$  SUBSTRATE. DIFFRACTION CONTRAST ANALYSIS OF A DISLOCATION NETWORK IN THIS SUBSTRATE IS SHOWN IN FIG. 5. ZERO VALUES OF  $\underline{g} \cdot \underline{b}$  FOR THE REFLECTIONS USED ARE GIVEN IN TABLE 3. AG ONLY ONE DISLOCATION APPEARS TO BE DECORATED

## DISCUSSION

CONTINUOUS NUCLEATION OF SF TETRAHEDRA AS EVIDENCED BY FIG. 2(A) SUGGESTS THAT IMPURITIES ARE DIFFUSING OUT OF THE SUBSTRATE, INTO THE EPILAYER AND PRECIPITATING ON THE SURFACE OF THE GROWING LAYER. SFs ARE THEN NUCLEATED WHEN THE PRECIPITATES ARE OVERGROWN WITH Si. THE DIFFUSION COULD BE ASSISTED BY THE DISLOCATIONS THREADING THE EPILAYERS. THE DECORATED DISLOCATIONS FOUND IN THE SUBSTRATES WHICH HAD BEEN HEAVILY OXIDISED, FIGS. 4 AND 5, IMPLIES THAT IMPURITIES ARE "GETTERED" BY THE OXIDATION TREATMENT TO PRECIPITATE AS OXIDE COMPLEXES ON DISLOCATIONS. SINCE THE PRECIPITATES ARE STABLE DURING THE H<sub>2</sub> PREFIRE, THEY ARE LIKELY TO REMAIN SO DURING EPITAXY AND DO NOT ALLOW IMPURITIES TO DIFFUSE TO THE GROWING SURFACE.

THE IDENTITY OF THE IMPURITY BELIEVED RESPONSIBLE FOR THESE EFFECTS HAS NOT BEEN ESTABLISHED. EARLIER WORK ON LAYERS GROWN FROM ETHYLENE-CONTAMINATED SILANE UNDER UHV CONDITIONS (OGDEN, BRADLEY AND WATTS, (1974)) HAS SHOWN SIMILAR DEFECT STRUCTURES. PREVIOUSLY UNPUBLISHED MICROGRAPHS FROM THIS WORK, FIGS. 6 (A), (B) SHOW THAT STACKING FAULT TETRAHEDRA OF VARYING SIZE AND DISLOCATIONS OCCURRED IN AN EPILAYER WHERE GROWTH WAS COMMENCED WITH

50 PPM ETHYLENE AND THE FLOW TURNED OFF FOR THE FINAL 2 μm OF GROWTH. WHEN 2 μm OF THE LAYER WAS REMOVED BY ETCHING, RIBBON SFs AND DISLOCATIONS WERE DISCOVERED BUT NO SF TETRAHEDRA. PARTICLES OF β-SiC WERE ASSOCIATED WITH THE FORMATION OF TETRAHEDRA, BUT AT THE GROWTH TEMPERATURE USED IN THE PRESENT WORK DEFECT-FREE LAYERS WERE GROWN EVEN WITH HIGH LEVELS OF ETHYLENE AND SiC WAS NOT DETECTED. SINCE NO EVIDENCE OF SiC WAS FOUND IN THE PRESENT WORK, FURTHER DISCUSSION WOULD BE SPECULATIVE. IN SITU X-RAY ANALYSIS OF THE PRECIPITATES SHOWN IN FIGS. 4 AND 5 MAY PROVE FRUITFUL.

## ACKNOWLEDGEMENTS

THE AUTHOR THANKS THE DIRECTORS OF THE PLESSEY COMPANY LIMITED FOR PERMISSION TO PRESENT THIS CONTRIBUTED PAPER. THANKS ARE DUE TO NORMAN ROSS AND PETER STOREY AT PLESSEY (SWINDON) FOR SUPPLYING THE MATERIAL USED IN THIS STUDY AND FOR DETAILS OF PROCESSING SCHEDULES.

TABLE 1

SUMMARY OF RESULTS

DRIVE-IN AMBIENT	STRUCTURE OF OXIDISED & PREFIRED SUBSTRATE	STRUCTURE OF EPILAYER
20% O <sub>2</sub> /N <sub>2</sub>	10 <sup>5</sup> CM <sup>-2</sup> EDGE DISLOCATIONS IN NETWORKS, SOME DECORATED WITH PRECIPITATES, LOCATED IN ION-IMPLANTED REGIONS	10 <sup>2</sup> - 10 <sup>3</sup> CM <sup>-2</sup> SF DENSITY IN BOTH IMPLANTED & NON-IMPLANTED REGIONS
1% O <sub>2</sub> /N <sub>2</sub>	VERY FEW DEFECTS OBSERVED	10 <sup>6</sup> - 10 <sup>7</sup> CM <sup>-2</sup> SF AND DISLOCATION DENSITY OVER ION-IMPLANTED REGIONS. INTRINSIC SF TETRAHEDRA OF VARYING SIZE

TABLE 2

ZERO VALUES OF g.b FOR REFLECTIONS USED IN ANALYSIS SHOWN IN FIG.3

	$b \pm \frac{1}{2} [110]$	$\pm \frac{1}{2} [\bar{1}10]$	$\pm \frac{1}{2} [101]$	$\pm \frac{1}{2} [\bar{1}01]$	$\pm \frac{1}{2} [011]$	$\pm \frac{1}{2} [0\bar{1}1]$
g						
$\bar{2}20$	0					
$20\bar{2}$			0			
$0\bar{2}2$					0	
$\bar{1}11$	0		0			0
$1\bar{1}1$	0			0	0	
$\bar{1}1\bar{3}$		0				

TABLE 3

ZERO VALUES OF  $g \cdot b$  FOR REFLECTIONS USED IN ANALYSIS SHOWN IN FIG. 5

	$b \pm \frac{1}{2} [110]$	$\pm \frac{1}{2} [\bar{1}10]$	$\pm \frac{1}{2} [101]$	$\pm \frac{1}{2} [\bar{1}01]$	$\pm \frac{1}{2} [011]$	$\pm \frac{1}{2} [0\bar{1}1]$
$g_{022}$					0	
$g_{311}$						0
$g_{\bar{1}11}$	0		0			0
$g_{\bar{2}20}$	0					
$g_{\bar{2}02}$			0			
$g_{\bar{1}\bar{1}1}$	0			0	0	0
$g_{\bar{1}13}$		0				

## REFERENCES

- J F C BAKER AND R OGDEN, J MAT SCI 10,  
1259 (1975).
- G R BOOKER AND R STICKLER, J APP PHYS 33,  
3281 (1962).
- G R BOOKER AND R STICKLER, APP PHYS LETT 3,  
158 (1963).
- R H FINCH, H J QUEISER, G THOMAS AND J  
WASHBURN, J APP PHYS 34, 406 (1963).
- S MENDELSON, J APP PHYS 36, 2525 (1965).
- R A MOLINE, R LIEBERMAN, J SIMPSON AND  
A U MACRAE, J ELECTROCHEM SOC 121, 1362  
(1974).
- R OGDEN, PHYS STAT SOL (A) 28, K97 (1975).
- R OGDEN, R R BRADLEY AND B E WATTS, PHYS  
STAT SOL (A) 26, 135 (1974).
- R N THOMAS AND M H FRANCOMBE, APP PHYS LETT  
11, 134 (1967).

FIGURE CAPTIONS

FIG.1. OPTICAL MICROGRAPHS USING NORMANSKI INTERFERENCE

CONTRAST OF EPITAXIAL SILICON SURFACES

- (A) EPILAYER GROWN ON SUBSTRATE WITH 1% O<sub>2</sub> DRIVE-IN AMBIENT SHOWING SFs OVER BURIED n<sup>+</sup> REGIONS
- (B) EPILAYER GROWN ON SUBSTRATE WITH 20% O<sub>2</sub> DRIVE-IN AMBIENT OPTICAL MICROGRAPHS

FIG.2. DEFECTS IN EPITAXIAL LAYER GROWN ABOVE ION-IMPLANTED REGIONS ON SUBSTRATE WITH 1% O<sub>2</sub> DRIVE-IN

- (A) THICK FOIL REGION, LOW MAGNIFICATION SHOWING SF TETRAHEDRA OF VARYING SIZE
- (B) 2 BEAM  $s = 0$  CONDITION SHOWING THICKNESS FRINGES & SF FRINGES
- (C) THICK FOIL REGION SHOWING SF TETRAHEDRA & DISLOCATIONS 220 REFLECTIONS

TRANSMISSION ELECTRON MICROGRAPHS

FIG.3. ANALYSIS OF DISLOCATIONS IN EPILAYER GROWN ON SUBSTRATE WITH 1% O<sub>2</sub> DURING DRIVE-IN, ION-IMPLANTED REGION

BURGERS VECTORS OF DISLOCATION NETWORK

TRANSMISSION ELECTRON MICROGRAPHS

FIG.4. DECORATED DISLOCATION IN ION-IMPLANTED, 20% O<sub>2</sub> DRIVE-IN, H<sub>2</sub> PREFIRED SUBSTRATE

- (A) BRIGHT FIELD 220 REFLECTION,  $s = 0$
- (B) WEAK BEAM 220 REFLECTION, 660 MAIN REFLECTION

TRANSMISSION ELECTRON MICROGRAPHS

FIG.5. ANALYSIS OF DISLOCATION NETS IN ION-IMPLANTED, 20% O<sub>2</sub> DRIVE-IN, H<sub>2</sub> PREFIRED SUBSTRATE

BURGERS VECTORS OF DISLOCATIONS

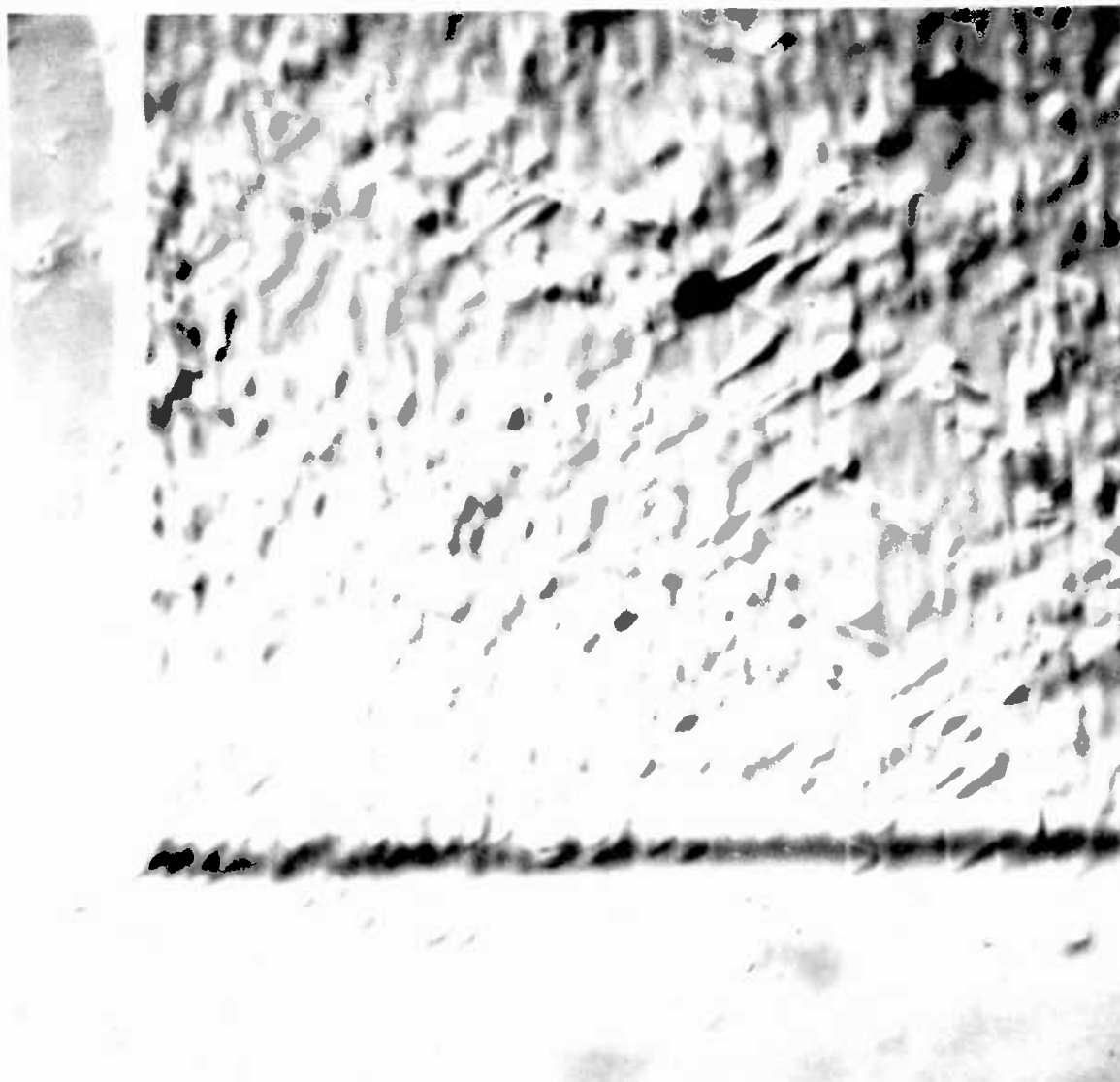
TRANSMISSION ELECTRON MICROGRAPHS

FIG.6.

- (A) {111} EPILAYER GROWN AT 850°C BY PYROLYSIS OF SILANE CONTAMINATED WITH 50 PPM ETHYLENE DURING INITIAL STAGES OF GROWTH IN UHV SYSTEM, SHOWING VARYING SIZE SF TETRAHEDRA & DISLOCATIONS

(B) EPILAYER AS ABOVE REMOVED BY ETCHING DOWN TO ETHYLENE-CONTAMINATED  
PORTION SHOWING SHOCKLEY-BOUNDED SF LOOPS & DISLOCATIONS  
TRANSMISSION ELECTRON MICROGRAPHS

# OPTICAL MICROGRAPHS USING NOMARSKI INTERFERENCE



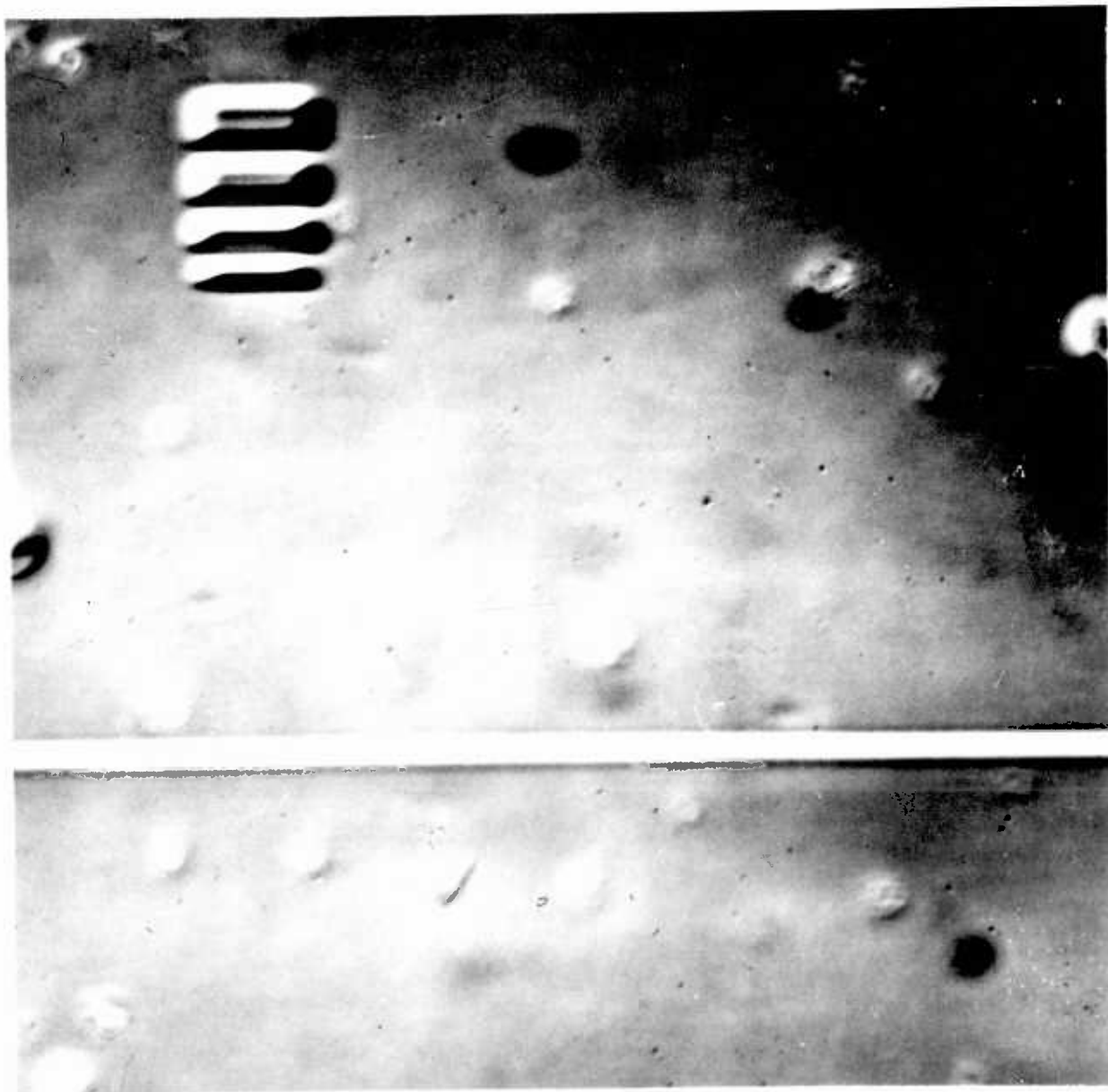
(A)

PILAYER GROWN ON SUBSTRATE WITH 1% O<sub>2</sub> DRIVE-IN  
AMBIENT SHOWING SFs OVER BURIED n<sup>+</sup> REGIONS

OPTICAL

# CONTRAST OF EPITAXIAL SILICON SURFACES

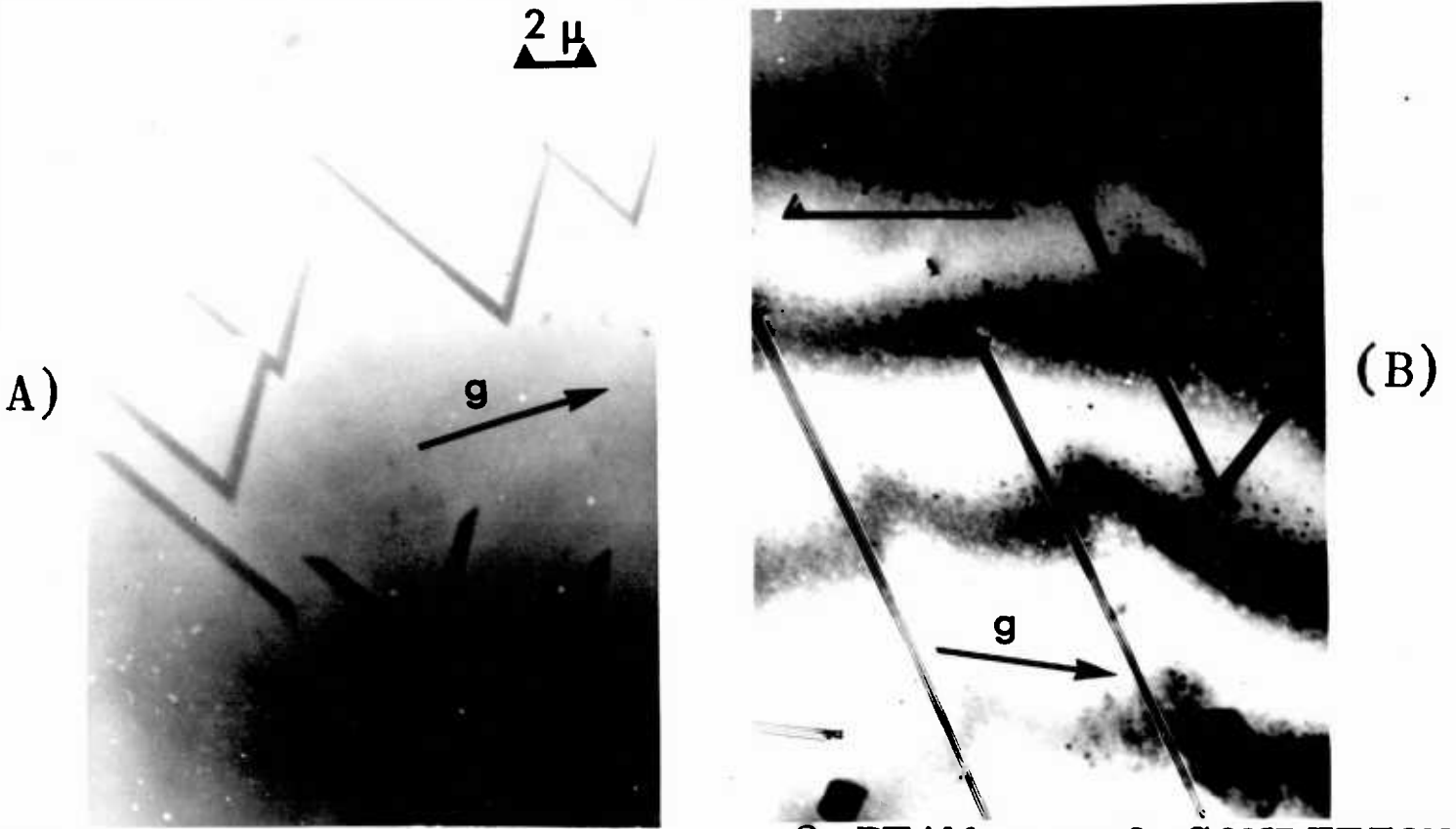
(B)



EPILAYER GROWN ON SUBSTRATE WITH 20%  $O_2$   
DRIVE-IN AMBIENT

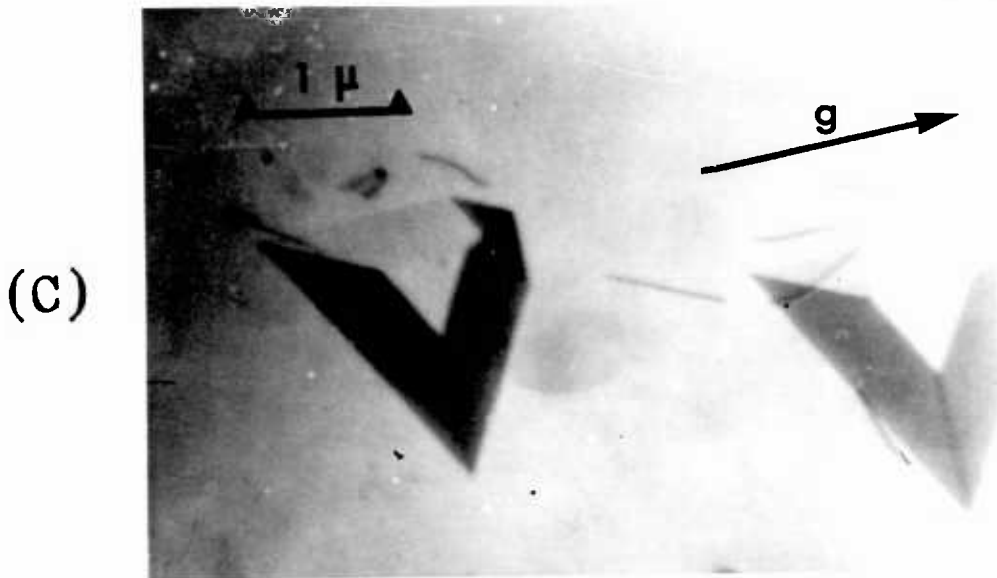
FIG.2.

DEFECTS IN EPITAXIAL LAYER GROWN ABOVE ION-  
LANTED REGIONS ON SUBSTRATE WITH 1% O<sub>2</sub> DRIVE-IN



THICK FOIL REGION, LOW  
MAGNIFICATION SHOWING SF  
TETRAHEDRA OF VARYING SIZE

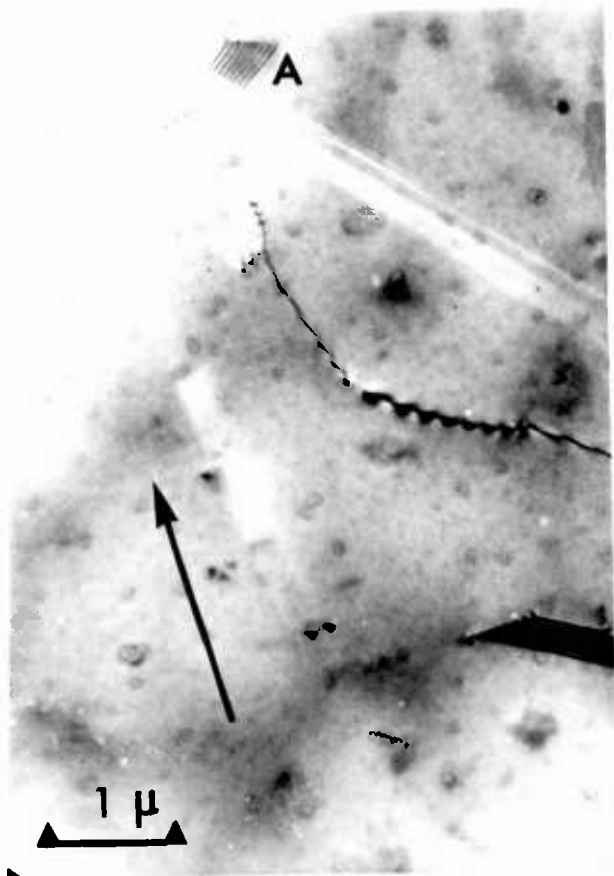
2 BEAM  $s = 0$  CONDITION  
SHOWING THICKNESS  
& SF FRINGES



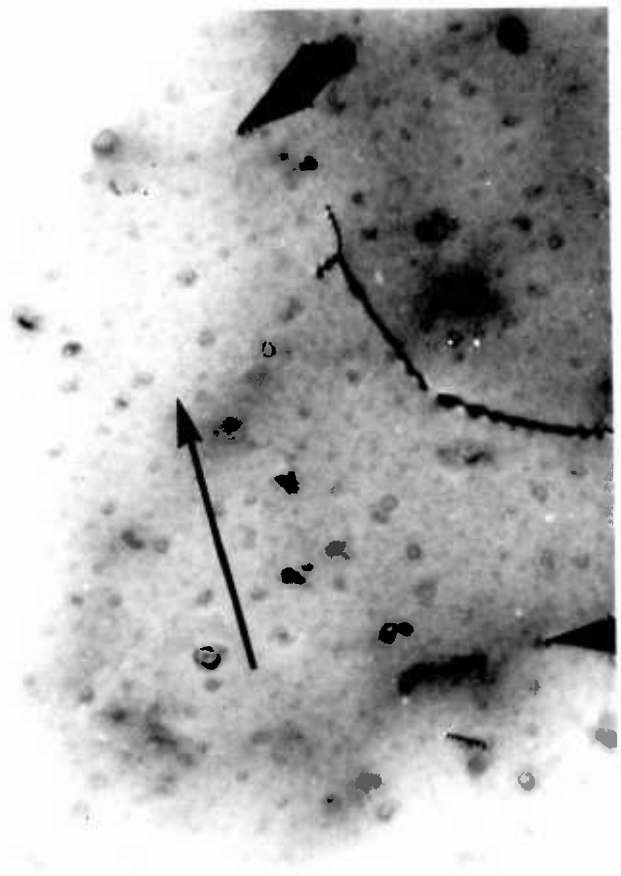
THICK FOIL REGION SHOWING SF  
TETRAHEDRA & DISLOCATIONS

TRANSMISSION ELECTRON MICROGRAPHS

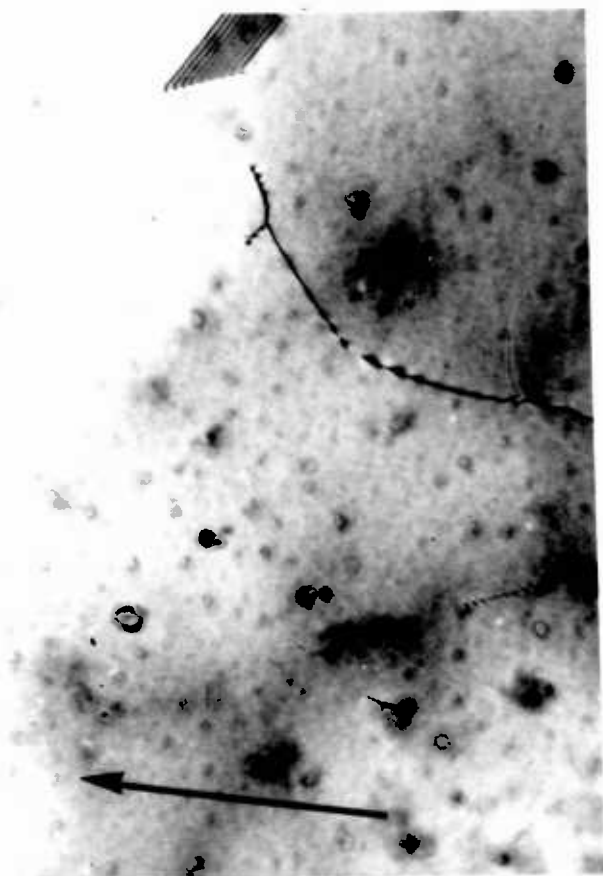
FIG. 3. ANALYSIS OF DISLOCATIONS WITH 1% O<sub>2</sub> DURING



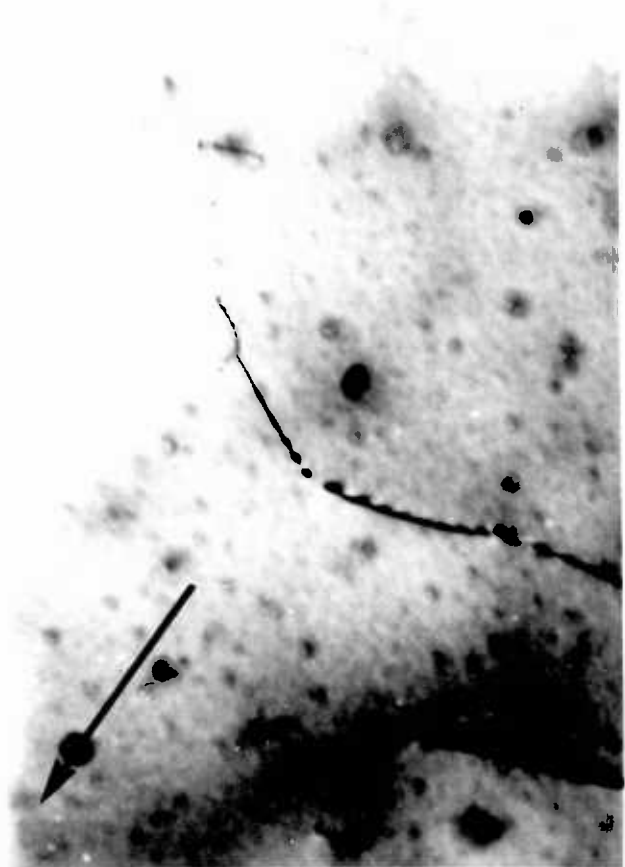
$2\bar{2}0, s=0$



$2\bar{2}0, s>0$



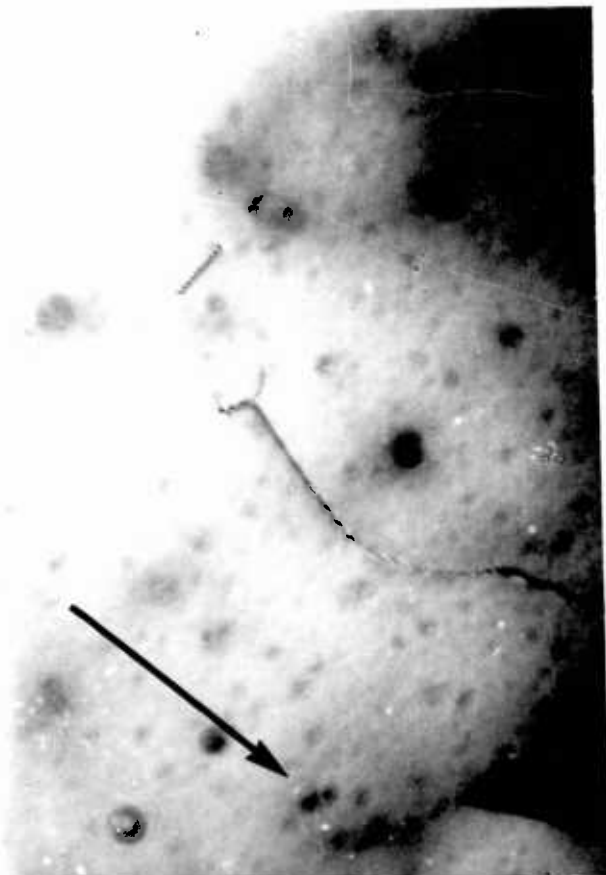
$20\bar{2}$



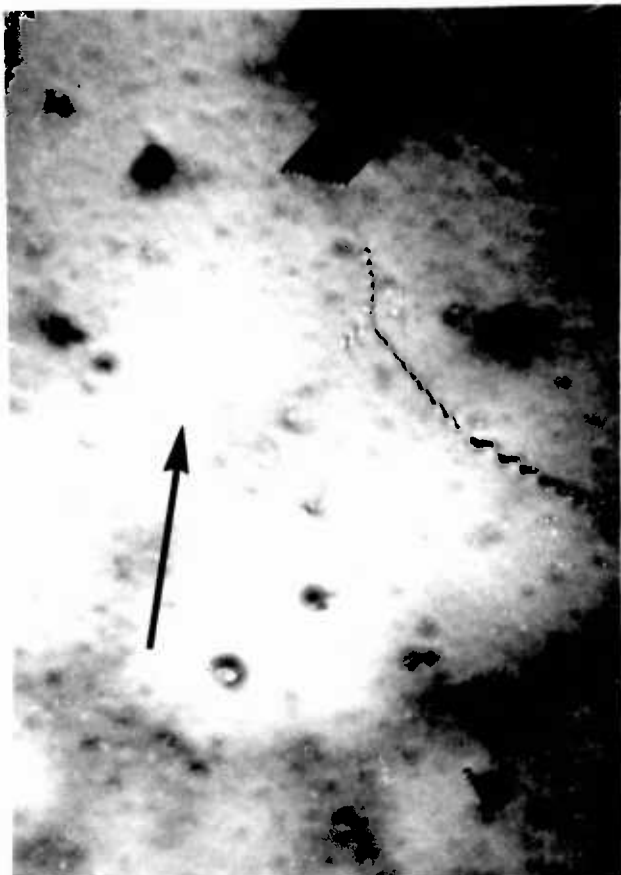
$02\bar{2}$

TRANSMISSION ELECTRON

N EPILAYER GROWN ON SUBSTRATE  
RIVE-IN, ION-IMPLANTED REGION

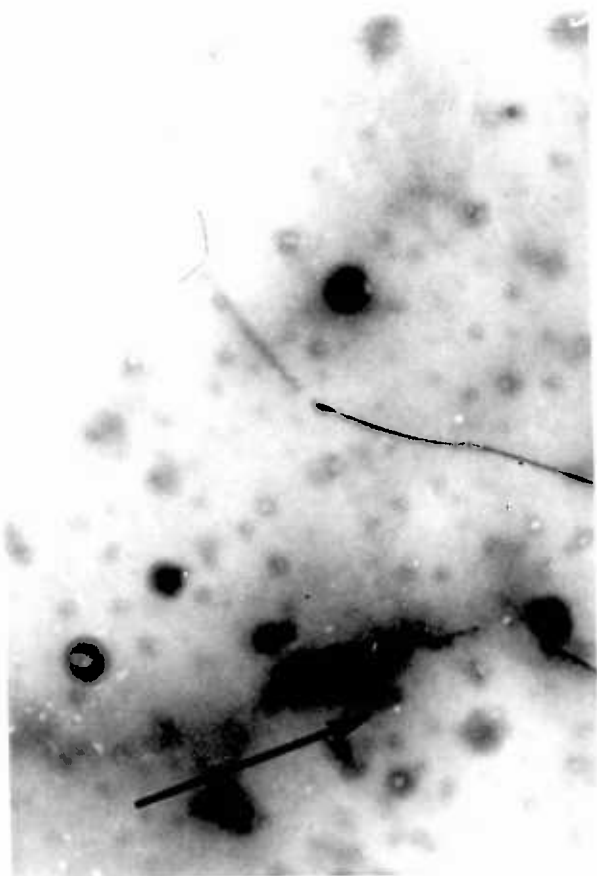
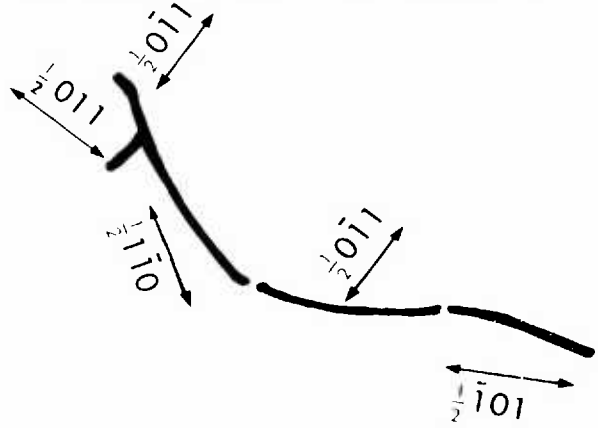


$\bar{1}\bar{1}\bar{1}$



$\bar{1}\bar{1}\bar{1}$

BURGERS VECTORS OF  
DISLOCATION NETWORK



$\bar{1}\bar{1}\bar{3}$

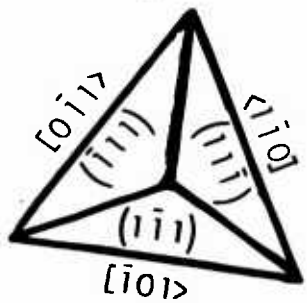
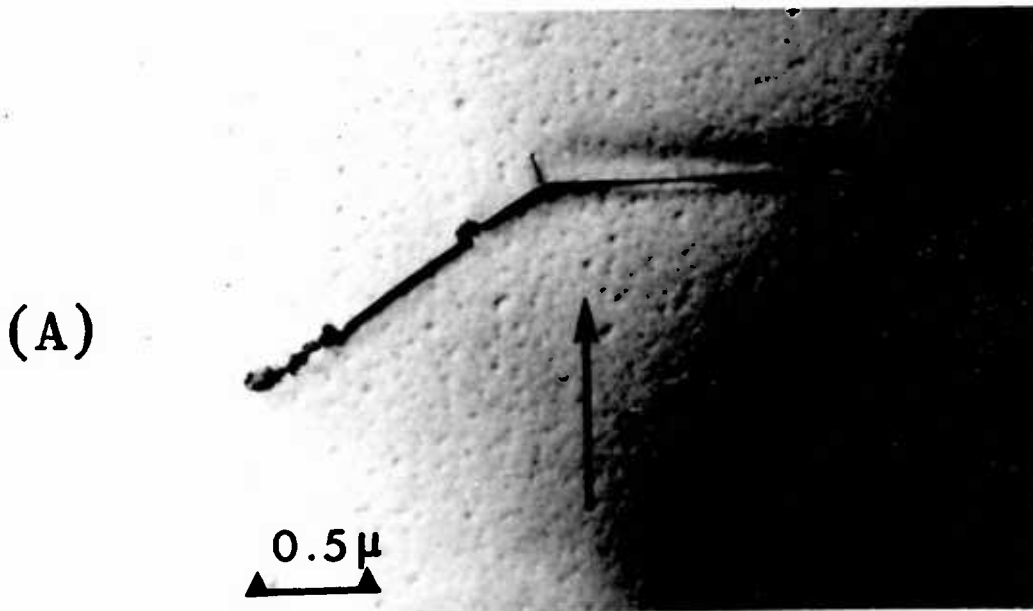


**FIG.4.**

**DECORATED DISLOCATION IN ION-IMPLANTED,  
20% O<sub>2</sub> DRIVE-IN, H<sub>2</sub> PREFIRED SUBSTRATE**



**BRIGHT FIELD 220 REFLECTION,  $s = 0$**



**WEAK BEAM 220 REFLECTION,  
660 MAIN REFLECTION**

**TRANSMISSION ELECTRON MICROGRAPHS**

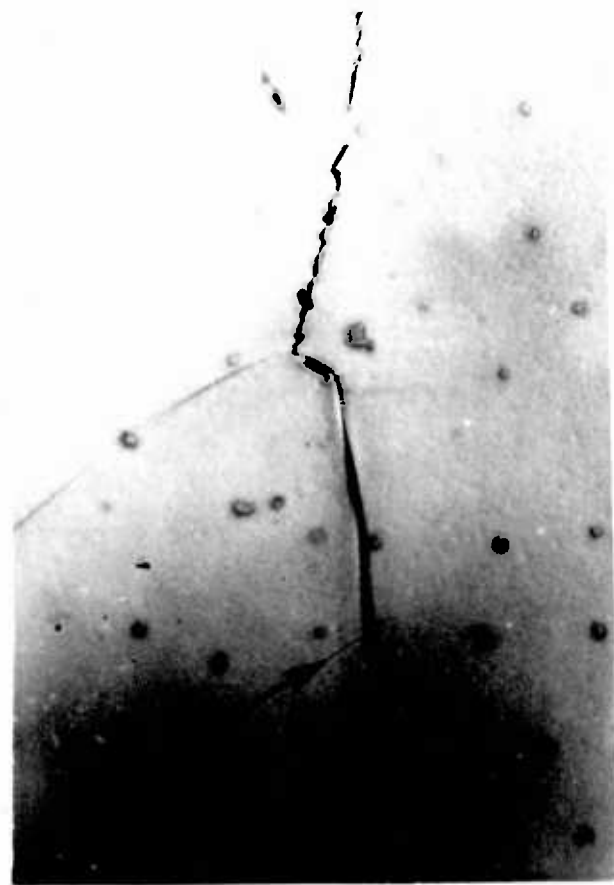
ANALYSIS OF DISLOCATION NETS IN ION-IMPLANTED,



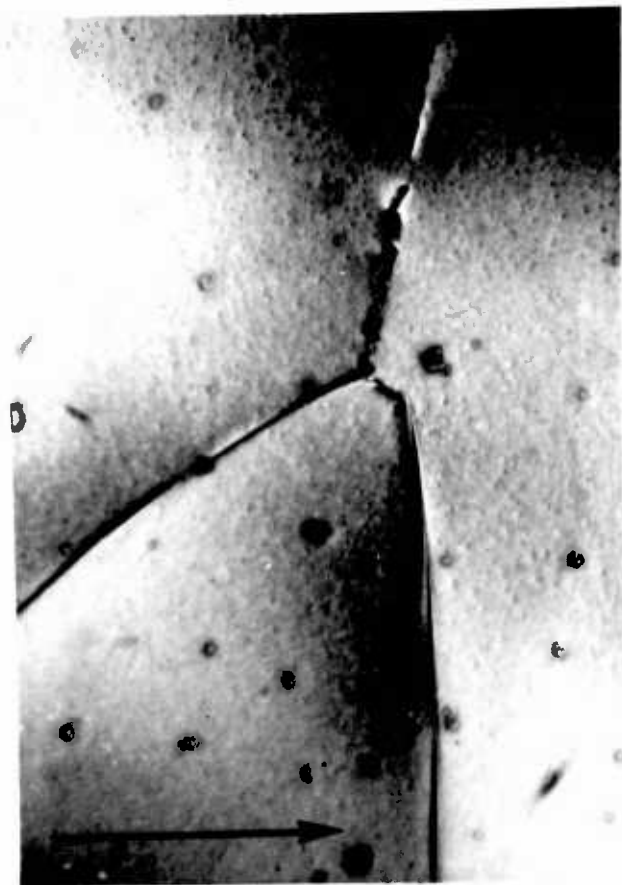
$02\bar{2}$



$3\bar{1}\bar{1}$

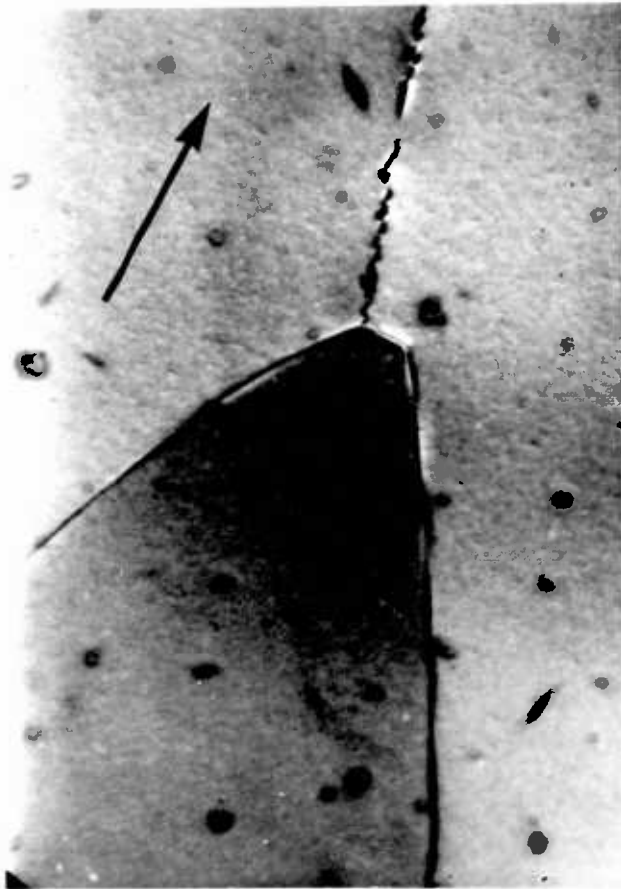


$\bar{1}\bar{1}\bar{1}$

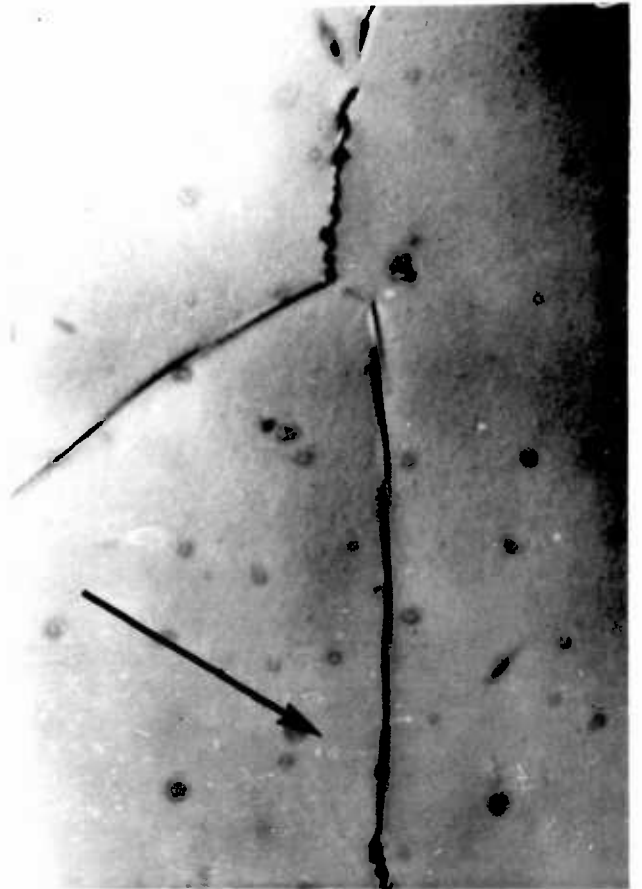


$\bar{2}\bar{2}\bar{0}$   
TRANSMISSION ELECTRON

0% O<sub>2</sub> DRIVE-IN, H<sub>2</sub> PREFIRED SUBSTRATE

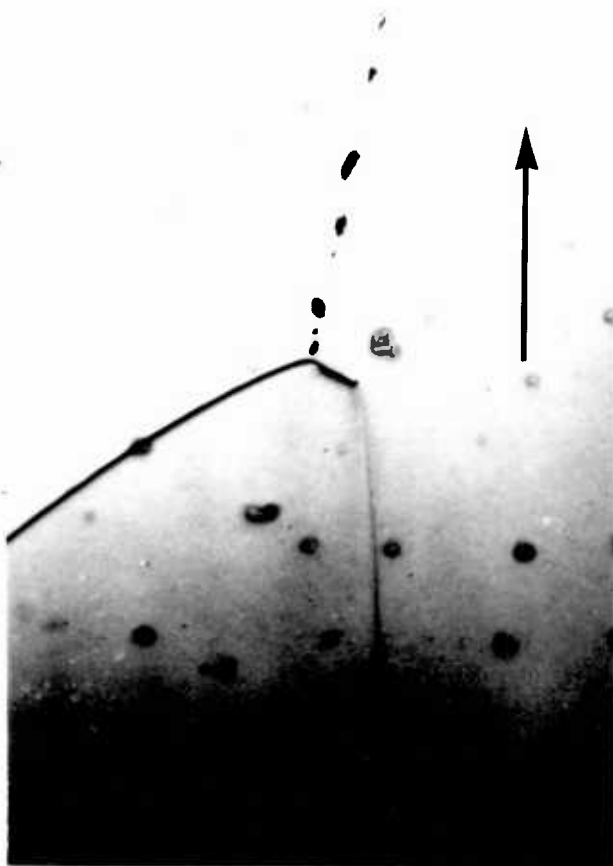


$\bar{2}02$



$\bar{1}\bar{1}\bar{1}$

BURGERS VECTORS OF DISLOCATIONS



$\bar{1}\bar{1}3$

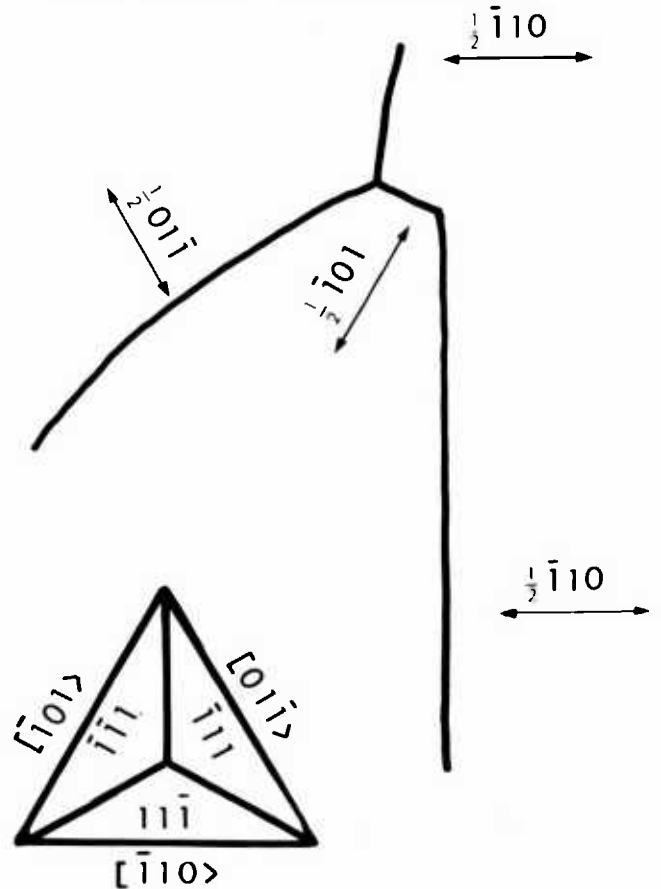
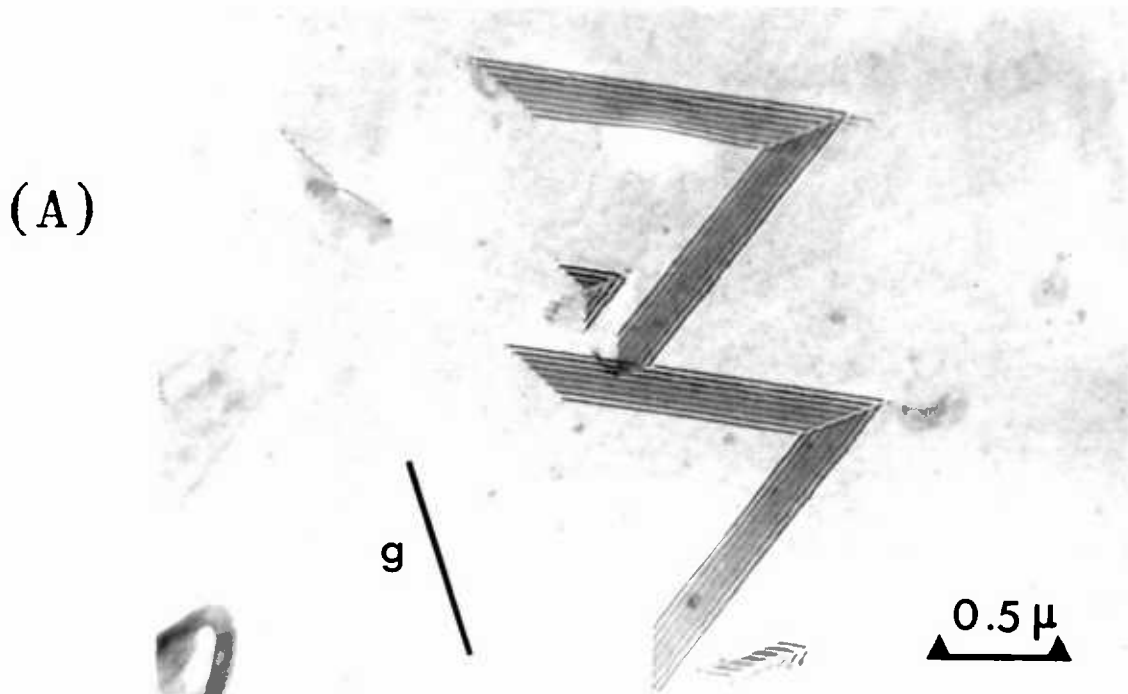
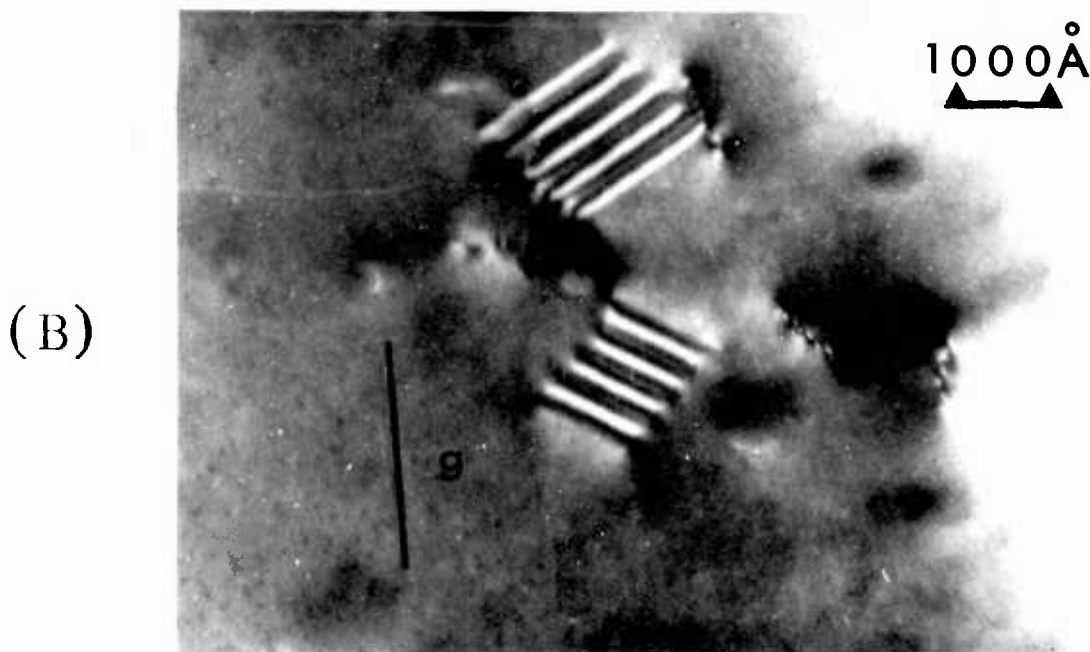


FIG.6.

{111} EPILAYER GROWN AT 850°C BY PYROLYSIS OF  
GAS CONTAMINATED WITH 50 PPM ETHYLENE DURING  
INITIAL STAGES OF GROWTH IN UHV SYSTEM



WING VARYING SIZE SF TETRAHEDRA & DISLOCATIONS



EPILAYER AS ABOVE REMOVED BY ETCHING DOWN TO  
ETHYLENE-CONTAMINATED PORTION SHOWING SHOCKLEY-  
PARTIAL DISLOCATIONS & DISLOCATIONS

TRANSMISSION ELECTRON MICROGRAPHS

CHARACTERISATION OF CRYSTAL DEFECTS AT  
LEAKAGE SITES IN CHARGE-COUPLED DEVICES

R. Ogden and J.M. Wilkinson

Allen Clark Research Centre,  
The Plessey Company Limited,  
Caswell, Towcester, Northants., U.K.

ABSTRACT

Crystal defects have been identified at the sites of high leakage (spikes) in charge-coupled devices operated in the integration mode. Oxidation-induced stacking faults and dislocations were observed using X-ray topography and selective etching, and identified by transmission electron microscopy. Electrical measurements showed that the stacking faults had a range of activity which is attributed to variation in the level of impurity decoration of the defects.

TEXT

Much effort has been devoted to the reduction of leakage currents in charge-coupled devices (CCD's). Gettering techniques to remove undesirable impurities have been reported (1,2,3) and oxidation induced stacking faults have been reduced by appropriate pretreatments (3,4) or furnace conditions (5). We have used the integration mode of operation (6,7) to measure the spatial variation of CCD leakage current, and crystal defects have been identified at the sites of high leakage using X-ray topography (XRT), transmission electron microscopy (TEM) and selective etching. Our results confirm those of Tanikawa, Ito and Sei (7), who found a strong correlation between the location of leakage spikes and etch pits which they attributed to stacking faults (SF's).

Much effort has been devoted to the reduction of leakage currents in charge-coupled devices (CCD's). Gettering techniques to remove undesirable impurities have been reported (1,2,3) and oxidation-induced stacking faults have been reduced by appropriate pretreatments (3,4) or furnace conditions (5). We have used the integration mode of operation (6,7) to measure the spatial variation of CCD leakage current, and crystal defects have been identified at the sites of high leakage using X-ray topography (XRT), transmission electron microscopy (TEM) and selective etching. Our results confirm those of Tanikawa, Ito and Sei (7), who found a strong correlation between the location of leakage spikes and etch pits which they attributed to stacking faults (SF's).

128 and 340 bit linear CCD's were fabricated using a buried channel process with non-overlapping metal gates (8). A range of processing schedules were evaluated, but in all cases the final gate oxidation was carried out at 1100°C in a dry oxygen atmosphere with 0.5% HCl.

The spatial variation of leakage current was measured using the stopped clock or integration mode of operation (6,7). One clock phase was held at a positive DC level for a period of between 0.2 and 100 mS. In some cases the level of leakage current was so great that even in the shorter period, a full well of charge was collected. In contrast, for the better devices, only a small fraction of a full well was collected after 100 mS representing an improvement of more than a factor of  $10^3$  in storage time. Figure 1(a) shows an output from the CCD at the end of the integration period.

Transmission and surface XRT plates were taken using a Lang X-ray camera. Figure 1(b) is the XRT micrograph corresponding to the device whose output is shown in Figure 1(a). The device is crossed by linear features or "scratches"

which can be seen from Figure 1(a) to correlate with areas of high leakage on the device. This observation was confirmed on all those slices examined where XRT revealed "scratches". To obtain further characterisation of the scratch features, specimens were prepared for TEM. The whole slice was lapped on the back down to about  $100\ \mu\text{m}$  and then mounted face upwards in black apiezon wax. Circular discs of 2 mm diameter were then cut ultrasonically at areas selected from the topographs where the "scratches" ran across the CCD channel. The discs were removed from the wax by warming and then washed in trichloroethylene. Oxide and metallisation were then removed by HF, and the discs were finally thinned to perforation by jet etching from the lapped side using an HF:HNO<sub>3</sub> mixture. Damage induced by the ultrasonic cutting stage was not found to be a problem since the silicon surface was protected by oxide. Optical micrographs of the thinned TEM specimens were taken using Normarski interference contrast prior to mounting in a tilt cartridge and insertion in the electron microscope. Areas of interest were located by taking electron micrographs at very low magnification using only the objective lens and comparing them with the optical micrographs. In this way it was established that the "scratches" observed by XRT were comprised of continuous bands of stacking faults and dislocations which emerged at the surface of the slice. Figure 2 shows a portion of a typical "scratch" which consists of stacking faults and dislocations in a band about  $5\ \mu\text{m}$  wide which runs at an angle of about  $12^\circ$  to a  $\langle 110 \rangle$  direction. Stacking faults, as shown here, are usually aligned along the  $\langle 110 \rangle$  direction nearest to the "scratch" direction.

Detailed analysis of the defects by diffraction contrast techniques in TEM showed that most dislocations were edge type with  $\frac{1}{2} \langle 110 \rangle$  Burgers vectors lying in the plane of the substrate. The stacking faults were extrinsic in nature and bounded by Frank partial dislocations with  $\frac{1}{3} \langle 111 \rangle$  Burgers vectors.

No evidence of precipitation could be detected at the fault planes or at the bounding partials. The character and distribution of the defects were unchanged by the region of the device through which the "scratch" band passed. Very few defects were found outside these bands. TEM examination of slices showing large differences in background leakage and spike to background ratio did not reveal any significant differences in character or distribution of the defect band. The defect bands are believed to be caused by scratch damage on the polished faces of incoming substrates and form during the initial oxidation of the slices. It is well known (9) that oxidation-induced stacking faults are easily generated by mechanical damage prior to oxidation.

Selective etching (10) was also used to locate the position of stacking faults and dislocations after electrical assessment. The spatial distribution of SF's fell into two groups: those associated with surface damage (the "scratches" which were only present on a few slices), and a random distribution, possibly the result of bulk nucleation sites (3). Although 80% of the locations of leakage spikes coincided with the position of SF's, the electrical activity of the SF's varied over a wide range, equivalent to between 4 and 590 pA per SF. No significant differences between the SF's were observed by TEM. For comparison, Table 1 shows the range of activity per SF deduced from previous work (7,9,11,12). In some cases leakage currents were measured on simple diode structures (9,11,12) and in others (7) and the present work, equivalent leakage currents were deduced from CCD measurements. The density and location of SF's were identified by etching techniques in most cases, although in the present work we have positively identified SF's by TEM. Leakage currents about 1000 X higher than ours were recorded by Ravi et al (9) who showed that their electrically active SF's were heavily decorated with precipitates. Rozgonyi and Kushner (11) used gettering techniques which reduced the density of SF's and perhaps were

also effective in producing the low level of activity per SF. All this work suggests that the stacking fault itself may not be a primary cause of electrical leakage, but it is acting as a nucleus where impurities congregate. The range of activity suggests that variable amounts of impurities are associated with our SF's, and although the leakage levels do not lead us to expect highly decorated SF's, work is continuing to detect and identify these impurities.

#### ACKNOWLEDGEMENT

The authors wish to thank the Directors of The Plessey Company Limited for permission to publish.

TABLE 1

LEAKAGE CURRENT PER STACKING FAULT DEDUCED FROM  
ELECTRICAL MEASUREMENTS AND STACKING FAULT COUNTS

Authors	Leakage Current per SF
Ravi et al (9)	15 $\mu$ A to 500 $\mu$ A
Tanaka et al (12)	60 nA to 6 $\mu$ A
Rozgonyi et al (11)	7 pA to 33 pA
Tanikawa et al (7)	$\sim$ 10 pA
Ogden and Wilkinson	4 pA to 590 pA

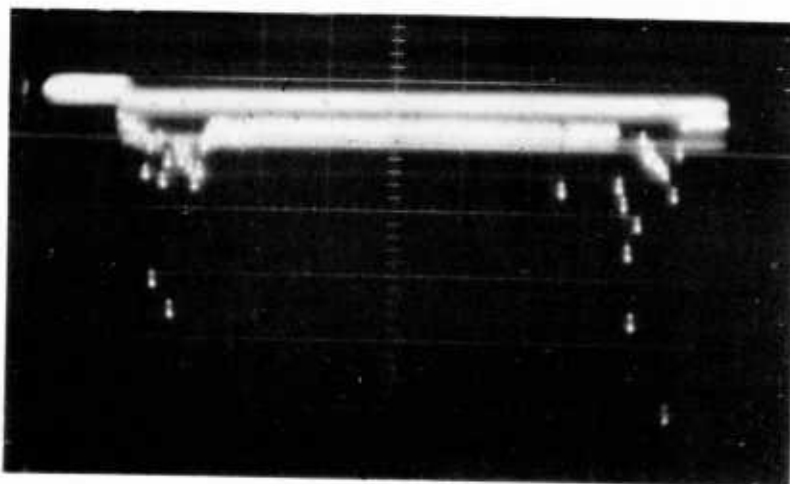
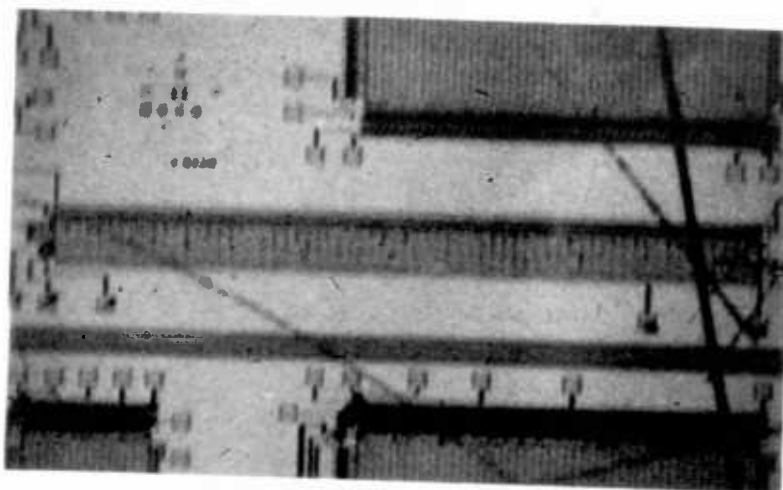


Fig 1

(a)



(b)

REFERENCES

- (1) T.E. Seidel, R.L. Meek, and A.G. Cullis.  
J. App. Phys. 46, 600 (1975).
- (2) A.G. Nassibian, V.A. Browne, and K.D. Perkins.  
J. App. Phys. 47, 992 (1976).
- (3) G.A. Rozgonyi, P.M. Petroff, and M.H. Read.  
J. Electrochem. Soc. 122, 1725 (1975).
- (4) H. Shiraki.  
Jap. J. App. Phys. 13, 1514 (1974).
- (5) H. Shiraki.  
Jap. J. App. Phys. 14, 747 (1975).
- (6) D.G. Ong, and R.F. Pierret.  
I.E.E.E. Trans. ED ED-22, 593 (1975).
- (7) K. Tanikawa, Y. Ito, and H. Sei.  
App. Phys. Letters 28, 285 (1976).
- (8) V.A. Browne, and K.D. Perkins.  
I.E.E.E. Trans. ED ED-23, 271 (1976).
- (9) K.V. Ravi, C.J. Varker, and C.E. Volk.  
J. Electrochem. Soc. 120, 533 (1973).
- (10) F. Secco D'Aragona.  
J. Electrochem. Soc. 119, 948 (1972).
- (11) G. Rozgonyi and R.A. Kushner.  
J. Electrochem. Soc. 123, 570 (1976).
- (12) K. Tanaka, G. Nakamura, M. Amano, and Y. Yukimoto.  
Extd. Abstracts of Electrochemical Society Fall Meeting, 1974.

FIGURE CAPTIONS

- Figure 1 Comparison of (a) spatial variation of CCD leakage with (b) damage bands on same device as revealed by XRT  $\text{CuK}\alpha_1$  radiation,  $\{422\}$  surface reflection.
- Figure 2 TEM micrograph of a portion of a typical damage band showing stacking faults and dislocations. Diffraction vector  $\underline{g} = \langle 400 \rangle$ .

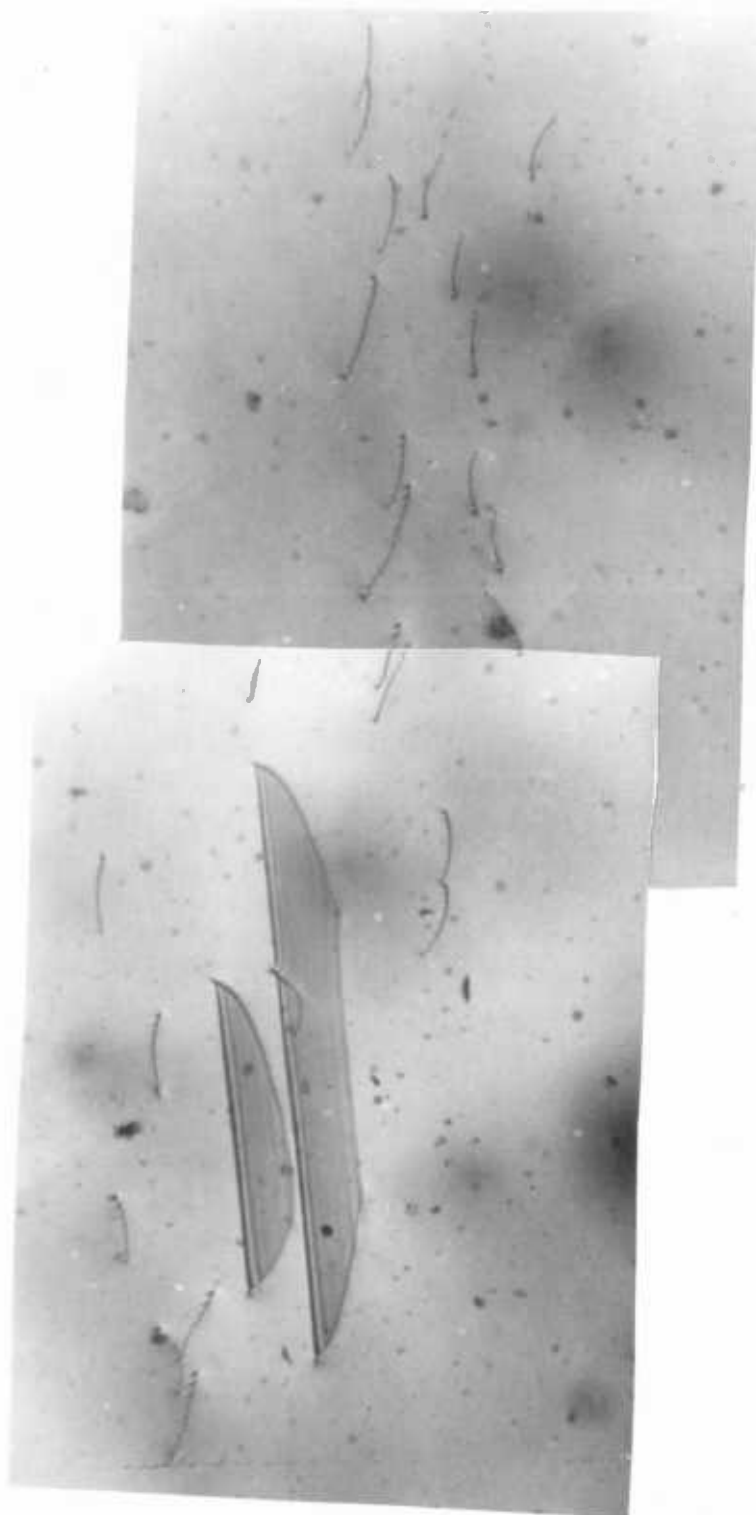


Fig 2

**short note**

reprinted from

**physica**

**status**

**solidi (a)**

phys. stat. sol. (a) 14, K101 (1972)

Subject classification: 10.2; 1.5; 22.1.2

Allen Clark Research Centre, The Plessey Company Limited,  
Caswell Towcester Northants

Shockley Loops in Epitaxial Silicon

By

R. OGDEN

Many studies have been made of stacking fault structures in epitaxial silicon (1 to 5). These structures have almost invariably been nucleated at the substrate: layer interface and form closed configurations such as tetrahedra composed of stacking faults intersecting at stair-rod dislocations. Ribbon stacking faults similar to those shown here in Fig. 1 and 2 have been reported occasionally (3, 4) but have not previously been analysed fully. For the present diffraction contrast analysis in the electron microscope, specimens were prepared from  $\{111\}$  epitaxial silicon layers grown at low temperatures ( $< 900^\circ\text{C}$ ) from silane deliberately contaminated with very low levels ( $\approx 100$  ppm) of ethylene. A high-tilt cartridge was used in the microscope to enable micrographs to be taken using reflections in both the 110 and 111 zones. Care was taken to select faults for analysis which were not overlapping and all micrographs were taken close to the 2 beam  $s = 0$  position. Indexing has been chosen so that the faults to be analysed lie on  $(1\bar{1}\bar{1})$  planes in both series shown in Fig. 1 and 2 which were taken from different specimens. Closely following an earlier analysis (6), the ribbon defects were confirmed as stacking faults by observation of fringe contrast in Fig. 1a to f. Examination of outer fringe contrast in dark field (7), Fig. 1g shows that both stacking faults are extrinsic. Similar micrographs have shown that the two stacking faults in Fig. 2 are also extrinsic. The possible Burgers vectors (6) of the bounding partials are  $+\frac{1}{3}[1\bar{1}\bar{1}]$ ,  $+\frac{1}{6}[\bar{1}\bar{1}\bar{2}]$ ,  $+\frac{1}{6}[\bar{1}\bar{2}\bar{1}]$ , or  $+\frac{1}{6}[2\bar{1}\bar{1}]$ . The partials show strong contrast in Fig. 1e, f but no contrast in Fig. 1a, b. Reference to Table 1 eliminates the Shockley partials  $+\frac{1}{6}[\bar{1}\bar{2}\bar{1}]$  and  $+\frac{1}{6}[2\bar{1}\bar{1}]$  since each of these partials should be visible for one set of  $\{111\}$  and  $\{311\}$  reflections where  $\vec{g} \cdot \vec{b} = +1$  or  $+\frac{2}{3}$  and invisible for the other set where  $\vec{g} \cdot \vec{b} = 0$  or  $+\frac{1}{3}$ .

The  $\frac{1}{3}[1\bar{1}\bar{1}]$  Frank partial is eliminated using the  $\bar{2}20$  reflection since very little contrast is observed at the partials. The black contrast patches in Fig. 1d

Table 1

$\vec{g} \cdot \vec{b}$  values of possible partials bounding stacking faults on  $(11\bar{1})$  planes

$\vec{g} \backslash \vec{b}$	$+\frac{1}{3} [11\bar{1}]$	$+\frac{1}{6} [\bar{1}\bar{1}\bar{2}]$	$+\frac{1}{6} [\bar{1}2\bar{1}]$	$+\frac{1}{6} [\bar{2}\bar{1}\bar{1}]$
$\bar{1}\bar{1}\bar{1}$	$+\frac{1}{3}$	$+\frac{1}{3}$	$+\frac{1}{3}$	$+\frac{2}{3}$
$1\bar{1}\bar{1}$	$+\frac{1}{3}$	$+\frac{1}{3}$	$+\frac{2}{3}$	$+\frac{1}{3}$
$00\bar{4}$	$+\frac{4}{3}$	$+\frac{4}{3}$	$+\frac{2}{3}$	$+\frac{2}{3}$
$\bar{1}\bar{1}\bar{3}$	$+1$	$+1$	0	$+1$
$1\bar{1}\bar{3}$	$+\frac{1}{3}$	$+\frac{1}{3}$	$+\frac{1}{3}$	0
$\bar{2}\bar{2}0$	0	0	$+\frac{1}{3}$	$+\frac{1}{3}$
$0\bar{2}\bar{2}$	$+\frac{4}{3}$	$+\frac{1}{3}$	$+\frac{1}{3}$	$+\frac{2}{3}$
$\bar{2}0\bar{2}$	$+\frac{4}{3}$	$+\frac{1}{3}$	$+\frac{2}{3}$	$+\frac{1}{3}$
$1\bar{3}\bar{1}$	$+1$	0	$+\frac{1}{3}$	$+\frac{1}{3}$
$\bar{3}1\bar{1}$	$+\frac{1}{3}$	0	$+\frac{1}{3}$	$+\frac{1}{3}$
$\bar{1}\bar{1}\bar{1}$	$+\frac{1}{3}$	0	0	0

and the black and white contrast patches in Fig. 2a, b (shown arrowed) are not characteristic of the "m" term contrast which the Frank partial would display. Although  $\vec{g} \cdot \vec{b}$  and m are both zero for the remaining  $+\frac{1}{6} [\bar{1}\bar{1}\bar{2}]$  Shockley partial, the patchy contrast may be expected since Head (8) has shown that inclined dislocations in  $\beta$ -brass can produce such contrast under these conditions.

The series of micrographs Fig. 2c to g confirms the  $+\frac{1}{6} [\bar{1}\bar{1}\bar{2}]$  Shockley partial since in no case is dislocation contrast observed at the faults although faint lines, possible due to decoration, are visible along part of the bounding partials in Fig. 2e. Table 1 shows that the Frank partial should be visible in all these micrographs and the previously eliminated Shockley partials should also be visible for most of them. Clareborough (9) has shown that partials may be invisible for  $\vec{g} \cdot \vec{b} = +\frac{2}{3}$  under certain conditions but Table 1 shows that there are sufficient cases where  $\vec{g} \cdot \vec{b}$  is zero or an integer to establish the Burgers vectors of partials without using this value.

Fig. 1h and 2h represent the stacking fault ribbons showing the Burgers vectors of the partials using the Thompson notation (10, 11). Plane (d) is the  $(11\bar{1})$  fault plane and the stacking faults can be regarded as loops  $\vec{\delta A}$  which are truncated by the foil surfaces. The majority of ribbon faults found were similar to those shown in Fig. 1 and 2 although some intrinsic loops occurred. In both cases the partials were predominantly in screw orientation with Burgers vectors of magnitude  $A\beta$ ,  $A\gamma$ , and  $A\delta$  lying on inclined planes b, c, and d respectively. However occasional examples of extended dislocations such as  $\vec{B\delta} + \vec{\delta A}$  were found. Full results and a proposed mechanism for the nucleation and growth of the ribbon faults based on the incorporation of carbon atoms on specific lattice sites are to be published separately.

The author is indebted to Dr. W.J. Tunstall and Mr. R.W. Bickness for useful discussion, to the Plessey Company for permission to publish this note, and to the Ministry of Defence (Naval Department) who supported this work.

#### References

- (1) J.M. CHARIG, B.A. JOYCE, D.J. STIRLAND, and R.W. BICKNELL, *Phil. Mag.* **7**, 1847 (1962).
- (2) G.R. BOOKER and R. STICKLER, *J. appl. Phys.* **33**, 3281 (1962).
- (3) R.H. FINCH, H.J. QUEISSER, G. THOMAS, and J. WASHBURN, *J. appl. Phys.* **34**, 406 (1963).
- (4) G.H. SCHWUTTKE and V. SILS, *J. appl. Phys.* **34**, 3127 (1963).
- (5) G.R. BOOKER and B.A. UNVALA, *Phil. Mag.* **11**, 11 (1965).
- (6) G.R. BOOKER and W.J. TUNSTALL, *Phil. Mag.* **13**, 71 (1966).
- (7) R. GEVERS, A. ART, and S. AMELINCKX, *phys. stat. sol.* **3**, 1563 (1963).
- (8) A.K. HEAD, *Austral. J. Phys.* **20**, 557 (1967).
- (9) L.M. CLAREBOROUGH, *Austral. J. Phys.* **24**, 79 (1971).
- (10) N. THOMPSON, *Proc. Phys. Soc.* **B66**, 481 (1953).
- (11) J.P. HIRTH and J. LÖTHER, *Theory of Dislocations*, Ser. Mat. Sci. & Engng., McGraw-Hill Publ. Co., 1968.

(Received September 15, 1972)

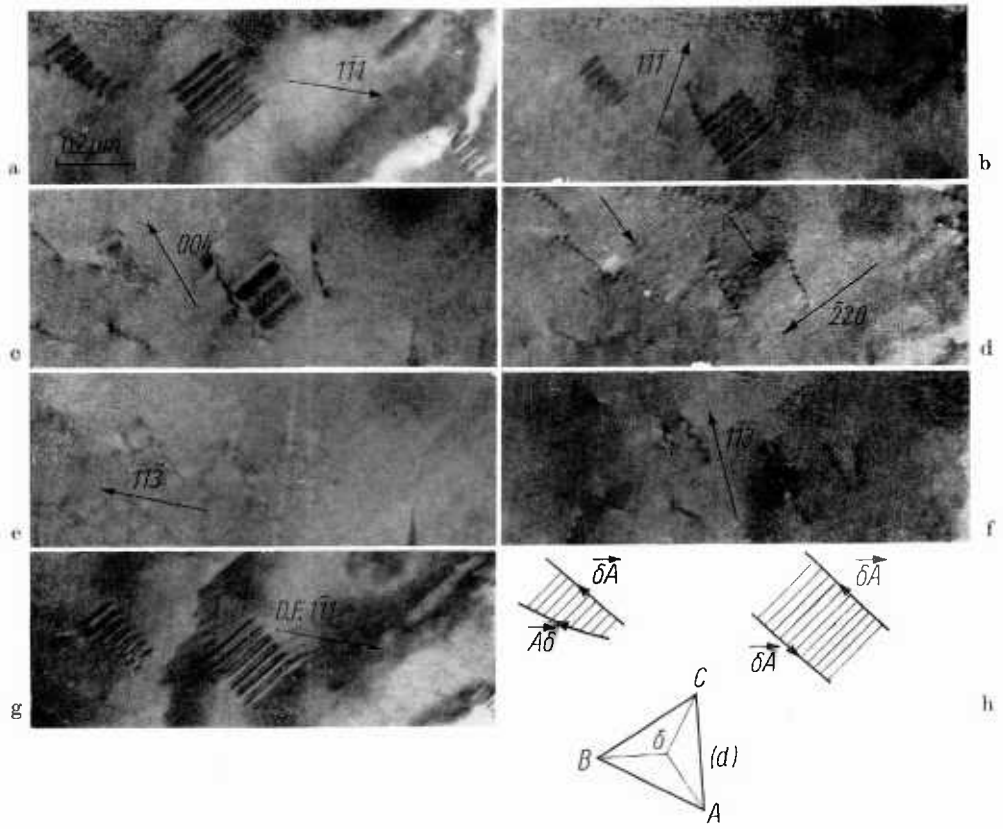


Fig. 1. Diffraction contrast analysis in 110 zone

See Short Note by R. OGDEN

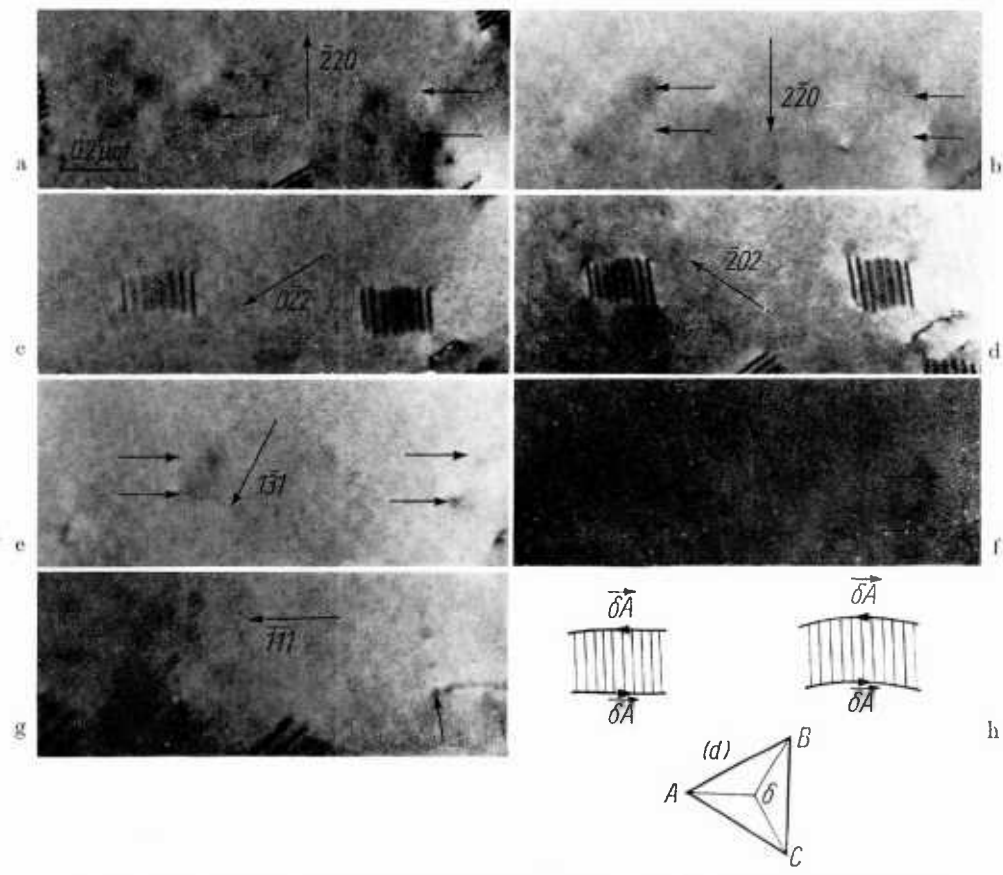


Fig. 2. Diffraction contrast analysis in 111 zone. h)  $\vec{CA} = 1/2 [011]$ ,  $\vec{BA} = 1/2 [101]$ ,  $\vec{BC} = 1/2 [1\bar{1}0]$ ,  $\vec{\delta A} = 1/6 [112]$ ,  $\vec{\delta B} = 1/6 [1\bar{2}1]$ ,  $\vec{\delta C} = 1/6 [1\bar{2}1]$ ; viewed from outside tetrahedron

phys. stat. sol. (a) **26**, 135 (1974)

Subject classification: 1.5 and 10.2; 22.1.2

*Allen Clark Research Centre, The Plessey Company, Ltd.,  
Caswell, Towcester, Northamptonshire*

## Stacking Fault Structures in Carbon-Contaminated Low-Temperature Epitaxial Silicon

By

R. OGDEN, R. R. BRADLEY, and B. E. WATTS

Stacking fault structures have been observed by transmission electron microscopy in {111} epitaxial Si layers grown from silane contaminated with trace amounts of ethylene. The type of fault structure depended upon the growth temperature: at low temperatures (830 to 940 °C) ribbon faults bounded by Shockley partial dislocation loops were found but at higher temperatures these gave way to configurations such as stacking fault tetrahedra. It is proposed that the fault structures are nucleated by carbon contamination during epitaxial growth and the difference in structure with temperature is interpreted by changes in the way carbon is incorporated in the layer. The presence of Shockley loops suggests a simple mechanism for the formation of stacking fault tetrahedra by the intersection of three loops on adjacent inclined {111} planes.

Es wurden Stapelfehlerstrukturen mittels Durchstrahlungselektronenmikroskopie in epitaxialen {111}-Si-Schichten, die aus mit Äthan verunreinigtem Silan hergestellt wurden, beobachtet. Die Struktur der Stapelfehler ist von der Wachstumstemperatur abhängig. Bei niedrigen Temperaturen (830 bis 940 °C) wurden Bandfehler, die durch Shockley-Teilversetzungsschleifen begrenzt wurden, und bei höheren Temperaturen hauptsächlich tetraedrische Anordnungen von Stapelfehlern gefunden. Es wird angenommen, daß die Keimbildung und die temperaturabhängigen Strukturunterschiede der Stapelfehler durch Verunreinigungen durch Kohlenstoff während des epitaxialen Wachstums hervorgerufen werden. Die Anwesenheit durch Shockley-Schleifen weist auf einen Mechanismus der tetraedrischen Stapelfehlerbildung durch drei sich einander schneidende Schleifen an geneigten {111}-Flächen hin.

### 1. Introduction

The development of chemical vapour deposition of auto-epitaxial silicon has advanced considerably in recent years and films of high perfection may be grown routinely at temperatures typically above 1000 °C. There is continuing interest however in growth at reduced temperatures, mainly to control the diffusion of doping impurities during deposition. It is well established that the cleanliness of the system and substrate is crucial and ultra-high vacuum (UHV) techniques have been used to grow high-quality epitaxial silicon layers at temperatures as low as 800 °C by the pyrolysis of silane [1, 2]. During a study of the influence of trace amounts of gaseous impurities, ethylene was found to have a marked effect on the structural perfection of epitaxial Si layers grown by this method. An analysis by transmission electron microscopy (T.E.M.) of stacking fault ribbons bounded by Shockley partial dislocations formed in the presence of ethylene in layers grown at 850 °C has already been published [3] and the present work describes an observed transition from these structures to the tetrahedral stacking fault figures more commonly found in epitaxial Si, at temperatures above 940 °C.

## 2. Experimental Procedures

The UHV techniques used for this study were developed from molecular beam experiments described earlier [1, 4]. Rectangular single crystal bars with one face cut and polished close to a {111} plane were mechanically and HCl vapour polished, and mounted on tantalum clips in a stainless-steel oil-diffusion pumped UHV system. The system was baked at 250 °C to achieve base pressures approaching  $1 \times 10^{-10}$  Torr. The silicon surface was thermally cleaned by direct resistance heating for 2 min at 1230 °C and the substrate then allowed to cool to room temperature. Ethylene was then leaked into the system to a predetermined pressure as indicated by a calibrated ionisation gauge. Silane was then introduced to give the desired silane: ethylene ratio. After stabilisation, the temperature of the substrate was quickly raised to 1200 °C and the total pressure in the system raised to typically  $3 \times 10^{-1}$  Torr by means of a throttle valve between the work chamber and the pump assembly. The substrate temperature was then reduced to the required growth temperature.

Specimens for T.E.M. were prepared by thinning from the substrate side by lapping, cutting into 2.2 mm diameter discs, and jet-etching with 1:3 HF:HNO<sub>3</sub>. The specimen discs were then mounted in a high-tilt ( $\pm 30^\circ$ ) Ward goniometer cartridge and examined in a Siemens Elmiskop I electron microscope. Layer surfaces were examined by glancing angle electron diffraction (G.A.E.D.) and also by low-angle ( $\approx 10^\circ$ ) shadowed platinum/carbon replicas.

## 3. Results

In control runs with no ethylene added, epitaxial silicon layers with low defect densities ( $< 10^2 \text{ cm}^{-2}$ ) and very smooth surfaces were produced at all growth temperatures. The effects of ethylene addition are summarised in Table 1 and described in Sections 3.1, 3.2, and 3.3.

Table 1  
Summary of results

growth temperature (°C)	ethylene concentration (ppm)	direct T.E.M.	surface replica
830 to 1200	0	featureless	very smooth
830 to 860	4 to 10	ribbon stacking faults and tetrahedral-type stacking faults	terraced, pinning sites
830 to 860	20 to 100	ribbon stacking faults	faceted, strongly developed at higher ethylene levels
860 to 940	50 to 100	ribbon and tetrahedral faults	terraced, pinning sites
940 to 1160	4	featureless	very smooth
940 to 1070	50 to 100	tetrahedral faults, $\beta$ -SiC filaments	terraced, pinning sites
1100 to 1200	100	featureless	very smooth

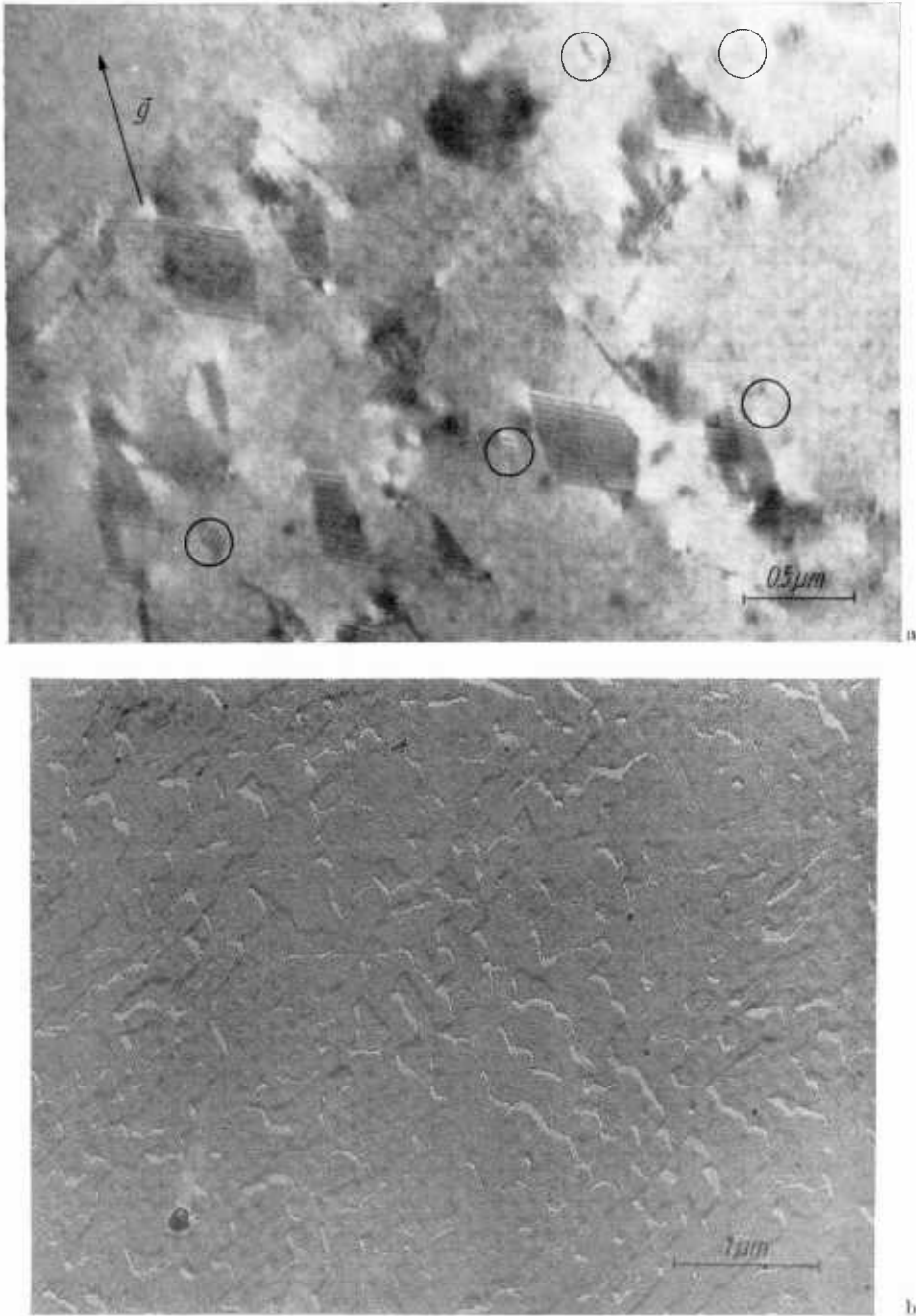


Fig. 1. Structure of Si layer grown with 92 ppm ethylene contamination at 850 °C. a) Dark-field T.E.M. 220 type reflection; b) Pt/C replica

### 3.1 Low-temperature growth (830 to 860 °C)

Ethylene contamination in this temperature range induced ribbon-like stacking faults lying on inclined  $\{11\bar{1}\}$  planes. The faults were often overlapping and had irregular edges. A transmission electron micrograph of a layer grown at 850 °C with a high ethylene concentration (Fig. 1a) shows a stacking fault density  $\approx 10^9 \text{ cm}^{-2}$ . The ribbon faults are between 0.1 and 0.4  $\mu\text{m}$  wide and are usually truncated by both specimen surfaces and hence are of indeterminate length. Analysis of the faults by diffraction contrast experiments [3] showed that most of them were bounded by Shockley partial dislocation loops having vectors of  $\frac{1}{6}\langle 112 \rangle$  perpendicular to the intersection of the (111) specimen surface and the  $\{11\bar{1}\}$  habit plane of the faults. Outer fringe contrast [5] shows that the majority of the stacking faults in Fig. 1a are extrinsic. Although the micrograph was taken from a region of foil  $\approx 1 \mu\text{m}$  thick, several small stacking faults (shown ringed) are only a few fringes long, and dark-field studies [6] have shown that some can terminate well below the top surface of the epitaxial layer. Fig. 1a also contains many inclined undissociated dislocations. Examination of the image contrast of these, using 111 reflections, showed that they had  $\frac{1}{2}\langle 110 \rangle$  Burgers vectors inclined to the foil surface. An electron micrograph of a Pt/C replica of the surface of the same layer (Fig. 1b) shows that the surface was faceted with steps up to 200 Å high. These steps were also observed by direct T.E.M. using the two-beam,  $s = 0$  condition in regions of foil two to four fringes thick. Straight portions of the surface facets tended to lie along  $\langle 110 \rangle$  directions, parallel to the stacking fault fringes, i.e. parallel to the intersection of the faults with the surface.

As the level of ethylene contamination was reduced, the stacking fault densities dropped and the ribbon faults tended to be wider. A long extrinsic fault in

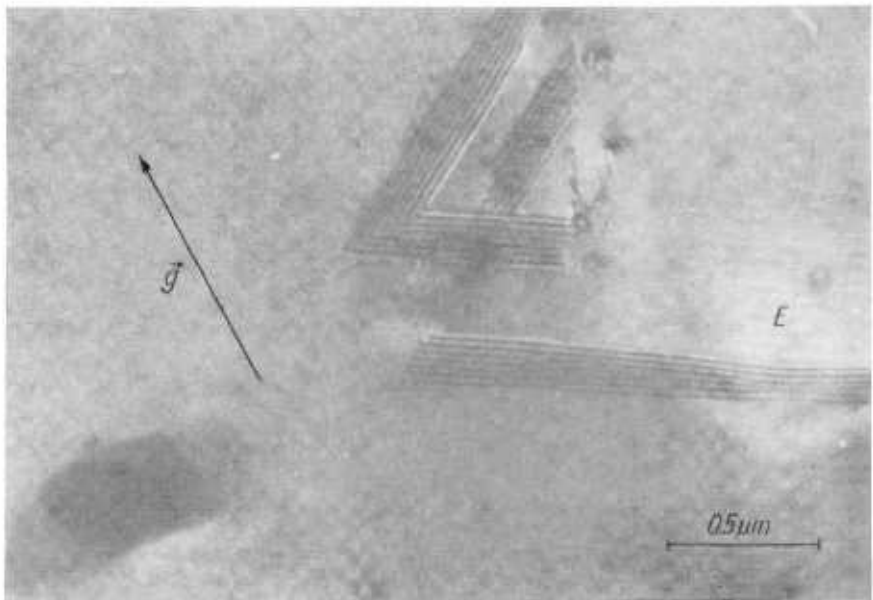


Fig. 2. Stacking fault structure formed at 850 °C, 4 ppm ethylene, dark-field T.E.M.

a layer grown with only four parts per million (ppm) ethylene contamination with respect to silane is marked E in Fig. 2 which also shows two intrinsic faults which have intersected to form a stair-rod dislocation. In addition to ribbon faults, stacking fault tetrahedra were observed at these very low contamination levels. The surfaces of layers grown at levels of ethylene contamination between 20 and 50 ppm were smoother than that shown in Fig. 1 b and the steps were more irregular. At the lowest ethylene levels (4 to 10 ppm) surfaces more typical of higher growth temperatures (as described below) were observed.

Experiments were made to determine the effect of annealing on the ribbon fault structures. Specimens were annealed at 1200 °C for half an hour in  $H_2$ ,  $N_2$ , and in vacuum at  $10^{-9}$  and  $10^{-5}$  Torr. No changes in size or character of the faults were detected, although a thick polycrystalline  $\beta$ -SiC contamination film formed on the specimen annealed at  $10^{-5}$  Torr.

In one experiment, Si growth was commenced with 50 ppm ethylene in the silane with the substrate at 850 °C. The ethylene flow was turned off after the growth of about 2  $\mu$ m of silicon, and growth continued for a further 2  $\mu$ m. Examination by T.E.M. showed that the outer micron of the layer contained some small intersecting ribbon stacking faults similar to that in Fig. 2, but no Shockley loops. However many Shockley loops were discovered below the top surface when 2  $\mu$ m of the surface had been removed by etching.

### ***3.2 Moderate and high-temperature growth (860 to 1200 °C)***

As the growth temperature was increased, the number of ribbon faults decreased. Above 860 °C stacking fault tetrahedra were observed in greater numbers, and above about 940 °C stacking fault structures were invariably in the form of tetrahedra and other configurations which have been described in earlier papers [7, 8] (Fig. 3a and 4). These structures, terminating in  $\langle 110 \rangle$  stair-rod dislocations, are of the type commonly found in  $\{111\}$  epitaxial silicon. Stacking fault densities of  $10^7$  to  $10^8$   $cm^{-2}$  were typical at 100 ppm ethylene contamination levels. The surface of the layer at this level (Fig. 3 b) is smoother than that shown in Fig. 1 b although it contains numerous pits associated with terraced surface areas.

An important difference between the stacking fault structures which we report here and those found in earlier studies [7, 8] is that nucleation is not confined to the substrate-layer interface. Fig. 3a shows examples of stacking fault tetrahedra which clearly have formed at different times during epitaxial growth. Also of interest in this micrograph is the presence of a very small stacking fault configuration, shown ringed, which has been nucleated within 0.2  $\mu$ m of the top of the layer, and appears to be associated with an inclusion. There is evidence, discussed below, that this may be a crystallite of  $\beta$ -SiC.

At high growth temperatures ( $>1100$  °C) the stacking fault density fell to  $<10^3$   $cm^{-2}$  and the surfaces were extremely smooth.

Previous work [9] has shown that small particles of  $\beta$ -SiC are formed epitaxially on Si substrates exposed to ethylene at temperatures between 700 and 1100 °C. Surface replicas were therefore examined to see if SiC particles could be extracted from the layers but none were positively identified, neither was SiC detected by G.A.E.D. on the surface of any of the specimens produced in these experiments. However, replicas of many pinning sites were observed to contain small holes (e.g. B, Fig. 3b) consistent with the presence of angular particles embedded in the bottom of each site. It was noticed also that specimens prepared for T.E.M. from layers grown above 940 °C were often contaminated with tangled filaments

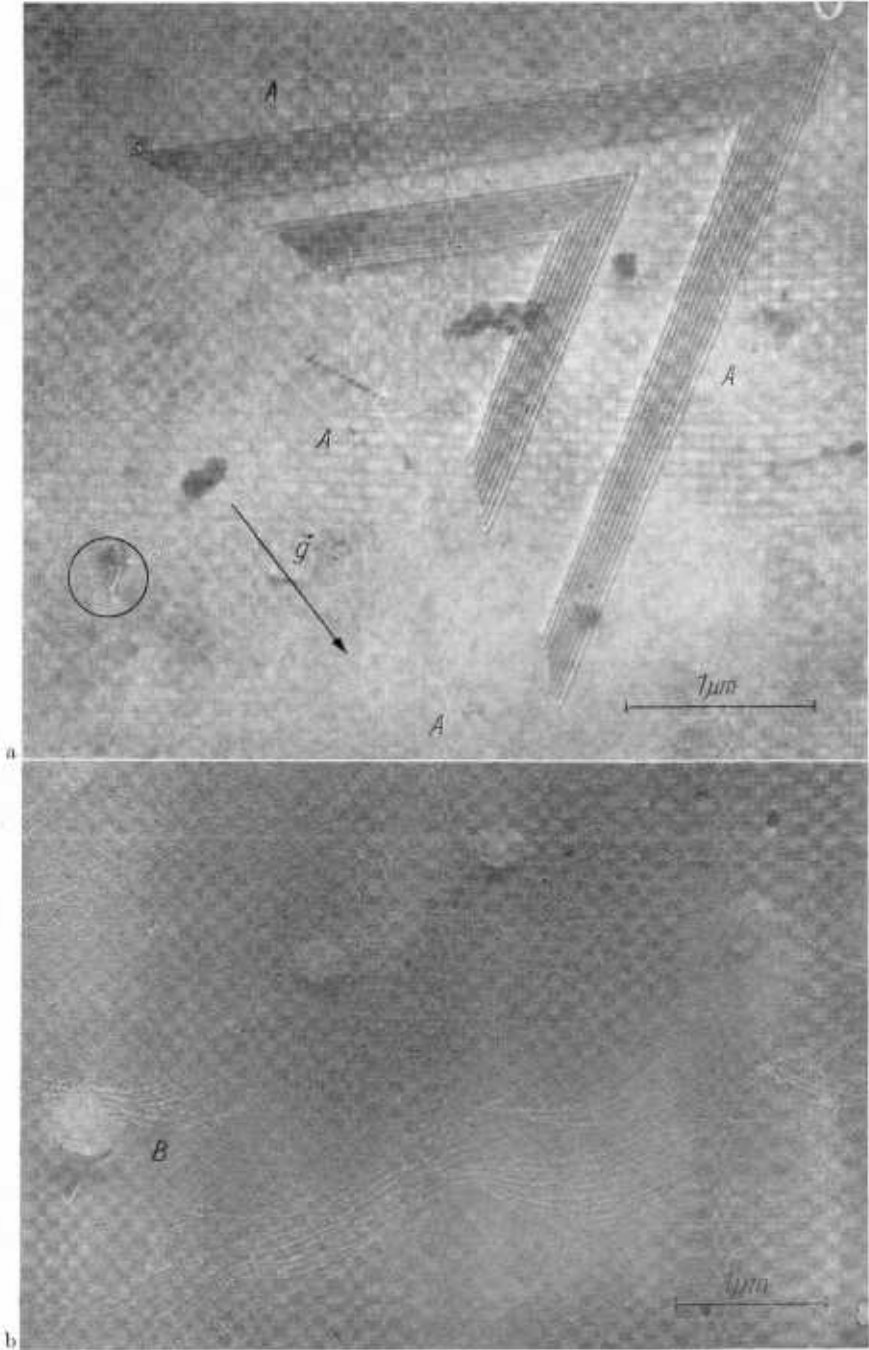


Fig. 3. a) Structure of Si layer grown with 50 ppm ethylene at 1065 °C, bright-field T.E.M. 220 type reflection. The closing stacking faults parallel to the diffraction vector are out of contrast. Note second phase particles (marked A), probably SiC; b) Pt/C replica of layer grown with 100 ppm ethylene at 1065 °C

of material lying on the foil surface (Fig. 4). Selected area electron diffraction (S.A.E.D.) on thin areas of silicon gave a spotty ring pattern of  $\beta$ -SiC, inset Fig. 4, and dark-field micrographs showed that the filaments contained particles of SiC up to 200 Å across. The SiC filaments must have formed on the growing surface and were then incorporated into the layer during subsequent epitaxial growth.

#### 4. Discussion

The occurrence of Shockley-bounded stacking fault ribbons as shown in Fig. 1a and 2 is unusual in epitaxial silicon. Finch et al. [8] showed examples of stacking fault ribbons which did not terminate in  $\langle 110 \rangle$  stair-rod dislocations, but were unable to identify the bounding partials, since diffraction contrast analysis in the electron microscope was not sufficiently advanced at that time for correct characterisation. This is also true of the early work of Schwuttke and Sils [10], who claimed to have observed Shockley partials in thick epitaxial Si layers using Lang X-ray topography. In addition the poor resolution of this latter technique compared to T.E.M. makes interpretation of their results very uncertain.

We have shown that stacking fault ribbons were formed when ethylene was continuously present during Si epitaxial growth from silane at low temperatures (830 to 940 °C). The moderately high stacking fault energy (S.F.E.) of Si of  $\approx 50$  erg cm<sup>-2</sup> was determined experimentally by Ray and Cockayne [11] using the weak beam technique in T.E.M. to resolve Shockley partial separations of  $< 100$  Å in plastically deformed specimens. The presence of widely separated Shockley partials in the present work clearly shows that the stacking faults are not in equilibrium with the Si lattice and indicates that carbon segregation to the faults has occurred.

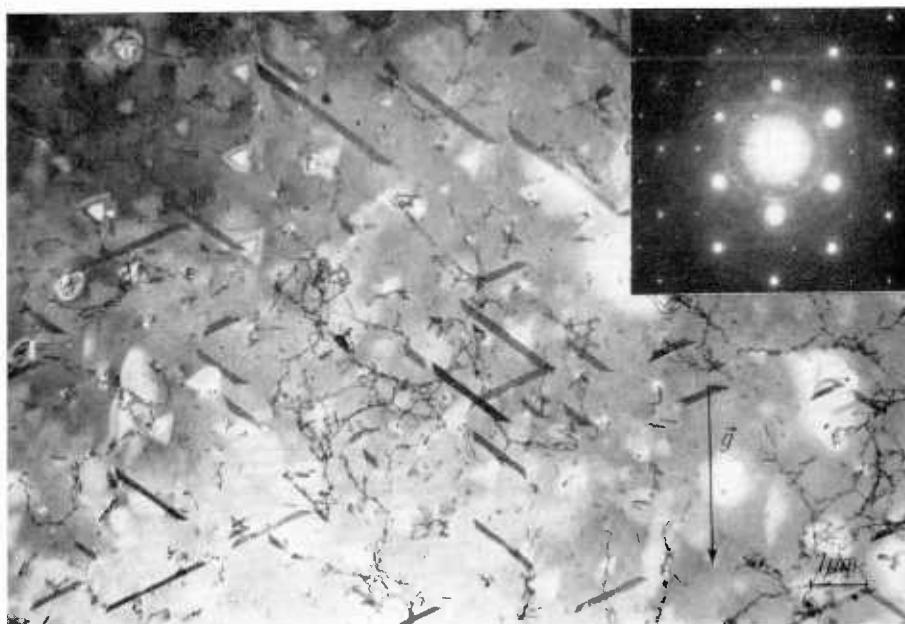


Fig. 4. Structure of Si layer grown at 960 °C with 100 ppm ethylene showing  $\beta$ -SiC debris on foil surface. Inset is electron diffraction pattern from thin area of foil showing [111] Si post pattern and  $\beta$ -SiC polycrystalline ring pattern

#### 4.1 Surface effects

When the results in Section 3 are studied with respect to surface structure, three distinct types of surface are evident:

1. Very smooth in the absence of ethylene at all growth temperatures, and with ethylene present at temperatures above 1100 °C.

2. Terraced and pitted at low and intermediate growth temperatures (830 to 1070 °C) as shown in Fig. 3 b.

3. Faceted, three-dimensional growth at low growth temperatures (830 to 860 °C) and high ethylene contamination levels as shown in Fig. 1 b.

The formation of these different types of surfaces can be interpreted using the model of Burton et al. [12] whereby crystal growth occurs by the propagation of two-dimensional growth centres. The mode of growth of {111} silicon layers was demonstrated by Abbink et al. [13] using an in-situ replica technique with which they were able to identify monolayer steps ( $\approx 3$  Å high) in a film grown by evaporation under UHV conditions. These steps generally lay in  $\langle 110 \rangle$  directions and propagated in the perpendicular  $\langle 11\bar{2} \rangle$  directions. Departure from ideal step propagation was attributed to the presence of impurity atoms on the surface in refinements to the above model made by Frank [14] and by Cabrera and Vermilyea [15]. Impurity atoms are not readily adsorbed into the step and slow down its motion by temporarily occupying sites in the step front which would otherwise be filled with majority atoms. Steps thus bunch to form terraces, and impurities are 'swept' ahead of the steps into high concentration regions. Eventually step 'hopping' occurs and the impurities are incorporated into the growing layer.

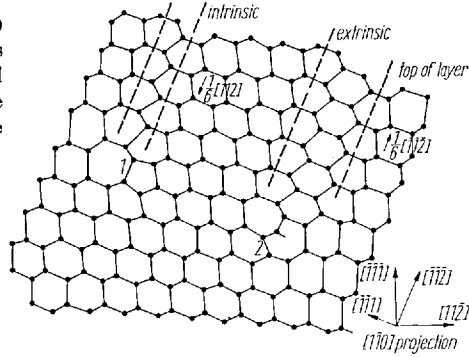
Surface structures very similar to those in Fig. 3 b have been found previously [13, 16] on evaporated {111} Si epitaxial layers, in which step propagation was apparently pinned by particles of  $\beta$ -SiC on the growing surface. We found that, irrespective of growth temperature, Fig. 3 b was typical of layers containing tetrahedral-type stacking fault structures and on the basis of this and earlier work [17, 18] it is reasonable to suppose that these structures were nucleated when  $\beta$ -SiC particles were eventually overgrown by silicon. The stacking fault structure shown ringed in Fig. 3 a seems to be associated with an inclusion but it is apparent that similar inclusions marked A in this micrograph are not associated with stacking faults.

The faceting observed at low growth temperatures as shown in Fig. 1 b was also found by Joyce et al. [1] who deposited silicon onto Si substrates precontaminated by ethylene, using silane under UHV conditions. Auger spectroscopy studies [19] carried out in parallel with the above work showed carbon impurity on the surface. We believe that faceting arises from the slowing down of step motion by carbon which builds up ahead of steps to reach high concentrations. This leads to the formation of  $\langle 110 \rangle$  rows containing a high proportion of carbon atoms in low-temperature growth layers and to the presence of  $\beta$ -SiC filaments in epitaxial layers grown at higher temperatures (Fig. 4).

#### 4.2 Nucleation of ribbon stacking faults

Assuming, as in the case of stacking fault tetrahedra [7, 8], that the stacking fault ribbons are nucleated on or close to the growing layer surface, then the bounding Shockley partials will initially lie in  $\langle 110 \rangle$  orientations parallel to the substrate. It follows from the  $\frac{1}{6}\langle 112 \rangle$  Burgers vectors of the partials that they

Fig. 5. Ribbon stacking faults lying on (111) planes showing bounding Shockley partials in edge orientation. The lines of the partial dislocations are perpendicular to the plane of the paper. The dashed lines denote the twin plane



will be edge in character. The projection onto a vertical (110) plane of the bond configurations of edge Shockley partials bounding intrinsic and extrinsic stacking faults lying on inclined (111) planes [20, 21] and which intersect the (111) growth surface have been drawn in Fig. 5. The diagram shows that distortion of bonds from the [111] orientation (i.e. those marked 1 and 2) during epitaxial growth could lead directly to the formation of the ribbon faults of each type, if bonds in equivalent sites in the  $\langle 110 \rangle$  row perpendicular to the plane of the paper were similarly distorted. We suggest that the incorporation of carbon in  $\langle 110 \rangle$  rows provides this distortion, owing to the smaller size of the carbon atom. A similar argument can be applied to the formation of undissociated dislocations in Fig. 1a.

We can show that our proposed mechanism is feasible using elastic energy considerations. Bullough and Newman [22] have shown that the maximum binding energy of a carbon atom to an edge dislocation in Si is  $\approx 0.9$  eV. This energy must be reduced when the dislocation lies near to the surface, owing to relaxation of the strain field. Substituting expressions for the stress components of an edge dislocation corrected for image forces given by Head [23] into (9) of [22] leads to the function plotted in Fig. 6 (curve a).

The relaxation of elastic energy of a carbon atom near to the surface in Si, unassociated with a dislocation, has been derived from equations given in a standard text [24], and is as plotted in Fig. 6 (curve b). The curves a and b in Fig. 6 are similar in that elastic energy quickly reaches its maximum value only a few angstroms below the surface, but a dislocation lying parallel to the surface increases its self-energy relatively slowly with increasing  $R$  [24] as shown in curve c in Fig. 6. This figure shows that at some distance just below the sur-

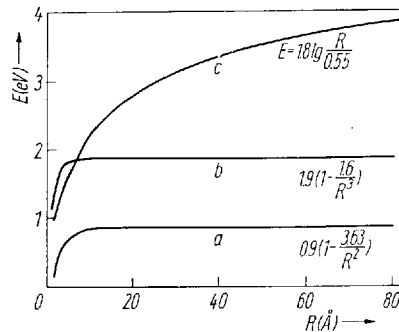


Fig. 6. Elastic energy ( $E$ ) variation of carbon atom and edge Shockley partial dislocation close to Si surface ( $R$  is the distance of defect below surface). (a) Binding energy of carbon atom to Shockley partial; (b) elastic energy of carbon atom in substitutional site due to size difference; (c) self-energy of edge Shockley partial per  $\frac{1}{2}\langle 110 \rangle$  unit length of dislocation

face, the binding energy of our proposed  $\langle 110 \rangle$  row of carbon atoms to an edge dislocation is comparable with the self-energy of the dislocation. This means that if there is a sufficiently high concentration of carbon atoms, the misfit strain can be relieved by the nucleation of an edge Shockley close to the surface of the growing epitaxial layer. An approximate value for this critical carbon level can be derived by balancing the total binding energy of the number of carbon atoms ( $n$ ) in the region of the dislocation with the self-energy per unit length of the edge Shockley partial. We assume that the average binding energy per carbon atom is about half the maximum since only one carbon atom can occupy the most favourable strain-relieving site near the core of the dislocation with the maximum binding energy. When  $n \approx 4$  per  $\frac{1}{2} \langle 110 \rangle$  unit length there is a net reduction in energy on formation of the edge Shockley partial. Thus if four or more  $\langle 110 \rangle$  carbon filaments are incorporated into the lattice close together, then the elastic strain energy of the system is lowered by the formation of an edge Shockley dislocation lying parallel to the rows.

It is justifiable to ask why  $\frac{1}{3} \langle 11\bar{1} \rangle$  Frank loops were not observed, since our explanation for the formation of the observed  $\frac{1}{6} \langle 112 \rangle$  and  $\frac{1}{2} \langle 110 \rangle$  dislocations could also be applied to the Frank dislocation. However, the Shockley and perfect dislocations lie in the  $\{11\bar{1}\}$  slip planes and form by shear in the direction of the free surface, whereas the Frank dislocation must form by climb into the crystal, inserting or removing a  $\langle 11\bar{1} \rangle$  double-layer of atoms and it appears that this mechanism is not favoured.

#### 4.3 Propagation of ribbon faults

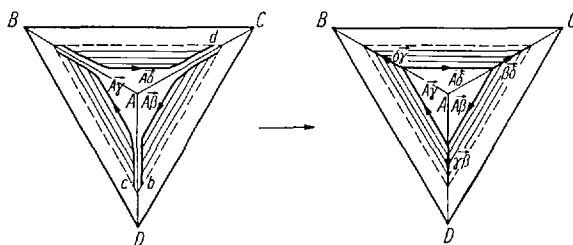
The failure of ribbon faults to propagate when the ethylene flow was cut off during epitaxial growth is evidence that the ribbon stacking faults are stabilised by carbon segregation. It is possible that lattice sites where the faults intersect the growing epitaxial surface are preferentially occupied by carbon atoms. It is significant that the ribbons on Fig. 1a are not wider than  $\approx 0.4 \mu\text{m}$  which is the maximum length of the straight portions of the surface steps in Fig. 1b. Competition for carbon atoms from neighbouring faults or changes in surface topography could terminate the carbon supply to a particular fault. During subsequent epitaxial growth, the fault will not propagate but will terminate within the layer, forming a buried loop as some of the ringed examples in Fig. 1a. The behaviour is quite different from that of the more usual type of stacking fault structures as shown in Fig. 3a and 4 which, once formed, propagate with the epitaxial layer.

No determination of carbon concentration in the contaminated epitaxial layers was carried out. In the absence of adequate models of impurity effects on S.F.E. [24, 25] it is doubtful whether such data could be usefully applied in this context.

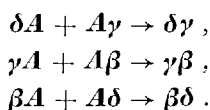
#### 4.4 New model for nucleation of stacking fault tetrahedra

The occurrence of the Shockley stacking fault loops with similar Burgers vectors and the presence of the stair-rod dislocation in Fig. 2 suggests a simple model for the nucleation of stacking fault tetrahedra in epitaxial Si. This model is proposed as an alternative to that of Booker and Stickler [26] which was based on the decomposition of a Frank loop by the Silcox and Hirsch mechanism [27]. The stair-rod in Fig. 2 could be the direct product of the interaction of two Shockley partials on adjacent inclined  $\{111\}$  planes. We have shown earlier

Fig. 7. Formation of intrinsic stacking fault tetrahedron from three Shockley loops. Viewed from outside Thompson tetrahedron, apex A pointing upwards. Intersection of stacking faults with layer surface shown dashed



[3] that the Burgers vectors of the ribbon loops, using the Thompson notation, have magnitude  $A\beta$ ,  $A\gamma$ , and  $A\delta$  lying on the inclined  $\{111\}$  planes  $b$ ,  $c$ , and  $d$ , respectively. Fig. 7 shows the Thompson tetrahedron viewed from its apex A with the growth direction into the paper. If two intrinsic loops  $A\delta$  and  $A\gamma$  intersect at an acute angle, then a low-energy stair-rod dislocation  $\delta\gamma$  is formed along the common  $\langle 110 \rangle$  direction AB. If a third loop  $A\beta$  existed on plane  $b$ , two more stair-rods could be formed. The three reactions can be written as



We suggest that lattice distortion due to small patches of contamination or particles on the substrate: layer interface nucleate Shockley stacking fault loops. Three independent loops lying on adjacent  $\{111\}$  planes, if sufficiently close to interact, will form stair-rod dislocations along the inclined  $\langle 110 \rangle$  directions. The tetrahedron thus formed will propagate with layer growth. Loops which fail to intersect will not continue to grow in the absence of a continuous supply of contaminant as discussed in the previous section. Other configurations such as intrinsic : extrinsic pairs can be formed by similar mechanisms.

An objection to this model is that the formation of extrinsic loops would result in the formation of extrinsic tetrahedra, whereas intrinsic tetrahedra are invariably observed in  $\{111\}$  silicon layers. This led Booker and Stieckler [26] to propose that their initial Frank loop was extrinsic although this was insufficiently observed. An explanation which answers the above objection can be found in Hirth and Lothe's text [24]. This shows that an extrinsic tetrahedron requires the formation of two stair-rod dislocations at each intersection e.g.  $\delta\gamma$  and  $\delta C/D\gamma$  of  $\frac{1}{6}\langle 110 \rangle$  and  $\frac{1}{3}\langle 110 \rangle$  type, respectively. The combination of these produces a Burgers vector of  $\gamma\delta$  i.e. equal and opposite to the corresponding intrinsic case, and with the same elastic energy. But since the double stair-rods are so close together, their core energy is higher than the intrinsic stair-rod and reactions which could lead to the formation of extrinsic tetrahedra are suppressed.

## 5. Summary and Conclusions

Examination by T.E.M. of  $\{111\}$  epitaxial Si layers grown by pyrolysis of silane contaminated with 4 to 100 ppm ethylene has shown stacking fault structures, whose nature depends primarily upon the growth temperature. Ribbon stacking faults bounded by Shockley partials of both intrinsic and extrinsic type occurred at growth temperatures from 830 to 940 °C. These faults could terminate within the epitaxial layer and only propagate with the contin-

uous presence of ethylene contamination during epitaxial growth. We propose that the ribbon faults are nucleated close to the growing surface owing to the incorporation by surface step motion of carbon impurity atoms lying in  $\langle 110 \rangle$  rows. The ribbon faults are stabilised during subsequent epitaxial growth by the continued segregation of carbon atoms to the region of the fault plane. At temperatures above 940 °C the more usual stacking fault tetrahedra and related configurations were predominant. These structures are associated with the presence of  $\beta$ -SiC crystallites. The results directly lead to a new model for the nucleation of intrinsic stacking fault tetrahedra based on the intersection of three Shockley partial dislocation loops.

#### Acknowledgements

The authors wish to thank the Directors of The Plessey Company, Ltd., for permission to publish this paper. This work has been carried out with the support of the Procurement Executive, Ministry of Defence. We gratefully acknowledge helpful discussions with Dr. R. W. Bicknell at Caswell, Dr. D. B. Holt at Imperial College, and Dr. L. M. Brown at the Cavendish Laboratory.

#### References

- [1] B. A. JOYCE, J. H. NEAVE, and B. E. WATTS, *Surface Sci.* **15**, 1 (1969).
- [2] R. C. HENDERSON and R. H. HELM, *Surface Sci.* **30**, 310 (1972).
- [3] R. OGDEN, *phys. stat. sol. (a)* **14**, K101 (1972).
- [4] B. A. JOYCE and R. R. BRADLEY, *Phil. Mag.* **14**, 289 (1966).
- [5] R. GEVERS, A. ART, and S. AMELINCKX, *phys. stat. sol.* **3**, 1563 (1963).
- [6] W. L. BELL and G. THOMAS, *phys. stat. sol.* **12**, 843 (1965).
- [7] G. R. BOOKER and R. STICKLER, *J. appl. Phys.* **33**, 3281 (1962).
- [8] R. H. FINCH, H. J. QUEISSER, G. THOMAS, and J. WASHBURN, *J. appl. Phys.* **34**, 406 (1963).
- [9] A. S. BROWN and B. E. WATTS, *J. appl. Cryst.* **3**, 172 (1970).
- [10] G. H. SCHWUTTKE and V. SILS, *J. appl. Phys.* **34**, 3127 (1963).
- [11] I. L. F. RAY and D. J. H. COCKAYNE, *Proc. Roy. Soc. A325*, 543 (1971).
- [12] W. K. BURTON, N. CABRERA, and F. C. FRANK, *Phil. Trans. Roy. Soc. (London)* **243A**, 299 (1951).
- [13] H. C. ABBINK, R. M. BROUDY, and G. P. MCCARTHY, *J. appl. Phys.* **39**, 4673 (1968).
- [14] F. C. FRANK, *Growth and Perfection of Crystals*, Ed. R. H. DOREMUS et al., Wiley, 1958 (p. 411).
- [15] N. CABRERA and D. A. VERMILYEA, *ibid.* (p. 393).
- [16] A. G. CULLIS and G. R. BOOKER, *J. Crystal Growth* **9**, 132 (1971).
- [17] G. R. BOOKER, *Disc. Faraday Soc.* **38**, 298 (1964).
- [18] S. MENDELSON, *J. appl. Phys.* **35**, 1570 (1964).
- [19] J. M. CHARIG and D. K. SKINNER, *Surface Sci.* **15**, 277 (1969).
- [20] J. HORNSTRA, *J. Phys. Chem. Solids* **5**, 129 (1958).
- [21] S. AMELINCKX, *Solid State Phys. (Suppl.)* **6**, 279 (1964).
- [22] R. BULLOUGH and R. C. NEWMAN, *Progr. Semicond.* **7**, 100 (1963).
- [23] A. K. HEAD, *Proc. Phys. Soc.* **B66**, 793 (1953).
- [24] J. P. HIRTH and J. LOTHE, *Theory of Dislocations*, Ser. Mater. Sci. and Engng., McGraw-Hill Publ. Co., 1968.
- [25] L. J. CHEN and L. M. FALICOV, *Phil. Mag.* **29**, 1 (1974).
- [26] G. R. BOOKER and R. STICKLER, *Appl. Phys. Letters* **3**, 158 (1963).
- [27] J. SILCOX and P. B. HIRSCH, *Phil. Mag.* **4**, 72 (1959).

(Received August 30, 1974)

# **short note**

reprinted from

**physica**  
**status**  
**solidi (a)**

phys. stat. sol. (a) 28, K97 (1975)

Subject classification: 10.2; 1.5; 22.1.2

Allen Clark Research Centre, The Plessey Company Limited, Caswell, Towcester,  
Northants

The Nature of Stacking Fault Pyramids in {100} Epitaxial Silicon

By

R. OGDEN

Observations have been made on stacking fault pyramids grown in {100} epitaxial silicon. The stacking faults lie on all four inclined {111} planes and nucleate at the apex of the pyramid which is usually located at or near the substrate: epitaxial layer interface, and they intersect the surface of the layer to form a square base. Booker (1) observing stacking fault fringe contrast using transmission electron microscopy (T. E. M.), found that the pyramids consisted of alternate intrinsic:extrinsic stacking faults. It was pointed out that with this arrangement, low energy stair-rod dislocations with Burgers vectors  $\vec{b} = 1/6\langle 110 \rangle$  formed at the inclined  $\langle \bar{1}10 \rangle$  intercepts, and a parallel was drawn with the intrinsic stacking fault tetrahedra formed in {111} epitaxial Si layers (2). This note reports the occurrence of pyramids in {100} epitaxial Si layers, grown on ion-implanted substrates, consisting of stacking faults which were all intrinsic. A more detailed description of the results will be published separately.

Fig. 1a and b show T. E. M. micrographs of a stacking fault pyramid taken using bright field 220 type reflections in the 2 beam  $s = 0$  condition. It can be seen that the outer fringe contrast for each pair of stacking faults is identical when compared with the direction of the diffraction vector  $\vec{g}$ . This means (3) that all four stacking faults must be of the same type. The intrinsic nature of the faults is established (4) from the outer fringe contrast in dark field, Fig. 1c, i. e. bright outer fringe away from the sense of  $\vec{g}$ . Diffraction contrast analysis was then made to determine the Burgers vectors of the four stair-rod dislocations using reflections from the [001], [114], and [ $\bar{1}\bar{1}4$ ] zones in the  $s \geq 0$  condition. The series micrographs shown in Fig. 2a to h confirms that the stair-rods have  $\vec{b} = 1/3 \langle 100 \rangle$ . Table 1 gives  $\vec{g} \cdot \vec{b}$  values of low energy stair-rods of  $\vec{b} = 1/6 \langle 110 \rangle$  and  $1/3 \langle 100 \rangle$  type for the reflections used. Since partial dislocations (5) show strong contrast for  $\vec{g} \cdot \vec{b}$  values

Table 1

 $\vec{g} \cdot \vec{b}$  value of possible low energy stair-rod dislocations

$\vec{g} \backslash \vec{b}$	$+1/6 [101]$	$+1/6 [\bar{1}01]$	$+1/6 [0\bar{1}1]$	$+1/6 [01\bar{1}]$	$+1/3 [100]$	$+1/3 [010]$
$2\bar{2}0$	$+1/3$	$+1/3$	$+1/3$	$+1/3$	$+2/3$	$+2/3$
$\bar{2}20$	$+1/3$	$+1/3$	$+1/3$	$+1/3$	$+2/3$	$+2/3$
400	$+2/3$	$+2/3$	0	0	$+4/3$	0
$0\bar{4}0$	0	0	$+2/3$	$+2/3$	0	$+4/3$
$\bar{1}31$	0	$+1/3$	$+1/3$	$+2/3$	$+1/3$	$+1$
$3\bar{1}\bar{1}$	$+1/3$	$+2/3$	$+0$	$+1/3$	$+1$	$+1/3$
$31\bar{1}$	$+1/3$	$+2/3$	$+1/3$	$+0$	$+1$	$+1/3$
$\bar{1}\bar{3}1$	0	$+1/3$	$+2/3$	$+1/3$	$+1/3$	$+1$

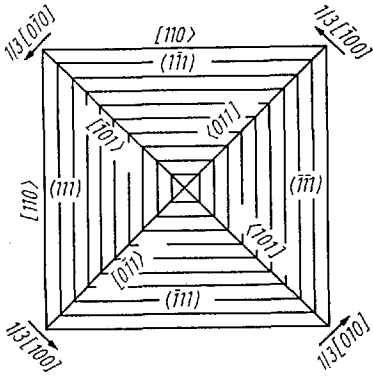


Fig. 3

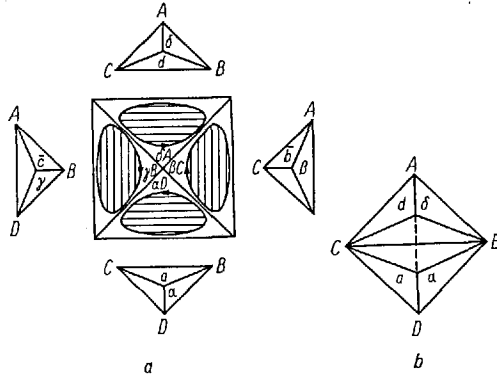


Fig. 4

Fig. 3. Diagram showing stacking fault pyramid orientation (apex down) with stair-rod directions and Burgers vectors

Fig. 4. a) Intrinsic Shockley loops which could form observed stair-rods, apex of pyramid pointing up, also showing each projected face of Thompson tetrahedron against appropriate loop  
b) Completed Thompson tetrahedron viewed from above

of  $\frac{+4}{3}$ ,  $\frac{+2}{3}$ , and  $+1$ , it can be seen from the table that one pair of stair-rods lying on  $[011]$  and  $[0\bar{1}1]$  has  $\vec{b} = \frac{+1}{3}[100]$  and the other pair lying on  $[101]$  and  $[\bar{1}01]$  has  $\vec{b} = \frac{+1}{3}[010]$ . Fig. 3 shows the crystallography of the pyramid and the Burgers vectors of the stair-rods. The energy of the partial dislocations is twice that of the  $\frac{1}{6}\langle 110 \rangle$  type but is still comparatively low.

Consideration of the dislocation reactions which could nucleate the pyramids yields an interesting result. Four Shockley partial dislocation loops, with  $\vec{b} = \frac{1}{6}\langle 211 \rangle$  lying on different inclined  $\{111\}$  planes and formed by shear in the direction of the epitaxial layer surface, could interact directly to form the stacking fault pyramid. In Thompson notation (6, 7) the loops, Fig. 4 a, have Burgers vectors  $\vec{\alpha D}, \vec{\beta C}, \vec{\gamma B},$  and  $\vec{\delta A}$  lying on planes a), b), c, and d) respectively. Fig. 4 b shows the Thompson tetrahedron orientated with respect to the pyramid. The reactions between these loops are

$$\begin{aligned} \vec{\alpha D} + \vec{\beta C} &\rightarrow \vec{\alpha\beta}/\vec{DC}, \\ \vec{\alpha D} + \vec{\gamma B} &\rightarrow \vec{\alpha\gamma}/\vec{DB}, \\ \vec{\delta A} + \vec{\gamma B} &\rightarrow \vec{\delta\gamma}/\vec{AB} = -\vec{\alpha\beta}/\vec{DC}, \\ \vec{\delta A} + \vec{\beta C} &\rightarrow \vec{\delta\beta}/\vec{AC} = -\vec{\alpha\gamma}/\vec{DB}, \end{aligned}$$

and the stair-rod products are both  $1/3\langle 100 \rangle$  type. We have shown earlier (8) that Shockley loops lying on inclined  $\{11\bar{1}\}$  planes and having Burgers vectors in the direction of the surface exist in carbon-contaminated  $\{111\}$  epitaxial Si layers grown at low temperatures. This led (9) to a proposed mechanism for the nucleation of stacking fault tetrahedra in  $\{111\}$  layers based on the intersection of three of these loops. The present work is evidence that our mechanism may be more general. Similar consideration of possible dislocation reactions leading to the arrangement of alternate intrinsic-extrinsic stacking faults in pyramidal formation in  $\{100\}$  layers shows that four perfect dislocations with inclined  $1/2\langle 110 \rangle$  Burgers vectors could dissociate into Shockley partials which then react to form  $1/6\langle 110 \rangle$  type stair-rods. However, we have not to date observed this type of defect.

The author is indebted to Drs. B.E. Watts and I.R. Sanders for supplying the material used in this study, and to the Plessey Company for permission to publish this note.

#### References

- (1) G.R. BOOKER, J. appl. Phys. 37, 441 (1966).
- (2) G.R. BOOKER and R. STICKLER, Appl. Phys. Letters 3, 158 (1963).
- (3) P.B. HIRSCH et al., Electron Microscopy of Thin Crystals, Butterworths, 1965.
- (4) R. GEVERS, A. ART, and S. AMELINCKX, phys. stat. sol. 3, 1563 (1963).
- (5) J.M. SILCOCK and W.J. TUNSTALL, Phil. Mag. 10, 361 (1964).
- (6) N. THOMPSON, Proc. Phys. Soc. B66, 481 (1953).
- (7) J.P. HIRTH and J. LÖTHE, Theory of Dislocations, Ser. Mat. Sci. Engng., McGraw Hill Publ. Co., 1968.
- (8) R. OGDEN, phys. stat. sol. (a) 14, K101 (1972).
- (9) R. OGDEN, R.R. BRADLEY, and B.E. WATTS, phys. stat. sol. (a) 26, 135 (1974).

(Received February 4, 1975)

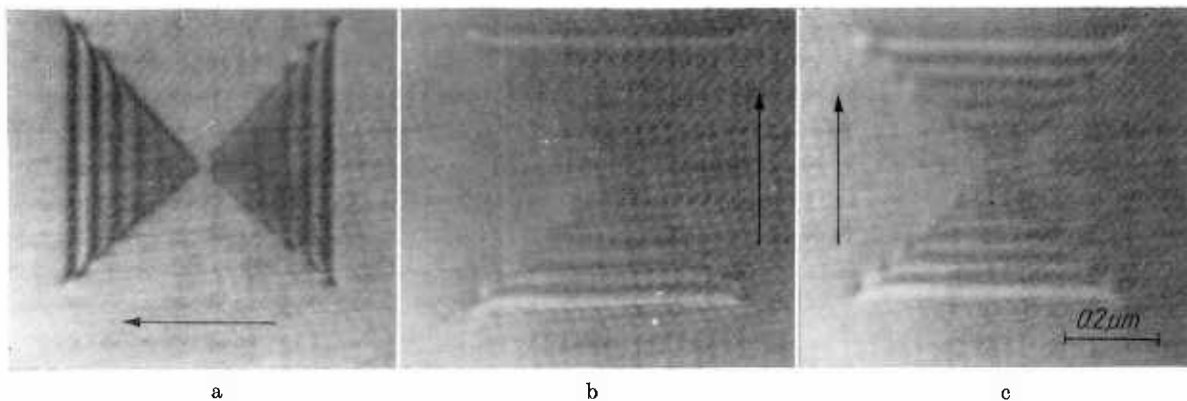


Fig. 1. T.E.M. micrographs of stacking fault pyramid; a) bright field  $(220)$  reflection, b) bright field  $(220)$  reflection, c) dark field  $(220)$  reflection

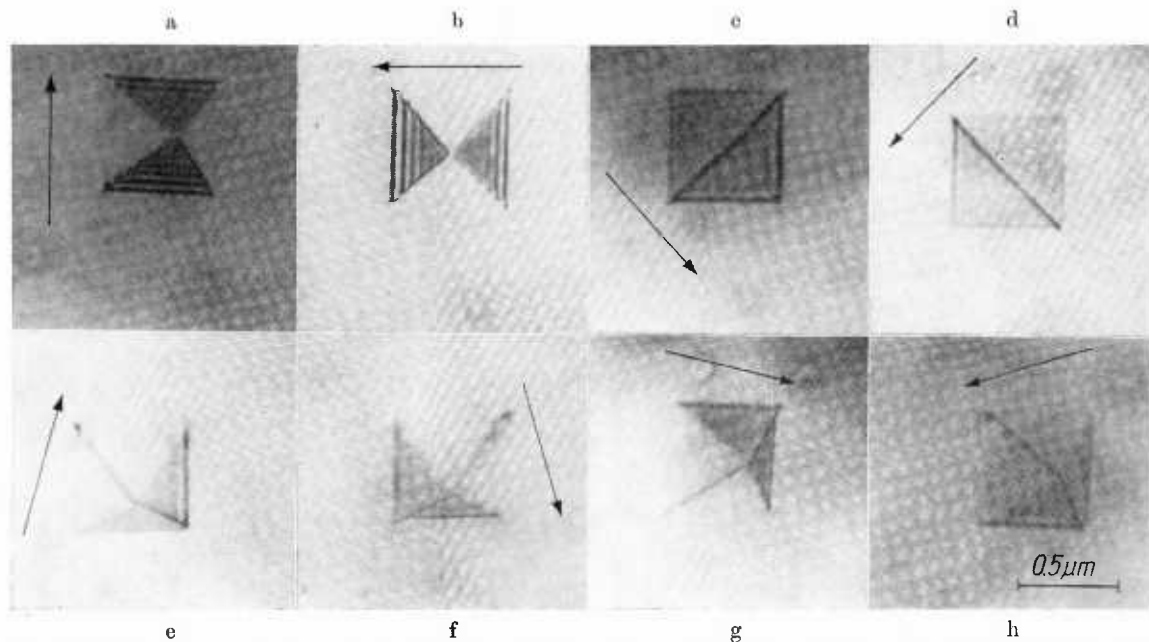


Fig. 2. Diffraction contrast analysis of stair-rod dislocations,  $s \geq 0$ . The arrow indicates the direction of  $\mathbf{g}$ ;  
 a)  $2\bar{2}0$ , b)  $\bar{2}\bar{2}0$ , c)  $400$ , d)  $0\bar{4}0$ , e)  $1\bar{3}1$ , f)  $3\bar{1}1$ , g)  $3\bar{1}1$ , h)  $\bar{1}\bar{3}1$

### Crystal imperfections in silicon epitaxial layers grown on ion-implanted substrates

Ion implantation is now being introduced into many semi-conductor manufacturing processes. Generally, it is extremely successful, but recently Moline *et al.* have observed that crystal defects can be generated in an epitaxial layer grown on an ion-implanted substrate [1]. They grew epitaxial layers by silane pyrolysis on substrates implanted with arsenic ions at 150 kV. The general perfection of growth was monitored by Berg-Barret X-ray topography but the individual defects were not identified. We have investigated a similar experimental system and have found the same imperfect growth. Further, we have used transmission electron microscopy (TEM) to identify the defects present as edge dislocations and epitaxial stacking faults.

2 in. diameter 5  $\Omega$ -cm p-type Si slices were implanted with arsenic ions at 100 kV and 1 mA through a thermal oxide mask. This mask consisted of fingers of oxide 650  $\mu$ m wide with

650  $\mu$ m spacing which was aligned parallel with the long axis of the ribbon beam of ions. The beam was held stationary while the slice was passed under the beam, moving perpendicular to the fingers of the mask. After each pass the slice was moved  $\sim$  1 mm parallel with the fingers of the mask and then passed under the beam in the opposite direction. The total dose received by the slice was  $\sim$   $10^{16}$  ions  $\text{cm}^{-2}$ . After implantation the slices were oxidized at 1200°C for 2 h. We examined the slices before and after epitaxial growth using Lang X-ray topography (XRT), platinum/carbon replicas and TEM.

The conditions of epitaxial growth and the observations made by the various techniques are shown in Table I.

Fig. 1 is a transmission X-ray topograph of part of a slice with 0.5  $\mu$ m epitaxial layer grown from silane at 1050°C. The ion implantation gives rise to bands of contrast running approximately parallel to the direction of movement of the slice as it passed under the ion beam. These bands are cut by the fingers of the oxide mask

TABLE I

Material	Visual inspection	XRT	Pt/C replica	TEM
Substrate after implantation and oxidation	Smooth polished surface	Bands of contrast, slip, "swirls"	Very smooth	Edge dislocation loops
Epitaxial layer grown from silane at 1050°C	Bands showing diffuse reflection	Bands of contrast, slip	Shallow circular depressions with pits at bottom	Epitaxial stacking faults $\sim$ $10^4$ $\text{cm}^{-2}$ ; edge dislocation segments $\sim$ $10^7$ $\text{cm}^{-2}$
Epitaxial layer grown from $\text{SiCl}_4$ at 1140°C	Smooth polished surface	Bands with slight contrast	Very smooth	Epitaxial stacking faults $\sim$ $10^4$ $\text{cm}^{-2}$

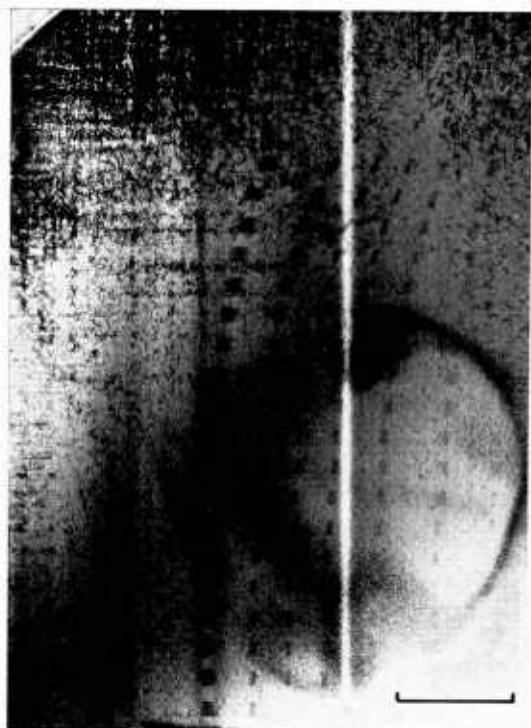


Figure 1  $220 \text{ MoK}\alpha_1$ , transmission X-ray topograph. Bar = 500  $\mu\text{m}$ .



Figure 2 Transmission electron micrograph of dislocation loops.  $220$  type reflection, bright-field. Bar = 1  $\mu\text{m}$ .

and result in the rectangles of high contrast seen in Fig. 1. Each of these rectangles contains defects too closely spaced to be individually resolved by X-ray techniques. TEM has high resolving power but requires specimens with a relatively high concentration of defects. We used XRT as a non-destructive method of selecting areas of high defect density for thinning for TEM. Fig. 1 also shows "swirling", which is believed to be due to point defects in the substrate [2] and dislocations generated by thermal slip. Fig. 2 is a transmission electron micrograph of one of the regions of high contrast seen in Fig. 1. The micrograph shows dislocation loops lying on (110) planes perpendicular to the (001) substrate plane. A complete Burgers vector analysis showed that they were sessile in nature with  $\frac{1}{2}\langle 110 \rangle$  Burgers vectors lying in the plane of the slice. Most of these dislocation loops penetrated  $> 1 \mu\text{m}$  into the substrate so that only the outer ends of the loop are seen in the micrograph. Similar dislocations are observed in heavily doped emitters and it has been suggested [3] that these dislocations are produced by a climb process using vacancies moving from

the surface. Alternatively, Hu [4] suggested that silicon interstitials are responsible for the climb. In either process, the layer of ion-implanted damage could supply either the vacancies or the interstitials required.

Although we observed a low density of epitaxial stacking faults, no oxidation-induced stacking faults were found. It is also worth noting that the pits revealed by Pt/C replicas on grown layers (Table I) were not associated with dislocations. It is known [5] that similar depressions can be caused by crystallites of SiC formed on the substrate surface due to contamination. Glancing angle electron diffraction was carried out on an ion-implanted substrate but no evidence of additional crystalline material was detected.

The observation that a large-area beam of ions produced narrow bands with high defect density was unexpected. The area covered by one pass of the beam had a large overlap with areas covered on preceding passes. The causes of this effect are not understood but are probably related to heating of the slice by the implanting beam.

The epitaxial layers grown from  $\text{SiCl}_4$  at  $1150^\circ\text{C}$  appeared to have a smooth shiny surface under visual inspection. Platinum/carbon replicas confirmed that the surface was free from steps of height greater than  $50 \text{ \AA}$ . However, XRT and TEM showed that defects were still present, though at low densities.

It is well known [6] that ion implantation creates an amorphous layer just below the surface of the crystal. As the surface is oxidized this layer is partly absorbed into the oxide and partly annealed out. Our work shows that the damage is not completely removed but that dislocation loops propagate into the crystal by a climb process. Most of these loops propagate more than  $1 \mu\text{m}$  into the crystal, a finding which is in conflict with Moline *et al.* [1]. These authors reported that the damage in their slices could be eliminated by etching only  $0.2 \mu\text{m}$  from the surface.

Under some conditions of epitaxy the ends of these dislocation loops propagate with the layer where they form the majority of defects found ( $\sim 10^7 \text{ cm}^{-2}$ ). The density of epitaxial stacking faults was much less ( $\sim 10^4 \text{ cm}^{-2}$ ). Although the growth from  $\text{SiCl}_4$  was much more successful, some defects were still present in those layers.

Work is continuing to elucidate the mechanisms by which the dislocations are formed. In particular we wish to investigate the effect of beam heating as both our results and those of

Moline *et al.* suggest that the defect density may be related to substrate temperature during implantation.

### Acknowledgements

We would like to thank Drs B. E. Watts and I. R. Sanders for supplying samples and for interesting discussions. The permission of the Plessey Company Limited to publish this work is acknowledged.

### References

1. R. A. MOLINE, R. LIEBERMAN, J. SIMPSON and A. U. MACRAE, *J. Electrochem. Soc.* **121** (1974) 1362.
2. A. J. R. DE KOCK, *Philips Res. Repts. Suppl.* (1973) No. 1.
3. M. YOSHIDA, E. ARAI, H. NAKAMURA and Y. TERUNUMA, *J. Appl. Phys.* **45** (1974) 1498.
4. S. M. HU, *ibid* **45** (1974) 1567.
5. A. G. CULLIS and G. R. BOOKER, *J. Crystal Growth* **9** (1971) 132.
6. R. W. BICKNELL, *Phil. Mag.* **26** (1972) 273.

Received 31 January

and accepted 17 February 1975

J. F. C. BAKER  
R. OGDEN

*Allen Clark Research Centre,  
The Plessey Company Limited,  
Caswell, Towcester,  
Northants, UK*

# OBSERVATION OF DISLOCATIONS IN A SILICON PHOTOTRANSISTOR BY SCANNING ELECTRON MICROSCOPY USING THE BARRIER ELECTRON VOLTAIC EFFECT

D. B. HOLT

Department of Metallurgy and Materials Science, Imperial College of Science and Technology, London SW7 2BP, U.K.

and

R. OGDEN

Allen Clark Research Centre, The Plessey Co. Ltd., Caswell, Towcester, Northants. U. K.

(Received 23 November 1974; in revised form 10 March 1975)

**Abstract**—Silicon planar phototransistors crossed by slip planes were examined both by X-ray topography and by conductive mode scanning electron microscopy using the barrier electron voltaic effect current as video signal. Only a few of the dislocations visible in the topographs gave rise to contrast in the scanning electron micrographs. This observation of single dislocations by means of the barrier electron voltaic effect is particularly valuable for the study of the role of defects in device failure and production yields as it renders visible only the electrically effective defects. Quantitative analysis of the barrier electron voltaic effect short circuit current obtained on scanning across an electrically effective dislocation provides a new means for measuring the electrical properties of dislocations. Repeated scanning produced lines of enhanced contrast across the surfaces of the devices. These lines were visible in surface X-ray topographs. This observation is believed to be due to beam induced damage in the oxide and interface region.

## 1. INTRODUCTION

The influence of crystallographic imperfections on the electrical behaviour of semiconductor devices has proved extremely complex [1, 2] and continues to be of major concern to manufacturers [3]. Although general correlations between device performance or device yields and imperfections have been reported [1, 2, 4] much work remains to be done to identify the mechanisms responsible and to obtain a quantitative understanding of the effects involved. It is necessary for this purpose to employ a number of different techniques of microscopy to ensure that all the important types of defects and inhomogeneities are detected. In addition techniques are needed to determine which specific defects are electrically active in each case and to measure the electrical properties of those defects. A programme of research of this type is in progress employing transmission electron microscopy, X-ray topography and scanning electron microscopy to examine silicon devices. It is found that the conductive mode of scanning electron microscopy employing barrier electron voltaic effect currents as video signal gives contrast due to electrical effects only [5, 6]. This technique therefore can select only the electrically active defects and give information relevant to their role in device operation. For example, using this technique in conjunction with transmission electron microscopy, Ravi *et al.* [7, 8] have recently succeeded in establishing that stacking faults cause leakage in silicon planar diodes only if the decorated partial dislocations which bound the stacking fault loops run through the depletion region of the junction.

This paper reports the result of examining phototransistors, from a region of a silicon slice crossed by slip, by

means of both X-ray topography (XRT) and the scanning electron microscope (SEM) using the barrier electron voltaic effect (barrier e.v.e.) and comparison is made with the results of transmission electron microscope observations of dislocations in adjacent areas of the slice.

## 2. EXPERIMENTAL METHODS

The test vehicle was an OPT 500 phototransistor fabricated in (111)  $8\ \Omega\ \text{cm}$  *n*-type Si. After a gas polish in HCl at  $1200^\circ\text{C}$ , a boron diffusion was carried out to form a base with a concentration in the solid of approximately  $C_b = 3 \times 10^{18}\ \text{cm}^{-3}$ , followed by a phosphorus emitter diffusion giving  $C_e \sim 10^{21}\ \text{cm}^{-3}$ . Contact was made to an Al land on the emitter and to the back of the chip as collector. Figure 1 shows a section through the device as well as the SEM signal detection circuit.

Transmission X-ray topographs were made of the slice using a Lang camera with  $\text{MoK}\alpha$  radiation and 220 reflections. The slice was then scribed and diced into squares each containing four devices, mounting the slice on PTFE tape to prevent scrambling. Selected devices were mounted on a TO5 header with a common collector post and the four emitters were wired to separate posts.

Specimens were examined in a Cambridge Instruments Stereoscan Mark IIA SEM in the conductive mode using the barrier e.v.e. current as signal. The barrier e.v.e. is analogous to the barrier photovoltaic effect and it produces a signal due to the separation of electron-hole pairs by the built-in field of a barrier such as the base-collector *p-n* junction in the present case. The magnitude of the resultant "charge collection current" is dependent on the charge collection efficiency of the barrier [5-8]. This charge collection efficiency will be reduced by any defects

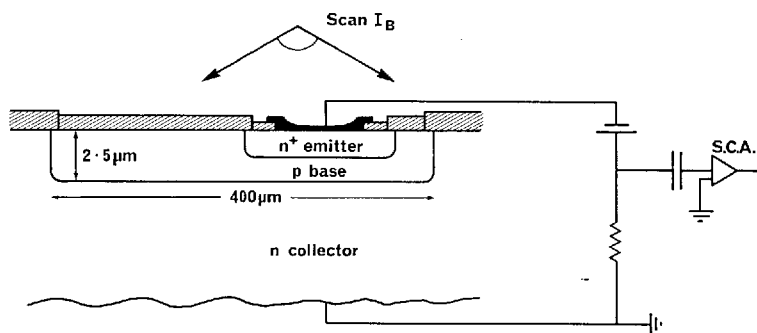


Fig. 1. Barrier electron voltaic effect detection circuit for the examination of planar devices scanned in plan view.

which either promote trapping or recombination of holes or electrons or which reduce the width of the depletion region of the barrier. The barrier e.v.e. is one of several phenomena sometimes referred to by the acronym "EBIC" for electron beam induced current. Terms specific to one mechanism such as the barrier e.v.e. current are preferable to the obscure general term. The barrier e.v.e. current was displayed as video signal on a C.R.T. screen scanned in synchronism with the scanning of the SEM electron beam over the surface of the phototransistor. This produced SEM micrographs in which contrast showed the location of those defects which affected the charge collection efficiency locally. In addition the signal was recorded, graphically, as a "Y-modulation line scan trace", for quantitative analysis. This was done for a line scan passing through the electrically active defects. The barrier e.v.e. detection circuit, as can be seen in Fig. 1, applied a reverse bias to the base-collector junction to widen the depletion region and increase the collecting field. The collector contact was a.c. coupled to the Cambridge Instruments "Specimen Current Amplifier" (S.C.A.) which fed into the video amplifier. Other specimens from the same slice were prepared for transmission electron microscope (TEM) examination by jet thinning in an HF plus HNO<sub>3</sub> reagent.

### 3. RESULTS

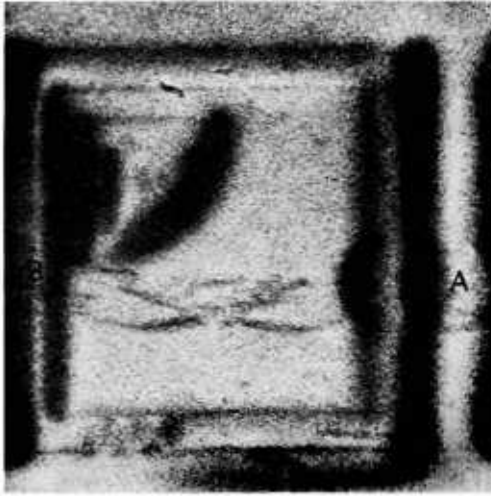
XRT showed a wide variation in dislocation density to occur across the slice. The most heavily dislocated areas were found mainly near the edge. Other work showed that the slip dislocations were mainly generated during the gas polishing treatment probably due to radial temperature gradients and consequent stresses across the slice[9]. Examination by TEM confirmed that other defects such as stacking faults and precipitates were not present in high concentrations although emitter edge dislocations[10] were sometimes found. Such dislocations could not be observed by XRT because of window contrast at the emitter.

SEM observations on some devices revealed prominent spots of black/white contrast in the barrier e.v.e. micrographs. These spots did not correspond to any surface features visible in this secondary electron emissive mode SEM micrographs. Comparison with the XRT micrographs showed that the barrier e.v.e. spots were associated with regions containing dislocations. A device which

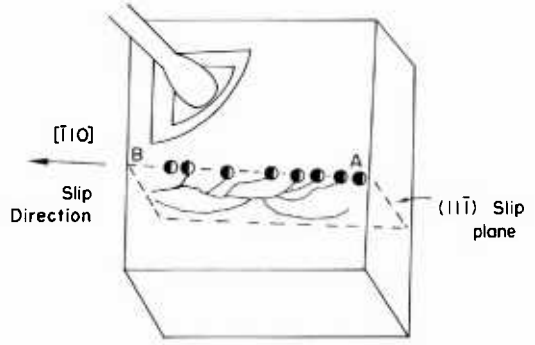
illustrates this observation, containing a few dislocations distributed in a narrow slip band across the device, is shown in Fig. 2a. In the corresponding barrier e.v.e. micrograph, Fig. 2b, some but not all of the dislocations display contrast. The row of point contrast features running across the diode along the line B-A in Fig. 2b correspond to the ends of dislocations lying along the top edge of the band of slip visible on Fig. 2a. Since the XRT transmission technique reveals dislocations throughout the entire 200 μm thickness of the slice, it is clear that along most of their lengths most dislocations will lie below the depletion region of the junction and hence will not contribute to the image. The considerable projected length of some of these dislocations shows that they run approximately parallel to the (111) plane of the slice. The geometry of the slip plane is indicated in Fig. 2c. This diagram was produced by superimposing tracings of identical sized prints of figures (a) and (b). It can be seen that dislocations visible in (a) were found to end in each of the point contrast features along line B-A except for the two outermost ones. These each occur in regions in which visibility is lost in the X-ray topograph in the large dark areas due to the elastic strain fields arising at the edges of the emitter and base regions. Crystallographically it was established that the (111) plane is inclined as shown and therefore the ends of dislocations which give rise to barrier e.v.e. contrast are specifically those at the top of the slice, i.e. those which come up through the base-collector junction.

The smaller, more sharply defined spots in Fig. 2b are due to surface debris which is also visible in the secondary emissive mode micrograph, Fig. 2d.

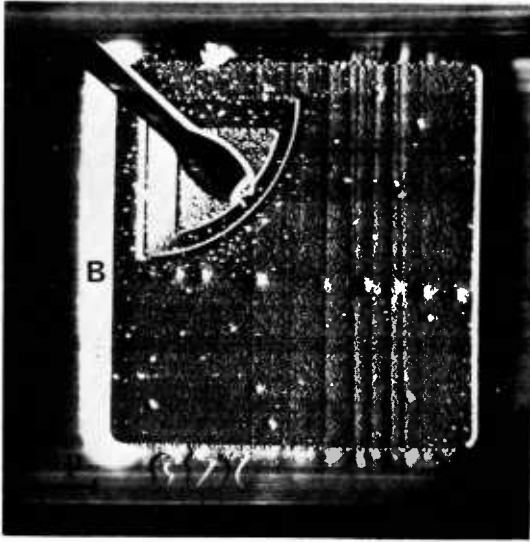
A number of other examples of the correspondence of rows of barrier e.v.e. point contrast features and slip planes containing dislocations were examined. It was seen that dislocations give rise to contrast in the conductive mode SEM micrographs only inside the transistors, when heavily dislocated slip bands crossed a series of devices. This fact proves that this form of contrast arises only where dislocations intersect the *p-n* junctions and eliminates any possibility of explaining the effect by any non-barrier mechanism. It was seen that some rows of barrier e.v.e. point contrast features correspond to slip that was hardly visible in the X-ray topographs. This emphasised the importance of the multi-technique approach to the analysis of structural defects in devices.



(a)



(c)



(d)

Fig. 2. Silicon phototransistor crossed by a slip band. (a) X-ray projection topograph (Lang technique). (b) SEM conductive mode micrograph. The barrier e.v.e. short circuit current was used as video signal. (c) The geometry of the slip plane containing the dislocations in this device. (d) Secondary electron SEM micrograph showing the surface topography of the phototransistor.

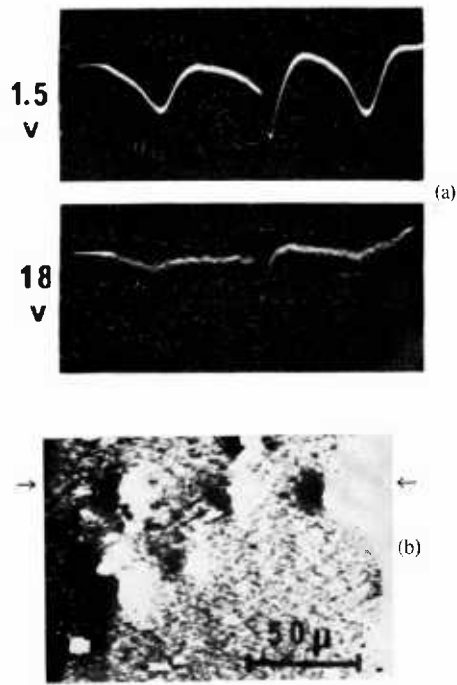


Fig. 3. (a) Barrier e.v.e. short circuit current for two values of reverse bias voltage, vs distance scanned along a line marked through the three point contrast features in (b).

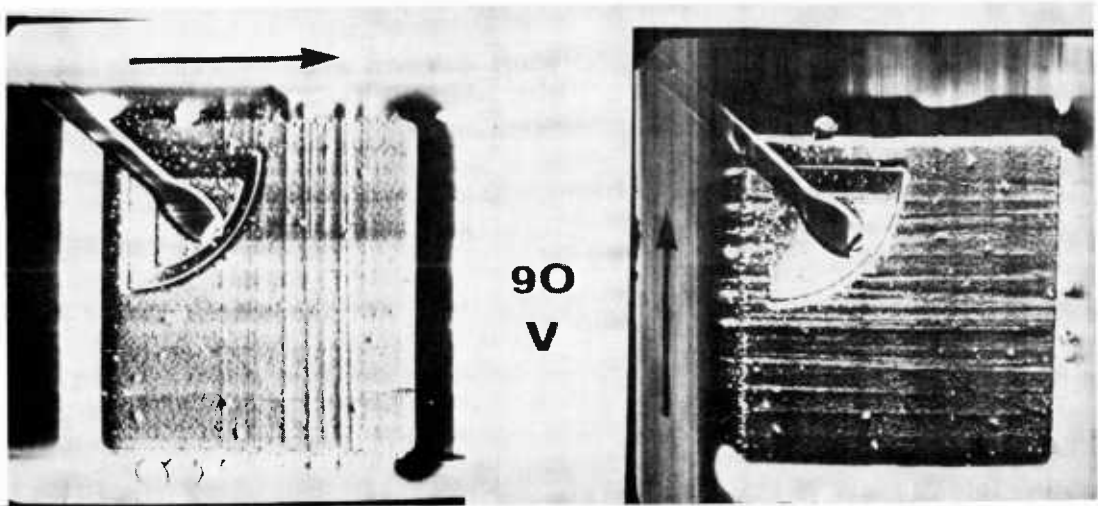


Fig. 4. Two barrier e.v.e. micrographs of the device shown in Fig. 2(b). The scan direction in (a) was horizontal, that in (b) was vertical. The lines of enhanced contrast which appear in each case are those orthogonal to the scan direction.

Any one technique will direct attention primarily to those defects which are prominently visible by that technique, and leave others in obscurity. For a complete analysis of structure a combination of techniques must be used and then it must be determined which, if any, defects are responsible for a particular physical effect. In the present case the dislocations responsible for the line D to G run nearly vertically through the slice and therefore appear only as relatively short lines in the X-ray topograph.

Barrier electron voltaic contrast due to dislocations diminishes with increasing junction reverse bias as shown by the barrier e.v.e. current traces of Fig. 3. These are Y-modulation line scans recorded along the line marked by arrows in Fig. 3(b) passing through three barrier e.v.e. point contrast features. There was a surface dust particle almost coincident with centre of the middle point contrast feature of the three. This cannot be seen in (b) but was readily detected in the emissive mode SEM micrograph of this area. This dust particle was responsible for the deep, narrow minimum occurring within the broader, central trough in the 1.5 V trace. It can be seen that this narrow minimum in the barrier e.v.e. signal was still readily distinguished in the trace recorded with a bias of 18 V, whereas the barrier e.v.e. point contrast minima were virtually eliminated. Correspondingly, the point contrast features disappeared from conductive mode barrier e.v.e. micrographs recorded at high junction biases.

Another significant observation appears in Fig. 2b. That is the set of prominent horizontal lines across the device. These were produced as a result of prolonged scanning of the lines concerned and are parallel to the scan directions employed. This is illustrated in Fig. 4. Due to the capacitive coupling of the amplifier (Fig. 1) enhanced signal strength during the scanning of a line (i.e. a raised or lowered d.c. signal) does not appear in the video display. Thus for horizontal or vertical scanning only the lines of contrast in the orthogonal direction appear as can be seen in Figs. 4a and b. The dislocations do not appear in Fig. 4 because increasing the reverse bias on the *p-n* junction decreased the dislocation contrast. At the value of 90 V applied in Fig. 4 the dislocations are no longer visible. Surface X-ray topography employing rays reflected at a glancing angle, showed up the same lines, as can be seen in Fig. 5.

#### 4. DISCUSSION

##### 4.1. First observation of individual dislocations by barrier electron voltaic contrast

This is believed to be the first unambiguous observation of dislocations by means of barrier e.v.e. contrast in conductive mode SEM micrographs. There have been a number of previous reports of such observations. Several papers contained SEM micrographs using the barrier e.v.e. current as video signal and showing Si *p-n* junctions crossed by dark lines which were ascribed to diffusion induced dislocations[11-14].

This interpretation was supported by comparison of the patterns on the SEM micrographs with the results of etching the diodes[12] and a calculation of the lifetime and capture radius for recombination at the

dislocations[14]. Neither of these was conclusive and in fact it is now clear that the lines seen in barrier e.v.e. micrographs of diodes in which diffusion induced slip has occurred are slip planes containing many dislocations rather than individual dislocations. This is known from comparison of the results of transmission electron microscope studies which are capable of resolving the individual dislocations with the results of XRT or etching studies which cannot resolve the individual dislocations in the case of such high dislocation densities as occur in diffusion induced slip specimens.

Dark lines were also observed around indentations in Si diodes after annealing and these were ascribed to dislocations[13]. It was subsequently shown that a similar observation, which was also supported by comparison with etching observations was in fact due to cracks, not dislocations[15]. Etching is not generally capable of unambiguously distinguishing one type of defect from another. This doubt applies also to the recent report of dark lines seen on barrier e.v.e. micrographs of GaP diodes[16]. In the present case, XRT applied to diodes containing low densities of dislocations, as confirmed by transmission electron microscopy, does unambiguously show that the spot contrast features of for example Fig. 2b do correlate with individual dislocations.

##### 4.2. Mechanism of barrier electron voltaic effect contrast

The barrier e.v.e. operates in a manner analogous to that of the better-known barrier photovoltaic effect. The built-in field of the barrier separates hole-electron pairs generated by electron bombardment (barrier e.v.e.) or light (barrier p.v.e.) in or near the depletion region. The charges are separated or "collected", holes in the *p*-type and electrons in the *n*-type material, so that the barrier is forward biased. The theory of barrier e.v.e. contrast is concerned with the use of the short circuit current,  $I_{sc}$  as SEM video signal. It can be shown[6] that

$$I_{sc} = \eta_{ec} G I_b / q \quad (1)$$

where  $\eta_{ec}$  is the charge collection efficiency of the barrier,  $G$  is the generation factor, i.e. the number of hole-electron pairs generated per incident electron,  $I_b$  is the electron beam current and  $q$  the charge on an electron.

In plan-view scanning which is the geometry involved in the examination of planar devices as employed in this type of work[6, 8, 11-16] defect contrast arises from variations in  $\eta_{ec}$ . The problem of quantitative interpretation of the contrast due to defects then is to calculate their effect on  $\eta_{ec}$ . The form of the line scan traces of Fig. 3 is of course influenced by the response characteristics of the detection circuit of Fig. 1 as well as by the effect of the dislocations on  $\eta_{ec}$ . In principle, analysis of this type of observation provides a new high-resolution method for measuring certain of the electrical properties of dislocations and other defects[7, 8, 17]. An analysis of this information is in progress.

The contrast in barrier e.v.e. micrographs arising from some particles on the surface, e.g. as shown in Fig. 3 arises as follows. These particles appear in bright contrast

in emissive mode micrographs such as Fig. 2(d). This shows that they cause increased emission of beam energy in the form of emitted electrons. There is therefore a corresponding reduction in the effective beam energy dissipated as hole electron pairs, i.e.  $GI_e$ , is reduced in eqn 1. Since there is a difference in the contrast mechanisms of dislocations and surface particles, it is understandable that the two react differently to changes in junction bias as in Fig. 3(a).

#### 4.3. Beam-induced line contrast

The lines of enhanced contrast visible in Figs. 4a and b were produced by prolonged beam scanning (of the order of a minute, along a single line at 30 KV and about  $10^{-10}$  A). They have an analogous form of contrast to the dislocations. That is, the initial effect on scanning across these lines is dark, due to a reduction in the barrier e.v.e. current, followed by bright due to an increased signal. Two possible explanations are obvious. This effect might be due to radiation damage due to electron bombardment or to the deposition of hydrocarbon films which generally results from the electron bombardment of the vacuum pump oil deposits which occur in conventional SEMs. The XRT micrograph in Fig. 6 indicates that internal crystallographic imperfections were present in these lines. It may be therefore that this is a direct observation of the phenomenon responsible for the fact that SEM examination of Si devices and the operation of electron bombarded semiconductor (EBS) devices is not truly non-destructive but does gradually degrade device performance [18]. The nature of this phenomenon is also under further investigation.

*Acknowledgements*—This work was supported by the Science Research Council and the Plessey Co. Ltd. It is a pleasure to thank Mr. J. B. Steyn for his assistance with the scanning electron microscope.

#### REFERENCES

1. H. F. John, *Proc. IEEE* **55**, 1249 (1967).
2. G. H. Schwuttke, *Microelectronics and Reliability* **9**, 397 (1970).
3. H. R. Huff and R. R. Burgess, Editors, *Semiconductor Silicon 1973, Proc. 2nd Int. Symp. on Si Mater. Sci. and Technol.*, Chicago. Electrochem. Soc.: Princeton, New Jersey (May 1973).
4. J. M. Fairfield and G. H. Schwuttke, *J. Electrochem. Soc.* **113**, 1229 (1966).
5. D. B. Holt and B. D. Chase, *Phys. Stat. Sol.* **a20**, 135 (1973).
6. D. B. Holt, In *Quantitative Scanning Electron Microscopy*, (Edited by D. B. Holt, M. D. Muir, P. R. Grant and I. M. Boswarva) Chap. 8. Academic Press, London (1974).
7. K. V. Ravi, C. J. Varker and C. E. Volk, *J. Electrochem. Soc.* **120**, 533 (1973).
8. C. J. Varker and K. V. Ravi, *J. Appl. Phys.* **45**, 272 (1974).
9. J. Bloem and A. H. Goermans, *J. Appl. Phys.* **43**, 1281 (1972).
10. G. H. Schwuttke and G. K. Howard, *J. Appl. Phys.* **37**, 4394 (1966).
11. J. J. Lander, H. Schreiber, T. M. Buck and J. R. Mathews, *Appl. Phys. Letts.* **3**, 206 (1963).
12. W. Czaja and G. H. Wheatley, *J. Appl. Phys.* **35**, 2782 (1964).
13. W. Czaja and J. R. Patel, *J. Appl. Phys.* **36**, 1476 (1965).
14. W. Czaja, *J. Appl. Phys.* **37**, 4236 (1966).
15. N. F. B. Neve and P. R. Thornton, *Solid-St. Electron.* **9**, 900 (1966).
16. G. B. Stringfellow, P. F. Lindquist, T. R. Cass and R. A. Burmeister, *J. Electronic Materials* **3**, 497 (1974).
17. H. F. Matare and C. W. Laakso, *J. Appl. Phys.* **40**, 476 (1969).
18. D. J. Bates, A. Silars and A. Ballonoff, *Solid-St. Technology* **31** (July 1974).